Electronic Thesis and Dissertation Repository

6-18-2012 12:00 AM

Investigation of in-vivo hindfoot and orthotic interactions using bi-planar x-ray fluoroscopy

Kristen M. Bushey
The University of Western Ontario

Supervisor
Dr. Thomas Jenkyn
The University of Western Ontario

Graduate Program in Mechanical and Materials Engineering
A thesis submitted in partial fulfillment of the requirements for the degree in Master of Engineering Science
© Kristen M. Bushey 2012

INVESTIGATION OF *IN-VIVO* HINDFOOT AND ORTHOTIC INTERACTIONS USING BI-PLANAR X-RAY FLUOROSCOPY

(SPINE TITLE: EFFECT OF ORTHOTICS ON HINDFOOT USING BI-PLANAR FLUOROSCOPY)

(Thesis Format: Integrated Article)

by

Kristen M. <u>Bushey</u>

Department of Mechanical and Materials Engineering Graduate Program
in Engineering Science

A thesis submitted in partial fulfillment
of the requirements for the degree of
Master of Engineering Science

The School of Graduate and Postdoctoral Studies
The University of Western Ontario
London, Ontario, Canada

UNIVERSITY OF WESTERN ONTARIO
School of Graduate and Postdoctoral Studies

CERTIFICATE OF EXAMINATION

Supervisor   Examiners

_____   _____
Dr. Thomas R. Jenkyn, Ph.D, P.Eng   Dr. Sam Asokanthan, Ph.D
Department of Mechanical & Materials   Department of Mechanical & Materials
Engineering   Engineering
School of Kinesiology

                                            _____
                                            Dr. Louis Ferreira, Ph.D, P.Eng
                                            Department of Mechanical & Materials
                                            Engineering

                                            _____
                                            Dr. Jim Lacefield, Ph.D, P.Eng
                                            Deparment of Electrical and Computer
                                            Engineering
                                            Department of Medical Biophysics

The thesis by

Kristen Melissa <u>Bushey</u>

Entitled:

Investigation of *in-vivo* hindfoot and orthotic interactions using bi-planar x-ray fluoroscopy

is accepted in partial fulfillment of the
requirements for the degree of
Master of Engineering Science

_____   _____
Date   Chair of the Thesis Examination Board

ii

ABSTRACT

A markerless RSA method was used to determine the effect of orthotics on the normal, pes planus and pes cavus populations. Computed tomography (CT) was used to create bone models that were imported into the virtual environment. Joint coordinate systems were developed to measure kinematic changes in the hindfoot during weight-bearing gait and quiet standing. The objectives of this thesis were to (1) implement a fluoroscopy-based markerless RSA system on the foot, (2) determine the effect of various orthotics at midstance of fully weight-bearing dynamic gait, and (3) determine the effect of orthotics as measured using three different techniques. Every individual in this study reacted differently depending on the footwear condition tested. Despite the change in alignment caused by orthotics lacking statistical significance it appears the change may be significant with more subjects. Fluoroscopy should enable substantial improvements in orthotic design for optimal results in the future.

Keywords: fluoroscopy; radiostereometric analysis (RSA); hindfoot; orthotics; kinematics; computed tomography (CT); pronation; supination

CO-AUTHORSHIP

This work could not have been completed without the help of others, whom the author acknowledges. The contributions they have made are detailed below.

Chapter 1: Kristen Bushey- wrote manuscript; Thomas Jenkyn- reviewed and revised manuscript.

Chapter 2: Kristen Bushey- designed study, collected data, analyzed data, and wrote manuscript; Megan Balsdon- collected data; Anglea Kedgley- developed components of system; Anne-Marie Fox- developed components of system; Colin Dombroski- designed the orthotics and assisted in study design; Thomas Jenkyn- reviewed and revised manuscript.

Chapter 3: Kristen Bushey- designed study, collected data, analyzed data, and wrote manuscript; Megan Balsdon- collected data; Anglea Kedgley- developed components of system; Anne-Marie Fox- developed components of system; Colin Dombroski- designed the orthotics and assisted in study design; Thomas Jenkyn- reviewed and revised manuscript.

Chapter 4: Kristen Bushey- designed study, collected data, analyzed data, and wrote manuscript; Megan Balsdon- collected data; Anglea Kedgley- developed components of system; Anne-Marie Fox- developed components of system; Colin Dombroski- designed the orthotics and assisted in study design; Thomas Jenkyn- reviewed and revised manuscript.

Chapter 5: Kristen Bushey- designed study, collected data, analyzed data, and wrote manuscript; Megan Balsdon- collected data; Colin Dombroski- designed the orthotics and assisted in study design; Thomas Jenkyn- reviewed and revised manuscript.

Chapter 6: Kristen Bushey- wrote manuscript; Thomas Jenkyn- reviewed and revised manuscript.

ACKNOWLEDGEMENTS

This thesis would not have been possible without the guidance and the help of several individuals who in one way or another assisted in the preparation and completion of this study.

First and foremost Dr. Tom Jenkyn, thank you for your support, knowledge, and the opportunity to pursue research in the biomechanics field. Thank you for all your advice and guidance throughout my studies at Western.

Thank you to my examiners Dr. Sam Asokanthan, Dr. Louis Ferreira, and Dr. Jim Lacefield for taking the time to read and critique this thesis.

This study would have never been possible without the help of others. A huge thank you must go to Megan Balsdon for helping keep me sane throughout this fluoro study. Thanks for being there throughout and mentally helping with the fluoroscopy system. To Angela Kedgley and Anne-Marie Fox, this thesis would have never been possible without your previous work in WOQIL, let alone all the emails you two answered along the way. Thank you to Ian Jones for all your help during the process. To all members of the WOBL thanks for making the days in the lab more enjoyable.

Thank you to Colin Dombroski for mentoring along the way, providing the orthotics for the study and helping with the recruitment of patients. Thank you for sharing your knowledge in the pedorthic field, editing and explaining things along the way. Your input is always appreciated.

Thank you to John Henry for taking such great fluoroscopy images, dealing with our syncing system and making testing days that much better. Thank you to all the subjects who agreed to participate in this work.

To my Mother, although you are not with me I know you would have supported me the entire time, and the memories of you have always been enough to continuously motivate me in life. Dad, I could have never made it through this without you. I appreciate all the help, love and support you have given me throughout. Matthew, you are the best brother I could have asked for! Thanks for always being there to chat about life, school, and anything. You can always put a smile on my face.

Finally, thank you to Michael Stitz I bet you never thought this day would come. Thanks for allowing me to discuss biomechanics with you and rationalize my thoughts. Thanks for being supportive over the years. I look forward to all our future adventures together.

TABLE OF CONTENTS

LIST OF TABLES

LIST OF FIGURES

LIST OF APPENDICES

LIST OF ABBREVIATIONS, SYMBOLS, AND NOMENCLATURE

°- degree(s)

>- greater than

<- less than

α – dorsi/plantar flexion

β – inversion/ eversion

γ – internal/external rotation

θ – rotation about the Z axis

2D – two dimensional (two dimensions)

3D – three dimensional (three dimensions)

ANOVA- Analysis of Varience

CAD – computer aided design

cal- calcaneus

cm – centimetre

CT – computed tomography

cub- cuboid

d – distance from the x-ray source (s) to the projection of the x-ray source on the image plane (s")

II – image intensifier

ISB – International Society of Biomechanics

kV – kilovoltage

kVp – peak kilovoltage

mA – milliampere(s)

mm – millimetre(s)

MRI – magnetic resonance imaging

nav- navicular

RMSE – root mean squared error

RSA – radiostereometric analysis

SEM – standard error of measurement

tibfib- tibia/fibula

wrt- with respect to

INDEX OF TERMS

Medical Definitions were cited or adapted from Dorland's Online Medical Dictionary (www.mercksource.com)

Abduct: To draw away from the midline of the body

Adduct: To draw towards the midline of the body

Anterior: Situated toward the front

Arthroplasty: The surgical repair of a joint

Articulation: The action or manner in which the parts of a joint come together

Aseptic: In the absence of pathological micro-organisms

Cadaveric: Pertaining to a human body preserved for anatomical study

Cartilage: A covering on the articular surface of bones in synovial joints, which allows for smooth joint motion

Coordinate System: A method of representing points in space of give dimensions by coordinates.

Coronal plane: A vertical plane, perpendicular to the sagittal plane that separates the body into anterior (front) and posterior (back) portions

Distal: Situated away from the point of attachment or centre of the body

Dorsiflexion: Movement which decreases the angle between the superior surface of the foot and the leg

Dynamics: Branch of mechanics that is concerned with the effects of forces on the motion of a body or system of bodies

External rotation: Is rotation away from the centre of the body.

Frontal plane: See coronal plane

Goniometer: An instrument for measuring angles

In-vitro: Outside the living body in an artificial environment

In-vivo: In the living body of a plant or animal

Inferior: Situated below, or directed downwards

Internal rotation: Rotation about the long axis of the tibia medially

Kinematics: The branch of mechanics dealing with the study of the motion of a body or a system of bodies without consideration of its mass or the forces acting on it

Kinetics: The study of motion and its causes

Lateral: Situated away from the midline of the body

Ligament: A tough band of tissue that connects bones

Medial: Situated closer to the midline of the body

Optimization: A mathematical algorithm that is used to find the best solution to an indeterminate system based on its objective function

Orthopaedics: A branch of surgery dealing with the preservation and restoration of the function of the skeletal system, its articulations, and associated structures

Pathology: The branch of medicine treating the essential nature of disease

Plantarflexion: movement which increases the angle between the front part of the foot and the shin

Posterior: Situated behind or toward the hind part of the body

Proximal: Situated toward or closer to the point of attachment or centre of the body

Radio opaque: Obstructing the passage of radiant energy, such as x-rays

Radiostereometric Analysis: The reconstruction of a three-dimensional object from two images

Sagittal plane: A vertical longitudinal plane that divides a body intro right and left halves

Superior: Situated above or directed upwards

Synovial joint: A specialized joint that permits more or less free movement, the union of the bony elements being surrounded by an articular capsule enclosing a cavity lined by synovial membrane

Tendon: A tough cord or band of connective tissue that attaches a muscle to bone or cartilage

Transverse plane: Horizontal plane passing through the body perpendicular to the coronal and sagittal planes, dividing the body into superior and inferior segments

Transformation: A coordinate transformation is a conversion from one coordinate system (i.e. laboratory coordinate system) to another (i.e. joint coordinate system) to describe the same space

Tuberosity: a projection or a protuberance, especially at the end of a bone for muscle or tendon attachment.

CHAPTER 1- INTRODUCTION

OVERVIEW: The current state of biomechanics research surrounding the foot and ankle region and the effect of orthotic insoles requires a more thorough analysis. This chapter begins by detailing the most common methods presently used for quantifying joint kinematics. It then outlines the history of radiostereometric analysis (RSA) and its applications. A brief summary of foot anatomy, orthotics, and kinematics that will be required for subsequent chapters is also given. The chapter concludes with rationale, objectives and hypotheses of this work.

1.1 TRADITIONAL METHODS TO ANALYZE JOINT BIOMECHANICS

Biomechanics is the study of mechanical behaviour of biological tissues, segments and bodies. The study of biomechanics dates back more than two thousand years ago. The biomechanical research of Aristotle (384-322 BC), Leonardo da Vinci (1452-1519), Galileo Galilei (1564-1642) are just a few examples that biomechanics was an important part of the Greek Revolution as well as the European Renaissance (Humphrey, 2002). Orthopaedics is the medical specialty that focuses on injuries and diseases of the body's musculoskeletal system including: bones, joints, ligaments, tendons, muscles and nerves. These are the fundamental aspects that allow for movement, work, and daily activity. The technological methods used to explain orthopaedic biomechanics are constantly evolving when questions still remain

unanswered regarding disease progression, compensation mechanisms, recovery techniques and success.

The study of biomechanics can be divided into two groups: kinematics and kinetics. Kinematics defines the range and nature of motion in any joint and describes the motion of a body segment in three planes: frontal (coronal or longitudinal), sagittal, and transverse (horizontal) (Nordin & Frankel, 2001). Kinematics is concerned with the description of motion, but not with the causes of motion. Kinetics on the other hand is concerned about the causes of motion. Kinetics is the study of forces and moments of force acting on tissues, body segments and joints both statically and dynamically (Nordin and Frankel, 2001). In this thesis the kinematics of interest are specifically those of the bones within the human foot and ankle.

There are numerous methods used to quantify human joint motion both *in-vivo* and *in-vitro*. *In-vivo* is considered to be experimentation using a whole, living organisms as opposed to an *in-vitro* which uses partial or dead organisms in a controlled environment. *In-vivo* testing is generally preferred over *in-vitro* because it's better suited for observing overall effects of an experiment on a living subject. In-vitro techniques include using cadavers to mimic real-life motions (Ferreira *et al.,* 2010), as well as testing implant wear (Burton *et al.,* 2012), and subjecting the specimen to scenarios that would never be approved in living creatures (Hashimoto *et al.,* 2012). The investigation of tissue loading, in particular, bone, ligaments and tendons are essential from a clinical perspective to gain insight into injury mechanisms, and biomechanical function. *In-vivo* experiments consist of two types: invasive and non-invasive. Ethically it becomes more

challenging with *in-vivo* experimentation especially one in which the technique used is invasive. Examples of some invasive measurement techniques involve the use of bone pins (McClure *et al.,* 2001) or transducers, and standard radiostereometric analysis (Kedgley, 2009). Invasive techniques require penetration of the skin which lends itself to complications (Tranberg, 2011). Invasive techniques may be more accurate and reproducible however they are generally less accessible and less safe for those involved (Tranberg, 2011). Non-invasive techniques to measure *in-vivo* kinematic measurement include: goniometers, potentiometers, inclinometers, photographic and video cameras, optical and electromagnetic tracking systems, and medical imaging techniques (Futai *et al.,* 2010; Allen, 2009; Svedmark *et al.,* 2011). Each technique is more applicable to certain applications, and includes both advantages and disadvantages.

1.1.1 GONIOMETER, POTENTIOMETER, AND INCLINOMETER

A goniometer is an instrument commonly used to measure a joint angle. This device is essentially a protractor containing two long arms which rotate about a central axis. The central axis may be attached to the joint of interest and the angle is read manually. Consequently, this device is limited to static positions. A potentiometer is a form of sliding-contact resistive transducers that converts a mechanical displacement input into an electrical output based on the change in the effective length of a conductive material located within the device. A potentiometer can be incorporated into a goniometer to allow electronic readings which can be used to measure both static and dynamic measurements. An inclinometer is an instrument for measuring angles of slope,

and elevation or depression of an object with respect to the horizontal. They can be read both manually or electronically.

Advantages with goniometers and inclinometers include that they are relatively inexpensive, provide immediate output and are portable. However, they are only able to measure relative angles not absolute, they may be difficult to align correctly with the bones of interest, and their measurements could be inaccurate due to their movement relative to the underlying anatomy during subject motion. Additionally, goniometers act as a simple hinge that can only measure motion about a single axis which could constrain the motion of a subject. With this in mind goniometers are not useful in measuring complex motions, making precise or accurate measurements, especially when there may be a significant mass of soft tissue between the skin and the bone (Winter, 2009). Goniometers are useful for a quick, single joint measurement where high precision and accuracy are not required.

1.1.2 PHOTOGRAPHIC AND VIDEO CAMERAS

High-speed photographic and video camera techniques are capable of capturing full body motion without interfering with the movement. Video cameras have been used to analyze factors in running such as step length, step frequency and contact time on the ground (Padulo *et al.,* 2011). In addition video cameras have been used to measure posture (Xu *et al.,* 2011), and body segment joint angles (Mizner *et al.,* 2012; Winter, 2009). The cameras can be high speed with capture rates around 210 frames per second (Padulo *et al.,* 2011) or can be standard capture at 30 frames per second (Mizner *et al.,* 2012). Generally, the camera is located far enough away from the subject so motion is

not interrupted and the angle is usually setup to be perpendicular to the plane of interest. For example if camera is located perpendicular to the sagittal plane motions step length (Padulo *et al.,* 2011) and posture (Xu *et al.,* 2011) can be measured. The aperture speed of the camera allows the movements to be captured without blurring. One advantage of the high speed cameras is the lack of image degradation during the subjects' movements. Multiple cameras are required if three-dimensional (3D) measurements are desired. Projection errors may occur if a single camera is used because the motion of the subject may not be directly in line with the cameras view (Bechard *et al.,* 2009). Analysis of kinematics using a video cameras sequence of images can be completed using motion analysis software such as Dartfish 5.5 Pro (Dartfish; Swiss Federal Institute of Technology, Fribourg, Switzerland) or ImageJ (ImageJ; National Institutes of Health, Bethesda, Maryland). These programs can be used to digitize the location of landmarks on the body or markers that have been attached to the body to determine kinematic changes during a study. The accuracy associated with this measurement technique is dependent on the sample rate used, the use of markers, and the distance from the subject. Data from at least two cameras can be combined by calibrating the volume of interest with an object of known dimensions using methods similar to optical motion tracking systems, described in the next section. This additional data will allow for the kinematics to be quantified in three dimensions.

1.1.3 OPTICAL AND ELECTROMAGNETIC TRACKING SYSTEMS

Three-dimensional optical and electromagnetic tracking systems are used to more accurately quantify kinematic motion in three dimensions. Optical motion systems

use a series of cameras that track sets of either passive (light-reflecting) or active (light-emitting) markers. Passive systems, such as the six-camera real-time motion analysis system (Hawk cameras, Cortex software system, Motion Analysis Corp., Santa Rosa, California, USA) at the Wolf Orthopaedic Quantitative Imaging Laboratory (WOQIL), track reflective markers. Active systems such as Cortex (Northern Digital Inc., Waterloo, Ontario, Canada) track infrared diodes that may either be wired or wireless. In both the passive and active systems markers are placed on anatomical landmarks or body segments of interest. In an optical motion capture system (passive or active) a person is required to have markers on some body parts. Reflective markers need to be placed in a location where the skin is close to the bone in order to reduce the introduction of skin motion artifact (explained in detail in section 1.1.4). The markers are generally placed on specific joint locations or feature points of interest on the human body. Optical motion capture systems are commonly used to analyze gait. There are two common marker sets used in gait analysis laboratories. These include the Cleveland Clinic Marker Set and the Helen Hayes Marker Set (Madihally, 2010). The Helen Hayes marker set was developed at the Helen Hayes Hospital and is the more popular of the two. In the Helen Hayes marker set, 15 markers are placed over bony landmarks. The markers are captured by the cameras to define joint centers and relevant axes of rotation. The markers typically reflect the infrared light, which is picked up by the cameras in a direct sight to the marker. So long as at least two cameras can image the marker, direct linear transformation (DLT or triangulation) and multi-based correlation methods are used to estimate the position of the markers with respect to the cameras and the laboratory

frame of reference (Madihally, 2010). Provided three markers per segment are triangulated, a post-processing software package (i.e. Cortex and OrthoTrak; Motion Analysis Corporation, Santa Rosa, CA, USA) calculates the position and orientation of the segment with respect to its more proximal segment. This is most often reported as Euler angles or joint angles. While some user intervention is sometimes required to manually identify markers whose trajectories are fragmented or truncated, the tracking of segments is almost entirely automated by the motion capture system. The disadvantage with optical motion capture is the requirement that at least two cameras have line of sight to each marker at all times. Otherwise if the marker is obstructed, there is ambiguity in the marker location and the segment cannot be tracked (Kapur *et al.,* 2010). Despite the limitations optical motion capture systems have been used to quantify *in-vivo* kinematics of the shoulder (McQuade and Smidt, 1998; Meskers *et al.,* 2007), the elbow (Van Roy *et al.,* 2005), the spine (Burnett *et al.,* 2008; Ma *et al.,* 2009), the hip, knee, ankle and foot (Gribble *et al.,* 2009; Jenkyn and Nicol, 2007; Jenkyn *et al.,* 2010).

Electromagnetic tracking devices such as 'Flock of Birds' (Ascension Technologies, Burlington, Vermont, USA) function by using a transmitter to track up to 16 receivers in six degrees of freedom (DOF; i.e. three rotations and three translations). The receivers are rigidly attached to the bony landmarks of interest within a joint. The transmitter emits an electromagnetic field which is detected by the receivers. Since the bones move the three-dimensional position and orientation of the receivers with respect to the transmitter's location is calculated and recorded. The device functions by measuring the

strength of the magnetic fields generated by sending a current through three small wire coils oriented orthogonal to one another. Applying a current to the wire allows each wire to be an electromagnet. By activating each of the wires and measuring the magnetic fields generated the position and orientation of the sending unit can be received and deciphered. This type of tracking system can be used for *in-vivo* and *in-vitro* studies. Electromagnetic tracking systems have been used to measure *in-vivo* kinematics such as neck mobility (Koerhuis, 2003), and ankle-hindfoot stability (Watanabe *et al.,* 2012). Electromagnetic tracking systems have also been used to measure *in-vitro* kinematics in the elbow (Sabo *et al.,* 2011), knee (Bjornaraa and Di Fabio, 2011), foot and ankle (Brown *et al.,* 2009). Milne *et al.* (1996) has shown that the receiver and transmitter distance has an optimal operational range between 22.5 and 64.0 cm. Over a 1° to 20° range the mean rotational error was found to be 1.6%. The 'Flock of Birds' electromagnetic device was sensitive enough to read positional and orientation changes of 0.25mm and 0.1°, respectively (Kedgley, 2009). Electromagnetic tracking systems have the advantage that magnetic fields can pass through most materials, metals excepted, so a direct line of site is not necessary between the transmitter and the receiver as required in optical motion capture. Each receiver is built with three coils thus creating its individual coordinate system. This is an advantage over the optical tracking systems where three non-collinear markers are required. Electromagnetic tracking systems are susceptible to interference from ferro-magnetic and conductive metals, producing errors in the locations of the position of the receivers being tracked (Kapur *et al.,* 2010). Despite the limitations of the electromagnetic

tracking systems they have been used to quantify *in-vivo* kinematics of the shoulder (Meskers *et al.,* 1998; Myers *et al.,* 2006), the spine (Shum *et al.,* 2007), the elbow (Bottlang *et al.,* 2000), and the hip, knee and ankle (Hemmerich *et al.,* 2006).

The advantages of using either an optical or electromagnetic tracking system include the capability of a fully dynamic analysis as well as the high sampling frequency. The Cortex system at the WOQIL can sample up to 200 frames per second, much faster than standard video cameras. The data is presented in an absolute reference frame, allowing for less complicated data processing. There are still disadvantages with these systems, including the high cost. Most electromagnetic and active marker based optical systems contain interference from the wires which may results in subjects producing movements not associated with uninhibited conditions. The greatest disadvantage with both optical motion capture and electromagnetic capture systems is the introduction of skin motion artifact error into the captured trajectories.

1.1.4 SKIN MOTION ARTIFACT

Skin motion artifact is inaccuracy in bony anatomy tracking measured with skin-mounted sensors or markers (such as in optical and electromagnetic systems) due to the skin moving relative to the underlying bone. When bony landmarks need to be located, they must be digitized through the skin with optical and electromagnetic systems. Skin motion artifact errors arise due to a combination of inertial effects of soft tissue, skin deformation and sliding, and motion due to the muscle contractions (Leardini *et al.,* 2005; Shultz *et al.,* 2011). Information about joint movement will have a limit to its accuracy so long as skin motion artifact error is present because the magnitudes of the

skin motion errors are usually larger than accuracy of optical and electromagnetic measurement systems, are task dependant, and are not reproducible between subjects (Leardini *et al.,* 2005; Shultz *et al.,* 2011). During toe-off of the foot the highest skin motion artifact was found for both the navicular and the calcaneus bones (Tranberg and Karlsson, 1998). The smallest errors were found for the bases and the heads of the metatarsals bone. The maximal deviation in the position of the markers was 4.3mm (Tranberg and Karlsson, 1998). Shultz *et al.,* found the skin motion artifact ranged between 6.46 to 16.72mm. The larger estimate of skin motion artifact errors in the Shultz study compared to the Tranberg and Karlsson study was thought to be caused by the increased inertia of the passive optical markers being organized in triad clusters (Shultz *et al.,* 2011).

In order to avoid the error associated with skin motion artifact, optical motion analysis systems and electromagnetic systems may be used in conjunction with markers attached with bone pins (Arndt *et al.,* 2007; Larfortune *et al.,* 1992; Karduna *et al.,* 2001). While the bone pin method provides good kinematic data it is generally too invasive to be practical for larger sized studies. The method has an inherent risk of infection; subjects may experience discomfort and as such may not be able to move in a normal manner. The large skin translations, passive motion of the skin and active muscle contraction may interfere with the bone pins by moving or bending them (Karduna *et al.,* 2000; Benoit *et al.,* 2006). Other solutions to the skin motion artifact problem include least-squares corrections post hoc (Sodkervist and Wedin, 1993; Chèze *et al.,* 1995; Veldpaus *et al.,* 1998; Klous and Klous, 2010), linear interpolation post hoc (Dumas

and Cheze, 2009), linear regression post hoc (Meskers *et al.,* 1998), and filtering of marker trajectories with smoothing filters (Cerveri *et al.,* 2005).

1.1.5 MEDICAL IMAGING TECHNIQUES

One of the biggest factors limiting the improvement of the study of human joint motion is skin motion artifact, particularly in the joints of the foot (Shultz *et al.,* 2011; Arndt *et al.,* 2007). Medical imaging has the advantage of allowing the bones to be viewed directly, removing error associated with skin motion artifact. There are three main techniques used in orthopaedic biomechanics. These include x-ray and fluoroscopy, computed tomography (CT) and magnetic resonance imaging (MRI).

1.1.5.1   PLANE X-RAY AND FLUOROSCOPY

Plane x-ray images are two-dimensional (2D) projections of an object onto a film (or digitally onto a flat panel), produced by the interaction of x-rays with the various tissues of the body. Fluoroscopy is an imaging technique that is used to obtain real-time dynamic images of the internal structures of a patient through the use of a fluoroscope. Fluoroscopy units contain an image intensifier (II) along with a closed-looped television system. The principal component of the imaging chain that distinguishes fluoroscopy from plane x-ray is the image intensifier (Bushberg, 2002). The imaging chain of a typical fluoroscopy machine is seen in Figure 1.1.
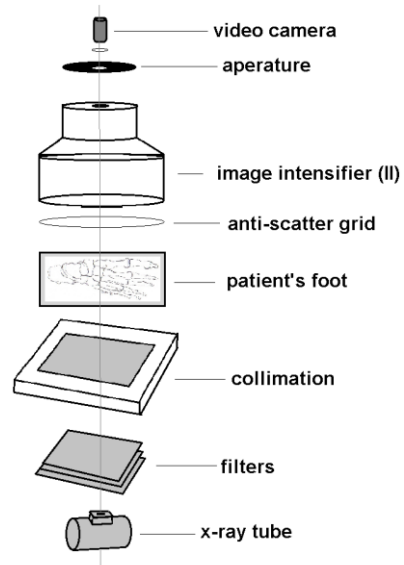
Figure 1.1: Fluoroscopy imaging chain loop.

The diameter of the II can be as large as 16 inches. Fluoroscopy imaging is capable of 'real-time' capture rates, 30 interlaced frames per second, which is the same as the standard television frame rate. Clinically, fluoroscopy units are used to help visualize internal anatomy and components during procedures such as angiography and orthopaedic nailing and rodding. Plane x-rays have the advantage of being a commonly available in medical practices. Plane x-rays have been used to study kinematics of the knee (Frankel *et al.,* 1971; Mu *et al.,* 2011), the shoulder (Poppen and Walker, 1976; Howell *et al.,* 1988; Burkhart, 1992), the foot (Tranberg and Karlsson, 1998; Löfvenberg *et al.,* 1989), and the spine (Dunk *et al.,* 2009). Plane fluoroscopy has been used to examine several joints including the shoulder (Talkhani and Kelly, 2001), the spine (Auerbach *et al.,* 2007), the knee (Wada *et al.,* 2001) and the foot (Wearing *et al.,* 1998). The subject is limited to static image capture during a plane x-ray examination, but during fluoroscopy motion can be captured. Dynamic fluoroscopy has previously tested

knee kinematics while walking on a treadmill (Forokji *et al.,* 2012). Plane fluoroscopy may have the subject hold positions as instructed by the technician to compare bone kinematics of the left and right shoulder (Matsuki *et al.,* 2011). Plane fluoroscopy has previously been used in the foot to measure deformable characteristics (Wrbaskić, 2007), as well as motion in the human arch during gait (Wearing *et al.,* 1998).

The main disadvantages of plane x-rays and fluoroscopy is the mandatory exposure to ionizing radiation. The use of 2D imaging techniques to record a 3D motion will result in projection errors that are unavoidable. It is highly unlikely that the motion of interest will occur exactly in the plane of the image. In order for this to be possible the axis of rotation of the joint of interest should be perpendicular to the image plane (van der Helm and Pronk, 1995; de Groot, 1999). However, the axes of most joints are not consistently in one plane throughout their range of motion (ROM) (Duck *et al.,* 2003). In addition to this it is difficult to ensure that volunteers precisely position themselves in the plane of interest as required (Howell et al, 1988).

1.1.5.2   COMPUTED TOMOGRAPHY (CT) SCAN

A CT scan is an x-ray based imaging method that uses multiple x-ray views and tomography to create a three dimensional image of internal anatomy. A CT combines a series of x-ray views taken from multiple angles to produce cross-sectional images of both the bones and soft tissues inside the body (Bushberg, 2002). The tomograms (also known as the cuts) for the CT are usually made approximately 5mm or 10mm apart (these values can vary) (Bushberg, 2002). The CT machine rotates 360 degrees around the subject's body. The machine picks up and records the absorption rates of the varying

thicknesses of both bone and tissue. Three-dimensional reconstruction of the CT slices is possible through the use of computer software such as OsiriX (Advanced Open-Source PACS Workstation DICOM Viewer, Antoine Rosset, USA). It has been shown that CT scans have a spatial accuracy of 99.2±0.8% of distances measured (Smith *et al.,* 1989). Multi-planar reconstruction is the simplest technique which creates the 3D model by stacking the axial slices. Another method is surface rendering. This uses the idea of a threshold value set by the operator, for example, a threshold value that corresponds to bone. Through the use of this threshold value a three-dimensional model of the bone can be created using edge detection image processing techniques. Multiple models can be created by using various threshold values (i.e. for muscle or for cartilage). CT scans can be used in conjunction with other methods or on their own. A CT image can be used to measure three-dimensional kinematics statically of the arm (Kataoka *et al.,* 2012; Roach, 2012), the spine (Hioki *et al.,* 2011), and the foot and ankle (Green *et al.,* 2011). The greatest disadvantage is the exposure to ionizing radiation. A disadvantage for biomechanical studies solely using CT imaging is only being able to capture static images. When motion occurs during a CT image acquisition the final result becomes blurry and difficult to analyze. The subject also needs to hold their position for much longer than would be required for a plane x-ray image to be captured.

1.1.5.3   MAGNETIC RESONANCE IMAGING (MRI)

An MRI is a medical imaging technique that also provides a three-dimensional image of internal structures of the body. An MRI machine uses a powerful magnetic field to align the magnetization of some atoms within the body (Bushberg, 2002). Since the

body is largely composed of water molecules (each containing two-hydrogen nuclei or protons) when a person enters an MRI machine the powerful magnetic field of the scanner affects the magnetic moments of some of these water nuclei. These change and align with the direction of the created field. An MRI machine uses a radio frequency transmitter to produce the electromagnetic field. Just the right amount of energy is used to flip the spin of the aligned protons in the body. The position information is found using the resulting signal by the mathematical Fourier transform technique (Bushberg, 2002). An image can be constructed this way because the protons in the tissues return to their equilibrium state at different rates which can be detected. MRI is particularly useful for imaging parts of the body with many hydrogen nuclei and little density contrast, such as the brain, muscle, connective tissue and most tumours. MRI is superior to CT in that it does not require the use of ionizing radiation. However, this imaging technique makes it more difficult to create a bone model due to the low bone contrast. MRI has been used on its own to measure kinematics in the body during static conditions in the foot (Fassbind *et al.,* 2011) and the knee (Kothari *et al.,* 2012). MRI is limited in measuring kinematics alone due to the slowness associated with its acquisition. This type of medical imaging requires the subject stay static for the time of the scan.

When analyzing implant motion the manufacturer may have a generic 3D computer aided design (CAD) model that can be used in place of individual CT or MRI models of the anatomy. The CAD model technique cannot be used *in-vivo* unless only the kinematics of implanted portion is of interest. A CT scan was used to create 3D bone

models during the work of this thesis due to its advantages outweighing the disadvantages associated with this imaging technique compared to the other techniques discussed.

Clinical measurements pertaining to joint range of motion define the anatomical position. This is necessary to track 3D joint motion in order to quantitatively measure the effects of medical interventions such as orthopaedic surgeries, physiotherapy programs, and pedorthic foot adjustments. Skeletal kinematics can provide information regarding the normal joint function, development and progression of musculoskeletal diseases, and injuries. Currently there are various methods available to assess joint kinematics, but it remains difficult to do so both accurately and non-invasively.

1.2 HISTORY OF RADIOSTEREOMETRIC ANALYSIS (RSA)

1.2.1 STANDARD RSA

Stereophotogrammetry is a method of using two simultaneous two dimensional images to create a three dimensional image of a structure of interest (Selvik, 1989). The method is more than a century old; however in 1974 Selvik applied the technique to x-ray stereophotogrammetry in order to measure a relative rigid body motion of a skeletal system (Selvik, 1989). Selvik named his method Roentgen stereophotgrammetric analysis (RSA), which is presently interchangeable with the terms radiostereometric analysis and radiostereometry (Valstar, 2005). The method of RSA developed by Selvik will be considered standard RSA when continuing onto discuss markerless RSA techniques.

Standard RSA relies on tantalum makers placed in the bone surrounding as well as on an implant to be measured. In order to determine the pose of a rigid body at least three non-collinear markers are required on the body at known locations. The combination of position and orientation refers to the pose of an object. It is recommended to use between six and nine markers since the markers can be obscured by metal objects and can become out of view during the motion (Valstar, 2005). Small spherical tantalum markers are used almost exclusively as well-defined landmarks. They can be inserted into the bone and can also be attached to surgical implants (Valstar, 2005). Tantalum markers are considered bio-inert and as such have been determined to be biochemically acceptable as a biomaterial. Clinically, a tantalum bead is used as a marker for standard RSA due to its high density, making it easy to distinguish after being x-rayed. The beads are implanted during surgery. A maximal error reported by Selvik in the laboratory environment using standard RSA ranged between 0.02mm to 0.45mm and from 0.02° to -0.19° (Selvik, 1989). The implantation of markers onto the bone has some ethical challenges associated with the invasive process required for the insertion of the tantalum beads. The reasoning for conducting this invasive method is due to its high accuracy in measuring skeletal kinematics. Standard RSA has found wide application in orthopedic implant research. Standard RSA can be done using either an x-ray or a fluoroscopy medical imaging device. X-ray is able to take a static roentgen image whereas a fluoroscopy unit is able to capture dynamic images in addition to static. The use of x-ray RSA or fluoroscopy based RSA kinematic analysis comes with both advantages and disadvantages. Common benefits to conducting research using standard

RSA techniques include its high accuracy in measuring skeletal kinematics. Fluoroscopy RSA has the advantage over x-ray RSA of being able to capture x-ray images in real time. Standard RSA has been used to measure kinematics of the shoulder (Kedgley, 2009), knee (Hurschler *et al.,* 2009; Fleming, 2001), and implant migration (Hurschler *et al.,* 2008).

1.2.2 MARKERLESS RSA

Markerless RSA relies on anatomical landmarks. Rather than relying on embedding tantalum markers in the bone, image processing techniques have been used to locate the position of the bone. In this thesis surface models of the bone were segmented and matched to the radiographic image pairs by the approach used in the model-based method. An algorithm is used to recreate the experimental conditions. The choice in segmentation software may also affect accuracy. The bone segmentation program used in this thesis (OsiriX DICOM Viewer) has been validated by previous researchers comparing results to leading medical imaging software available and has proven to have a maximal error of 0.3mm (Kim *et al.,* 2012).

If a study were to use tantalum beads, in the case of standard RSA, to study implant wear the cost would drastically increase in addition to the period of time required to complete the research. Markerless RSA removes the need to insert beads into bones and implants under study. Studies have discussed that marking the implant with beads can compromise the strength of the implant as well as the beads causing a local stress risers. These stress risers could result in cracks in the bone cement as well reduced bone fixation (Kaptein *et al.,* 2003). Although the markerless RSA technique on

its own is relatively new its origins actually date back to the first RSA study to analyze total hip prostheses wear and movement (Baldursson *et al.,* 1979). Baldursson *et al.* not only used the inserted beads as markers but the femoral head and the ends of the wire in the acetabular socket as additional markers. Other groups have used prosthetic landmarks such as the head, shoulder, and tip of the femoral components.

The use of markerless RSA techniques today needs to be able to analyze complex landmarks. More generally, applicable markerless RSA methods were developed in order to accommodate these complex landmarks. These markerless RSA methods have various names depending on the algorithms employed and laboratories in which the studies were conducted. Some of these names include image-based RSA (IBRSA) (de Bruin, 2008), image matching method (Fox, 2011; Allen, 2009; Kedgley, 2009; Bingham and Rowell, 2006; Li *et al.,* 2006), model-based tracking (Kaptein *et al.,* 2003; Komistek *et al.,* 2000), and model based Roentgen stereophotogrammetry (Valstar, 2001).

A previous study evaluated the translational and rotational motions of the distal tibia relative to the talus in subjects that have had total ankle arthroplasty (TAA). The group completing this study used three-dimensional CAD models of the components of interest within the TAA (Komistek *et al.,* 2000). This CAD method of markerless RSA is only possible if you are only interested in a manufactured part that could have been modeled prior to implantation. Markerless RSA is superior to traditional RSA because it is unnecessary to implant beads onto a bone. The implantation of tantalum beads is generally only approved if surgery on the joint of study is going to be preformed

regardless. This means studying the normal population becomes impossible with traditional RSA techniques.

1.3 HUMAN FOOT

This thesis focuses on the affect orthotics have on the human hindfoot during an *in-vivo* study. Therefore, a brief description of the anatomy and kinematics of the human foot will be given with a focus on the hindfoot region.

The human foot consists of 28 bones (including the sesamoids) whose motions are closely interrelated. The foot not only functions as a structural supporting platform capable of withstanding repetitive loads multiple times bodyweight, but it must also be able to adapt to different ground surfaces and varying speeds of locomotion. Footwear may consist of a rigid ski boot to a soft slipper. The change in material worn may alter normal foot biomechanics.

1.3.1 ANATOMY

The human foot can be functionally divided into three areas; these are the forefoot, midfoot and hindfoot. The forefoot consists of five metatarsals, two phalanges attached to the first metatarsal, and three phalanges attached to the remaining metatarsals (figure 1.2). The midfoot and hindfoot contain the bones of interest for this study. The midfoot consists of the cuboid, navicular, medial cuneiform, intermediate cuneiform, and lateral cuneiform (figure 1.2). The midfoot forms the foot's arch and serves as a shock absorber. The bones of the midfoot are connected to the forefoot and the hindfoot via several joints that are moved and stabilized by muscles and the plantar

fascia (arch ligament). The hindfoot is composed of of only one bone, the calcaneus, which has three joints and links the midfoot to the talus (ankle). The calcaneus is the largest bone in the foot. It joins the talus to form the subtalar joint. This joint has complex motion in three planes and produces the motions of supination and pronation. The subtalar joint and the transverse tarsal joint are both responsible for transforming tibial rotation into forefoot supination and pronation.

It is possible for an extra bone lump to be lcoated at the navicular. This is known as accessory navicular syndrome and could result in painful symptoms.

1.3.2 BONES AND ARTICULATIONS

The bones of interest in this study are located in the hindfoot and midfoot and include: the calcaneus, cuboid and navicular. The relationship of the tibia and fibula with respect to the foot complex are also of interest.

Within the calcaneus there are several important landmarks present. The Achilles tendon insertion site is located in roughed area on the superior-posterior side of the calcaneus bone. Also on the superior side of the calcaneus is the location for the articulation with the talus bone (Nordin and Frankel, 2001). The talus bone is the second largest bone in the tarsus. The talus allows for motion in the foot overall with respect to the lower leg and transfers the body's weight onto the foot. The talus articulates with the tibia creating the tibiotalar joint. The cuboid (figure 1.2) bone is one of the several bones located in the tarsal region of the body. The function of the cuboid bone is to help support the body's weight, locomotion, and maintaining lateral foot stability. The navicular (figure 1.2) is a relatively small bone in the tarsal region; it helps in the function

of locomotion and body support. The navicular contacts five other bones. These include: three cuneiforms, the talus bone, and the cuboid bone.
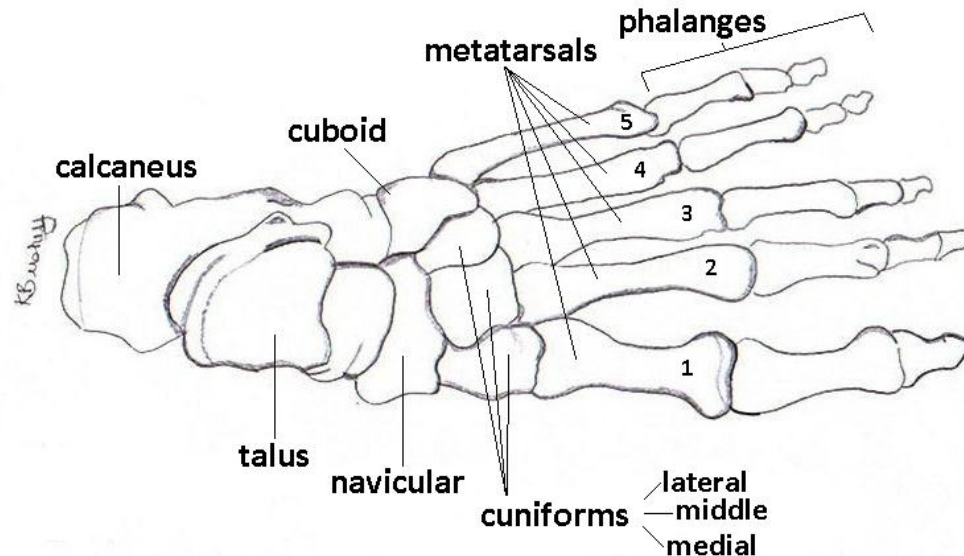
Figure 1.2: The bones of the foot, specifically a left foot (sesamoids excluded).

The tibia and fibula are the lower leg bones that articulate with the talus. The tibia is located on the medial side of the leg and the fibula is located on the lateral side of the leg. The tibia and the fibula can be used to evaluate subtalar motion. Previous research has linked the motion of tibia/fibula to the subtalar joint (Wu *et al.,* 2002). When the tibia internally rotates, the subtalar joint everts (pronates). Conversely, external rotation of the tibia results in subtalar inversion (supination) (Nordin and Frankel, 2001).

The subtalar joint occurs with the meeting of the talus and the calcaneus bones. Root et al describes the subtalar joint neutral (STJN) position as a position in which the joint is neither pronated or supinated (Root *et al.,* 1977). The location of the STJN

position is determined clinically by palpating the congruency of the talar head proximal to the navicular (Chuter *et al.*, 2003).

1.3.3 KINEMATICS

The overall motion of the foot is complex and occurs on three planes. Flexion-extension occurs in the sagittal plane, abduction-adduction occurs in the transverse plane, and inversion-eversion occurs in the coronal (frontal plane) (figure 1.3). Pronation and supination are terms generally used to describe positioning of the plantar surface of the foot. Supination is the combination of inversion, plantarflexion, and internal rotation. Pronation is a combination of eversion, dorsiflexion, and external rotation (Nordin and Frankel, 2001).
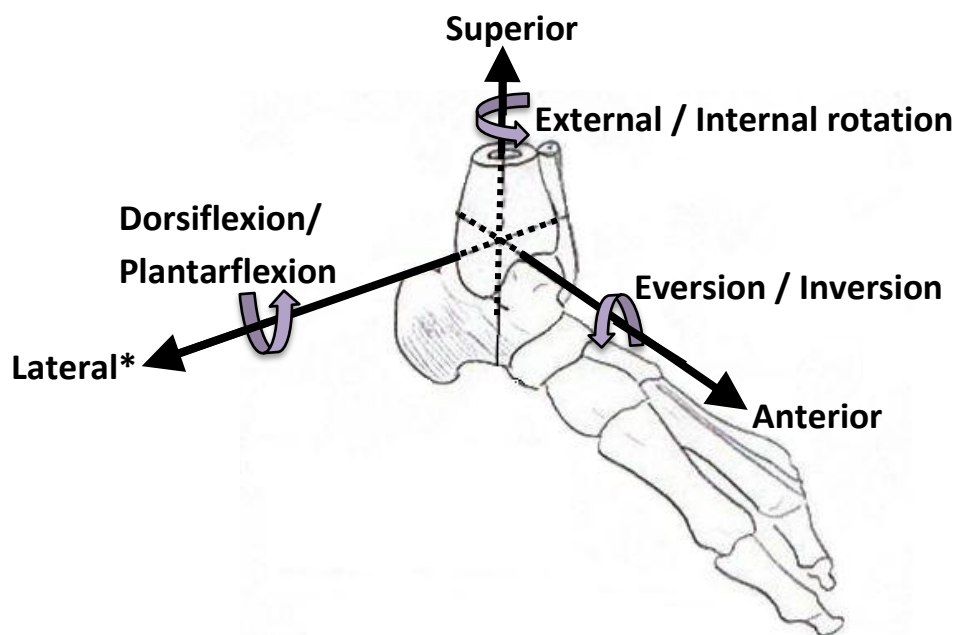
Figure 1.3: Motion of the foot around three axes.

*Note: Lateral direction based on the 'right-handed' coordinate system (i.e. medial and lateral defined based on the right foot).

International standards have been developed to enable comparisons of kinematic data between labs, and these will be followed where possible during this thesis. Data for such kinematic analysis have been obtained using all the biomechanical methods described in section 1.1 and will be highlighted below.

1.4 ORTHOTICS

Orthotics are commonly prescribed for the conservative treatment of musculoskeletal disorders of the foot and ankle such as pes cavus or pes planus. Pes cavus is defined as having a high arch in the foot and pes planus is defined as having a low arch in the foot. Orthotics are thought to alter the motion of the bones of the foot by applying constraint or support to various structures on the plantar surface. Orthotics can be either custom-made by a pedorthist or bought 'off-the-shelf'. Custom-made orthotics can be constructed of a 4mm plastazote (soft), compliant material or with a 3mm RCH-500 (rigid) material, depending on the preference and the clinician and the amount of control desired (Fields, Sykes, Walker, & Jackson, 2010). Currently, there are three techniques for moulding an orthotic, plaster wrap, the foam box technique, and the application of laser technology. The plaster wrap casting technique requires the patient lie prone in a figure four position during the process. A negative impression of the foot is taken while being locked in the subtalar neutral position. Historically plaster casting has been the standard method, however, the foam box technique has increased in popularity. The foam box technique has the practitioner guide the patient's foot into a foam tray that takes a negative impression of the foot while in the subtalar neutral

position (Laughton *et al.*, 2002). The foam box eliminates the drying process required in plaster casting. More recently laser technology has developed to a more affordable technique to cast orthotics. This technology has the ability to obtain either a partial weight bearing or a non-weight bearing representation of the foot (Laughton *et al.*, 2002).

Orthotics are associated with controlling excessive foot pronation. To date results from previous studies provide some evidence that orthotics, motion control shoes and even therapeutic taping were able to reduce hindfoot eversion. Despite this many of these studies contained methodological flaws and are more likely to provide optimistic estimates of treatment effects (Pinto *et al.,* 2012). Whether orthotic interventions are effective in controlling this excessive pronation is still unclear.

Merton Root is a name often associated with scientific techniques used to understand the inner workings of the foot for pedorthists. The Root Theory of biomechanics attempts to explain the function of the foot and lower extremity. In terms of orthotic casting Roots theory states that the orthotic should be casted in the STJN position. This STJN approach is based upon the belief that the foot functions normally during gait when the subtalar joint is in the neutral position following heel-strike and midstance (Watkins, 2009). In the subtalar neutral approach, the foot is assessed by casting the foot in the subtalar neutral position while non-weight bearing in order to capture the forefoot-hindfoot orientation and the calcaneal inclination angle. Objection on this particular position is quite evident in the scientific community. The argument is that the STJN occurs for a fraction of the gait cycle during stance phase; the time-frame

is not evidence enough to build a cast on this position. As such this area requires a more quantifiable analysis.

1.5 KINEMATICS OF THE HINDFOOT

During normal gait the foot experiences complex characteristics reflective of the multi-planar contact at the plantar surface. Based on kinematic data obtained using optical motion capture systems with a multi-segment foot model the hindfoot has been shown to experience motion in three planes during stance phase. Previous studies have shown hindfoot motion in the sagittal, transverse, and coronal plane. The hindfoot has been reported during midstance to enter dorsiflexion, and externally rotate (Kidder *et al.,* 1996; Harris *et al.,* 2008). The motion in the inversion/eversion plane has previously been reported to maintain near the neutral position during midstance (Kidder *et al.,* 1996; Harris *et al.,* 2008).

A coordinate system is often used to specify the position of a point relative to a known location (the origin of the coordinate system). A bone coordinate system defines a global position on a rigid segment that is used to determine relative motion of the joints. This relative motion is done by defining joint coordinate systems. A joint coordinate system is described by two segment-fixed axes (or bone coordinate systems). In order to compare the motion of joints in the foot between two individuals, a common method of defining joint motion is required. This is done by creating joint coordinate systems that are defined with respect to well defined anatomical landmarks.

To quantify hindfoot joint motion, the position and orientation of the navicular and cuboid relative to the calcaneus are required. To relate results to previously defined

coordinate systems the position and orientation of the calcaneus relative to the tibia and fibula is required. A coordinate system must be established on each of these bones the same way between subjects and conditions. Coordinate systems are created according to the convention established by the International Society of Biomechanics (ISB) (Wu *et al.,* 2002). As there are three rotational degrees of freedom (DOF) in the hindfoot, three rotations are required to describe the orientation of the navicular and cuboid relative to the calcaneus, and the calcaneus relative to the tibia/fibula complex. The axes of the bone coordinate systems are placed to allow these rotations to be clinically significant (i.e. the rotation to the plane in which internal/external rotation, plantar/dorsi flexion, inversion/eversion occurs).

Coordinate systems are first created by obtaining a three-dimensional model of the bones of interest. This can be done through the use of technologies such as a CT scan, MRI, or generic bone models. Models of the bones are created using image processing software. Each landmark is digitized with a point and their positions are determined. The digitization process must be conducted carefully. Errors made in the location of the bony landmark result in fixed errors in the location of the bone coordinate systems, and therefore in the rotations of the joint (Della Croce *et al.,* 2005).

Once bony landmarks are digitized, bone coordinate systems are created. A 3 by 3 rotation matrix relating the bone coordinate system to the laboratory coordinate system is defined as,

$$\ _{bone}^{lab}R = \begin{bmatrix} ^{lab}\vec{X}_{bone} & ^{lab}\vec{Y}_{bone} & ^{lab}\vec{Z}_{bone} \end{bmatrix} \qquad \textbf{(Eq. 1. 1)}$$

where, $^{lab}\vec{X}_{bone}$, $^{lab}\vec{Y}_{bone}$, $^{lab}\vec{Z}_{bone}$ are the bone coordinate system axes (i.e. 3 by 1 matrices) described in the laboratory reference frame. A transformation matrix of the bone relative to the lab,

$$_{bone}^{lab}T = \begin{bmatrix} _{bone}^{lab}R & ^{lab}O_{bone} \\ 0\ 0\ 0 & 1 \end{bmatrix}$$
(Eq. 1. 2)

follows, in which:

$_{bone}^{lab}R$= the rotation matrix relating the bone coordinate system to the lab coordinate system,

$^{lab}O_{bone}$= the location of the origin of the bone coordinate system in the lab-based coordinate system.

This transformation matrix is consistently changing. The process above needs to be repeated for each frame of data collected during a dynamic trial.

1.5.1 CALCANEUS COORDINATE SYSTEM

In this study, to enable the creation of the calcaneus coordinate system four bony landmarks (figure 1.4) are digitized. These landmarks are the most superior point on the posterior surface of the calcaneus (calA), the lateral process of the calcaneal tuberosity (calB), the tuberosity located on the medial side in the posterior third of the calcaneus (calC), and the medial process of the calcaneal tuberosity (calD).

The lateral axis of the coordinate system, $\vec{Z}_{cal,1}$, is defined as a unit vector from calA to calB. A vector located at the midpoint of calA and calB, defined midAB is created to aid in the creation of an anterior directed unit vector. The anterior directing vector, $\vec{X}_{cal,1}$, is defined as the unit vector from midAB to calC. The superior directing

vector, $\vec{Y}_{cal,1}$, is defined as the cross product of $\vec{Z}_{cal,1}$ and $\vec{X}_{cal,1}$. The final calcaneus

coordinate system vectors were done by completing cross products between the

previously defined unit vectors to ensure each vector is orthogonal to one another (i.e.

$\vec{X}_{cal}$ was created as the cross product of $\vec{Y}_{cal,1}$ and $\vec{Z}_{cal,1}$).

The origin of the calcaneus coordinate system is, $\vec{O}_{cal}$, is established as the point

calA. Therefore, the transformation matrix between the lab coordinate system and the

calcaneus coordinate system may be written as:

$$\begin{smallmatrix}lab\\cal\end{smallmatrix}T= \begin{bmatrix} ^{lab}\vec{X}_{cal} & ^{lab}\vec{Y}_{cal} & ^{lab}\vec{Z}_{cal} & ^{lab}\vec{O}_{cal} \\ 0 & 0 & 0 & 1 \end{bmatrix} \qquad \textbf{(Eq. 1.3)}$$
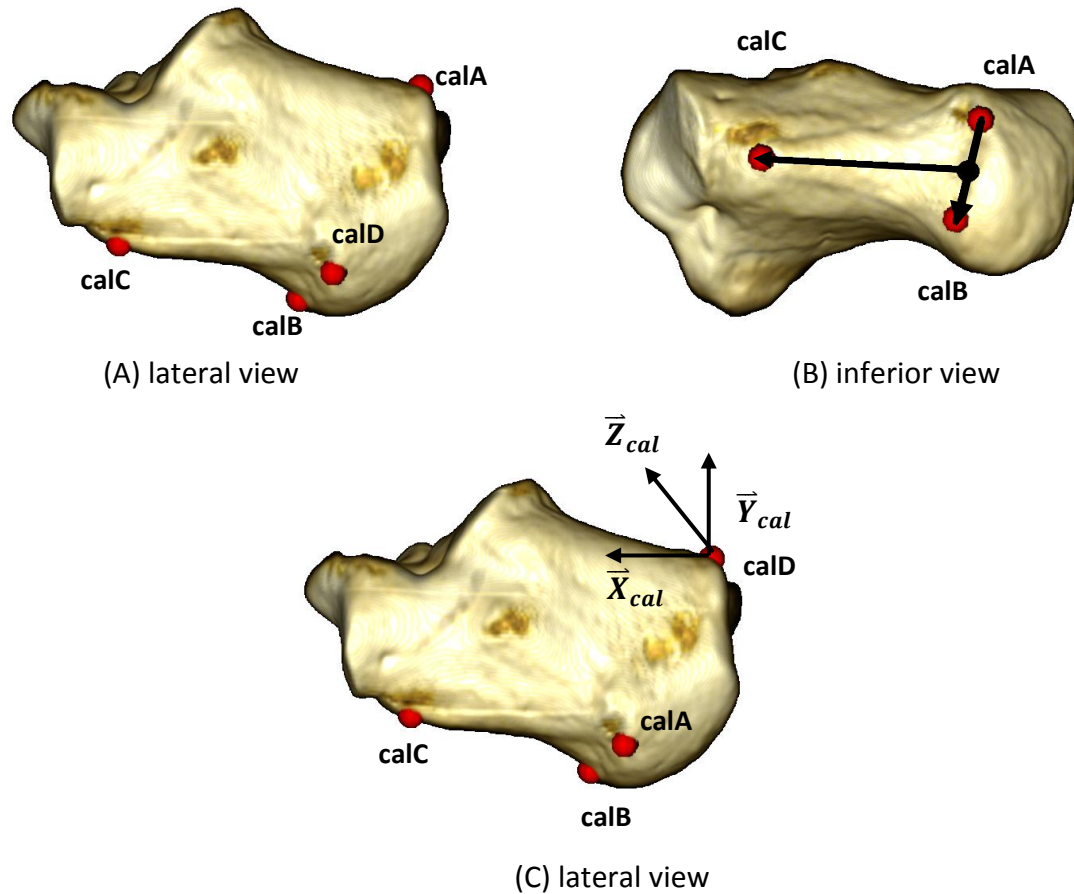
Figure 1.4: The calcaneus coordinate system.

(A) The digitized landmarks on the calcaneus: the medial process of the calcaneal tuberosity (calA), the lateral process of the calcaneal tuberosity (calB), the tuberosity located on the medial side in the posterior third of the calcaneus (calC), and the most superior point on the posterior surface of the calcaneus (calD). **(B)** The vectors used in the creation of **(C)** the calcaneus coordinate system. Images of the model created from a clinical CT scan with points added in OsiriX.

1.5.2 NAVICULAR COORDINATE SYSTEM

In this study, to enable the creation of the navicular coordinate system three bony landmarks (figure 1.5) are digitized. These are the tuberosity found on the most lateral aspect (navA), the most superior aspect above the facet for the second cuneiform (navB), and the most posterior point (navC).

The superior axis of the navicular coordinate system was created as a unit vector from navC to navB and defined as $\vec{Y}_{nav,1}$. The coordinate located at the midpoint of navB and nav C was used to aid the creation of the lateral directing vector. The lateral axis of the navicular coordinate system was created as a unit vector from midBC to navA. The lateral axis vector was defined as $\vec{Z}_{nav,1}$. The anterior directed axis of the navicular coordinate system was created from the cross product of the vector $\vec{Z}_{nav,1}$ and $\vec{Y}_{nav,1}$. The final navicular coordinate system vectors were created by completing the cross products between the previously defined unit vectors to ensure each vector is orthogonal to one another (i.e. $\vec{Y}_{nav}$ was created as the cross product of $\vec{Z}_{nav,1}$ and $\vec{X}_{nav,1}$).

The origin of the navicular, $\vec{O}_{nav}$, was defined to be navA. It then follows that the transformation matrix between the lab coordinate system and the navicular coordinate system may be written as:

$$_{nav}^{lab}T = \begin{bmatrix} ^{lab}\vec{X}_{nav} & ^{lab}\vec{Y}_{nav} & ^{lab}\vec{Z}_{nav} & ^{lab}\vec{O}_{nav} \\ 0 & 0 & 0 & 1 \end{bmatrix} \qquad \textbf{(Eq. 1. 4)}$$
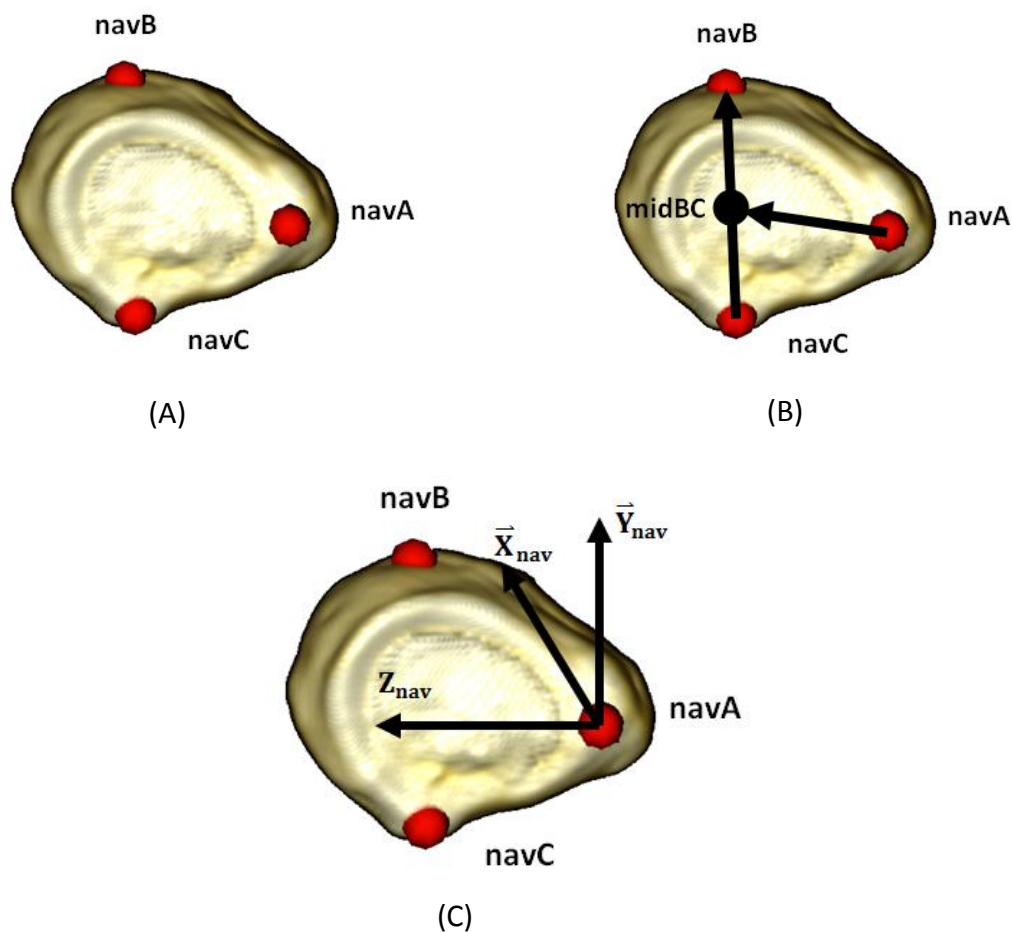
Figure 1.5: The navicular coordinate system, from a posterior view**.**

(A) The digitized landmarks on the navicular: the tuberosity found on the most lateral aspect (navA), the most superior aspect above the facet for the second cuneiform (navB), and the most posterior point (navC). **(B)** The vectors used in the creation of **(C)** the navicular coordinate system. (Images of the model created from a clinical CT scan with points added in OsiriX).

1.5.3 CUBOID COORDINATE SYSTEM

In this study, to enable the creation of the cuboid coordinate system three bony landmarks (figure 1.6) are digitized. These are the lateral tuberosity beside the calcaneus facet (cubA), the medial plantar tuberosity beside the calcaneus facet (cubB), the plantar tuberosity adjacent to the third cuneiform (cubC), and the tuberosity on the most distal portion of the plantar surface (cubD).

The anterior axis of the cuboid coordinate system, $\vec{X}_{cub,1}$, was created as a unit vector from the midpoint of cub A and cubB, defined as midAB, to cubC. The lateral axis of the cuboid coordinate system was defined as the vector, $\vec{Z}_{cub,1}$, created as a unit vector from cubB to cubA. The superior axis of the cuboid coordinate system, $\vec{Y}_{cub,1}$, was created from the cross product of $\vec{Z}_{cub,1}$ and $\vec{X}_{cub,1}$. The final cuboid coordinate system vectors were created by completing the cross products between the previously defined unit vectors to ensure each vector is orthogonal to one another (i.e. $\vec{X}_{cub}$ was created as the cross product of $\vec{Y}_{cub,1}$ and $\vec{Z}_{cub,1}$).

The origin of the cuboid, $\vec{O}_{cub}$, was defined to be cubA. It then follows that the transformation matrix between the lab coordinate system and the navicular coordinate system may be written as:

$$\substack{lab\\cub}T= \begin{bmatrix} ^{lab}\vec{X}_{cub} & ^{lab}\vec{Y}_{cub} & ^{lab}\vec{Z}_{cub} & ^{lab}\vec{O}_{cub} \\ 0 & 0 & 0 & 1 \end{bmatrix} \qquad \textbf{(Eq. 1. 5)}$$
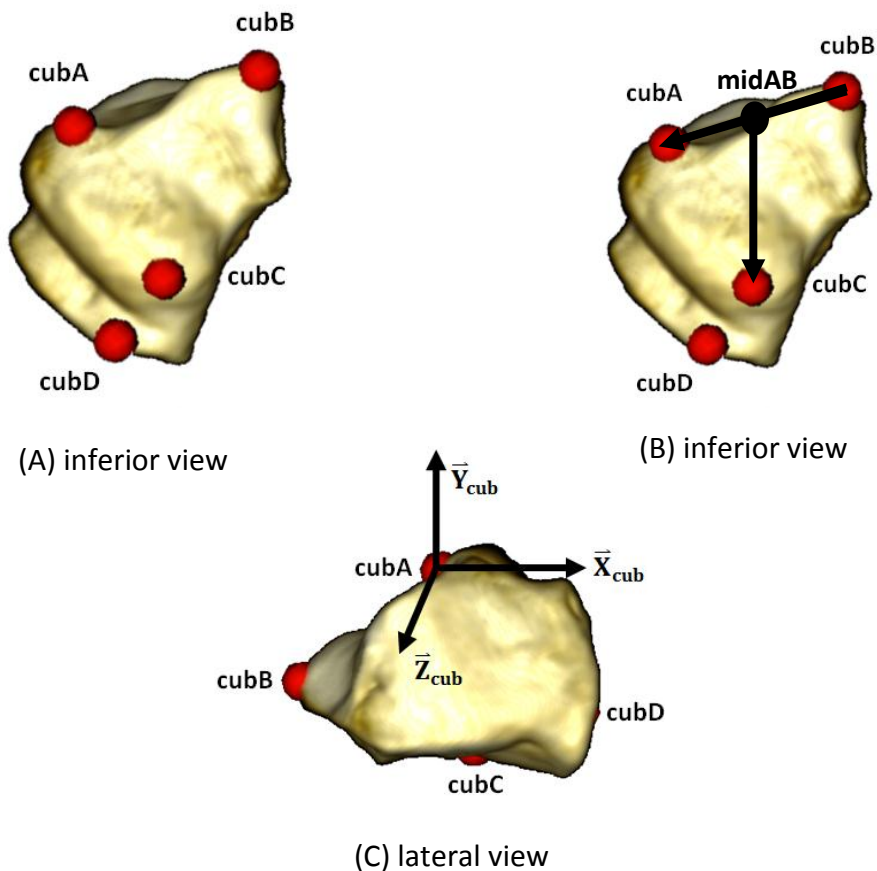
Figure 1.6: Cuboid Coordinate System, views as defined.

(A) The digitized landmarks on the cuboid: the lateral tuberosity beside the calcaneus facet (cubA), the medial plantar tuberosity beside the calcaneus facet (cubB), the plantar tuberosity adjacent to the third cuneiform (cubC), and the tuberosity on the most distal portion of the plantar surface (cubD). **(B)** The vectors used in the creation of **(C)** the cuboid coordinate system. (Images of the model created from a clinical CT scan with points added in OsiriX).

1.5.1.1   TIBIA AND FIBULA COORDINATE SYSTEM

In this study, to enable the creation of the tibia/fibula coordinate system six bony landmarks (figure 1.7) are digitized. These are the lateral malleolus on the fibula (fibA), the medial malleolus on the tibia (tibB), the most medial portion of the superior end of the tibia (tibC), most lateral portion of the superior end of the tibia (tibD), the most medial potion of the superior end of the fibula (fibE), and the most lateral portion of the superior end of the fibula (fibF). MATLAB was used to calculate the midpoint of fibA and fibB, this was defined as midAB (The MathWorks, Natick, MA, USA).

The lateral axis of the tibia/fibula coordinate system, $\vec{Z}_{tibfib,1}$, is initially defined as the unit vector from tibB and midAB. The superior axis of the tibia/fibula coordinate system, $\vec{Y}_{tibfib,1}$, is defined as the unit vector from midAB to midCF. The anterior axis of the tibia/fibula coordinate system, $\vec{X}_{tibfib,1}$, is defined by the cross product of $\vec{Z}_{tibfib,1}$ and $\vec{Y}_{tibfib,1}$. The final tibia/fibula coordinate system vectors were created by completing the cross products between the previously defined unit vectors to ensure each vector is orthogonal to one another (i.e. $\vec{Y}_{tibfib}$ was created as the cross product of $\vec{X}_{tibfib,1}$ and $\vec{Z}_{tibfib,1}$).

The origin of tibia/fibula, $\vec{O}_{tibfib}$, was defined to be midAB. It then follows that the transformation matrix between the lab coordinate system and the navicular coordinate system may be written as:

$$ {}^{lab}_{tibfib}T = \begin{bmatrix} {}^{lab}\vec{X}_{tibfib} & {}^{lab}\vec{Y}_{tibfib} & {}^{lab}\vec{Z}_{tibfib} & {}^{lab}\vec{O}_{tibfib} \\ 0 & 0 & 0 & 1 \end{bmatrix} \qquad \textbf{(Eq. 1. 6)} $$
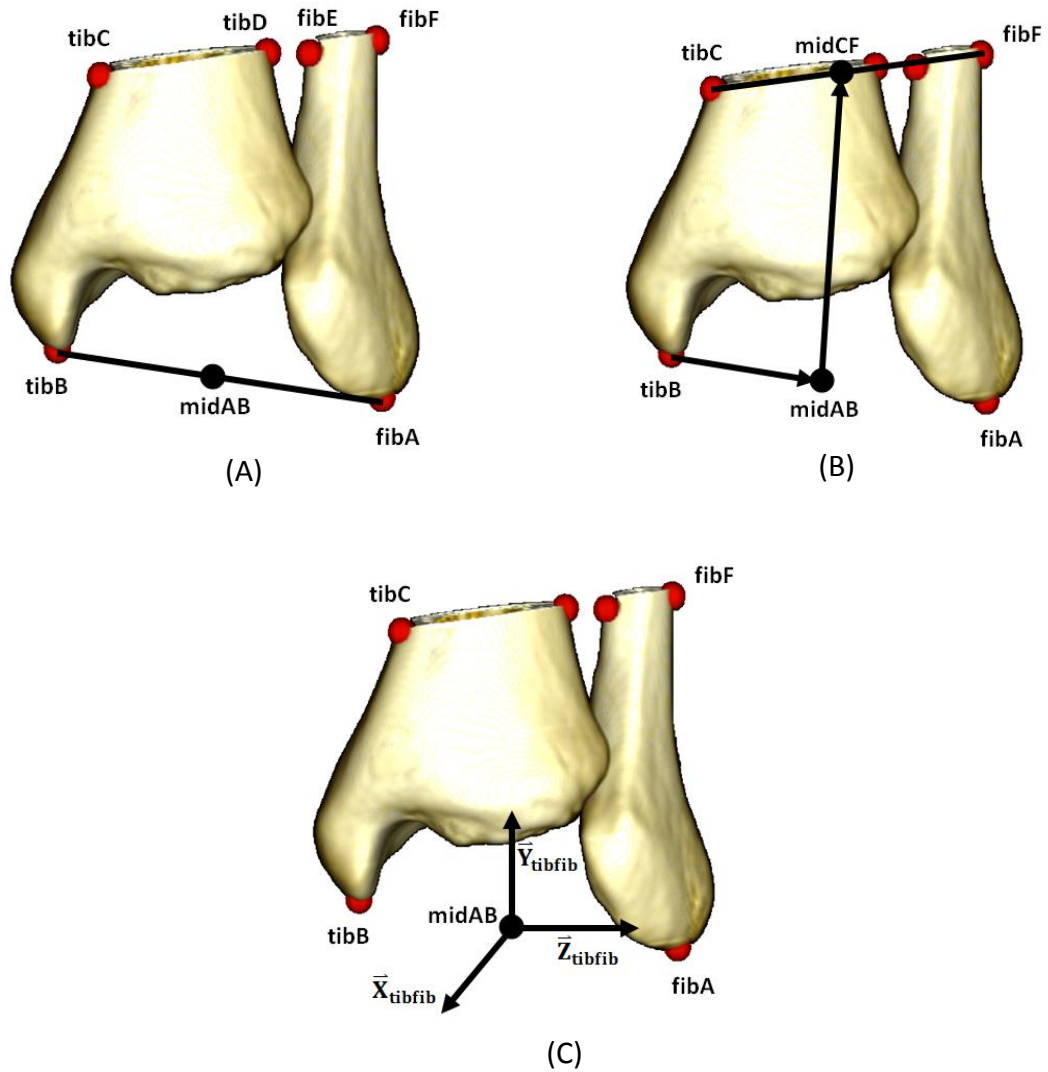
Figure 1.7: Tibia and fibula coordinate system

(A) The digitized landmarks on the tibia-fibula: the lateral malleolus on the fibula (fibA), the medial malleolus on the tibia (tibB), the most medial portion of the superior end of the tibia (tibC), most lateral portion of the superior end of the tibia (tibD), the most medial potion of the superior end of the fibula (fibE), and the most lateral portion of the superior end of the fibula (fibF)). **(B)** The vectors used in the creation of **(C)** the tibia-fibula coordinate system. (Images of the model created from a clinical CT scan with points added in OsiriX).

1.5.1.2   SIGN CONVENTIONS

In order to obtain consistent kinematic outcome measures between subjects only the left foot was studied. The following motions were established as being positive: inversion, dorsiflexion, and internal rotation according to the ISB standard.

1.5.4 HINDFOOT JOINT KINEMATICS

Since the desired results of kinematic analyses are those that are clinically meaningful interpretations of the rotations and translations that occur at a joint, the relationship between the coordinate systems on the calcaneus, cuboid, navicular and the tibia/fibula must be established. This was also done according to the conventions established by the ISB (Wu *et al.,* 2002). The translation of the calcaneus relative to the tibia-fibula is simply the change in position of O_{Cal} within the tibia-fibula frame of reference. The translation of the cuboid relative to the tibia/fibula is simply the change in position of O_{Cub} within the tibia/fibula frame of reference. The translation of the navicular relative to the tibia/fibula is simply the change in position of O_{Nav} within the tibia-fibula frame of reference.

Clinically relevant rotations of the hindfoot (with respect to the tibia/fibula joint) are calculated by Z-X-Y Euler angle analysis (Winter, 2009; Wu. *et al.,* 2002). An Euler angle analysis defines the orientation of one object with respect to another through three independent rotation parameters. These rotations take place about the axes of a Cartesian coordinate system. The orientation of the axis about which each rotation takes place is dependent upon the previous rotation(s). This means that the order of the rotations has an effect on the outcome orientation. It is assumed that the two frames of

reference are initially aligned (figure 1.9). The rotation sequence will be explained with reference to the calcaneus with respect to the tibia/fibula reference frame. The information can be repeated with the cuboid and the navicular in the same manner as described below (thus it will not be repeated for each bone). Rotations are then taken about: (A) the Z-axis of the tibia-fibula coordinate system ($\vec{Z}_{tibfib}$), giving the rotation to the plane in which dorsi/plantar flexion occurs (α); (B) the X-axis of the tibia-fibula coordinate system ($\vec{X}_{cal}$), giving the rotation of the plane in which inversion/eversion rotation occurs (β); and (C) the Y-axis of the tibia-fibula coordinate system ($\vec{Y}_{cal}$), giving the rotation of the plane in which internal/external rotation occurs (γ). Since the assumption behind the kinematics is that the coordinate systems were initially aligned, the initial rotation may equivalently have taken place about $\vec{Z}_{cal}$, and it will be referred to as this from now on. The sequence of the rotations can be written in matrix form as the product of three individual rotation matrices, or combined as a single rotation matrix for the three rotations as shown:

$$^{tibfib}_{cal}\mathbf{R} = \mathbf{rot}(\vec{\mathbf{Z}}_{\mathbf{cal}}, \boldsymbol{\alpha}) \cdot \mathbf{rot}(\vec{\mathbf{X}}_{\mathbf{cal}}, \boldsymbol{\beta}) \cdot \mathbf{rot}(\vec{\mathbf{Y}}_{\mathbf{cal}}, \boldsymbol{\gamma}) \qquad \text{(Eq. 1.7)}$$

$$= \begin{bmatrix} cos\alpha & -sin\alpha & 0 \\ sin\alpha & cos\alpha & 0 \\ 0 & 0 & 1 \end{bmatrix} \begin{bmatrix} 1 & 0 & 0 \\ 0 & cos\beta & -sin\beta \\ 0 & sin\beta & cos\beta \end{bmatrix} \begin{bmatrix} cos\gamma & 0 & sin\gamma \\ 0 & 1 & 0 \\ -sin\gamma & 0 & cos\gamma \end{bmatrix}$$

$$= \begin{bmatrix} \cos(\alpha)\cos(\gamma) - \sin(\alpha)\sin(\beta)\sin(\gamma) & -\sin(\alpha)\cos(\beta) & \cos(\alpha)\sin(\gamma) + \sin(\alpha)\sin(\beta)\cos(\gamma) \\ \sin(\alpha)\cos(\gamma) + \cos(\alpha)\sin(\beta)\sin(\gamma) & \cos(\alpha)\cos(\beta) & \sin(\alpha)\sin(\gamma) - \cos(\alpha)\sin(\beta)\cos(\gamma) \\ -\cos(\beta)\sin(\gamma) & \sin(\beta) & \cos(\beta)\cos(\gamma) \end{bmatrix}$$

where:

$\mathbf{rot}(\vec{\mathbf{Z}}_{\mathbf{cal}}, \boldsymbol{\alpha})$= rotation about $\vec{\mathbf{Z}}_{\mathbf{cal}}$ of magnitude α;
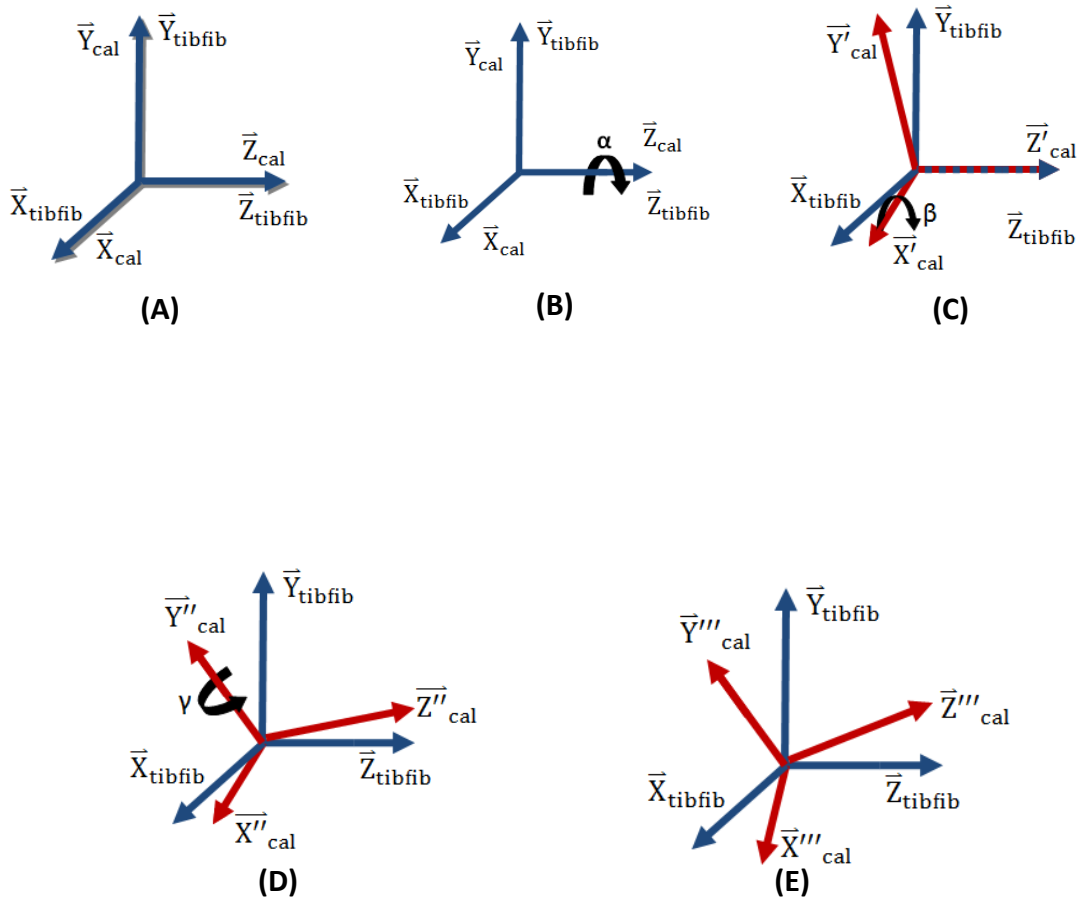
Figure 1.8: Euler Z-X-Y rotations

(A) The coordinate systems initial set up, calcaneus and tibia-fibula coordinate systems overlap. **(B)** The rotation starts about the Z-axis of the tibia-fibula coordinate system, **(C)** rotation about the X'-axis of the calcaneus coordinate system, and **(D)** rotation about the Y''-axis of the calcaneus coordinate system. **(D)** The resulting coordinate systems.

In order to describe the location of the calcaneus relative to the tibia-fibula, transformation matrices must be combined as shown:

$$^{tibfib}_{cal}T = {}^{tibfib}_{lab}T \cdot {}^{lab}_{cal}T$$

$$= \left[\begin{array}{ccc|c} & ^{tibfib}_{cal}R & & P_{cal,origin} \\ \hline 0 & 0 & 0 & 1 \end{array}\right] \qquad \textbf{(Eq. 1. 8)}$$

$$= \begin{bmatrix} r_{11} & r_{12} & r_{13} & x \\ r_{21} & r_{22} & r_{23} & y \\ r_{31} & r_{32} & r_{33} & z \\ 0 & 0 & 0 & 1 \end{bmatrix}$$

where:

$^{tibfib}_{lab}T = \left[^{lab}_{tibfib}T\right]^{-1}$ = the transformation matrix describing the position and orientation of the lab coordinate system relative to tibia-fibula bone coordinate system;

$^{lab}_{cal}T$ = the transformation matrix describing the position and orientation of the calcaneus bone coordinate system relative to the lab; and

$^{tibfib}_{cal}T$ = the transformation matrix describing the position and orientation of the calcaneus bone coordinate system relative to the tibia-fibula bone coordinate system.

In order to describe the rotation of the calcaneus relative to the tibia-fibula, Equation 1.7 is compared with Equation 1.8 to obtain:

Dorsi/Plantar flexion: $\boldsymbol{\alpha = \text{arctan2}\left(\frac{r_{12}}{r_{22}}\right)}$ **(Eq. 1. 9)**

Internal/External rotation: $\boldsymbol{\gamma = \text{arctan2}\frac{-r_{13}}{r_{33}}}$ **(Eq. 1. 10)**

Inversion/Eversion: $\boldsymbol{\beta = \frac{r_{23}}{r_{33}} \cdot \cos(\gamma)}$ **(Eq. 1. 11)**

where arctan2 is the four quadrant inverse tangent function, with results between pi and -pi. Differing from the standard inverse tangent function which results in a solution within the first and fourth Cartesian quadrants only.

1.5.5 THE STUDY OF THE HINDFOOT JOINT BIOMECHANICS

Each study of this thesis aims specifically to quantify the kinematics of the calcaneus, cuboid, and navicular relative to the tibia-fibula. One of the major obstacles in studying the foot is that the motions of the internal bones during weight-bearing or walking gait are relatively unknown. By understanding the kinematics of the foot, specifically the hindfoot, the treatment of problems such as foot pain, plantar fasciitis, and other foot pathologies may be better assessed and possibly improved. The effect of orthotics can be quantified and their designs can potentially be optimized for better performance.

Due to the scarcity of palpable bony landmarks, and the awkward location of landmarks there are, it is difficult to track foot kinematics during dynamic activities (Shultz *et al.,* 2011) using optical (Wolf *et al.,* 2008; Jenkyn and Nicol, 2007) and electromagnetic (Hemmench *et al.,* 2006; Brown *et al.,* 2009) tracking techniques. As previously discussed soft tissue artifact is an unavoidable error associated with these measurement techniques. This error has be shown to be task dependent and not reproducible among subjects making this error difficult if not impossible to filter from the actual motion of interest (Leardini *et al.,* 2005). The hindfoot has multiple bony landmarks but many of them are not palpable. Those landmarks that may be palpable are located in locations in which dynamic motions would not be possible to measure

with or without shoes. To more accurately measure joint kinematics others have used bone pins which have been directly implanted into the target bone through the skin (Arndt *et al.,* 2007; Larfortune *et al.,* 1992; Karduna *et al.,* 2001), however this technique has many negative drawbacks as discussed in section 1.1.4.

Imaging techniques used for measuring foot kinematics include 2D x-ray (Tranberg and Karlsson, 1998; Lofverberg *et al.,* 1989), and single plane fluoroscopy (Wearing *et al.,* 1998).

1.6 STUDY RATIONALE

The rationale behind this work consists of several distinct parts. The incorporation of fluoroscopy with markerless RSA will allow the capture of moving images and therefore further facilitate the study of *in-vivo* kinematics under dynamic conditions. Using x-ray fluoroscopy the kinematic analysis will be much more reliable since skin motion artifact will have been eliminated. This study will provide a better kinematic analysis of the foot through use of the markerless RSA and individual bone coordinate systems. The examination of the effects orthotics have on the internal foot bones will provide insight into changes in their design (if necessary).

1.7 OBJECTIVES AND HYPOTHESES

The objectives of this thesis were: (1) to implement a fluoroscopy-based markerless RSA system on the foot, (2) to determine the effect of various orthotics at midstance of fully weight-bearing walking gait (dynamic), and (3) determine the effect of various orthotics during weight-bearing standing (static).

The primary hypothesis (1) is that markerless RSA is a feasible method to measuring foot kinematics when compared to existing biomechanical tracking technology. It was also hypothesized (2) that differences in orthotics types can be measured and the coordinate systems designed could be considered to be equivalent to the current ISB standard coordinate system in the foot. Finally, it was hypothesized that (3) the fluoroscopy-based markerless RSA system would prove to be a useful clinical tool, able to quantify changes in kinematics following a conservative treatment in the foot.

1.8 THESIS OVERVIEW

Chapter 2 describes the effect of a foam casted orthotic and a neutral cushioning running shoe on the normal population. Chapter 3 contains the results of the study for the plaster casted orthotic on the normal population. Chapter 4 contains the results of foam casted orthotics on the pes cavus and pes planus populations. Chapter 5 compares three different analysis techniques for measuring the effect of orthotics at altering foot pronation. Chapter 6 summarizes the conclusions drawn from this work, outlines its significance, and suggests some potential work which may follow.

1.9 REFERENCES

Arndt, a, Wolf, P., Liu, a, Nester, C., Stacoff, a, Jones, R., Lundgren, P., *et al.* (2007). Intrinsic foot kinematics measured in vivo during the stance phase of slow running. *Journal of biomechanics*, *40*(12), 2672-8.

Auerbach, J. D., Wills, B. P. D., McIntosh, T. C., & Balderston, R. A. (2007). Evaluation of spinal kinematics following lumbar total disc replacement and circumferential fusion using in vivo fluoroscopy. *Spine*, *32*(5), 527-536.

Baldursson, H., Egund, N., Hansson, L. I., & Selvik, G. (1979). Instability and wear of total hip prostheses determined with roentgen stereophotogrammetry. *Arch Orthop Trauma Surg*, *95*(4), 257-263.

Bechard, D. J., Nolte, V., Kedgley, A. E., & Jenkyn, T. R. (2009). Total kinetic energy production of body segments is different between racing and training paces in elite Olympic rowers. *Sports biomechanics International Society of Biomechanics in Sports*, *8*(3), 199-211.

Benoit, D. L., Ramsey, D. K., Lamontagne, M., Xu, L., Wretenberg, P., & Renström, P. (2006). Effect of skin movement artifact on knee kinematics during gait and cutting motions measured in vivo. *Gait & Posture*, *24*(2), 152-64.

Bingham, Jeffrey Thomas. (2006). An automated matching algorithm for dual orthogonal fluoroscopy. *Thesis, Massachusetts Institute of Technology*, *Cambridge*.

Bjornaraa, J., & Di Fabio, R. (2011). Knee kinematics following ACL reconstruction in females; The effect of vision on performance during a cutting task. *International journal of sports physical therapy*, *6*(4), 271-284.

Bottlang, M., Madey, S. M., Steyers, C. M., Marsh, J. L., & Brown, T. D. (2000). Assessment of elbow joint kinematics in passive motion by electromagnetic motion tracking. *Journal of Orthopaedic Research*, *18*(2), 195-202.

Brown, K. M., Bursey, D. E., Arneson, L. J., Andrews, C. A., Ludewig, P. M., & Glasoe, W. M. (2009). Consideration of digitization precision when building local coordinate axes for a foot model. *Journal of Biomechanics*, *42*(9), 1263-1269.

Brown, K. M., Bursey, D. E., Arneson, L. J., Andrews, C. A., Ludewig, P. M., & Glasoe, W. M. (2009). Consideration of digitization precision when building local coordinate axes for a foot model. *Journal of Biomechanics*, *42*(9), 1263-1269.

Burkhart, S. S. (1992). Fluoroscopic comparison of kinematic patterns in massive rotator cuff tears. A suspension bridge model. *Clinical Orthopaedics and Related Research*, (284), 144-152.

Burnett, A., O'Sullivan, P., Ankarberg, L., Gooding, M., Nelis, R., Offermann, F., & Persson, J. (2008). Lower lumbar spine axial rotation is reduced in end-range sagittal postures when compared to a neutral spine posture. *Manual Therapy, 13*(4), 300-306.

Burton A, S, W., CL, B., & J., F. (2012). In Vitro Comparison of Fixed- and Mobile Meniscal-Bearing Unicondylar Knee Arthroplasties: Effect of Design, Kinematics, and Condylar Liftoff. *The Journal of arthroplasty*. http://dx.doi.org/10.1016/j.arth.2012.02.011

Bushberg, J. T. (2002). *The Essential Physics of Medical Imaging*. (J.-R. John, A. Snyder, & T. DeGeorge, Eds.)*Medical Physics* (2nd ed., Vol. 30, pp. 231-465). Philadelphia, PA: Lippencott Williams & Wilkins.

Cerveri, P., Pedotti, A., & Ferrigno, G. (2005). Kinematical models to reduce the effect of skin artifacts on marker-based human motion estimation. *Journal of Biomechanics*, *38*(11), 2228-2236.

Chuter, V., Payne, C., & Miller, K. (2003). Variability of neutral-position casting of the foot. *Journal of the American Podiatric Medical Association*, *93*(1), 1-5.

Chèze, L., Fregly, B. J., & Dimnet, J. (1995). A solidification procedure to facilitate kinematic analyses based on video system data. *Journal of Biomechanics*, *28*(7), 879-884.

De Bruin, P. W., Kaptein, B. L., Stoel, B. C., Reiber, J. H. C., Rozing, P. M., & Valstar, E. R. (2008). Image-based RSA: Roentgen stereophotogrammetric analysis based on 2D-3D image registration. *Journal of Biomechanics*, *41*(1), 155-164.

De Groot, J H. (1999). The scapulo-humeral rhythm: effects of 2-D roentgen projection. *Clinical Biomechanics*, *14*(1), 63-68.

Della Croce, U., Leardini, A., Chiari, L., & Cappozzo, A. (2005). Human movement analysis using stereophotogrammetry. Part 4: assessment of anatomical landmark misplacement and its effects on joint kinematics. *Gait & Posture*, *21*(2), 226-237.

Duck, T. R., Dunning, C. E., King, G. J. W., & Johnson, J. A. (2003). Variability and repeatability of the flexion axis at the ulnohumeral joint. *Journal of Orthopaedic Research*, *21*(3), 399-404.

Dumas, R., & Cheze, L. (2009). Soft tissue artifact compensation by linear 3D interpolation and approximation methods. *Journal of Biomechanics*, *42*(13), 2214-2217.

Dunk, N. M., Kedgley, A. E., Jenkyn, T. R., & Callaghan, J. P. (2009). Evidence of a pelvis-driven flexion pattern: are the joints of the lower lumbar spine fully flexed in seated postures? *Clinical Biomechanics*, *24*(2), 164-8.

Farrokhi, S., Tashman, S., Gil, A. B., Klatt, B. A., & Fitzgerald, G. K. (2012). Are the kinematics of the knee joint altered during the loading response phase of gait in individuals with concurrent knee osteoarthritis and complaints of joint instability? A dynamic stereo X-ray study. *Clinical Biomechanics*, *27*, 384-389.

Fassbind, M., Rohr, E., Haynor, D., Siegler, S., Sangeorzan, B., & Ledoux, W. (2011). Evaluating foot kinematics using magnetic resonance imaging: from maximum plantar flexion, inversion, and internal rotation to maximum dorsiflexion, eversion, and external rotation. *Journal of Biomechanical Engineering*, *133*(10), 104502.

Ferreira, L. M., Johnson, J. A., & King, G. J. (2010). Development of an active elbow flexion simulator to evaluate joint kinematics with the humerus in the horizontal position. *Journal of Biomechanics*, *43*(11), 2114-2119.

Fox, A.-M. V., Kedgley, A. E., Lalone, E. A., Johnson, J. A., Athwal, G. S., & Jenkyn, T. R. (2011). The effect of decreasing computed tomography dosage on radiostereometric analysis (RSA) accuracy at the glenohumeral joint. *Journal of Biomechanics*, *44(16)*, 2847-2850.

Futai, K., Tomita, T., Yamazaki, T., Murase, T., Yoshikawa, H., & Sugamoto, K. (2010). In vivo three-dimensional kinematics of total elbow arthroplasty using fluoroscopic imaging. *International Orthopaedics*, *34*(6), 847-854.

Green, C., Fitzpatrick, C., FitzPatrick, D., Stephens, M., Quinlan, W., & Flavin, R. (2011). Definition of coordinate system for three-dimensional data analysis in the foot and ankle. *Foot & Ankle International*, *32*(2), 193-199.

Gribble, P. A., & Robinson, R. H. (2009). Alterations in knee kinematics and dynamic stability associated with chronic ankle instability. *Journal of Athletic Training*, *44*(4), 350-355.

Harris, G. F., Smith, P. A., & Marks, R. M. (2008). *Foot and Ankle Motion Analysis: Clinical Treatment and Technology* (pp. 300-400). Boca Raton, FL: Taylor & Francis Group.

Hashimoto, T., Thoreson, A. R., An, K.-N., Amadio, P. C., & Zhao, C. (2012). Comparison of step-cut and Pulvertaft attachment for flexor tendon graft: a biomechanics

evaluation in an in vitro canine model. *The Journal of Hand Surgery (European Volume)*, April, 1-7, DOI: 10.1177/1753193412442460.

Hemmerich, A., Brown, H., Smith, S., Marthandam, S. S. K., & Wyss, U. P. (2006). Hip, knee, and ankle kinematics of high range of motion activities of daily living. *Journal of Orthopaedic Research*, *24*(4), 770-781.

Hioki, A., Miyamoto, K., Shimizu, K., & Inoue, N. (2011). Test-retest repeatability of lumbar sagittal alignment and disc height measurements with or without axial loading: a computed tomography study. *Journal of Spinal Disorders and Techniques*, *24*(2), 93-98.

Howell, S. M., Galinat, B. J., Renzi, A. J., & Marone, P. J. (1988). Normal and abnormal mechanics of the glenohumeral joint in the horizontal plane. *Journal of Bone and Joint Surgery*, *70*(2), 227-232.

Humphrey, J. D. (2002). Continuum biomechanics of soft biological tissues. *Proceedings of the Royal Society*, *459*, 3-46.

Hurschler, C., Seehaus, F., Emmerich, J., Kaptein, B., & Windhagen, H. (2008). Accuracy of model-based RSA contour reduction in a typical clinical application. *Clinical Orthopaedics and Related Research*, *466*(8), 1978-1986.

Hurschler, C., Seehaus, F., Emmerich, J., Kaptein, B., & Windhagen, H. (2009). Comparison of the model-based and marker-based roentgen stereophotogrammetry methods in a typical clinical setting. *Journal of Arthroplasty*, *24*(4), 594-606.

Jenkyn, T R, Shultz, R., Giffin, J. R., & Birmingham, T. B. (2010). A comparison of subtalar joint motion during anticipated medial cutting turns and level walking using a multi-segment foot model. *Gait & Posture*, *31*(2), 153-158.

Jenkyn, T., & Nicol, A. C. (2007). A multi-segment kinematic model of the foot with a novel definition of forefoot motion for use in clinical gait analysis during walking. *Journal of Biomechanics*, *40*(14), 3271-3278.

Kaptein, B. (2003). A new model-based RSA method validated using CAD models and models from reversed engineering. *Journal of Biomechanics*, *36*(6), 873-882.

Kapur, P., Jensen, M., Buxbaum, L. J., Jax, S. A., & Kuchenbecker, K. J. (2010). Spatially distributed tactile feedback for kinesthetic motion guidance. *2010 IEEE Haptics Symposium*, 519-526.

Karduna, A R, McClure, P. W., & Michener, L. A. (2000). Scapular kinematics: effects of altering the Euler angle sequence of rotations. *Journal of Biomechanics*, *33*(9), 1063-1068.

Karduna, A R, McClure, P. W., Michener, L. A., & Sennett, B. (2001). Dynamic measurements of three-dimensional scapular kinematics: a validation study. *Journal of Biomechanical Engineering* (Vol. 123, pp. 184-190).

Kataoka, T., Moritomo, H., Omokawa, S., Iida, A., Murase, T., & Sugamoto, K. (2012). Ulnar variance: its relationship to ulnar foveal morphology and forearm kinematics. *The Journal of Hand Surgery*, *37*(4), 729-735.

Kidder, S. M., Abuzzahab, F. S. J., Harris, G. F., & Johnson, J. E. (1996). A system for the analysis of foot and ankle kinematics during gait. *IEEE transactions on rehabilitation engineering*, *4*(1), 25-32.

Kim, G., Jung, H., Lee, H., Lee, J., Koo, S., & Chang, S. (2012). Accuracy and Reliability of Length Measurements on Three-Dimensional Computed Tomography Using Open-Source OsiriX Software. *Journal of Digital Imaging*, http://dx.doi.org/ 10.1007/ s10278-012-9458-6.

Klous, M., & Klous, S. (2010). Marker-based reconstruction of the kinematics of a chain of segments: a new method that incorporates joint kinematic constraints. *Journal of Biomechanical Engineering*, *132*(7).

Koerhuis, C., Winters, J., van der Helm, F., & Hof, A. (2003). Neck mobility measurement by means of the "Flock of Birds" electromagnetic tracking system. *Clinical biomechanics (Bristol, Avon)*, *18*(1), 14-18.

Komistek, R. D., Stiehl, J. B., Buechel, F. F., Northcut, E. J., & Hajner, M. E. (2000). A determination of ankle kinematics using fluoroscopy. *Foot & ankle international / American Orthopaedic Foot and Ankle Society [and] Swiss Foot and Ankle Society*, *21*(4), 343-50.

Kothari, A., Haughom, B., Feeley, B., Li, X., & Ma, C. (2012). Evaluating rotational kinematics of the knee in ACL reconstructed patients using 3.0Tesla magnetic resonance imaging. *The Knee,* http://dx.doi.org/10.1016/j.knee.2011.12.001.

Lafortune, M. A., Cavanagh, P. R., Sommer, H. J., & Kalenak, A. (1992). Three-dimensional kinematics of the human knee during walking. *Journal of Biomechanics*, *25*(4), 347-357.

Laughton, C., McClay Davis, I., & Williams, D. S. (2002). A comparison of four methods of obtaining a negative impression of the foot. *Journal of the American Podiatric Medical Association*, *92*(5), 261-268.

Leardini, A., Chiari, L., Della Croce, U., & Cappozzo, A. (2005). Human movement analysis using stereophotogrammetry. Part 3. Soft tissue artifact assessment and compensation. *Gait & Posture*, *21*(2), 212-225.

Li, G., Van de Velde, S. K., & Bingham, J. T. (2008). Validation of a non-invasive fluoroscopic imaging technique for the measurement of dynamic knee joint motion. *Journal of biomechanics*, *41*(7), 1616-22.

Lofvenberg, R., Karrholm, J., Selvik, G., & Hanssont, L.-Ingvar. (1989). Roentgen stereophotogrammetry of talar position. *Acta Orthopaedica Scandinavica*, *60*(1), 34-39.

Ma, H. T., Griffith, J. F., Yang, Z., Kwok, A. W. L., Leung, P. C., & Lee, R. Y. W. (2009). Kinematics of the lumbar spine in elderly subjects with decreased bone mineral density. *Medical & Biological Engineering & Computing*, *47*(7), 783-789.

Madihally, S. V. (2010). *Principles of Biomedical Engineering*. Norwood, MA: Artech House.

Matsuki, K., Matsuki, K. O., Mu, S., Yamaguchi, S., Ochiai, N., Sasho, T., Sugaya, H., *et al.* (2011). Are the kinematics of the knee joint altered during the loading response phase of gait in individuals with concurrent knee osteoarthritis and complaints of joint instability? A dynamic stereo X-ray study. *Journal of Shoulder and Elbow Surgery*, *20*(4), 659-665.

McClure, P. W., Michener, L. A., Sennett, B. J., & Karduna, A. R. (2001). Direct 3-dimensional measurement of scapular kinematics during dynamic movements in vivo. *Journal of Shoulder and Elbow Surgery*, *10*(3), 269-277.

McClure, P., Michener, L. A., Sennett, B. J., & Karduna, A. R. (2010). 3D measurement of scapular kinematics during dynamic movements in vivo. *International Orthopaedics*, *34*(6), 847-854.

McQuade, K. J., & Smidt, G. L. (1998). Dynamic scapulohumeral rhythm: the effects of external resistance during elevation of the arm in the scapular plane. *The Journal of orthopaedic and sports physical therapy*, *27*(2), 125-133.

Meskers, C G M, Vermeulen, H. M., De Groot, J. H., Van Der Helm, F. C. T., & Rozing, P. M. (1998). 3D shoulder position measurements using a six-degree-of-freedom electromagnetic tracking device. *Clinical Biomechanics*, *13*(4-5), 280-292.

Meskers, Carel G M, Van De Sande, M. A. J., & De Groot, J. H. (2007). Comparison between tripod and skin-fixed recording of scapular motion. *Journal of Biomechanics*, *40*(4), 941-946.

Milne, A. D., Chess, D. G., Johnson, J. A., & King, G. J. (1996). Accuracy of an electromagnetic tracking device: a study of the optimal range and metal interference. *Journal of Biomechanics*, *29*(6), 791-793.

Mizner, R., Chmielewski, T., Toepke, J., & Tofte, K. (2012). Comparison of 2-Dimensional Measurement Techniques for Predicting Knee Angle and Moment During a Drop Vertical Jump. *Clinical Journal of Sport Medicine*, 22(3), 221-227.

Mu, S, Moro-Oka, T., Johal, P., Hamai, S., Freeman, M. A. R., & Banks, S. A. (2011). Comparison of static and dynamic knee kinematics during squatting. *Clinical Biomechanics*, *26*(1), 106-108.

Myers, J., Jolly, J., Nagai, T., & Lephart, S. (2006). Reliability and precision of in vivo scapular kinematic measurements using an electromagnetic tracking device. *Journal of Sport Rehabilitation*, *15*(2), 125-143.

Nordin, M., & Frankel, V. H. (2001). *Basic Biomechanics of the Musculoskeletal System*. (D. Leger, Ed.) (3rd ed., pp. 178-190). Baltimore: Lippincott Williams & Wilkins.

Padulo J, G, A., GM, M., S, D., & J, T. (2012). Kinematics of Running at Different Slopes and Speeds. *Journal of Strength and Conditioning Research / National Strength & Conditioning Association*, *26*(5), 1331-1339.

Pierrynowski, M. R., and Smith, S. B. (1996). Rear foot inversion/eversion during gait relative to the subtalar joint neutral position. *Foot & Ankle International*, *17*(7), 406-412.

Pinto, R., Souza, T., & Maher, C. (2012). External devices (including orthotics) to control excessive foot pronation. *British Journal of Sports Medicine*, *46*(2), 110-111.

Poppen, N. K., & Walker, P. S. (1976). Normal and abnormal motion of the shoulder. *The Journal of Bone and Joint Surgery*, *58*(2), 195-201.

Roach, N., Lieberman, D., Gill, T. 4th, Palmer, W., & Gill, T. 3rd. (2012). The effect of humeral torsion on rotational range of motion in the shoulder and throwing performance. *Journal of Anatomy*, *220*(3), 293-301.

Root, M., Orien, W., & Weed, J. (1977). *Normal and Abnormal Function of the Foot*. Los Angeles, CA, USA: Clinical Biomechanics Corp.

Rougée, A., Picard, C. L., Trousset, Y. L., & Ponchut, C. (1993a). Geometrical calibration for 3D x-ray imaging. *Proceedings of SPIE*, *1897*, 161-169.

Rougée, A., Picard, C., Ponchut, C., & Trousset, Y. (1993b). Geometrical calibration of X-ray imaging chains for three-dimensional reconstruction. *Computerized medical imaging and graphics the official journal of the Computerized Medical Imaging Society*, *17*(4-5), 295-300. {IEEE} Press.

Sabo, M., McDonald, C., Ng, J., Ferreira, L., Johnson, J., and King, G. (2011). A morphological analysis of the humeral capitellum with an interest in prosthesis design. Journal of Shoulder and Elbow Surgery, 20(6), 880-884.

Sabo, M., Shannon, H., Luce, S., Lalone, E., Ferreira, L., Johnson, J., and King, G. (2012). Elbow Kinematics After Radiocapitellar Arthroplasty. *The Journal of Hand Surgery*, 37(5), 1024-1032.

Seehaus, F., Olender, G., Kaptein, B., Ostermeier, S., & Hurschler, C. (2012). Markerless Roentgen Stereophotogrammetric Analysis for in vivo implant migration measurement using three dimensional surface models to represent bone. *Journal of Biomechanics*, 8(11),1540-1545.

Selvik, G. (1989). Roentgen stereophotogrammetry. A method for the study of the kinematics of the skeletal system. *Acta orthopaedica Scandinavica Supplementum*, *60*(4), 1-51.

Shultz, R., Kedgley, A. E., & Jenkyn, T. R. (2011). Quantifying skin motion artifact error of the hindfoot and forefoot marker clusters with the optical tracking of a multi-segment foot model using single-plane fluoroscopy. *Gait & Posture*, *34*(1), 44-8.

Shum, G. L. K., Crosbie, J., & Lee, R. Y. W. (2007). Movement coordination of the lumbar spine and hip during a picking up activity in low back pain subjects. *European spine journal: official publication of the European Spine Society the European Spinal Deformity Society and the European Section of the Cervical Spine Research Society*, *16*(6), 749-758.

Smith, D. K., Berquist, T. H., An, K. N., Robb, R. A., & Chao, E. Y. (1989). Validation of three-dimensional reconstructions of knee anatomy: CT vs MR imaging. *Journal Of Computer Assisted Tomography*, *13*(2), 294-301.

Svedmark, P., Lundh, F., Németh, G., Noz, M. E., Maguire, G. Q. J., & Zeleznik, Michael P. Olivecrona, H. (2011). Motion analysis of total cervical disc replacements using computed tomography: Preliminary experience with nine patients and a model. *Acta Radiologica*, *52*(10), 1128-1137.

Söderkvist, I., & Wedin, P. A. (1993). Determining the movements of the skeleton using well-configured markers. *Journal of Biomechanics*, *26*(12), 1473-1477.

Talkhani, I. S., & Kelly, C. P. (2001). Movement analysis of asymptomatic normal shoulders: a preliminary study. *Journal of Shoulder and Elbow Surgery*, *10*(6), 580-584.

Tranberg, R., & Karlsson, D. (1998). The relative skin movement of the foot: a 2-D roentgen photogrammetry study. *Clinical biomechanics*, *13*(1), 71-76.

Tranberg, R., Saari, T., Zügner, R., & Kärrholm, J. (2011). Simultaneous measurements of knee motion using an optical tracking system and radiostereometric analysis (RSA). *Acta Orthopaedica*, *82*(2), 171-176.

Valstar, E. (2002). The use of Roentgen stereophotogrammetry to study micromotion of orthopaedic implants. *ISPRS Journal of Photogrammetry and Remote Sensing*, *56*(5-6), 376-389.

Valstar, E R, de Jong, F. W., Vrooman, H. a, Rozing, P. M., & Reiber, J. H. (2001). Model-based Roentgen stereophotogrammetry of orthopaedic implants. *Journal of biomechanics*, *34*(6), 715-22.

Valstar, Edward R, Gill, R., Ryd, L., Flivik, G., Börlin, N., & Kärrholm, J. (2005). Guidelines for standardization of radiostereometry (RSA) of implants. *Acta orthopaedica*, *76*(4), 563-72.

Van Der Helm, F. C., & Pronk, G. M. (1995). Three-dimensional recording and description of motions of the shoulder mechanism. *Journal of Biomechanical Engineering*, *117*(1), 27-40.

Van Roy, P., Baeyens, J. P., Fauvart, D., Lanssiers, R., & Clarijs, J. P. (2005). Arthro-kinematics of the elbow: study of the carrying angle. *Ergonomics*, *48*(11-4), 1645-1656.

Veldpaus, F. E., Woltring, H. J., & Dortmans, L. J. (1988). A least-squares algorithm for the equiform transformation from spatial marker co-ordinates. *Journal of Biomechanics*, *21*(1), 45-54.

Wada, M., Tatsuo, H., Kawahara, H., Sato, M., & Baba, H. (2001). In vivo kinematic analysis of total knee arthroplasty with four different polyethylene designs. *Artificial Organs*, *25*(1), 22-28.

Watanabe, K., Fujii, T., Kitaoka, H., Kotajarvi, B., Luo, Z., & An, K. (2012). Analysis of ankle-hindfoot stability in patients with ankle instability and normals. *International Orthopaedics*, *36*(1), 89-94.

Wearing, S. C., Urry, S., Perlman, P., Smeathers, J., & Dubois, P. (1998). Sagittal plane motion of the human arch during gait: a videofluoroscopic analysis. *Foot ankle international American Orthopaedic Foot and Ankle Society and Swiss Foot and Ankle Society*, *19*(11), 738-742.

Winter, D. A. (2009). *Biomechanics and Motor Control of Human Movement*. *Motor Control* (4th ed.). New Jersey: John Wiley & Sons, Inc.

Wolf, S., Simon, J., Patikas, D., Schuster, W., Armbrust, P., & Döderlein, L. (2008). Foot motion in children shoes: a comparison of barefoot walking with shod walking in conventional and flexible shoes. *Gait & Posture*, *27*(1), 51-59.

Wrbaskić, N., & Dowling, J. (2007). An investigation into the deformable characteristics of the human foot using fluoroscopic imaging. *Clinical biomechanics (Bristol, Avon)*, *22*(2), 230-238.

Wu, G., Siegler, S., Allard, P., Kirtley, C., Leardini, A., Rosenbaum, D., Whittle, M., *et al.* (2002). ISB recommendation on definitions of joint coordinate system of various joints for the reporting of human joint motion--part I: ankle, hip, and spine. International Society of Biomechanics. *Journal of Biomechanics*, *35*(4), 543-548.

Xu, X., Chang, C., Faber, G., Kingma, I., & Dennerlein, J. (2011). The Validity and Interrater Reliability of Video-Based Posture Observation During Asymmetric Lifting Tasks. *Human Factors*, *53*(4), 371-382.

CHAPTER 2- THE EFFECT OF FOAM CASTED ORTHOTICS ON THE NORMAL FOOT USING MARKERLESS RSA

OVERVIEW: This chapter describes the effect of a foam casted orthotic and a neutral cushion running shoe compared to barefoot on the alignment of the bones of the foot in a normal population compared a to barefoot condition. Bi-planar x-ray fluoroscopy and the markerless RSA technique are used to determine the change in pronation of the normal population at midstance during gait.

2.1 INTRODUCTION

Orthotics are commonly prescribed for the conservative treatment of musculoskeletal disorders in the foot and ankle, such as pes cavus or pes planus. These devices are intended to alter the motion of the foot bones by applying constraint or support to various structures on the plantar surface. However, there have been very few studies to quantify the effects of orthotic devices on the human foot during weight-bearing activities, especially within the normal population. The subtalar joint consists of two bones, the talus and calcaneus. The subtalar neutral position is considered the point when the subtalar joint is neither pronated nor supinated. Clinicians who assess foot posture frequently use the definition of a neutral foot when referring to the subtalar neutral (STN) position. When casting an orthotic in the subtalar neutral position the

clinician must palpate the talonavicular joint and determine the mid-position (Houck *et al.,* 2008). The normal population is considered to have a foot that experiences approximately 5° eversion in the frontal plane during walking gait. The normal population is considered to be those with an arch that pronates less than pes planus and more than pes cavus individuals during level walking gait. The pes planus population is considered to have an arch that collapses due to excessive pronation. The pes cavus population remains in fixed plantarflexion during walking gait. The pes cavus population is characterized by an abnormally high medial longitudinal arch. Excessive supination is present in the pes cavus population during walking gait. The pronated foot is one where the arch collapses inward (or the sole of the foot faces laterally) (Nordin and Frankel, 2001). Pronation is considered to be a combination of external rotation, dorsiflexion, and eversion. Supination is considered to be the combination of internal rotation, plantarflexion, and inversion.

Markerless radiostereometric analysis (RSA) systems show promise in tracking skeletal kinematics while using two fluoroscopes without requiring the insertion of beads into the bones of interest (as required with traditional RSA). Using the markerless RSA technique, based on the work completed by Allen and Kedgley, a three-dimensional (3D) computer model of the bones of interest is matched to the two fluoroscopic images taken simultaneously of the bones from different angles (Allen, 2009; Kedgley, 2009). The RSA method in this case determines the position and orientation of the bones of interest during walking gait to determine the effect orthotics have on the bones of the foot, specifically: the calcaneus, cuboid, navicular and

tibia/fibula. A difference of approximately 5° between barefoot and a shoed (orthotic or no orthotic) condition is the minimal difference expected to be clinically significant. A difference of approximately 5° between barefoot and a shoed (orthotic or no orthotic) condition is the minimal difference expected to be clinically significant. The barefoot condition is used as the reference position since pedorthists use barefoot walking to analyze a patient's gait and cast custom orthotics. A calibration technique was used to determine the relative positions of the two x-ray images (parameters include, the x-ray foci locations and the pose of both image planes). The location of the fluoroscope sources and projected image planes, provided by the calibration parameters, were accurately positioned in a virtual environment. The 3D computer bone model created from computed tomography (CT) scans could then be imported into the virtual environment and manually adjusted in 3D space until the projections matched the bone shadows on the radiographs.

The aims of this study were to quantify the change in pronation of the hindfoot in a normal population during weight-bearing walking gait. Four conditions were tested: (1) barefoot, (2) with neutral cushion running shoes, (3) a soft foam casted orthotic (foam soft), and (4) a rigid foam casted orthotic (foam hard). It was hypothesized that orthotics would change the alignment of the hindfoot, putting it into less pronation. It was also hypothesized that the rigid foam casted orthotic would reduce pronation by a greater amount than the soft foam orthotic.

2.2 METHODS

Ethics approval was obtained from the Health Sciences Research Ethics Board at The University of Western Ontario prior to the commencement of any data collection (Appendix A).

2.2.1 PLATFORM DESIGN

A platform was designed and built for this study that raised the test subjects off the ground and allowed them to walk through the capture volume of the two fluoroscopes. This was necessary since the C-arm fluoroscopes in the Wolf Orthopaedic Quantitative Imaging Laboratory (WOQIL) cannot be lowered down entirely to the floor. Two fluoroscopic views were captured, one was a dorsal-medial to plantar-lateral view and the second was a sagittal view. The platform was fabricated by the University Machine Shop at The University of Western Ontario. The concept drawing of the platform (figure 2.1) was completed using SolidWorks (SolidWorks; Dassault Systèmes SolidWorks Corp., Waltham, MA, USA).
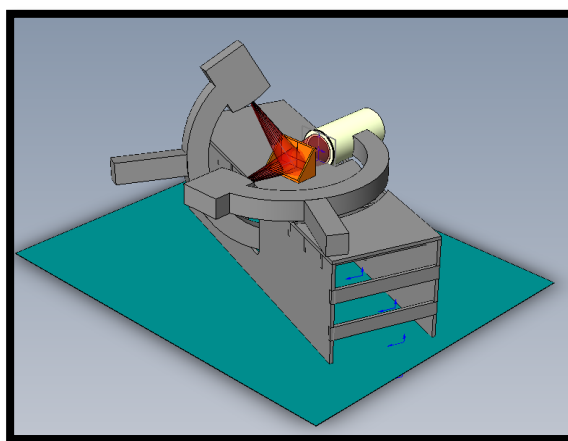
Figure 2.1: Platform concept drawing prior to being built.

2.2.2   DATA COLLECTION

Five (5) normally arched volunteers with no previous foot or ankle disorders, no foot or ankle pain, and no previous orthotic use were recruited to participate in this study. Individuals with previous fractures in the lower extremities were avoided and pre-screened for. Each volunteer had their feet examined by a certified pedorthist to ensure they fit the criteria for normal. Volunteers were asked to fill out a consent form after the study was explained as well as any risks involved. The volunteers were fitted for two pairs of custom-made orthotics with: (1) a 4mm plastazote (soft) and (2) 3mm RCH-500 (hard) material by the same Canadian certified pedorthist at the Fowler Kennedy Sport Medicine Clinic, London, ON, Canada. The pedorthist used a foam box casting technique for this study.

The fluoroscopes were positioned so the two images of the foot gave optimal views of the calcaneus at the instant of midstance of gait. At least one calibration image was captured prior to the volunteer's arrival for the study. The calibration process is described in detail in section 2.2.3. Each volunteer wore a wrap-around leaded apron and kilt on their upper and lower body respectively, including a thyroid collar (figure 2.2). This protected them from any secondary x-ray scatter and ensured that only the feet were exposed to the primary x-ray beams. Section 2.2.2.1 to section 2.2.2.4 were completed in a randomized order. To reduce repetition it is assumed the order was completed as written.

Figure 2.2: Final platform design, the wrap around leaded clothing, the fluoroscope set-up and foot location for a static trial in a neutral cushion shoe. The barefoot trial (with no footwear) and the orthotic trials (different insoles) require the volunteer to appear similar.

2.2.2.1   BAREFOOT

Each volunteer was asked to stand on the platform barefoot. The volunteer was asked to place their left foot in the field of view of the two fluoroscopes (figure 2.2). An x-ray technician ensured the two views of the calcaneus were optimal. The x-ray technician then outlined the location of the volunteer's foot to be used as a target during the dynamic walking trials. Each volunteer was asked to walk at their preferred pace along the platform and through the fluoroscopes field of view as the fluoroscopes recorded images of the left foot from heel strike to toe-off. Images were recorded at 60 interlaced frames per second (or 30 true frames per second). The images were recorded on the PC in the adjacent control room. The captured images were checked to ensure that the calcaneus and tarsus were sufficiently visible for the subsequent RSA procedure

before moving onto the next trial. If the calcaneus was not satisfactorily visible, the trial was repeated. The barefoot condition was repeated two times.

2.2.2.2   NEUTRAL CUSHION RUNNING SHOE

Each volunteer was asked to wear a neutral control running shoe, specifically, a New Balance (model 882) neutral cushioning running shoe for the purposes of this study. Each volunteer was asked to walk at their preferred pace along the platform as the fluoroscopes recorded images of the left foot from heel strike to toe-off. Images were recorded at 30 frames per second. The images were recorded on the control PC in the adjacent control room. As with the barefoot trials, if the calcaneus was not satisfactorily imaged the trial was repeated. The foam soft trial condition was repeated two times.

2.2.2.3   FOAM SOFT ORTHOTIC

Each volunteer was asked to wear the neutral cushioning running shoe (New Balance, model 882) with the custom-made soft foam casted orthotic insole inserted in place of the provided manufacturer's insole. Each volunteer was asked to walk at their preferred pace as the fluoroscopes recorded images of the left foot movement at 30 frames per second from heel strike to toe-off. The images were recorded on the control PC in the adjacent control room. As with the barefoot trials, if the calcaneus was not satisfactorily imaged the trial was repeated. The foam soft trial condition was repeated two times.

2.2.2.4   FOAM HARD ORTHOTIC

Each volunteer was asked to wear the neutral cushioning running shoe (New Balance, model 882) with the custom-made hard foam casted orthotic insole inserted in place of the manufacturer's insole. Each volunteer was asked to walk at their preferred pace as the fluoroscopes recorded the left foot movement at 30 frames per second from heel strike to toe-off. The images were recorded on the PC in the adjacent control room. As with the barefoot trials, if the calcaneus was not satisfactorily imaged the trial was repeated. The foam soft trial condition was repeated two times.

2.2.3   CALIBRATION

Bi-planar RSA uses two x-ray imaging devices. Fluoroscopy image intensifiers (II) were used for the purpose of this thesis. A calibration frame is used to establish a laboratory coordinate system for the capture volume through which the test subject will walk and determines the locations of the two imaging devices relative to one another. A calibration object is placed within the capture volume so that it can be seen by both fluoroscopes simultaneously. The calibration object is a cube with two fiducial planes and two control planes (figure 2.3). A calibration frame designed by Kedgley, was used as the calibration phantom for this thesis (Kedgley, 2009; Kedgley and Jenkyn, 2009). The custom-designed calibration frame was constructed using 9.5mm thick acrylic sheet. Each fiducial plane was embedded with 45 beads (1mm in diameter) at known 3D locations. The control plane was embedded with 45 beads (2mm in diameter) at known 3D locations. Each frame defined the laboratory coordinate system and was used to

determine the experimental set-up parameters necessary for analysis. The x-, y-, and z-axes are coloured red, green, and blue respectively, as seen in Figure 2.3.

In order to calibrate the capture volume each imaging device must have a view of one fiducial plane and one control plane on the calibration box. The fiducial plane is used to calculate a transformation from the image coordinate system to the laboratory coordinate system. The control plane determines the location of the focal point from which the x-rays originate in the laboratory frame (Kedgley and Jenkyn, 2009). A calibration algorithm is used to determine the relationship of the 3D bead locations and the two-dimensional (2D) images captured of the beads. For the calibration algorithm to be successful, it is assumed that the fiducial plane has been placed closest to the II (figure 2.3) of each fluoroscope (Kedgley, 2009). The parameters outputted from the calibration algorithm are used to reconstruct the experimental set-up in the virtual 3D environment (Rhinoceros, Robert McNeel & Associates, Seattle, WA, USA).
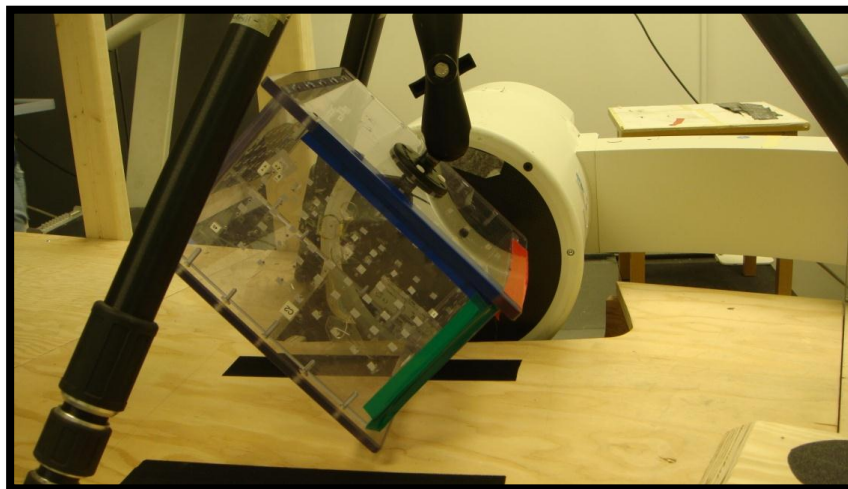
Figure 2.3: The calibration frame. The x-, y-, and z-axes are shown in red, green and blue respectively. The origin of the frame is located where all the colours intersect in the picture above.

Images of the calibration frame were captured, digitized and corrected for pincushion distortion (Kedgley, 2009). The image is captured such that the control beads and the fiducial beads superpose onto one image plane. It was ensured that at least 6 fiducial beads and 6 control beads were visible in each image. While this number of beads the minimum needed for calibration, accuracy of the calibration procedure is increased when a greater number of beads can be utilized. Prior to proceeding with the calibration procedure it was ensured that no beads were overlapped in the image. If this was the case, manipulation of the calibration frame was necessary until a good image of the fiducial and control planes could obtained for both fluoroscopes simultaneously. The distortion correction process required that an image of the distortion grid be captured and digitized on each fluoroscope during each set-up. The distortion grid, Figure 2.4, designed by Kedgley contains 131 beads embedded at known locations (Kedgley, 2009). The algorithm then corrected for distortion by using a fourth-order polynomial fit approach (Kedgley, 2009).
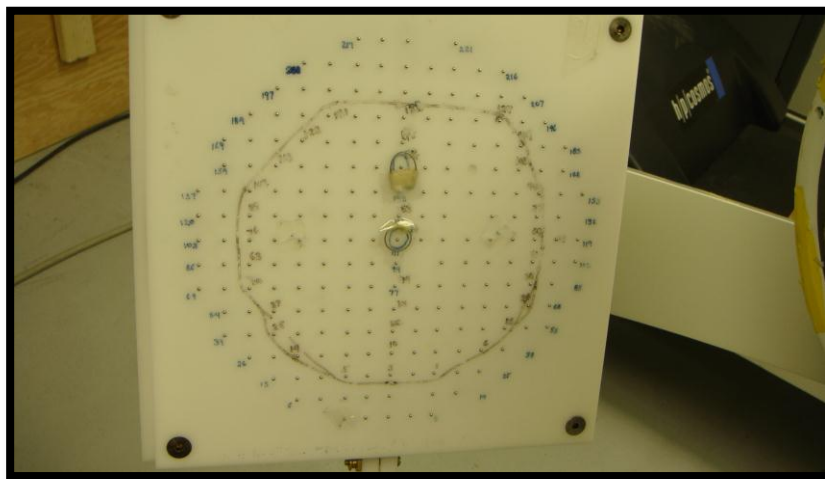
Figure 2.4: Distortion grid attached to fluoroscope for image capture.

The location of the fluoroscopes x-ray source was determined using an existing standard RSA code developed by Kedgley. The location of the x-ray source (x_s,y_s,z_s) was considered to be a known locations beyond this algorithms calculations (Kedgley, 2009; Allen, 2009).

2.2.3.1   CALIBRATION ALGORITHM

The algorithm used for the remainder of the calibration is based on the work of Rougée *et al.* (1993a and 1993b). Each fluoroscope is represented using a perspective projection model where the mathematical relationship between the 3D calibration points and their 2D projections are determined and defined for the algorithm to continue. Using the mathematical relationship and an optimization algorithm determines the calibration parameters necessary for an accurate model can be determined.

The derivation required for the calibration of a single fluoroscope will be shown in this thesis. The same technique can be used to model the second fluoroscope. The result of the derivation will be included for both fluoroscopes.

2.2.3.2   THE FLUOROSCOPE PROJECTION MODEL

Each fluoroscope is modeled as a pinhole camera using a perspective projection model. All x-rays are assumed to travel in straight lines and originate from a single point source. The derivation is based off the set-up used for this thesis as seen in Figure 2.5.
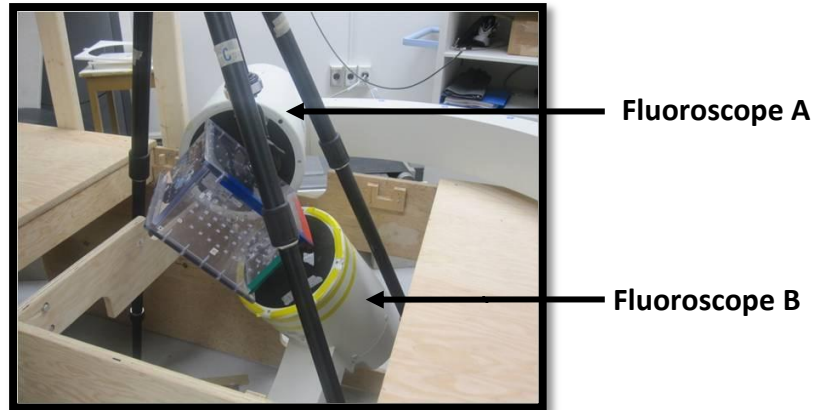
Figure 2.5: Example of the experimental set-up with the calibration frame in its position. The image intensifier (II) for fluoroscope A and fluoroscope B are labelled. The x-ray source for each fluoroscope cannot be seen in the image above.

The perspective projection model for fluoroscope A can be seen in Figure 2.6 where,

O- the origin of the calibration frame,

S- the position of x-ray source,

S'- the position of the projection of the x-ray source onto the image plane,

R= (o, X, Y, Z), calibration frame coordinate system (also known as the laboratory coordinate system),

R'= (s, X, Y, Z), the projection coordinate system.

The C and L axes define the 2D image plane coordinate system and are assumed parallel to the Z' and Y' axes respectively for the purposes of the model. All measurements are conducted in mm except for the image plane coordinate system. The image plane coordinate system is measured in pixels.
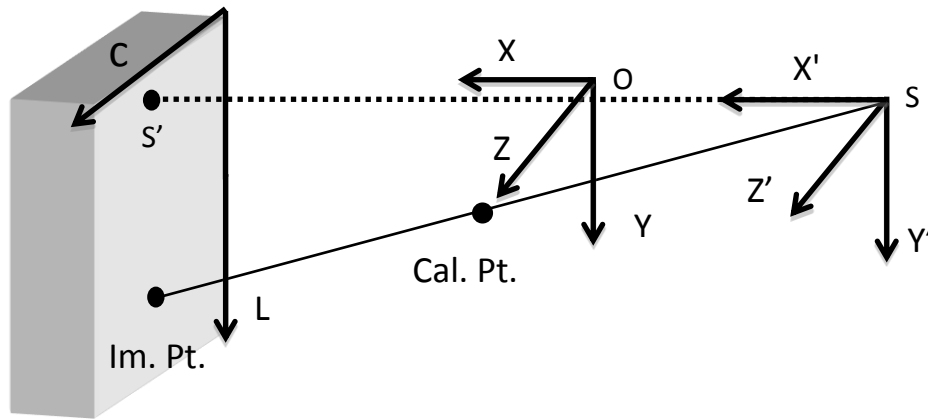
Figure 2.6: Perspective projection model illustrating the calibration frame coordinate system, and projection coordinate system. This is based on calibration set-up in Figure 2.5.
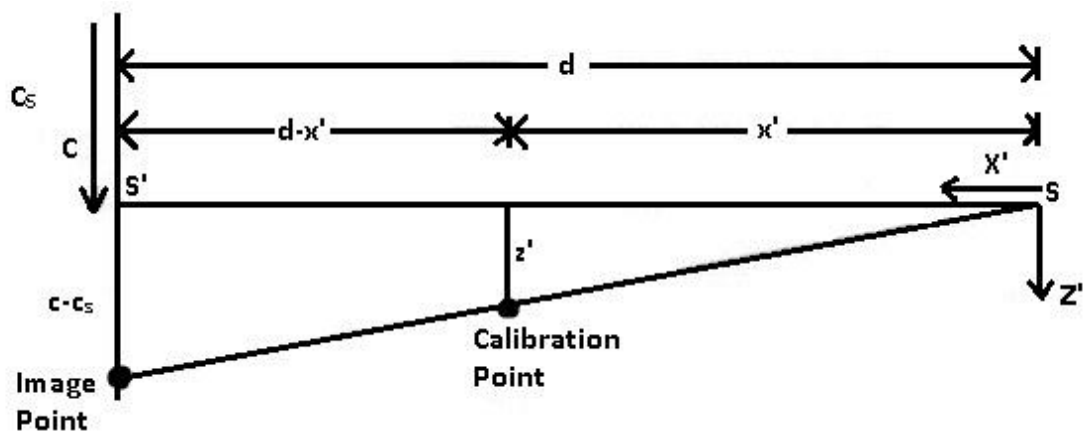
Figure 2.7: Planar view of the projection of a calibration point onto the image plane based on the calibration setup in figure 2.3. The distances labelled on the figure are used to determine the relationship between the coordinates of the calibration point in the projection coordinate system (x',y',z'), and the respective image point (c_s,l_s) in X'-Z' plane.
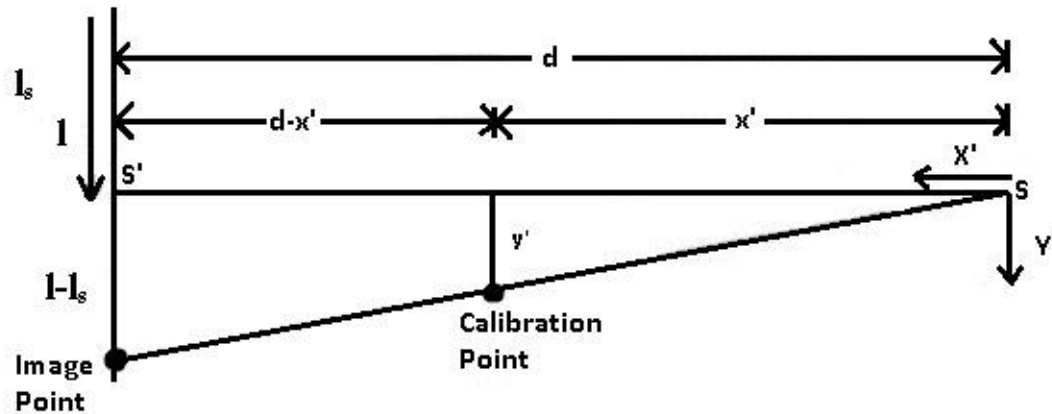
Figure 2.8: Planar view of the projection of a calibration point onto the image plane based on the calibration setup in figure 2.3. The distances labelled on the figure are used to determine the relationship between the coordinates of the calibration point in the projection coordinate system (x',y',z') and the respective image point (c_s,l_s) in the X'-Y' plane.

The perspective projection model in the Y-direction (figure 2.7) and Z-direction (figure2.8), is used to develop a mathematical relationship by way of similar triangles between the coordinates of the calibration point in the projection coordinate system (x', y', z') and its image point (c, l). The equations developed by the relationship are represented in equations 2.1 and 2.2.

$$\left(\frac{c-c_s}{d}\right) S_p = \frac{z'}{x'}$$ (Eq. 2. 1)

$$\left(\frac{l-l_s}{d}\right) S_p = \frac{Y'}{x'}$$ (Eq. 2. 2)

where:

d= distance from s to s' (mm),

S_p= pixel size (mm),

(c,l)- coordinates of the image point (pixels),

(c_s, l_s)- coordinates of the projection of the source (pixels),

(x′,y′,z′)- calibration point in the projection coordinate system (mm).

Equation 2.1 and Equation 2.2 can be rearranged into equations 2.3 and 2.4 respectively.

$$\frac{c}{d}x' = \frac{c_s}{d}x' + \frac{Z\prime}{S_p}$$ (Eq. 2. 3)

$$\frac{l}{d}x' = \frac{l_s}{d}x' + \frac{Y\prime}{S_p}$$ (Eq. 2. 4)

Equations 2.3 and 2.4 can be written in matrix from (Eq. 2.5).

$$\frac{x\prime}{d}\begin{bmatrix} c \\ l \\ 1 \end{bmatrix} = \begin{bmatrix} \frac{c_s}{d} & 0 & \frac{1}{S_p} \\ \frac{l_s}{d} & \frac{1}{S_p} & 0 \\ \frac{1}{d} & 0 & 0 \end{bmatrix} \begin{bmatrix} x' \\ y' \\ z' \end{bmatrix}$$ (Eq. 2. 5)

where the matrix $\mathbf{P}(c_s, l_s, d)$ is defined as:

$$P(c_s, l_s, d) = \begin{bmatrix} \frac{c_s}{d} & 0 & \frac{1}{S_p} \\ \frac{l_s}{d} & \frac{1}{S_p} & 0 \\ \frac{1}{d} & 0 & 0 \end{bmatrix}$$ (Eq. 2. 6)

The coordinates of the calibration point in R′ (image plane coordinate system) are not known, however, the coordinates can be calculated using their known coordinates in R (the laboratory coordinate system).

$$\begin{bmatrix} x' \\ y' \\ z' \end{bmatrix} = R(\theta, \phi, \psi) \begin{bmatrix} x - x_s \\ y - y_s \\ z - z_s \end{bmatrix}$$ (Eq. 2. 7)

where:

$R(\theta, \phi, \psi)$=Y-Z-X Euler angle sequence associated with the axes change from R to R′,

θ= the rotation about the Y-axis,

Φ= the rotation about the Z-axis,

Ψ= the rotation about the X-axis.

The rotation chosen is based upon the relative positioning of the two fluoroscopes and their relationship to the laboratory custom calibration frame used in this study as done using a geometrical three-dimensional reconstruction technique (Rougée *et al.*, 1993a; Rougée *et al.*, 1993b).

The rotation matrix **R** is calculated by:

$$\mathbf{R}(\theta, \phi, \psi) = rot(Y, \theta) \bullet rot(Z, \phi) \bullet rot(X, \psi) \qquad \text{(Eq. 2. 8)}$$

$$\mathbf{R}(\theta, \varphi, \psi) = \begin{bmatrix} \cos\theta & 0 & \sin\theta \\ 0 & 1 & 0 \\ -\sin\theta & 0 & \cos\theta \end{bmatrix} \begin{bmatrix} \cos\phi & -\sin\phi & 0 \\ \sin\phi & \cos\phi & 0 \\ 0 & 0 & 1 \end{bmatrix} \begin{bmatrix} 1 & 0 & 0 \\ 0 & \cos\psi & -\sin\psi \\ 0 & \sin\psi & \cos\psi \end{bmatrix} \text{(Eq. 2. 9)}$$

where,

rot(Y, θ)= rotation about the Y-axis of magnitude θ ,

rot(Z, φ)= rotation about the Z-axis of magnitude φ,

rot(X, ψ)= rotation about the X-axis of magnitude ψ.

Equation 2.7 can now be written as:

$$\begin{bmatrix} x' \\ y' \\ z' \end{bmatrix} = \mathbf{R}(\theta, \varphi, \psi) \mathbf{T}(x_s, y_s, z_s) \begin{bmatrix} X \\ y \\ z \\ 1 \end{bmatrix} \qquad \text{(Eq. 2. 10)}$$

where,

$$\mathbf{T}(x_s, y_s, z_s) = \begin{bmatrix} 1 & 0 & 0 & -x_s \\ 0 & 1 & 0 & -y_s \\ 0 & 0 & 1 & -z_s \end{bmatrix} \qquad \text{(Eq. 2. 11)}$$

Substituting equations 2.6 and 2.10 into equation 2.5 yields:

$$\frac{x'}{d}\begin{bmatrix} c \\ l \\ 1 \end{bmatrix} = P(c_s, l_s, d) \bullet R(\theta, \varphi, \psi) \bullet T(x_s, y_s, z_s) \begin{bmatrix} x \\ y \\ z \\ 1 \end{bmatrix}$$ (Eq. 2. 12)

A portion of equation 2.12 can be represented as:

$$M(\xi) = P(c_s, l_s, d) \bullet R(\theta, \varphi, \psi) \bullet T(x_s, y_s, z_s)$$ (Eq. 2. 13)

Therefore equation 2.12 can be simplified:

$$\frac{x'}{d}\begin{bmatrix} c \\ l \\ 1 \end{bmatrix} = M(\xi) \begin{bmatrix} x \\ y \\ z \\ 1 \end{bmatrix}$$ (Eq. 2. 14)

where,
$(\xi_j)_{j=1,9}$= calibration parameters (x_s, y_s, z_s, θ, ϕ, ψ, c_s, l_s, d).

Equation 2.14 shows the required relationship between 3D points and their 2D projections. Utilizing the known coordinates of the 3D calibration points (x_i, y_i, z_i) and their measured corresponding 2D projected image points (c_i, l_i), each point [i=1,N] must satisfy equation 2.14. Equation 2.14 can be re-written for easier calculation purposes as Equation 2.15 and Equation 2.16.

$$c_i = \frac{m_{11}x_i + m_{12}y_i + m_{13}z_i + m_{14}}{m_{31}x_i + m_{32}y_i + m_{33}z_i + m_{34}}$$ (Eq. 2. 15)

$$l_i = \frac{m_{21}x_i + m_{22}y_i + m_{23}z_i + m_{24}}{m_{31}x_i + m_{32}y_i + m_{33}z_i + m_{34}}$$ (Eq. 2. 16)

where, m_{kl} is the kth row and the lth column.

2.2.3.3   PIXEL SIZE CALCULATION

The pixel size is not considered a calibration parameter but rather a known value throughout the calibration algorithm. The pixel size for each fluoroscope is assumed to remain constant. To determine the pixel size of each fluoroscope Allen and Kedgley had a pixel grid manufactured with 0.2mm diameter holes at known locations (Allen, 2009). Using custom-written MATLAB script titled "Pixel_Size_Calculator" found in Appendix A.2 of Allen's 2009 thesis work the average pixel size was calculated (MATLAB; The MathWorks, Natick, MA, USA) (Allen, 2009). The pixel size for fluoroscope A and fluoroscope B were found to be 0.3847mm and 0.3819mm, respectively.

2.2.3.4   CALIBRATION PARAMETER ESTIMATION

An optimization technique was completed using the information of the pixel size, and the relationship between the 3D calibration points and their 2D image plane projections. A program created initially by Allen using MATLAB was modified for each calibration in this thesis (Allen, 2009). This MATLAB script used the 'fmincon' function that calculates the minimum of a constrained non-linear multivariable function by way of numerical optimization. The calibration parameters that are optimized during this process include: the known 3D calibration coordinates (x_i, y_i, z_i), and the distortion corrected 2D image point coordinates (c_i, l_i).

The 2D image point coordinates were determined by first digitizing the calibration images followed by a distortion correction algorithm. The digitization process involves identifying each calibration bead visible. Distortion correction was completed on the 2D image point coordinates using custom-written MATLAB script (Kedgley, 2009).

The 3D calibration points were matched with the corresponding 2D images points that were used for the optimization of those input parameters. The optimization algorithm created by Allen minimized the root mean squared error (RMSE) between the digitized 2D calibration image points (c_i, l_i) and the 2D image points $c_i(\xi)$, $l_i(\xi)$ (Allen, 2009). Where the $c_i(\xi)$, $l_i(\xi)$ are the 2D coordinates of the projection points calculated using (x_i, y_i, z_i) by applying equations 2.15 and 2.16. The symbolic equations for $c_i(\xi)$, $l_i(\xi)$ were written in Maple (Maplesoft, Waterloo, ON, Canada) which were then imported into the MATLAB code used to calculate $c_i(\xi)$, $l_i(\xi)$ for the purpose of estimating the initial calibration parameters (Allen, 2009).

According to the fluoroscopes operating manual (SIREMOBIL Compact (L), Siemens Medical Solutions USA Inc., Malvern, PA, USA) the distance d, as represented in Figure 2.6 and Figure 2.7, should be 1000 mm. The coordinates of the projected source (c_s, l_s) should be located at (0,0) provided that the distortion grid was placed directly at the centre of the II. However, since the fluoroscopes manual did not contain the manufacturing tolerances and the distortion grid may have been placed slightly off-centered it was believed that it was reasonable to constrain the projected source to within 2 pixels of (0,0) and d to within 5mm of 1000mm (Allen, 2009).

Initial Euler angle estimates were calculated by iteration through several angle values to calculate the combination that resulted in the lowest RMSE. The Euler angles determine the rotation required by the image plane to match the orientation of the 3D calibration frame relative to the laboratory coordinate system. The initial Euler angles were iterated between $-\pi$ radians to π radians with a step size of $\pi/16$ radians. Two

additional iterations were then performed to determine more precise initial estimates for the Euler angles.

2.2.3.5   IMAGE PLANE CORRECTION

The calibration algorithm discussed in sections 2.2.3.1-2.2.3.4 of this thesis described the method by which the input parameters were calculated. The image plane correction determines the rotation and translation required for the image plane to match the laboratory coordinate systems location.

To ensure this step goes smoothly when the distortion grid was imaged on the fluoroscope it was important that the grid was manually positioned on the input screen of the image intensifier. The lines of the distortion grid are visually lined up to avoid large rotations and translations during the distortion correction process (figure 2.9). Having the distortion grid placed differently will result in a successful calibration; however, visually it will be less appealing. Custom MATLAB and RhinoScript programs developed by Allen were used to correct for any additional image rotations and translations (Rhinoceros; Robert McNeel & Associates, Seattle, WA, USA). This allowed for an initial estimate of the image plane rotation and translation of the distortion grid with respect to the pixel coordinate system. An optimization technique was then completed to find the final image pose for the virtual experimental re-creation.
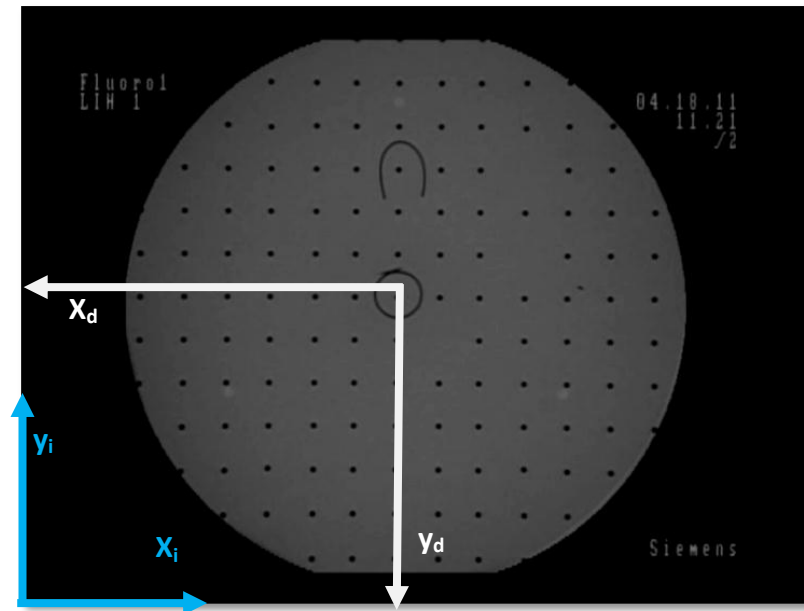
Figure 2.9: Image of the distortion grid. The axis of X_d and y_d represent the distortion grid coordinate system. The axis of x_i and y_i represent the image plane coordinate system.

Detailed steps to describe the process required in the recreation of the experimental set-up in the virtual environment can be found in Appendix E of Allen's 2009 thesis work. When completing the final Rhinoscript code titled "ImportPoints" described in Allen's Appendix E only the points which have been previously digitized and corrected for distortion onto the image (figure 2.10) were included during this codes use. These 2D points were considered the distortion corrected points. Although it may appear as though more points could have been digitized (figure 2.11) the control and fiducial points are actually overlapped. It is important not to digitize points if they are too close to each other as it will result in a failed calibration since the algorithm will not be able to compute the x-ray focus accurately.
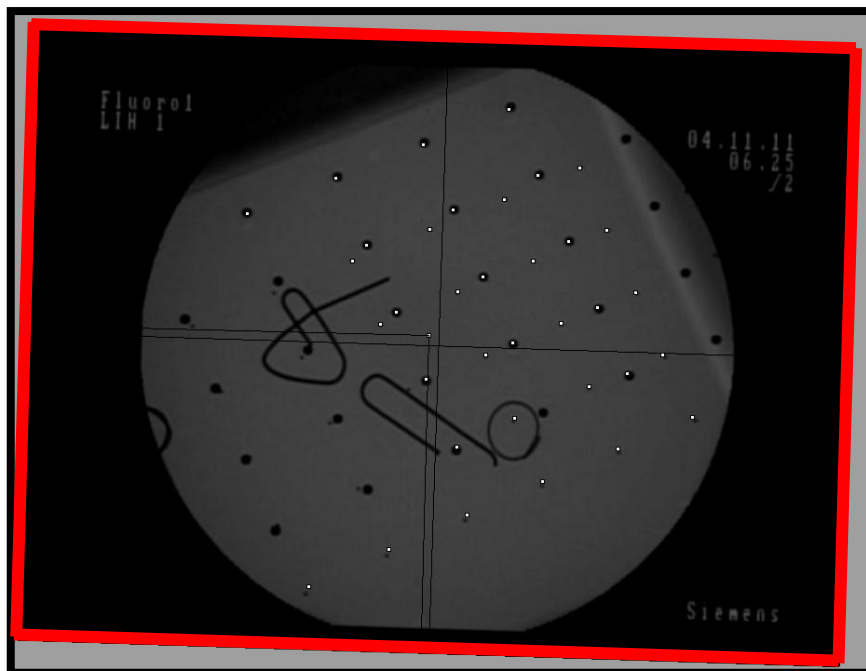
Figure 2.10: Calibration Image of the distortion-corrected 2D calibration points. The distortion corrected points are represented as open squares and the uncorrected points are represented as black circular image points. The image plane is outlined in red.
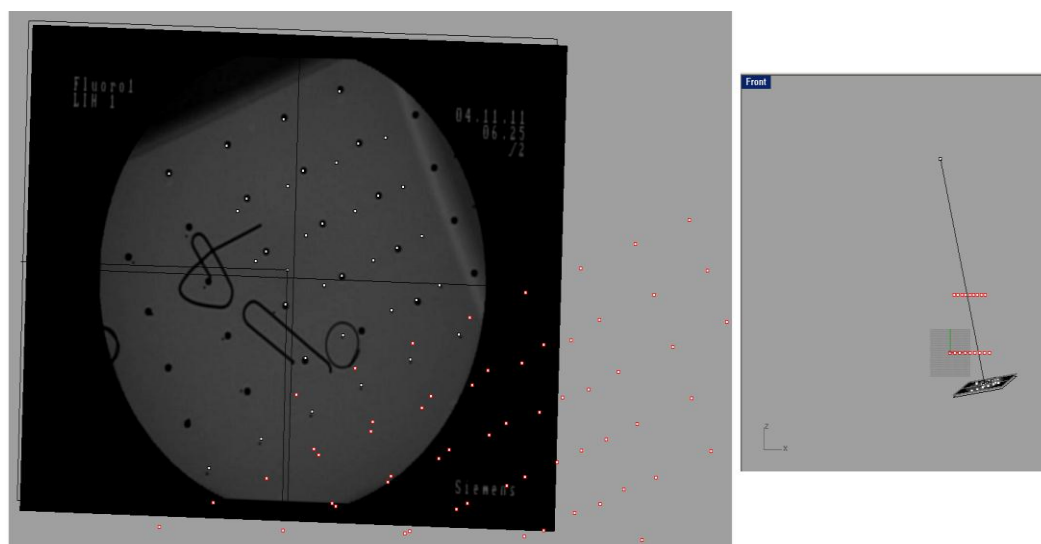
Figure 2.11: The 3D calibration points associated with this fluoroscope are represented as open red squares ("Frame Points-F2C2.3dm"). Right: View of fluoroscope A's source and the image on the left is a front view. It can be seen that the points do not line up with those in the fluoroscopes image and require further correction.

With the experimental set-up roughly modeled in the virtual environment the 3D calibration frame points can be imported into the experimental set-up file (figure 2.11). These calibration files are titled "Frame Points-F1C1.3dm" and "Frame Points-F2C2.3dm" and contain the 3D location of the beads with respect to each other and considered the laboratory coordinate system. Each file corresponds to fiducial plane 1 (F1) and control plane 1 (C1) or fiducial plane 2 (F2) and control plane 2 (C2). Based on Figure 2.5 the calibration of fluoroscope A was associated with the "Frame Points-F2C2.3dm" file. Similarly, fluoroscope B is associated with F1C1 since they both cannot be associated with the same sides of the calibration frame.

It becomes obvious that the laboratory coordinate system (red points in figure 2.11) does not match up with the respective projections on the image plane. Therefore further optimization is required to find the rotation and translation required to correct the positioning of the distortion corrected points. The MATLAB script titled "Rot_Trans_ImPlane" developed by Allen was used to optimize the location of the image plane and the distortion corrected points (Allen, 2009). This code functions by minimizing the error between the 3D calibration points and the 2D distortion corrected image points resulting with the location that projects the points onto the image plane. Minimizing the error of the rotation and translation for the image plane and the calibration frame points to align will be outputted by the code. Applying the rotation and translation as outputted by the program the resulting position and orientation of the fluoroscope is obtained with respect to the calibration frame.

The points that can be projected by the Rhinoscript must have been digitized during that process described earlier and located within the image plane (figure 2.10). In addition, the points must have been corrected for distortion in the previous steps. The image plane coordinate system and distortion grid coordinate system are outlined in figure 2.9 and are bound by the black outline of the fluoroscopes image file. This means that points lying outside of the black image cannot be projected even if they were previously digitized and corrected for distortion. Completing the steps outlined in Allen's Appendix F thesis results in the image plane correction required to yield the final pose of the image plane. The red 3D calibration points should now match up with the 2D projected calibration image (figure 2.12). The final file is saved as FluoroA-Calibration.3dm and contains the final image plane pose for fluoroscope A. This file will be used in conjunction with the calibration of second fluoroscope.
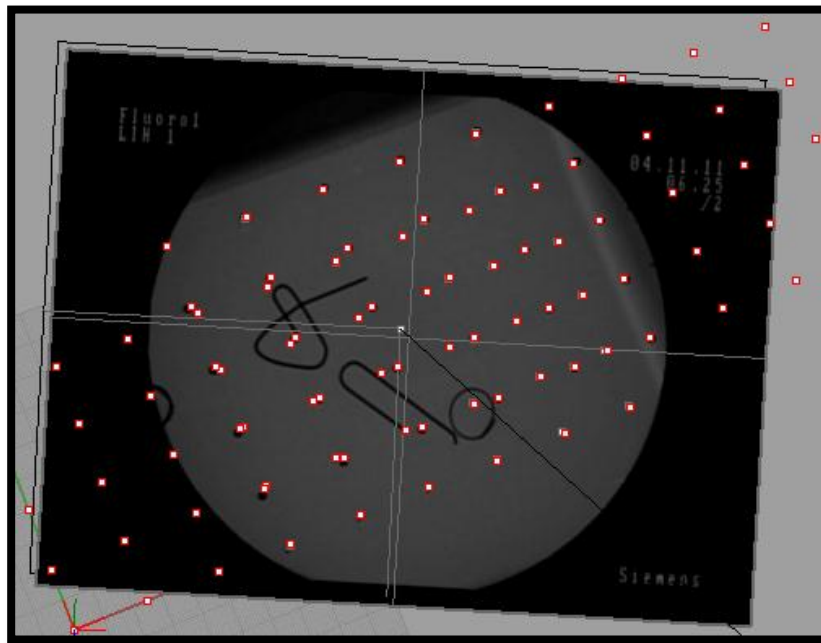
Figure 2.12: Final Image plane pose.

2.2.3.6   CALIBRATION FOR SECOND FLUOROSCOPE

Sections 2.2.3.1-2.2.3.5 are repeated for the second fluoroscope after a determination required to change the matrix P(c_s,l_s,d) is applied since its projection is related to a different plane on the calibration frame. The mathematical relationship determined for fluoroscope B, by way of similar triangles, is identical to the method described in the previous section, however, the result will yield a different matrix P(c_s,l_s,d) than that relationship for fluoroscope A. The resulting matrix P(c_s,l_s,d) for fluoroscope B for the set-up in figure 2.3 is defined as:

$$P(c_s, l_s, d) = \begin{vmatrix} 0 & \frac{1}{s_p} & \frac{c_s}{d} \\ \frac{1}{s_p} & 0 & \frac{l_s}{d} \\ 0 & 0 & \frac{1}{d} \end{vmatrix}$$

(Eq. 2.17)

where: d=distance from S to S' (mm),

s_p= pixel size (mm),

(c_s,l_s)= coordinates of the project of the source (pixels).

The Euler angle sequence associated with fluoroscope B is X-Y-Z based on the set-up in figure 2.3. Using these modifications the remaining steps in sections 2.2.3.1-2.2.3.5 now can be continued for fluoroscope B. The final experimental set-up file for fluoroscope B will be named FluoroB-Calibration.3dm.

2.3 VIRTUAL RECREATION OF EXPERIMENTAL SET-UP

Using the final files created in sections 2.2.3.1-2.2.3.6 (FluoroA-Calibration.3dm and FluoroB-Calibration.3dm) a single file is created titled FluoroAB-Calibration.3dm. This is done by opening one of the calibration files (i.e. FluoroA-Calibration.3dm) and importing the second calibration file (i.e. FluoroB-Calibration.3dm). The setup is verified visually to ensure it looks like the fluoroscopes setup during testing day. Each of the fluoroscopes were modelled as a perspective projection camera as outlined in Appendix E of Allen's thesis (Allen, 2009). The camera and target are set to the x-ray focus and image plane centre respectively. By setting the view up properly one could accurately recreate the 3D reality (figure 2.13).
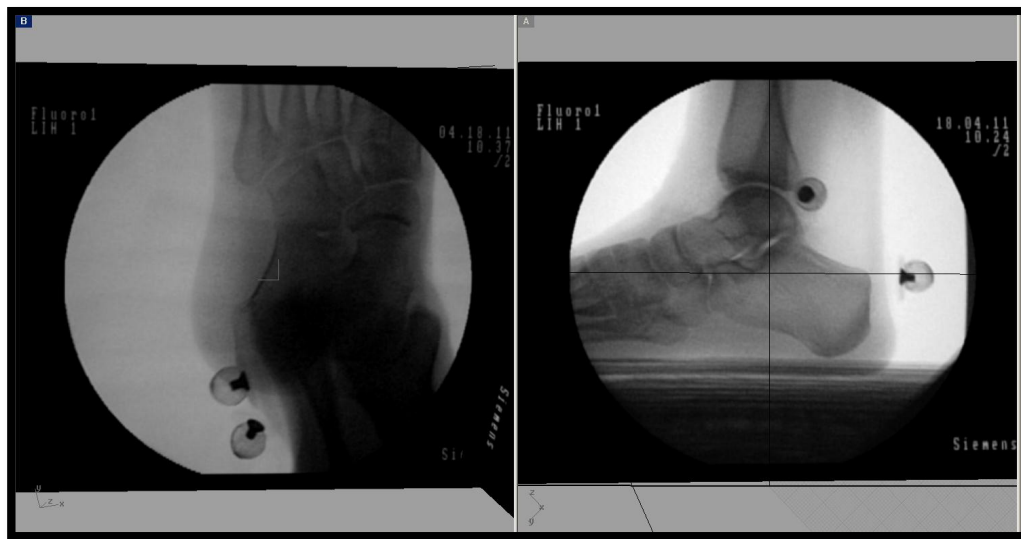
Figure 2.13: The two viewpoints from the x-ray foci. Left: Fluoroscope B, Right: Fluoroscope A.

2.4 BONE MODEL CREATION

Three-dimensional models of the bones under study were created using a computed tomography (CT) scan of the volunteer's foot and the program OsiriX-DICOM Viewer (Advanced Open-Source PACS Workstation DICOM Viewer, Antoine Rosset, USA). Detailed steps on how to segment the bone(s) of interest from a CT scan using OsiriX imaging software are provided in Appendix B. The bone models were converted to a triangular mesh of file format stereolithography (.stl) (or object file .obj). Figure 2.14 shows the 3D rendered model of the calcaneus, cuboid, navicular, and tibia/fibula. The landmarks of interest were located as described in chapter 1 (section 1.5.1) of this thesis were marked on each of the bone models as indicated.

(A) Calcaneus   (B) Cuboid

(C) Navicular   (D) Fibula (left), tibia (right)
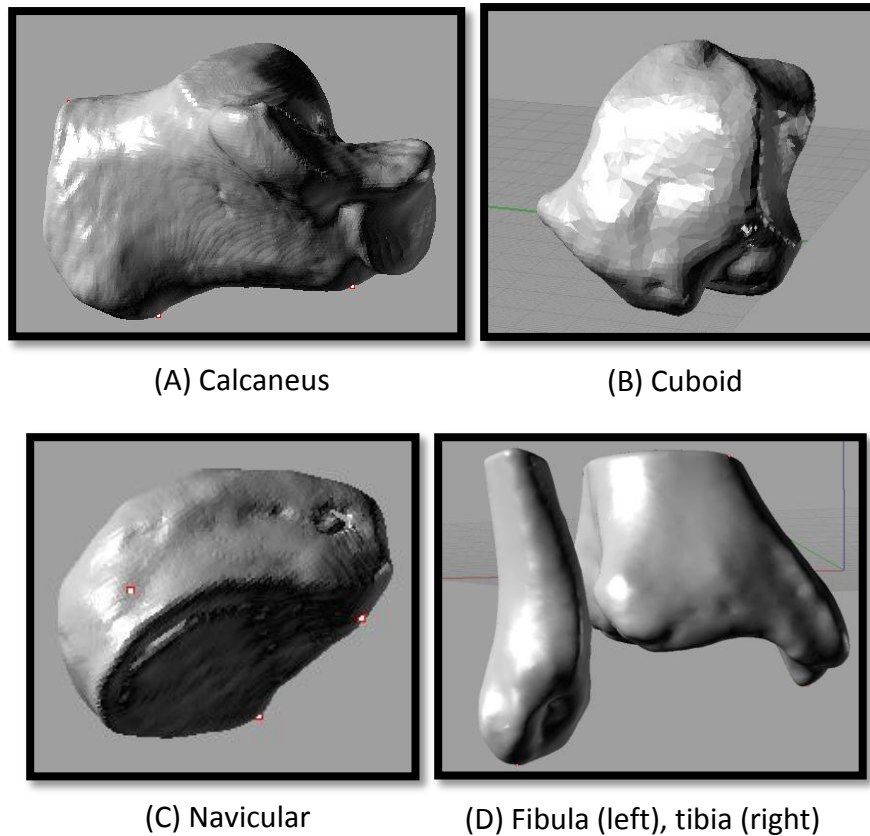
Figure 2.14: Rendered 3D model of the: (A) calcaneus, (B) cuboid, (C) navicular and (D) tibia/fibula as viewed in Rhinoceros.

2.5 MATCHING BONES TO IMAGE PLANE

The matching process recreates the pose of the bones captured by the two fluoroscopes. The computer bone models (section 2.4) are imported into the virtual environment (e.g. into file FluoroA/B-Calibration.3dm). Initially the entire fluoroscopic image is viewed and each bones silhouette is matched closely to its entire bony outline on both images (fluoroscope A and fluoroscope B). Once the match appears close the image is enlarged (i.e. the lens length on the camera is increased). It is noted that the roller button on the mouse changes the camera and target location not the lens length

thus not providing a zoom-in but rather changing the view completely. A few easily identifiable landmarks are used to fine-tune the match. At this point the object is moved by increments as small as 0.01mm and 0.01° until the outline of the models bony landmarks completely matches the outline of the bony landmarks on the image in both views. It is still important to ensure that the overall match is still obtained when matching the specific landmarks. Once the match is complete the bony landmarks are exported to an excel spreadsheet using the "ExportPoints" Rhinoscript developed by Allen (Allen, 2009). This Rhinoscript is used to export the 3D coordinates of the bony landmarks for each frame.

For each position being studied the corresponding fluoroscopic images are imported into the virtual environment and the bone model is re-matched to the new image. Since this study is interested in dynamic trials more than one frame was used for each shoe and orthotic condition. The number of frames analyzed was dependant on the speed the individual walked across the platform while in view of the fluoroscopes. A minimum of five frames are analyzed during midstance for each condition. The calcaneus, cuboid, navicular, and tibia/fibula are shown matched in figure 2.15, figure 2.16, figure 2.17 and figure 2.18 respectively.
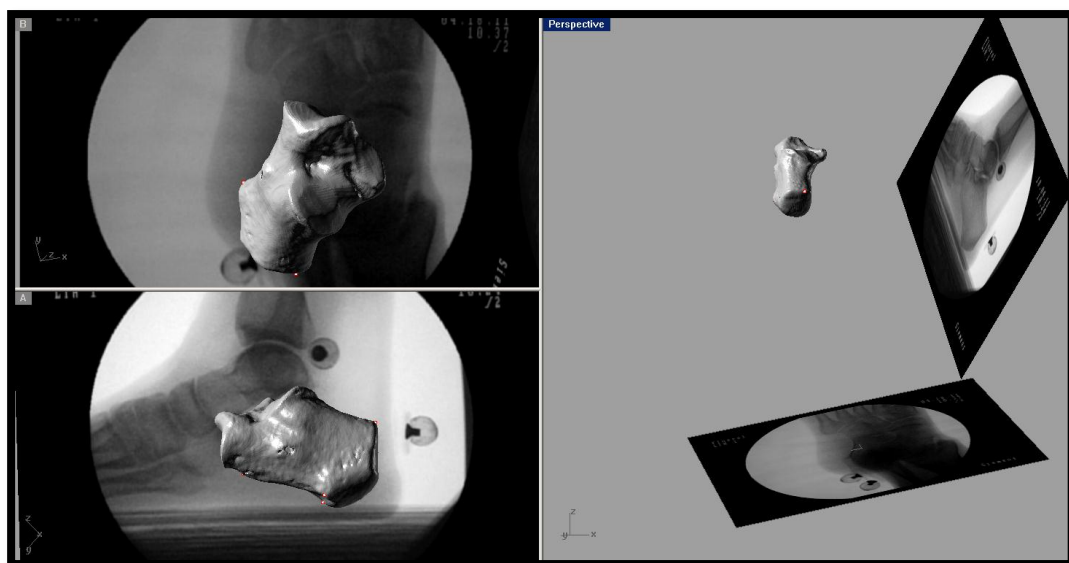
Figure 2.15: The calcaneus matched to the fluoroscopic images. Top left: Fluoroscope B, Bottom left: Fluoroscope A, Right side: 3D model of the calcaneus.
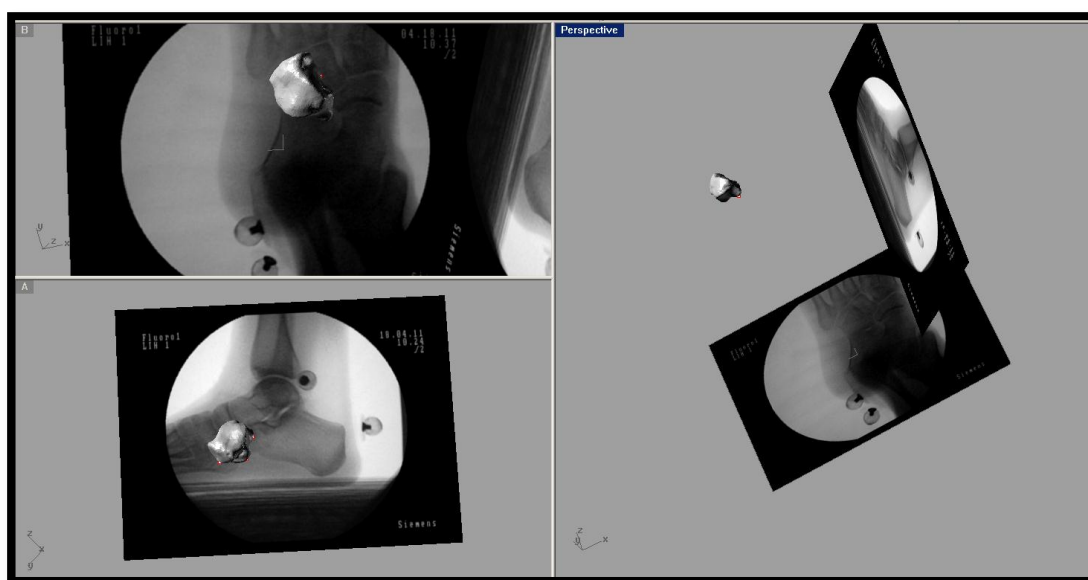
Figure 2.16: The cuboid matched to the fluoroscopic images. Top left: Fluoroscope B, Bottom left: Fluoroscope A, Right side: 3D model of the cuboid.
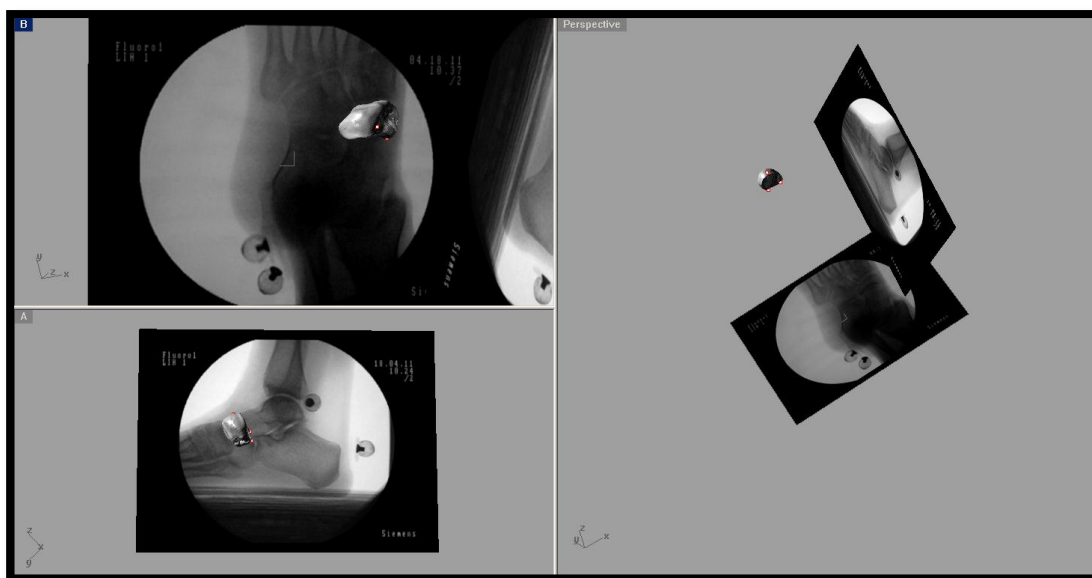
Figure 2.17: The navicular matched to the fluoroscopic images. Top left: Fluoroscope B, Bottom left: Fluoroscope A, Right side: 3D model of the navicular.
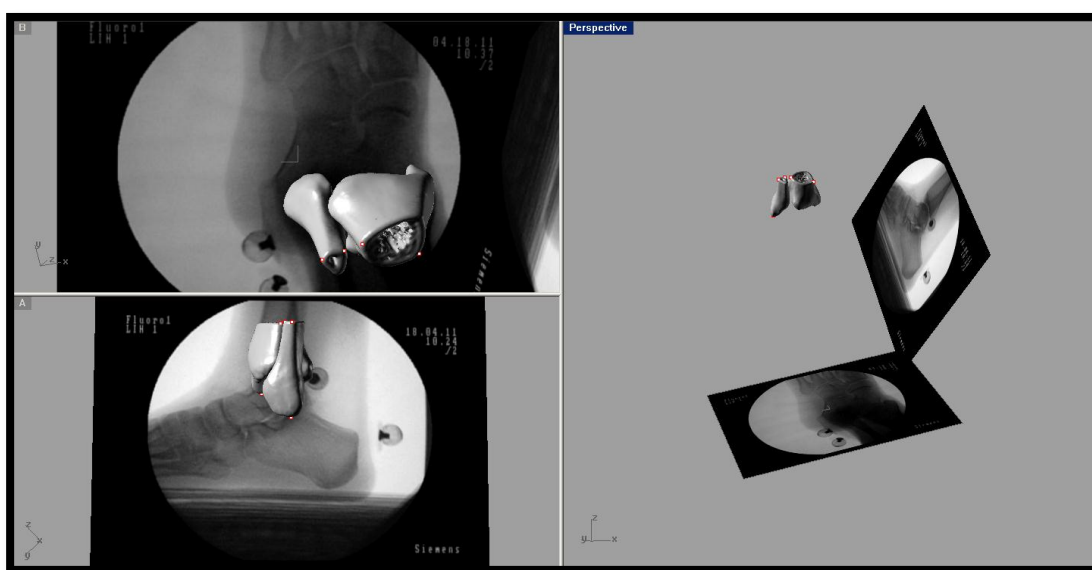
Figure 2.18: The tibia and fibula matched to the fluoroscopic images. Top left: Fluoroscope B, Bottom left: Fluoroscope A, Right side: 3D model of the tibia and fibula.

Once the matching process is completed the mathematical analysis to determine the change in alignment can be completed. Custom MATLAB script developed specifically for this thesis calculates the pronation angle in the foot (Appendix C). Pronation is defined as the combination of external rotation, dorsiflexion, and eversion. Using the excel files that contain the 3D coordinates of the bony landmarks on the calcaneus, cuboid, navicular, tibia and fibula as exported by the previous Rhinoscript (ExportPoints) the individual bone coordinate systems can be calculated. Bone coordinate systems are created using at least three non-collinear landmarks. Once the bone coordinate systems are calculated the change in pronation of calcaneus with respect to tibia and fibula can be determined. The MATLAB script is designed to output an excel spreadsheet containing the foots internal rotation, plantarflexion, and inversion angles for the various bones with respect to each other as represented in table 2.1. The calcaneus with respect to the tibia/fibula is calculated based on International Society of Biomechanics (ISB) joint coordinate system definition (section 1.6.1) (Wu *et al.*, 2002). The calcaneus with respect to the tibia and fibula was considered the standard measurement in this thesis due to the previous acceptance for measuring foot pronation by ISB (Wu *et al.*, 2002). The measurement was used to determine if the foot was pronating more or less than the barefoot condition. However, this was not the only measurement considered in this thesis. Since individual bone alignment in the foot has never been studied during dynamic trials to the authors' knowledge the changes in the cuboid and navicular were also considered during midstance. Therefore the alignments

of interest were summarized in table 2.1 using the MATLAB script "Calcaneuspronation_kinematics.m" in Appendix C.

Table 2.1: The alignment calculations completed using the custom MATLAB script in Appendix C.

Internal Rotation / Plantar/dorsi flexion / Inversion/ Eversion	Calcaneus with respect to the tibia/fibula	Navicular with respect to the tibia/fibula	Cuboid with respect to the tibia/fibula	Navicular with respect to the calcaneus	Cuboid with respect to the calcaneus

A repeated measures analysis of variance (ANOVA) using SPSS was produced to test for differences between measurement conditions (SPSS; IBM Corporation, Armonk, NY, USA). A probability level of $p < 0.05$ was used to indicate significance. All levels of significance are reported however, only where significance is found will the results be included in appendix F.

2.6 RESULTS

Using the output values from "Calcaneuspronation_kinematics.m" the impact of the different shoe conditions (neutral cushion running shoe, foam soft orthotic, and foam hard orthotic) can be determined on the normal population. The barefoot condition was used as the baseline measurement for each subject studied. Table 2.2 shows the average barefoot alignment as outputted from the Calcaneuspronation_kinematics program for each subject's barefoot condition in the

internal/external rotation plane, plantar/dorsi flexion plane, and inversion/eversion

plane of motion.

Table 2.2: Barefoot baseline angle results for the five (5) subjects used for this thesis. All entries are in degrees.

Measurement	Subject#	cal wrt tibfib	nav wrt cal	cub wrt cal	nav wrt tibfib	cub wrt tibfib
External Rotation	1	15.47	-13.33	61.17	33.97	-48.14
	2	46.47	22.02	87.11	50.84	-62.06
	10	47.68	6.42	89.29	65.82	-47.13
	11	31.20	5.61	65.19	36.85	-36.47
	23	43.32	27.13	87.79	41.77	-40.36
	Average	36.83	9.57	78.11	45.85	-46.83
	Standard Deviation	13.61	15.92	13.73	12.87	9.78
Dorsiflexion	1	183.09	-45.69	13.95	-127.12	-171.60
	2	148.79	-38.58	99.37	-168.45	-162.27
	10	155.63	-47.09	59.50	-132.82	-164.39
	11	164.20	-51.98	-22.35	-139.33	-151.92
	23	152.37	-37.89	-9.40	-159.83	-168.48
	Average	160.82	-44.25	28.21	-145.51	-163.73
	Standard Deviation	13.70	5.97	50.54	17.81	7.52
Eversion	1	166.70	22.96	14.14	140.97	164.37
	2	150.75	23.28	-115.48	123.54	156.38
	10	157.79	27.16	-74.80	123.77	163.51
	11	152.06	16.39	-33.57	134.32	169.05
	23	165.60	31.90	-74.29	128.43	174.37
	Average	158.58	24.34	-56.80	130.20	165.54
	Standard Deviation	7.41	5.73	49.10	7.45	6.70

Note: The output from the program was manipulated beyond this table to represent the results where positive represents the change in motion towards the direction that promotes an increase in supination.

Due to the large variance between subjects (table 2.2) every measurement

reported consists of the alignment difference compared to each volunteer's average

barefoot condition reported in table 2.2. The standard deviation for each subject was calculated for each condition and measurement. The average standard deviation for internal rotation, dorsiflexion, and inversion for individual subjects are shown in Appendix D (table D.1, table D.2, and table D.3) respectively. The values shown in these tables for each subject represent the average standard deviation for at least five frames during midstance for that particular subject. The average effect of the neutral cushion running shoe, and foam soft orthotics for each plane of motion (internal rotation, plantarflexion and inversion) is shown in figure 2.19, figure 2.20, and figure 2.21 respectively. All values in the graphs (figure 2.19, figure 2.20, and figure 2.21) have been created such that the positive values represent an increase in the direction towards supination for comparative purposes in the discussion (section 2.7) of this chapter.
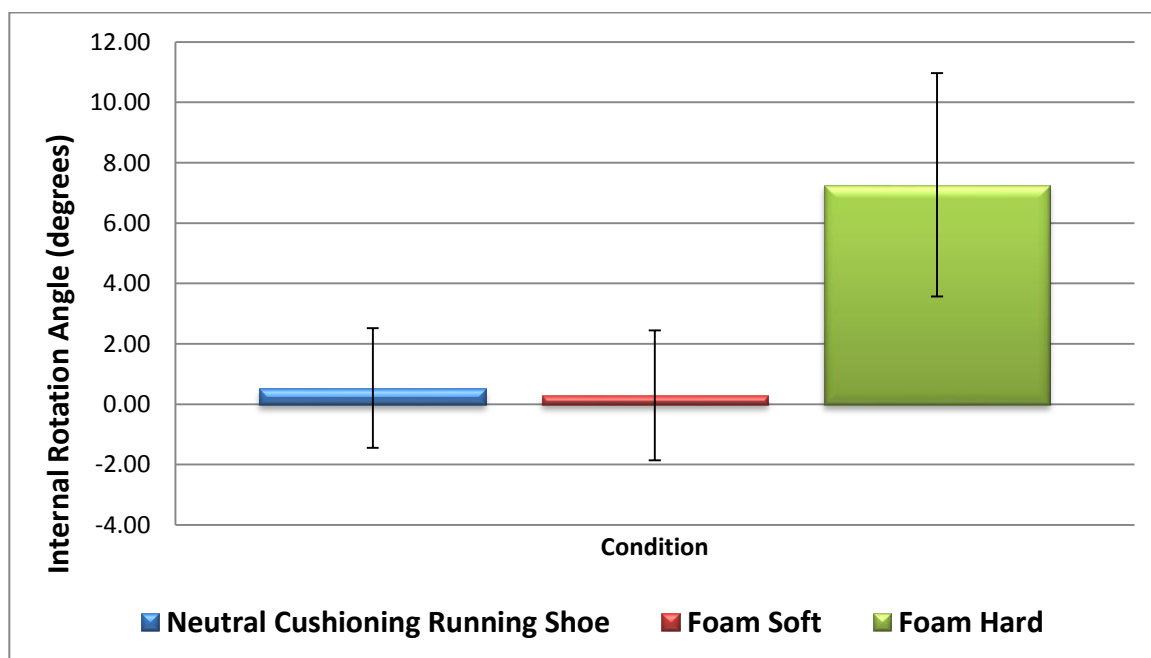
Figure 2.19: The average change in internal rotation for the calcaneus with respect to the tibia/fibula in the normal population. A positive change represents an increase in internal rotation, and a negative change represents an increase in external rotation.
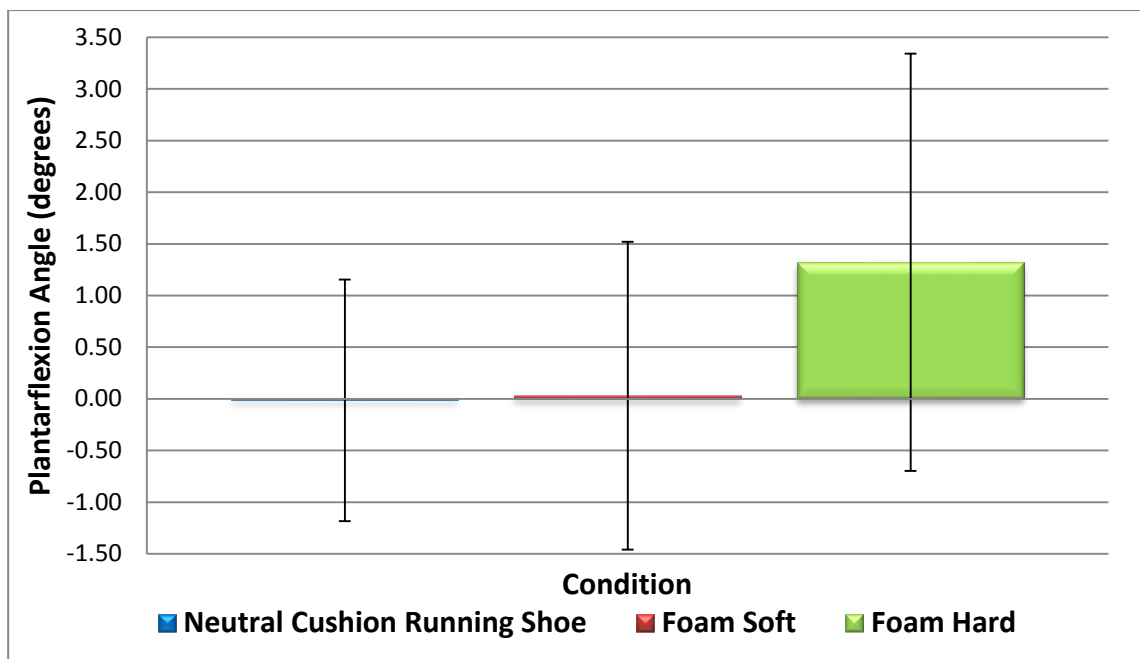
Figure 2.20: The average change in plantarflexion for the calcaneus with respect to the tibia/fibula in the normal populations. A positive change would represent an increase in dorsiflexion and a negative change represents an increase in plantarflexion.
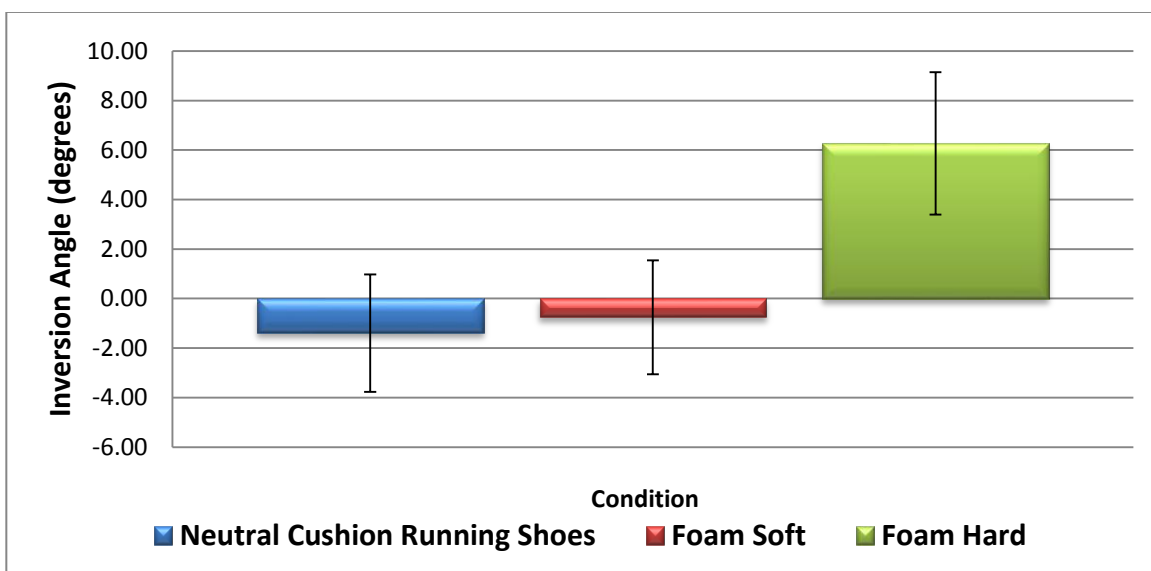
Figure 2.21: The average change in the inversion angle for the calcaneus with respect to the tibia/fibula on the normal population. A positive change represents an increase in inversion, and a negative change represents an increase in eversion.

The average effect of the neutral cushion running shoe on the pronation angle is summarized in table 2.3, table 2.4, and table 2.5 as internal rotation, plantarflexion, and inversion respectively. The average effect of the foam soft orthotic on the pronation angle is show in table 2.6, table 2.7, and table 2.8 as internal rotation, plantarflexion, and inversion respectively. The average effect of the foam hard orthotic on the pronation angle is shown in table 2.9, table 2.10, and table 2.11 as internal rotation, plantarflexion, and inversion respectively.

Table 2.3: Change in internal rotation for the neutral cushion running shoe condition. All entries are in degrees.

Neutral Cushion Running Shoe: Internal Rotation Angle

Subject#	cal wrt tibfib	nav wrt cal	cub wrt cal	nav wrt tibfib	cub wrt tibfib
1	5.27^+	4.28^+	17.11^+	2.05*	-9.94
2	17.36^+	7.97^+	-11.19	8.64^+	2.15^+
10	-11.94	-11.68	-14.10	-3.52	6.80^+
11	7.63^+	16.06^+	-10.50	-20.66	13.20^+
23	-15.64	-2.31	-13.34	-4.60	-3.84
AVERAGE	**0.54**	**2.86***	**-6.40**	**-3.62**	**1.67^+**

Note: A negative value indicates the opposite motion (i.e. external rotation). Those with a (*) represent a value which is significant to one standard deviation. Those with a (+) are significant to two standard deviations.

Table 2.4: Change in plantarflexion angle for the neutral cushion running shoe condition. All entries are in degrees.

Neutral Cushion Running Shoe: Plantarflexion Angle

Subject#	cal wrt tibfib	nav wrt cal	cub wrt cal	nav wrt tibfib	cub wrt tibfib
1	-2.58	3.74	26.43^{+}	-3.81	-5.70
2	-10.11	-0.08	18.95^{+}	-0.57	-3.07
10	3.40*	-3.35	3.38	-0.41	3.05*
11	2.01*	-6.00	-10.30	16.05^{+}	2.18
23	7.21^{+}	3.10	-39.18	-4.36	17.62^{+}
AVERAGE	**-0.01**	**-0.52**	**-0.14**	**1.38**	**2.82^{*}**

Note: A negative value represents the opposite motion (i.e. dorsiflexion). Those with a (*) represent a value which is significant to one standard deviation. Those with a (+) are significant to two standard deviations.

Table 2.5: Inversion/Eversion angle for the neutral cushion running shoe condition. All entries are in degrees.

Neutral Cushion Running Shoe: Inversion Angle

Subject#	cal wrt tibfib	nav wrt cal	cub wrt cal	nav wrt tibfib	cub wrt tibfib
1	1.83	2.16^{+}	-14.13	-0.35	12.13^{+}
2	-7.31	-2.40	-33.50	-2.75	-4.40
10	6.23^{+}	0.55	40.39^{+}	5.98^{+}	3.79^{+}
11	0.71	-5.74	22.55^{+}	9.26^{+}	-7.15
23	-8.41	-10.81	25.69^{+}	5.26*	-9.95
AVERAGE	**-1.39**	**-3.25**	**8.20***	**3.48***	**-1.12**

Note: A negative value represents the opposite motion (i.e. eversion). Those with a (*) represent a value which is significant to one standard deviation. Those with a (+) are significant to two standard deviations.

Table 2.6: Change in internal rotation angle for the foam soft orthotic condition. All entries are in degrees.

Foam Soft: Internal Rotation

Subject#	cal wrt tibfib	nav wrt cal	cub wrt cal	nav wrt tibfib	cub wrt tibfib
1	9.46[+]	4.24*	25.27[+]	13.62[+]	-19.89
2	32.68[+]	13.27[+]	-21.97	27.80[+]	-5.60
10	-9.41	-14.23	-16.96	-0.96	13.90[+]
11	9.76[+]	8.22[+]	4.15[+]	-3.53	3.51[+]
23	-6.13	-9.26	-26.52	-9.54	17.29[+]
AVERAGE	**7.27[+]**	**0.45**	**-7.21**	**5.48[+]**	**1.84***

Note: A negative value indicates the opposite motion (i.e. external rotation). Those with a (*) represent a value which is significant to one standard deviation. Those with a (+) are significant to two standard deviations.

Table 2.7: Change in plantarflexion rotational for the foam soft orthotic condition. All entries are in degrees.

Foam Soft: Plantarflexion

Subject#	cal wrt tibfib	nav wrt cal	cub wrt cal	nav wrt tibfib	cub wrt tibfib
1	-5.68	-0.78	70.61	-0.14	2.44*
2	-14.10	3.00	38.74	-10.15	25.63[+]
10	10.29[+]	1.50	-41.74	0.20	-0.63
11	-3.51	-3.67	-10.78	9.17[+]	0.30
23	13.15	1.12	-6.21	11.39[+]	1.86
AVERAGE	**0.03**	**0.24**	**10.12[+]**	**2.09***	**6.17[+]**

Note: A negative value represents the opposite motion (i.e. dorsiflexion). Those with a (*) represent a value which is significant to one standard deviation. Those with a (+) are significant to two standard deviations.

Table 2.8: Inversion angle for the foam soft orthotic condition. Each value represents the angle difference compared to the barefoot condition. All entries are in degrees.

Foam Soft: Inversion

Subject#	cal wrt tibfib	nav wrt cal	cub wrt cal	nav wrt tibfib	cub wrt tibfib
1	-5.80	4.84*	47.10$^+$	-11.14	-17.21
2	-3.33	0.58	-52.80	-19.22	-8.63
10	5.57$^+$	-1.17	36.72$^+$	5.97$^+$	9.79$^+$
11	1.21	-4.18	3.84$^+$	5.69$^+$	-2.95
23	-1.42	-2.21	47.65$^+$	4.51$^+$	2.99*
AVERAGE	**-0.75**	**-0.43**	**16.50$^+$**	**-2.84**	**-3.20**

Note: A negative value represents the opposite motion (i.e. eversion). Those with a (*) represent a value which is significant to one standard deviation. Those with a (+) are significant to two standard deviations.

Table 2.9: Change in internal rotation angle for the foam hard orthotic condition. All entries are in degrees.

Foam Hard: Internal Rotation

Subject#	cal wrt tibfib	nav wrt cal	cub wrt cal	nav wrt tibfib	cub wrt tibfib
1	10.23$^+$	4.02*	14.79$^+$	8.45$^+$	-3.24
2	-1.56	-9.00	2.18$^+$	22.18$^+$	9.56$^+$
10	-13.18	-10.56	-16.57	-11.70	11.45$^+$
11	2.74	16.48$^+$	4.39	-11.73	0.24
23	3.24	3.76$^+$	2.01$^+$	-9.06	-3.78
AVERAGE	**0.29**	**0.94**	**1.36**	**-0.37**	**2.84**

Note: A negative value indicates the opposite motion (i.e. external rotation). Those with a (*) represent a value which is significant to one standard deviation. Those with a (+) are significant to two standard deviations.

Table 2.10: Change in plantarflexion angle for the foam hard orthotic condition. All entries are in degrees.

Foam Hard: Plantarflexion

Subject#	cal wrt tibfib	nav wrt cal	cub wrt cal	nav wrt tibfib	cub wrt tibfib
1	-2.61	8.51^{+}	10.60*	-6.41	-1.90
2	1.40	-2.34	-39.17	-1.44	-4.03
10	10.29^{+}	1.50^{+}	-41.74	0.20	0.63
11	-1.28	-1.06	-17.72	7.70^{+}	-1.84
23	-1.18	-2.17	-64.60	5.60^{+}	-0.91
AVERAGE	**1.32**	**0.89**	**-30.53**	**1.13**	**-1.61**

Note: A negative value represents the opposite motion (i.e. dorsiflexion). Those with a (*) represent a value which is significant to one standard deviation. Those with a (+) are significant to two standard deviations.

Table 2.11: Inversion/Eversion angle for the foam hard orthotic condition. Each value represents the angle difference compared to the barefoot condition. All entries are in degrees.

Foam Hard: Inversion/Eversion

Subject#	cal wrt tibfib	nav wrt cal	cub wrt cal	nav wrt tibfib	cub wrt tibfib
1	1.45*	2.61^{+}	-2.43	-2.37	7.60*
2	0.99	9.30^{+}	37.13^{+}	-10.25	3.12^{+}
10	8.05*	-1.41	35.36^{+}	10.87*	-19.35
11	11.73^{+}	10.69^{+}	4.91	0.99	1.90
23	9.12^{+}	-3.49	-16.32	10.61	0.14
AVERAGE	$\mathbf{6.27^{+}}$	**3.54**	**11.73**	**1.97**	**-1.32**

Note: A negative value represents the opposite motion (i.e. eversion). Those with a (*) represent a value which is significant to one standard deviation. Those with a (+) are significant to two standard deviations.

2.7 DISCUSSION

This study quantifies the effect foam casted orthotics have on the normal population compared to each volunteers barefoot condition in three-dimensions. The findings suggest that the general population will see a reduction in pronation when wearing a foam casted orthotic although the results were not found to be statistically significant (Appendix F).

Each subject's data was evaluated with an ANOVA repeated measures statistical test using SPSS (SPSS; IBM Corporation, Armonk, NY, USA) to determine if there is a statistically significant difference between the each of the shoe conditions tested compared to the barefoot condition. Each plane of motion was analyzed separately. A probability level of $p<0.05$ was considered significant. While wearing the foam soft orthotic no significant changes were found in internal rotation ($p=0.385$), plantarflexion ($p=0.831$), and inversion ($p=0.581$). While wearing the foam hard orthotic no significant changes were found in internal rotation ($p=0.942$), plantarflexion ($p=0.601$), and inversion ($p=0.085$). While wearing the neutral cushioning running shoe no significant changes in alignment were found in internal rotation ($p=0.935$), plantarflexion ($p=0.997$), and inversion ($p=0.450$). It was discovered that there is no statistical difference in the foam soft, foam hard, and neutral cushion running shoe conditions for each plane of motion in the normal population. Significance may not have been reached because of the small sample size.

Based on the joint coordinate system motion work done by Wu *et al.* the calcaneus with respect to the tibia/fibula is considered the measure that most

accurately represents pronation when the three planes are taken into consideration. The results of the calcaneus with respect to the tibia/fibula were shown in figure 2.19, figure 2.20, and figure 2.21 for the internal rotation, plantarflexion, and inversion planes respectively. The graphs represent the normal population's average change compared to the barefoot condition. It was found that the foam soft orthotic had the greatest increase in internal rotation and inversion. However, the difference between this foam soft condition and the neutral running shoe and the foam hard orthotic was less than one standard deviation. The foam hard orthotic had the greatest increase in plantarflexion, but the change was within the standard deviation bars in figure 2.20. From this it was concluded that although a significant change may occur on the individual level the change is not predicable in the overall population. The remainder of the discussion will be presented at the individual level.

Even though the results were not found to be significant for the group as a whole the standard deviations were used to compare the different conditions and there effects on pronation. To determine if a condition had an effect on an individual level the concept of the normal distribution was used. Natural variance of several variables has the tendency to follow the normal distribution. With that in mind the normal distribution has the property of 68% of cases fit within one (1) standard deviation (SD). Even more significant is 95.5% of cases will fall within two (2) SD (Norman and Streiner, 2003; Portney and Watkins, 2000). Therefore when deciding significance of the results of those with one (1) standard deviation of significance were represented with an asterisk (*) and those with two (2) standard deviations were represented with a plus sign (+).

Since pronation is a combination of external rotation, dorsiflexion, and eversion a reduction in pronation requires the opposite combination to occur. Therefore, for the foot to experience a decrease in pronation (alignment change in the direction of supination) the foot must experience internal rotation, plantarflexion, and inversion when compared to the baseline (barefoot) condition.

Upon examination of the calcaneus with respect to the tibia/fibula while wearing the neutral cushioning running shoe a reduction in pronation was not found when an average among all subjects is calculated. While wearing the foam soft orthotic an overall reduction in external rotation was found for the calcaneus with respect to the tibia/fibula when the average among all subjects was calculated (>2SD). While wearing the foam hard orthotics a reduction in pronation occurred in all three planes of motion however, only the inversion plane had a significant decrease (>2SD). The reduction in pronation in the internal rotation plane, and plantarflexion plane was not found to be significant when averaged among all participants.

The evaluation of the navicular with respect to the calcaneus showed that the navicular responded to the neutral cushion running shoe and the orthotic conditions as well. While wearing the neutral cushion running shoe internal rotation (>1SD) was found to occur as an average of all subjects for the navicular with respect to the calcaneus. While wearing the foam soft orthotic no statistically significant motion was found to occur with the navicular with respect to the calcaneus. While wearing the foam hard orthotic it was found that the change in inversion (>2SD) occurred for the navicular with respect to the calcaneus.

The evaluation of the navicular with respect to the tibia/fibula showed that motion was not quite as evident. While wearing the neutral cushion running shoe an increase in inversion (>1SD) was found. While wearing the foam soft orthotic an increase in both internal rotation (>2SD), and plantarflexion (>1SD) occurred. While wearing the foam hard orthotic no significant motion occurred.

Upon examination of the cuboid with respect to the calcaneus significant motion two of the conditions tested. It was found that an increase in plantarflexion (>2SD) occurred while wearing the foam soft orthotic. It was found that the cuboid experienced an increase in inversion with respect to the calcaneus while wearing the neutral running shoe (>1SD) and the foam soft orthotic (>2SD).

Examining the cuboid with respect to the tibia/fibula resulted in significant alignment change; however, this change did not occur simultaneously while wearing the same type of footwear. An increase in internal rotation was found while wearing the neutral cushion running shoe (>2SD), and the foam soft orthotic (>1SD). An increase in plantarflexion motion was found while wearing the neutral cushion running shoe (>1SD) and, the foam hard orthotic (>2SD). No significant change in motion occurred in the inversion plane.

Although every individual reacted differently depending on the footwear condition tested, in addition to the bones analyzed it appears to be a safe conclusion that orthotics do have an impact on the alignment of the bones within the foot when compared to the barefoot condition. The difference between wearing a neutral cushion running shoe was not found to be statistically different than both orthotic conditions. It

was found that the type of material used in the orthotic does not have enough impact to deem the difference is statistically significant. This lack of significance between the material type may be related to the small sample size. With that in mind the comfort of the patient and the judgment of the pedorthist should be used to determine a material that is found to be qualitatively better overall.

2.8 REFERENCES

Allen, A.-M. V. (2009). *Development and Validation of a Markerless Radiostereometric Analysis (RSA) System*. University of Western Ontario.

Houck, J. R., Tome, J. M., & Nawoczenski, D. A. (2008). Subtalar neutral position as an offset for a kinematic model of the foot during walking. *Gait & Posture*, *28*(1), 29-37.

Kedgley, A. (2009). *Development of a fluoroscopic radiostereometric analysis system with an application to glenohumeral joint kinematics*. Thesis: University of Western Ontario.

Kedgley, A. E., & Jenkyn, T. R. (2009). RSA calibration accuracy of a fluoroscopy-based system using nonorthogonal images for measuring functional kinematics. *Medical Physics*, *36*(7), 3176.

Kedgley, A. E., Birmingham, T. B., & Jenkyn, T. R. (2009). Comparative accuracy of radiostereometric and optical tracking systems. *Journal of Biomechanics*, *42*(9), 1350-1354.

Nordin, M., & Frankel, V. H. (2001). *Basic Biomechanics of the Musculoskeletal System*. (D. Leger, Ed.) (3rd ed., pp. 178-190). Baltimore: Lippincott Williams & Wilkins.

Norman, G. R., & Streiner, D. L. (2003). *Pretty Darned Quick Statistics* (3rd ed., pp. 5-52). Hamilton: BC Decker Inc.

Portney, L. G., & Watkins, M. P. (2000). *Foundations of Clinical Research: Applications to Practice* (2nd ed.). Upper Saddle River, New Jersey, USA: Prentice-Hall Inc.

Rougée, A., Picard, C. L., Trousset, Y. L., & Ponchut, C. (1993). Geometrical calibration for 3D x-ray imaging. *Proceedings of SPIE*, *1897*, 161-169.

Rougée, A., Picard, C., Ponchut, C., & Trousset, Y. (1993). Geometrical calibration of X-ray imaging chains for three-dimensional reconstruction. *Computerized medical imaging and graphics the official journal of the Computerized Medical Imaging Society*, *17*(4-5), 295-300. {IEEE} Press.

Wu, G., Siegler, S., Allard, P., Kirtley, C., Leardini, A., Rosenbaum, D., Whittle, M., *et al.* (2002). ISB recommendation on definitions of joint coordinate system of various joints for the reporting of human joint motion--part I: ankle, hip, and spine. International Society of Biomechanics. *Journal of Biomechanics*, *35*(4), 543-548.

CHAPTER 3- THE EFFECT OF PLASTER CASTED ORTHOTICS ON THE NORMAL FOOT USING MARKERLESS RSA

OVERVIEW: This chapter describes the effect of plaster casted orthotics on the kinematics of the foot in a normal population compared to their barefoot behaviour. Bi-planar x-ray fluoroscopy and the markerless RSA technique are used to determine the change in pronation of the normal population at midstance during gait.

3.1 INTRODUCTION

Orthotics are frequently prescribed for the treatment of musculoskeletal disorders in the foot and ankle such as pes cavus or pes planus. Orthotics are intended to alter the motion of hindfoot and midfoot bones by applying constraint or support to various structures on the plantar surface. There has been relatively little *in-vivo* analysis completed on the normal human population. The normal foot is considered to be those that have a medial longitudinal arch that naturally pronates less than pes planus and more than pes cavus feet during weight-bearing activities such as walking. The subtalar joint consists of two bones the talus and calcaneus. The subtalar neutral (STN) position is considered the point when the subtalar joint is neither pronated nor supinated. Clinicians often use the STN position as a reference when casting an orthotic. The normal population is considered to have a foot that experiences approximately 5°

eversion in the frontal plane during walking gait. The pes planus population is considered to have an arch that collapses due to excessive pronation. The pes cavus foot is characterized by an abnormally high medial longitudinal arch. The pes cavus population remains in fixed plantarflexion during walking gait. The pronated foot is one where the arch collapses inward and is defined as a combination of eversion, dorsiflexion, and external rotation (Nordin and Frankel, 2001). Supination is the opposite of pronation and is considered to be the combination of inversion, plantarflexion, and internal rotation. A difference of approximately 5° between barefoot and a shoed (orthotic or no orthotic) condition is the minimal difference expected to be clinically significant. The barefoot condition is used as the reference position since pedorthists use barefoot walking to analyze a patient's gait and cast custom orthotics.

Markerless radiostereometric analysis (RSA) systems show promise in tracking skeletal kinematics. Building on the markerless RSA work by Allen, a three-dimensional (3D) computer model of the bones of interest is created and matched to the two radiographs captured simultaneously of the bone from two different angles (Allen, 2009). The RSA method in this case determines the position and orientation of the bones of the foot during walking gait. The effect orthotics have on the bones of interest can be determined following a detailed calibration process. A calibration technique is used to determine the relative positions of the two x-ray images (parameters include the x-ray foci locations of each fluoroscope and the corresponding pose of each image plane). The 3D computer bone model created from a computed tomography (CT) scan

were imported into the virtual environment and manually adjusted in 3D space until the projections matched the radiographs.

The aims of this study were to quantify the change in pronation of the hindfoot in the normal population during weight-bearing walking gait. Three conditions were tested: (1) barefoot, (2) with a soft plaster casted orthotic, and (3) with a hard plaster casted orthotic. It was hypothesized that the plaster casted orthotics would reduce pronation of the hindfoot during walking compared to the barefoot walking. It was also hypothesized that the hard plaster orthotic would have a greater effect in reducing pronation compared to the soft plaster orthotic.

3.2 METHODS

Ethics approval was obtained from the Health Sciences Research Ethics Board at The University of Western Ontario prior to the commencement of any data collection (Appendix A). The platform described in the previous study (section 2.2.1) was used in this study and allowed the test subjects to walk through the capture volume of the two fluoroscopes.

3.2.1 DATA COLLECTION

Five (5) normally arched volunteers with no previous foot or ankle disorders, no foot or ankle pain, and no previous orthotic use were recruited to participate in this study. Individuals with previous fractures in the lower extremities were avoided and pre-screened for. Each volunteer had their feet examined by a certified pedorthist to ensure they fit the criteria for normal. Volunteers were asked to fill out a consent form after the study was explained as well as any risks involved. The volunteers were fitted with two

pairs of custom-made orthotics with: (1) a 4mm plastazote (soft) and (2) a 2mm RCH-500 (rigid) material by the same Canadian certified pedorthist at the Fowler Kennedy Sport Medicine Clinic, London, ON. The pedorthist used the plaster wrap casting technique for this study. The plaster casting technique requires the patient lie prone in a figure four position during the process. A negative impression of the foot is taken while being locked in the subtalar neutral position. While plaster casting has historically been the standard method, foam box has increased in popularity.

The two fluoroscopes were positioned about the platform so that the two images of the foot gave optimal views of the calcaneus at the instant of midstance during walking gait. After positioning the fluoroscopes, they had to be calibrated using the RSA method. At least one pair of images of the calibration frame was captured prior to the volunteer's arrival for the study. The calibration process will be summarized briefly below in section 3.2.5. Each volunteer wore a wrap-around leaded apron and kilt on their upper and lower body respectively, including a thyroid collar (figure 3.1). It is noted that section 3.2.2 to section 3.2.4 were completed in a randomized order.

Figure 3.1: Platform and wrap-around leaded clothing.

3.2.2 BAREFOOT

Each volunteer was instructed to stand on the platform in the view of each fluoroscope barefoot. An x-ray technician ensured the two fluoroscopic views of the hindfoot were optimal from both angles. The x-ray technician then outlined the location of the volunteer's foot for a target during walking. Each volunteer was asked to walk at their preferred pace as the fluoroscopes recorded their left foot's motion at 30 frames per second from heel strike to toe-off. The captured images were checked to ensure that the calcaneus and tarsus were sufficiently visible for the subsequent RSA procedure before moving onto the next trial. If the calcaneus was not satisfactorily visible, the trial was repeated. Approved images were recorded on the control PC in the adjacent control room. The barefoot condition was repeated two times.

3.2.3 SOFT PLASTER ORTHOTIC

Each volunteer was instructed wear the neutral cushion running shoe (New Balance #882) with a soft plaster casted orthotic replacing the manufacturers insole. Each volunteer was asked to walk at their preferred pace as the fluoroscopes recorded their left foot's motion at 30 frames per second from heel strike to toe-off. The captured images were checked to ensure that the calcaneus and tarsus were sufficiently visible for the subsequent RSA procedure before moving onto the next trial. If the calcaneus was not satisfactorily visible, the trial was repeated. Approved images were recorded on the control PC in the adjacent control room. The soft plaster condition was repeated two times.

3.2.4 RIGID PLASTER ORTHOTIC

Each volunteer was instructed wear the neutral cushion running shoe (New Balance #882) with a rigid plaster casted orthotic replacing the manufacturers insole. Each volunteer was asked to walk at their preferred pace as the fluoroscopes recorded their left foot's motion at 30 frames per second from heel strike to toe-off. The captured images were checked to ensure that the calcaneus and tarsus were sufficiently visible for the subsequent RSA procedure before moving onto the next trial. If the calcaneus was not satisfactorily visible, the trial was repeated. Approved images were recorded on the control PC in the adjacent control room. The soft plaster condition was repeated two times.

3.2.5 CALIBRATION OVERVIEW

Both traditional and markerless bi-planar RSA requires two imaging devices. In this study two C-arm fluoroscopes with 9 inch image intensifiers (II) were used. A calibration frame was used to establish a coordinate system for the capture volume of interest (Kedgley, 2009). Calculations with the laboratory frame are used to determine the location of each imaging device. The calibration device was designed and used to determine the relationship of the 3D known bead locations and the two-dimensional images captured of the beads (Kedgley and Jenkyn, 2009). At least six fiducial and six control beads were visible to ensure a successful calibration. Images of the calibration frame were then digitized, and corrected for pincushion distortion. During the digitization process a space of at least 1 diameter of the bead must be visible as open space to ensure a smooth calibration. The MATLAB script uses the fiducial plane to

create a transformation from the image coordinate system to the laboratory coordinate system (MathWorks, Natick, MA, USA). The MATLAB script uses the control plane to determine the focal point from which the x-rays originate (Kedgley and Jenkyn, 2009). The calibration algorithm used in this thesis goes on to determine the parameters required to accurately recreate the experimental set-up in the virtual environment.

3.2.5.1 CALIBRATION ALGORITHM

Based on the work of Rougée *et al.* (1993a and 1993b) an algorithm was developed by Allen that was furthered modified for the setup used in this thesis. This required that each fluoroscope be represented as a perspective projection model. The mathematical relationship between the 3D calibration points and their 2D projections are defined. An optimization algorithm is used with the mathematical relationship to determine the calibration parameters required for the recreation of the experimental setup into the virtual environment are calculated.

The derivation required for the calibration of a single fluoroscope is detailed in section 2.2.3.2 of this thesis. The calibration setup used for this study is seen in figure 3.2.
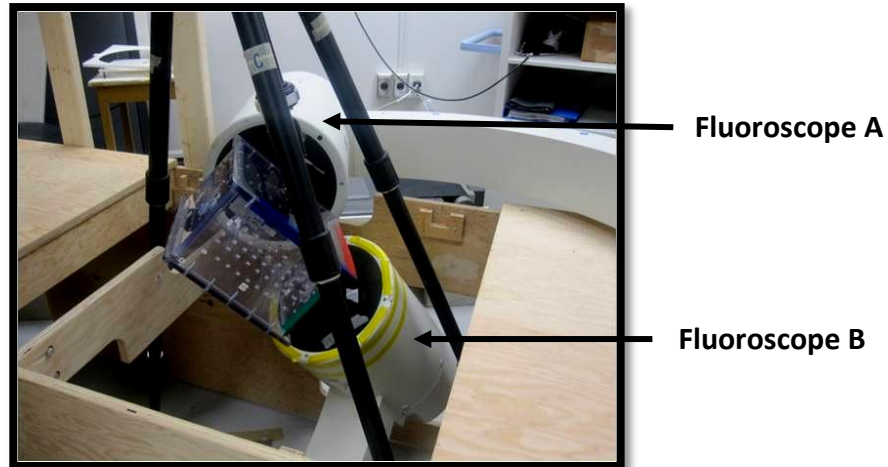
Figure 3.2: Calibration set-up for study. The image intensifier (II) of each fluoroscopes are labelled.

3.2.5.2   PIXEL SIZE CALCULATION

The pixel size of each fluoroscope is not considered to be a calibration parameter but rather a known value. The pixel size is assumed to remain a constant value. The pixel size for fluoroscope A and fluoroscope B were found to be 0.3847mm and 0.3819mm respectively.

3.2.5.3   CALIBRATION PARAMETER ESTIMATION

According to the fluoroscopes operating manual (SIREMOBIL Compact (L), Siemens Medical Solutions USA Inc., Malvern, PA, USA) the distance (d) between the image intensifier (II) and the x-ray source should be 1000mm. Since the manual did not contain the manufacturing tolerances and the distortion grid may not have been placed directly center on the II it was thought to be a reasonable assumption to constrain the projected source to within 2 pixels of (0,0) and d to within 5mm of 1000mm (Allen, 2009).

These initial Euler angle estimate were calculated by iteration through several angle values to find the combination that resulted in the lower root mean squared error (RMSE). The initial Euler angles were iterated between $-\pi$ radians to π radians with a step size of $\pi/16$ radians. Two additional iterations were then performed to determine more precise initial estimates for the Euler angle sequence.

An optimization technique was completed using the information of the pixel size and the mathematical relationship between the location of the 3D calibration points and their 2D projections onto the image plane. A custom-coded MATLAB script originally developed by Allen was modified for this study (Allen, 2009). A numerical optimization is employed to determine the rotation and translation required by the image plane. Detailed steps on how to obtain and utilize these calibration parameters are found in Appendix E of Allen's 2009 thesis work. Once this step is completed the experimental set-up should be accurately modeled in Rhinoceros (Rhinoceros, Robert McNeel & Associates, Seattle, WA, USA).

3.2.5.4   CALIBRATION OF THE SECOND FLUOROSCOPE

Calibration of the second fluoroscope follows the same process as the first fluoroscope, however, the matrix $P(c_s,l_s,d)$ contains a different mathematic relationship. Once this relationship is modified the process can be followed in the same manner as done for the calibration of the first fluoroscope.

3.3   VIRTUAL RECREATION OF EXPERIMENTAL SET-UP

Using the files created in sections 3.2.5 (FluoroA-Calibration.3dm and FluoroB-Calibration.3dm) a single file is created titled FluoroAB-Calibration.3dm. This is

computed by importing one of the files into the calibration file of the other fluoroscope (e.g. import FluoroB-Calibration.3dm into FluoroA-Calibration.3dm). Each fluoroscope should have a designated view and be modelled as a perspective projection camera in the program Rhinoceros. The camera location should be defined as the x-ray source coordinates and the cameras target location should be placed at the centre of the image plane for each fluoroscope. The resulting images of interest for this study are then viewed as seen from each x-ray source (figure 3.3).
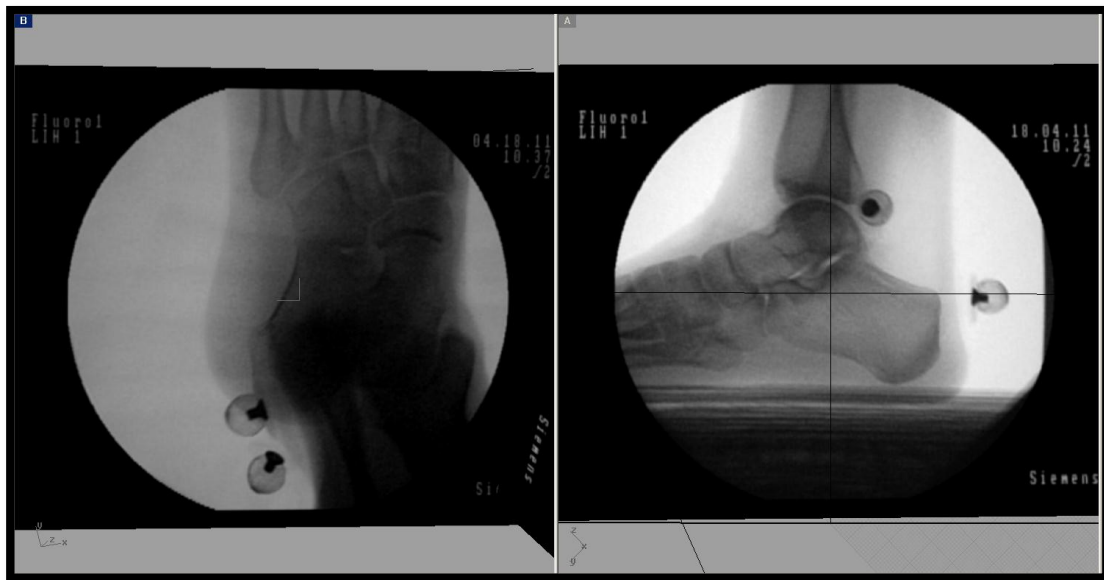
Figure 3.3: Two viewpoints from the x-ray foci. Left: Fluoroscope B, Right: Fluoroscope A.

3.4 BONE MODEL CREATION

Three-dimensional models of the bones under study were created using a computed tomography (CT) scan of the volunteer's foot and the program OsiriX-DICOM Viewer (Advanced Open-Source PACS Workstation DICOM Viewer, Antoine Rosset, USA). Detailed steps on how to segment the bone(s) of interest from a CT scan using OsiriX are provided in Appendix B. The models were converted to a triangular mesh of file format

stereolithography (.stl) (or object file .obj). Figure 3.4 shows the 3D rendered model of the calcaneus, cuboid, navicular, and tibia/fibula. The landmarks of interest were located as described in chapter 1 (section 1.5.1) of this thesis and marked on each of the bone models as indicated.

(A) Calcaneus

(B) Cuboid

(C) Navicular

(D) Fibula (left), Tibia (right)
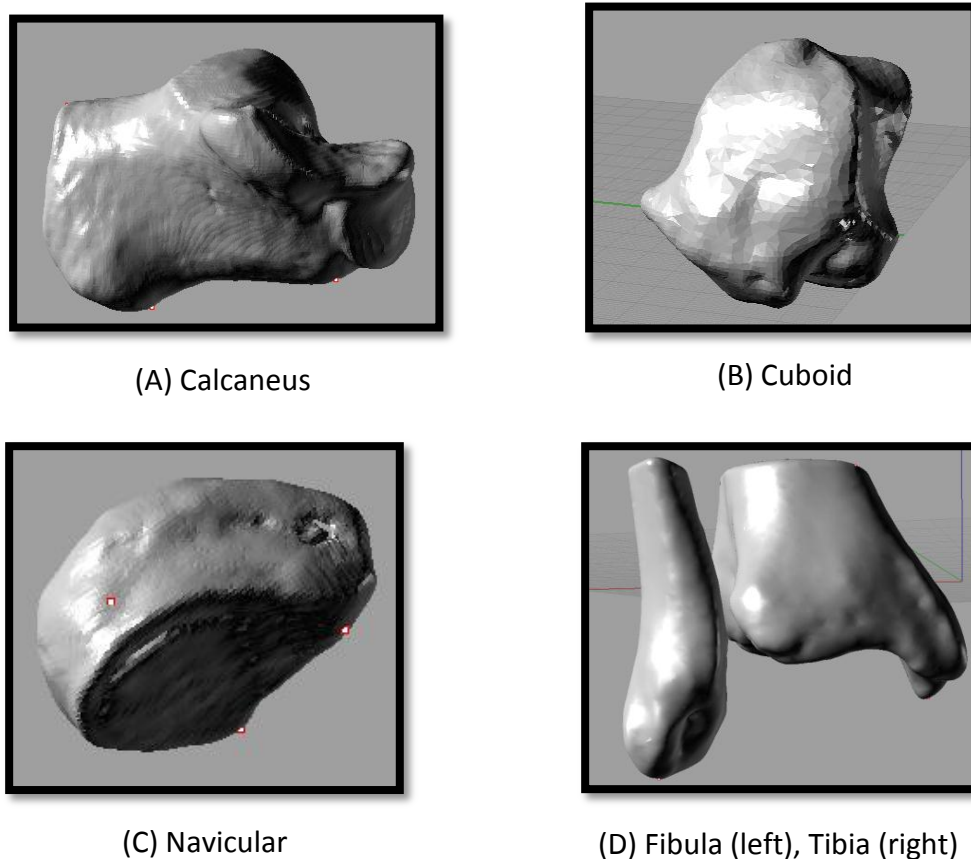
Figure 3.4: Rendered 3D model of: (A) calcaneus, (B) cuboid, (C) navicular and (D) tibia/fibula as viewed in Rhinoceros.

3.5 MATCHING BONES TO THE IMAGE PLANE

The matching process recreates the pose of the bones captured by the fluoroscopes. The computer bone models (section 3.4) are imported into the virtual environment. Initially the entire fluoroscopic image is viewed and each bones silhouette

is matched closely to its entire bony outline on both images (fluoroscope A and fluoroscope B). Once the match is close the image is enlarged (i.e. increase the lens length on the camera was increased) and a few easily identifiable landmarks are used to fine-tune the match. At this point the object is moved by increments as small as 0.01mm and 0.01° until the silhouette's of the bony landmarks completely matches the outline of the bony landmarks on the image. It is still important to ensure that the overall match is still obtained when the image is enlarged. Once the match is complete the bony landmarks are exported to an excel spreadsheet using the "ExportPoints" Rhinoscript developed by Allen (Allen, 2009). This Rhinoscript is used to export the bony landmark 3D coordinates of the bony landmarks.

For each condition being studied (barefoot, plaster hard orthotics, and plaster soft orthotics) the corresponding fluoroscope images are imported into the virtual environment and the model is re-matched. Since this study is interested in dynamic trials more than one frame was used for each condition. The number of frames used was dependant on the speed the individual walked while in the view of the fluoroscope. A minimum of five (5) frames were analyzed during midstance for each condition. The calcaneus, cuboid, navicular, and tibia/fibula are matched in figure 3.5, figure 3.6, figure 3.7, and figure 3.8 respectively.
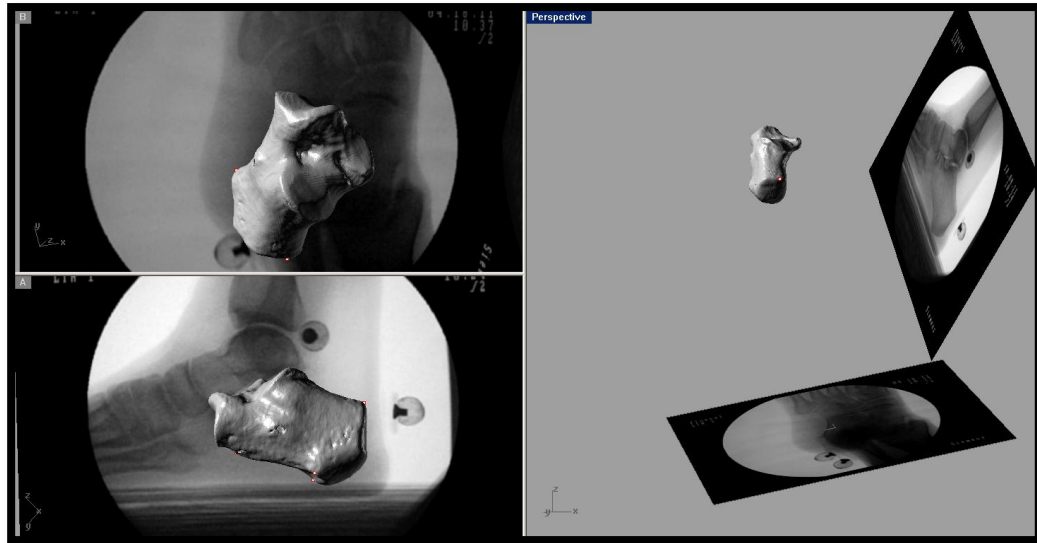
Figure 3.5: The calcaneus matched to both fluoroscope images. Top left: fluoroscope B, Bottom left: fluoroscope A, Right: 3D model of the calcaneus in virtual environment.
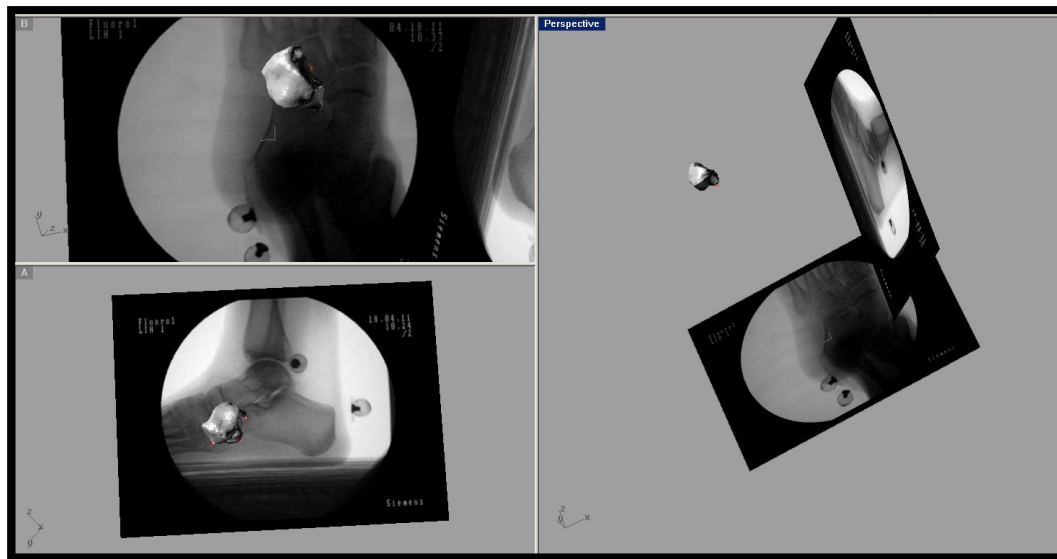
Figure 3.6: The cuboid matched to both fluoroscope images. Top left: fluoroscope B, Bottom left: fluoroscope A, Right: 3D model of the cuboid in the virtual environment.
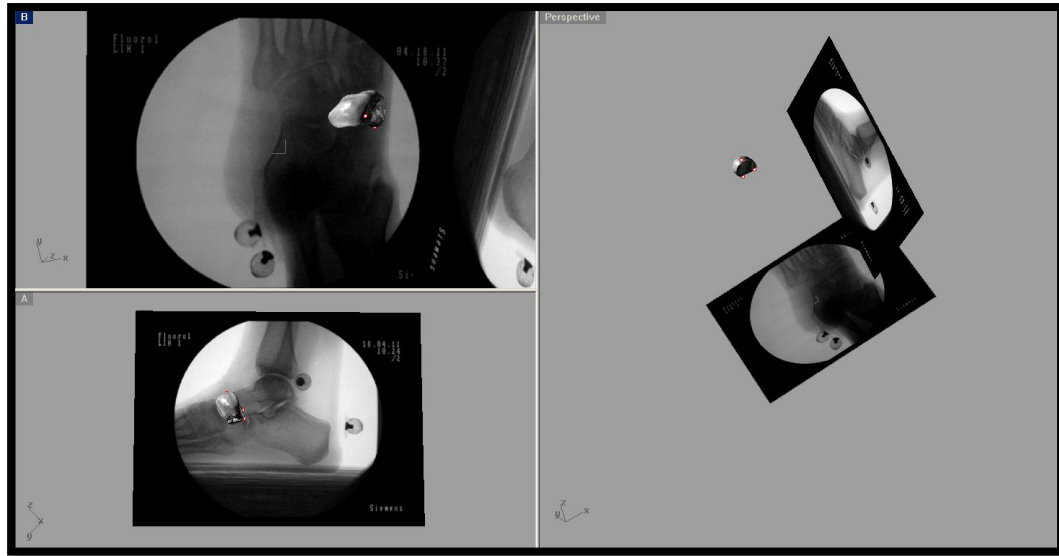
Figure 3.7: The navicular matched to both fluoroscope images. Top left: fluoroscope B, Bottom left: fluoroscope A), Right: 3D model of the navicular in the virtual environment.
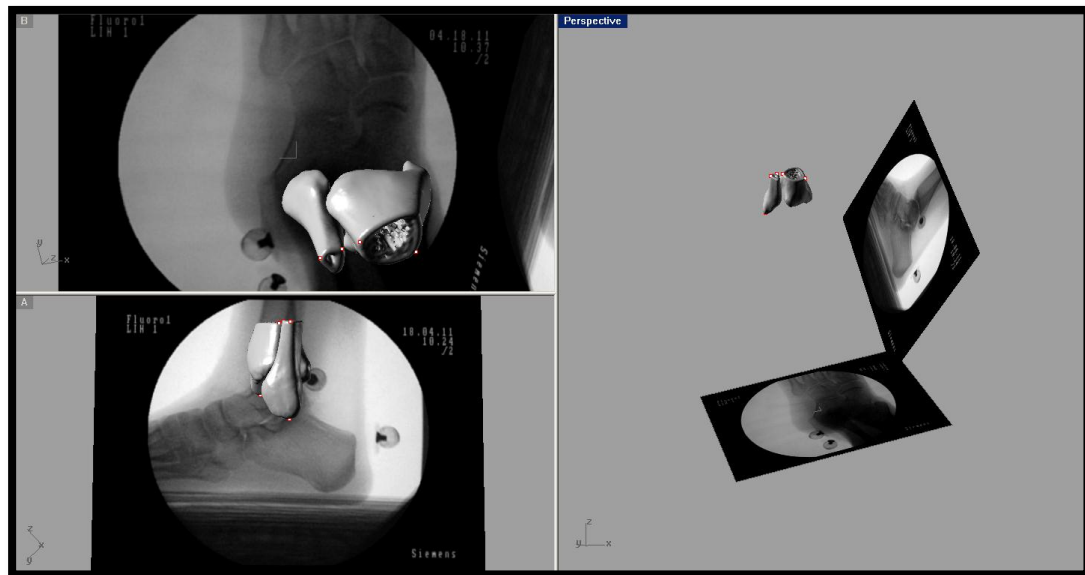
Figure 3.8: The tibia/fibula matched to both fluoroscope images. Top left: fluoroscope B, Bottom left: fluoroscope A, Right: 3D model of the tibia and fibula in the virtual environment.

Once the matching process is completed the mathematical analysis to determine the change in the alignment of the foot can be calculated. Custom MATLAB script (Calcaneuspronation_kinematics.m) was developed for this thesis (Appendix C). Using the excel files generated from the "ExportPoints" Rhinoscript containing the 3D coordinates of the bony landmarks on the calcaneus, cuboid, navicular, tibia and fibula individual bone coordinate systems can be calculated as described in chapter 1. Once the bone coordinate systems are calculated the change in pronation with respect to the calcaneus, and the tibia/fibula can be determined. The custom MATLAB script (Calcaneuspronation_kinematics.m) exports an excel spreadsheet which contains the foots internal rotation, plantarflexion, and inversion angles for the various bones with respect to each other as labelled (table 3.1). The calcaneus with respect to the tibia/fibula is calculated based on the International Society of Biomechanics (ISB) joint coordinate system definition (section 1.6.1) (Wu *et al.,* 2002). Since the calcaneus with respect to the tibia/fibula was considered the standard measurement it was used to determine if the foot was pronating overall. However, this was not the only measurement considered in this thesis. Since individual bone alignment in the foot has never been studied prior to this thesis work (to the author's knowledge) the changes in the cuboid and navicular were also considered during midstance.

Table 3.1: The calculations completed using the custom MATLAB script in Appendix C for the three planes of motion.

Internal/External Rotation Plantar/dorsi flexion Inversion/ Eversion	Calcaneus with respect to the tibia/fibula	Navicular with respect to the tibia/fibula	Cuboid with respect to the tibia/fibula	Navicular with respect to the calcaneus	Cuboid with respect to the calcaneus

A repeated measures analysis of variance (ANOVA) using SPSS was produced to test for differences between measurement conditions (SPSS; IBM Corporation, Armonk, NY, USA). A probability level of $p < 0.05$ was used to indicate significance. All levels of significance will be reported however, only where significance is found will the results of the statistical test be included in appendix F.

3.6 RESULTS

The impact of plaster casted orthotics on the hindfoot was determined by using a reverse engineering technique. By manipulating the bony landmark locations the variance in the bone coordinate systems can be used to determine the change in pronation on the population studied. The barefoot values were used for a baseline in this study and are found in table 3.2.

Table 3.2: Barefoot baseline angle measurements for the five (5) subjects. All entries in degrees.

Measurement	Subject#	cal wrt tibfib	nav wrt cal	cub wrt cal	nav wrt tibfib	cub wrt tibfib
External Rotation	1	15.47	-13.33	61.17	33.97	-48.14
	2	46.47	22.02	87.11	50.84	-62.06
	10	47.68	6.42	89.29	65.82	-47.13
	11	31.20	5.61	65.19	36.85	-36.47
	23	43.32	27.13	87.79	41.77	-40.36
	Average	36.83	9.57	78.11	45.85	-46.83
	Standard Deviation	13.61	15.92	13.73	12.87	9.78
Dorsiflexion	1	183.09	-45.69	13.95	-127.12	-171.60
	2	148.79	-38.58	99.37	-168.45	-162.27
	10	155.63	-47.09	59.50	-132.82	-164.39
	11	164.20	-51.98	-22.35	-139.33	-151.92
	23	152.37	-37.89	-9.40	-159.83	-168.48
	Average	160.82	-44.25	28.21	-145.51	-163.73
	Standard Deviation	13.70	5.97	50.54	17.81	7.52
Eversion	1	166.70	22.96	14.14	140.97	164.37
	2	150.75	23.28	-115.48	123.54	156.38
	10	157.79	27.16	-74.80	123.77	163.51
	11	152.06	16.39	-33.57	134.32	169.05
	23	165.60	31.90	-74.29	128.43	174.37
	Average	158.58	24.34	-56.80	130.20	165.54
	Standard Deviation	7.41	5.73	49.10	7.45	6.70

Note: The output from the program was manipulated beyond this table to represent the results where positive represents the change in motion towards the direction that promotes an increase in supination.

Due to the large variance between subjects each individual's barefoot condition (table 3.2) was used as their baseline value and only the change in pronation is reported. The standard deviation associated with each subject during all conditions and

measurements was calculated. This average standard deviation for the soft plaster casted orthotic and the rigid plaster casted orthotic is reported in Appendix E and is represented in table E.1 and table E.2 respectively. The values shown in these tables represent the standard deviation for at least five frames during midstance for that particular subject. The average effect of the plaster casted orthotic on the calcaneus with respect to the tibia/fibula for the three planes of motion: internal rotation, plantarflexion, and inversion can be found in figure 3.9, figure 3.10, and figure 3.11 respectively.

The average effect of the soft plaster casted orthotic on the pronation angle is shown in table 3.3, table 3.4, and table 3.5 for internal rotation, plantarflexion, and inversion respectively. The average effect of the rigid plaster casted orthotic is summarized in table 3.6, table 3.7, and table 3.8 for the internal rotation, plantarflexion, and inversion respectively.
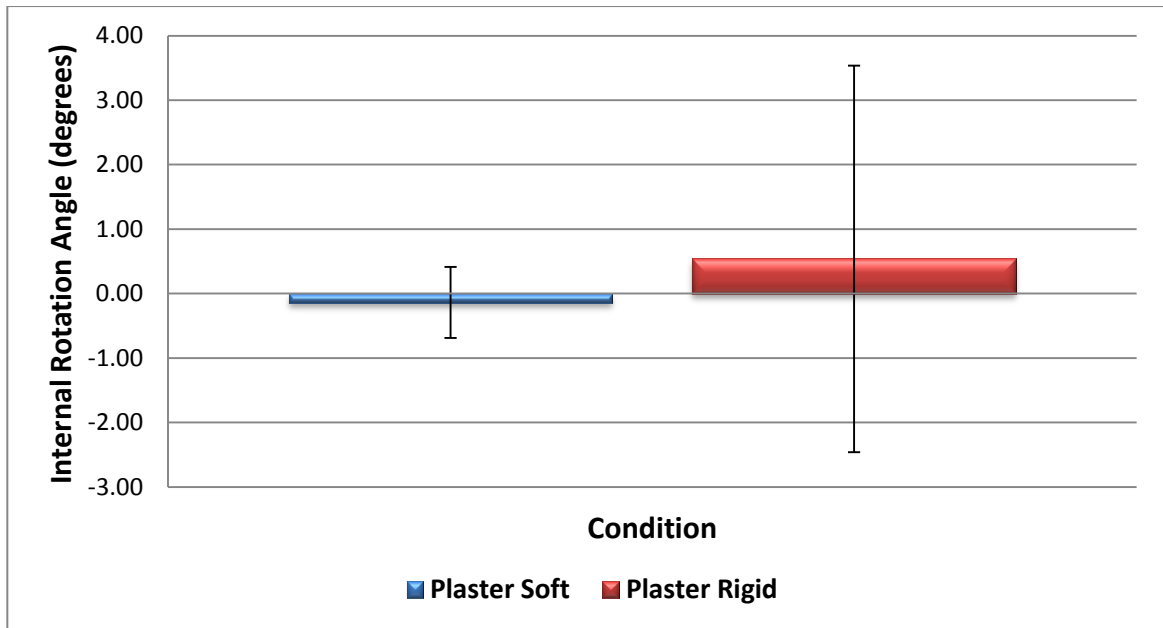
Figure 3.9: The average change in internal rotation for the normal population while wearing plaster casted orthotics. The internal rotation is measured for the calcaneus with respect to the tibia/fibula.
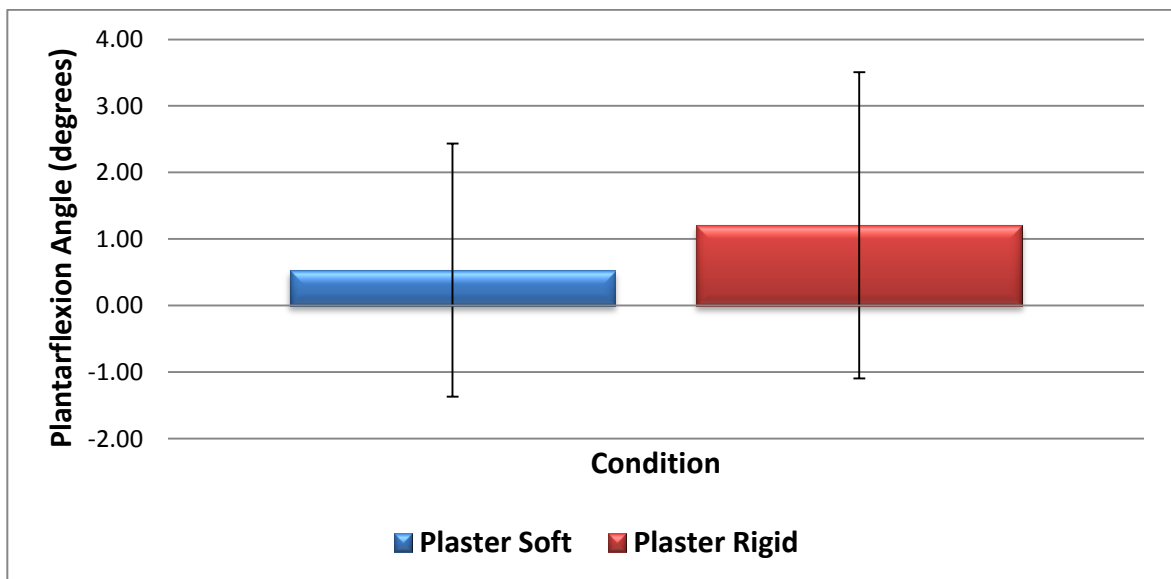
Figure 3.10: The average change in the plantarflexion angle in the normal population while wearing the plaster casted orthotics. A negative change represents an increase in plantarflexion, and a positive change indicates an increase in dorsiflexion.
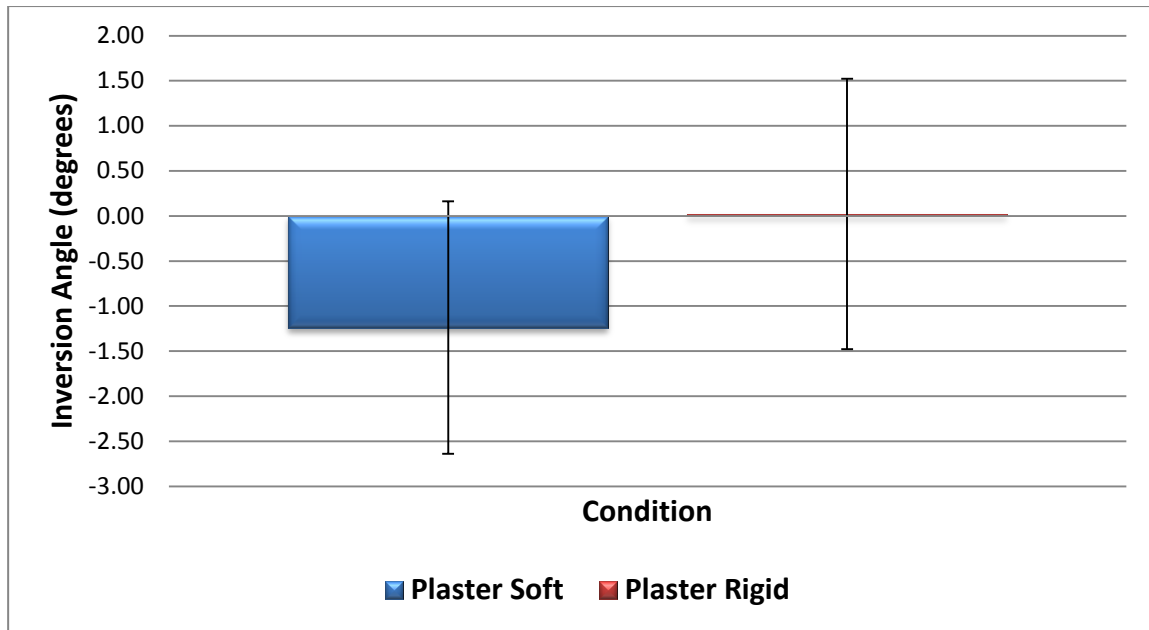
Figure 3.11: The average change in the inversion angle for the calcaneus with respect to the tibia/fibula while wearing plaster casted orthotics on the normal population.

Table 3.3: Results representing the internal rotation angle changes in the foot while wearing the soft plaster orthotic. All entries in degrees.

Soft Plaster Orthotic: Internal Rotation

Subject#	cal wrt tibfib	nav wrt cal	cub wrt cal	nav wrt tibfib	cub wrt tibfib
1	7.54^+	7.73^+	-4.43	3.66^+	9.30^+
2	19.96^+	12.82^+	-19.50	19.97^+	-8.54
10	-8.73	-4.20	-11.25	-0.90	4.21^+
11	-3.58	1.37	0.15	-9.10	2.82^+
23	-15.87	-6.94	-18.00	-10.57	-1.60
AVERAGE	**-0.14**	**2.16***	**-10.60**	**1.38***	**1.24***

Note: A negative value indicates the opposite motion (i.e. external rotation). Those with a (*) represent a value which is significant to one standard deviation. Those with a (+) are significant to two standard deviations.

Table 3.4: Results representing plantarflexion angle changes in the foot while wearing the soft plaster orthotic. All entries in degrees.

Soft Plaster Orthotic: Plantarflexion

Subject#	cal wrt tibfib	nav wrt cal	cub wrt cal	nav wrt tibfib	cub wrt tibfib
1	-3.69	3.14*	-26.00	-4.87	14.35^{+}
2	-10.76	-2.36	30.18^{+}	-2.71	15.15^{+}
10	7.41^{+}	1.97	-53.57	-4.71	1.25^{+}
11	3.27*	-1.19	2.58	9.19^{+}	-13.36
23	6.44^{+}	-1.05	5.71	-0.92	-2.43
AVERAGE	**0.53**	**0.10**	**-8.22**	**-0.80**	**2.99***

<u>Note</u>: A negative value represents the opposite motion (i.e. dorsiflexion). Those with a (*) represent a value which is significant to one standard deviation. Those with a (+) are significant to two standard deviations.

Table 3.5: Results representing Inversion angle changes in the foot while wearing the soft plaster orthotic. All entries in degrees.

Soft Plaster Orthotic: Inversion

Subject#	cal wrt tibfib	nav wrt cal	cub wrt cal	nav wrt tibfib	cub wrt tibfib
1	-4.20	2.34^{+}	-1.04	-6.04	-5.04
2	-16.01	4.81^{+}	-50.41	-14.51	-10.31
10	-0.86	4.92^{+}	48.18^{+}	-3.85	2.65^{+}
11	17.11^{+}	2.07^{+}	14.25^{+}	14.46^{+}	5.25^{+}
23	-2.22	1.81*	38.49^{+}	-1.76	-5.14
AVERAGE	**-1.24**	**3.19^{+}**	**8.82^{+}**	**-2.34**	**-2.52**

<u>Note</u>: A negative value represents the opposite motion (i.e. eversion). Those with a (*) represent a value which is significant to one standard deviation. Those with a (+) are significant to two standard deviations.

Table 3.6: Results representing internal rotation angle changes in the foot while wearing the rigid plaster orthotic. All entries in degrees.

Rigid Plaster Orthotic: Internal Rotation

Subject#	cal wrt tibfib	nav wrt cal	cub wrt cal	nav wrt tibfib	cub wrt tibfib
1	20.26^{+}	23.96^{+}	19.40^{+}	1.54	-1.92
2	10.04^{+}	3.99*	-10.12	1.31	2.10
10	-9.39	-8.33	-8.63	-1.65	6.46^{+}
11	-0.30	5.57^{+}	19.21	-10.35	-7.33
23	-17.92	-2.64	-9.42	-19.36	-5.29
AVERAGE	**0.54**	**4.51^{+}**	**2.09***	**-5.70**	**-1.20**

Note: A negative value indicates the opposite motion (i.e. external rotation). Those with a (*) represent a value which is significant to one standard deviation. Those with a (+) are significant to two standard deviations.

Table 3.7: Results representing the plantarflexion changes in the foot while wearing the rigid plaster orthotic. All entries in degrees.

Rigid Plaster Orthotic: Plantarflexion

Subject#	cal wrt tibfib	nav wrt cal	cub wrt cal	nav wrt tibfib	cub wrt tibfib
1	-7.87	4.60^{+}	18.14^{+}	-3.84	5.32^{+}
2	-8.12	-4.15	19.20^{+}	7.80^{+}	-12.50
10	7.94^{+}	2.52^{+}	-72.55	-8.13	8.84^{+}
11	8.37^{+}	-0.29	1.40	14.35^{+}	5.39*
23	5.70^{+}	-1.01	-10.28	0.35	3.06*
AVERAGE	**1.21***	**0.33**	**-8.82**	**2.11**	**2.02**

Note: A negative value represents the opposite motion (i.e. dorsiflexion). Those with a (*) represent a value which is significant to one standard deviation. Those with a (+) are significant to two standard deviations.

Table 3.8: Results representing inversion angle changes in the foot while wearing the rigid plaster orthotic. All entries in degrees.

Rigid Plaster Orthotic: Inversion

Subject#	cal wrt tibfib	nav wrt cal	cub wrt cal	nav wrt tibfib	cub wrt tibfib
1	-6.73	5.97[+]	14.44*	-9.67	-3.07
2	4.42[+]	-3.96	-30.74	6.34[+]	-3.09
10	-2.53	0.55*	29.88[+]	-1.24	12.76
11	3.19*	5.89[+]	-23.960	-0.80	18.27[+]
23	1.75	0.30	22.44[+]	3.34[+]	3.97[+]
AVERAGE	**0.02**	**1.75***	**2.44**	**-0.41**	**5.97[+]**

Note: A negative value represents the opposite motion (i.e. eversion). Those with a (*) represent a value which is significant to one standard deviation. Those with a (+) are significant to two standard deviations.

3.7 DISCUSSION

This study examines the effect that plaster casted orthotics have on the normal foot as compared to each individual participants barefoot condition in three-dimensions. By an Euler angle analysis the findings suggest that the general population will see a reduction in pronation when wearing a plaster casted orthotic although the results of this study were not found to be statistically significant (Appendix F).

Each subjects' data was evaluated with an ANOVA repeated measures statistical test using SPSS (SPSS; IBM Corporation, Armonk, NY, USA) to determine the statistical significance between each shoed condition as compared to the barefoot condition. Each plane of motion was analyzed separately. A probability level of $p<0.05$ was considered significant. While wearing the plaster soft orthotic no significant changes were found in internal rotation ($p=0.984$), plantarflexion ($p=0.884$), and inversion ($p=0.827$). While wearing the plaster hard orthotic no significant changes were found in internal rotation ($p=0.940$), plantarflexion ($p=0.766$), and inversion ($p=0.992$) planes of motion. It was

discovered that no overall statistical difference caused by wearing plaster soft and plaster hard orthotic insoles. Significance may not have been reached due to the small sample size.

Based on the kinematic joint coordinate system motion definition accepted by ISB the calcaneus with respect to the tibia/fibula is considered the measure that most accurately represents pronation when the three planes of motion are taken into consideration (Wu *et al.,* 2002). The results of the calcaneus with respect to the tibia/fibula were shown in figure 3.9, figure 3.10, and figure 3.11 for the internal rotation, plantarflexion, and inversion planes respectively. The graphs represent the normal population's average change in pronation compared to the barefoot condition between the soft and hard material based orthotic. It was found that the plaster rigid orthotic had the greatest increase in internal rotation and inversion (figure 3.9 and figure 3.11). However, the difference between the plaster soft condition and the plaster rigid orthotic was less than one standard deviation for the inversion plane of motion. The plaster soft orthotic had the greatest increase in plantarflexion, but the change still remained within one standard deviation in figure 3.10. From this it was concluded that although a significant change may occur on the individual level this change is not predicable in the overall population. The remainder of the discussion will be presented at the individual level.

To determine if a condition had an effect on an individual level the concept of the normal distribution was used. Natural variance of several variables has the tendency to follow the normal distribution curve. Meaning that 68% of all cases will fit within one

(1) standard deviation (SD), and 99.5% of all cases will fit within two (2) SD (Norman and Streiner, 2003; Portney and Watkins, 2000). Therefore when deciding significance in the results those found to have one standard deviation of significance were represented with an asterisk (*) and those with two standard deviations of significance were represented with a plus (+) sign.

Since the calcaneus with respect to the tibia/fibula is considered the measurement that most accurately represents pronation when the three planes of motion are taken into consideration (Wu *et al.,* 2002). The other measurements will be discussed as their single plane effect rather than on their effect to reduce pronation as a whole.

Pronation is defined as the combination of external rotation, dorsiflexion, and eversion. A reduction in pronation requires the opposite combination to occur in the three planes of motion. Therefore, for the foot to see an overall decrease in pronation (alignment change in the direction of supination) the foot must experience a change increasing internal rotation, plantarflexion, and inversion when compared to the barefoot (baseline) condition.

Examining the effect of the soft plaster orthotic shows that the calcaneus with respect to the tibia/fibula little variation for the overall average of all participants. As participants wore the rigid plaster orthotic all three planes of motion did not experience a significant reduction in pronation. The calcaneus with respect to the tibia/fibula experienced an increase in plantarflexion (>1SD) with no significant change visible in the internal rotation and inversion planes of motion.

The evaluation of the navicular with respect to the calcaneus showed that the navicular reacted to the orthotics. While wearing the soft plaster orthotic an increase in internal rotation (>1SD), and inversion (>2SD) was found to occur overall. While wearing the rigid plaster orthotic an increase in internal rotation (>2SD) and inversion (>1SD) was the resultant found for the overall normal subject population tested.

Examining the navicular with respect to the tibia/fibula less motion was evident by comparison to the navicular with respect to the calcaneus. The only significant change in alignment occurred while wearing the soft plaster casted orthotic in the internal rotation (>1SD) plane of motion.

Upon examination of the cuboid with respect to the calcaneus significant motion was found in one plane, although different, for each orthotic type tested. It was found that the cuboid experienced an increase in inversion (>2SD) while wearing the soft plaster orthotic, and an increase in internal rotation (>1SD) while wearing the rigid plaster orthotic.

The cuboid with respect to the tibia/fibula experienced a significant increase in motion in two planes while wearing the soft plaster orthotic. An increase in internal rotation (>1SD), and plantarflexion (>1SD) was found while wearing the soft plaster orthotic. While wearing the rigid plaster casted orthotic an increase in inversion (>2SD) was found.

Although each participant reacted differently during each footwear and orthotic condition tested. It is still evident that the plaster casted orthotics did have an impact on the alignment of the bones within the foot when compared to the barefoot condition. It

was found that the type of material used (soft or rigid) did not have a significant impact on the alignment, although while wearing the soft plaster orthotic more conditions experienced a significant change in alignment. Taking all things into consideration the patient and pedorthist should chose a material type that is found to be qualitatively more successful based on their past experiences.

3.8 REFERENCES

Allen, A.-M. V. (2009). *Development and Validation of a Markerless Radiostereometric Analysis (RSA) System*. University of Western Ontario.

Kedgley, A. (2009). *Development of a fluoroscopic radiostereometric analysis system with an application to glenohumeral joint kinematics*. University of Western Ontario.

Kedgley, A. E., & Jenkyn, T. R. (2009). RSA calibration accuracy of a fluoroscopy-based system using nonorthogonal images for measuring functional kinematics. *Medical Physics*, *36*(7), 3176.

Kedgley, A. E., Birmingham, T. B., & Jenkyn, T. R. (2009). Comparative accuracy of radiostereometric and optical tracking systems. *Journal of Biomechanics*, *42*(9), 1350-1354.

Nordin, M., & Frankel, V. H. (2001). *Basic Biomechanics of the Musculoskeletal System*. (D. Leger, Ed.) (3rd ed., pp. 178-190). Baltimore: Lippincott Williams & Wilkins.

Norman, G. R., & Streiner, D. L. (2003). *Pretty Darned Quick Statistics* (3rd ed., pp. 5-52). Hamilton: BC Decker Inc.

Portney, L. G., & Watkins, M. P. (2000). *Foundations of Clinical Research: Applications to Practice* (2nd ed.). Upper Saddle River, New Jersey, USA: Prentice-Hall Inc.

Rougée, A., Picard, C. L., Trousset, Y. L., & Ponchut, C. (1993). Geometrical calibration for 3D x-ray imaging. *Proceedings of SPIE*, *1897*, 161-169.

Rougée, A., Picard, C., Ponchut, C., & Trousset, Y. (1993). Geometrical calibration of X-ray imaging chains for three-dimensional reconstruction. *Computerized medical imaging and graphics the official journal of the Computerized Medical Imaging Society*, *17*(4-5), 295-300.

Wu, G., Siegler, S., Allard, P., Kirtley, C., Leardini, A., Rosenbaum, D., Whittle, M., *et al.* (2002). ISB recommendation on definitions of joint coordinate system of various joints for the reporting of human joint motion--part I: ankle, hip, and spine. International Society of Biomechanics. *Journal of Biomechanics*, *35*(4), 543-548.

CHAPTER 4- THE EFFECT OF FOAM CASTED ORTHOTICS ON THE PES PLANUS AND PES CAVUS FOOT USING MARKERLESS RSA

OVERVIEW: This chapter describes the effect foam casted orthotics have on altering the alignment of the bones in the hindfoot in the pes planus and pes cavus population. Bi-planar x-ray fluoroscopy and the markerless RSA technique are used to determine the change in pronation of the pes planus and pes cavus population at midstance during gait.

4.1 INTRODUCTION

Pes planus (or flat foot) is the condition in which the medial longitudinal arch of the foot collapses coming into complete or near-complete contact with the ground. The pes planus foot is considered to be one experiencing external rotation, dorsiflexion, and eversion (Yagerman *et al.,* 2011). A pes cavus (or high arch) foot has visual arch properties opposite to that of the pes planus foot. The pes cavus foot generally has a rigid medial longitudinal arch present. Conservative management of patients with painful pes planus or pes cavus feet typically involve the use of orthotics. Orthotics are a device inserted as a replacement for the manufacturer's insole with the intent to support and realign the foot. An orthotic device is used in attempt to reduce and redistribute the loading on the plantar surface. Altering the alignment in the foot bones is thought to reduce and redistribute load to certain regions of the foot. The change is

dependent on the type of orthotic and its aggressiveness. A difference of approximately 5° between barefoot and a shoed (orthotic or no orthotic) condition is the minimal difference expected to be clinically significant. The barefoot condition is used as the reference position since pedorthists use barefoot walking to analyze a patient's gait and cast custom orthotics.

Markerless radiostereometric analysis (RSA) systems have been shown to be a feasible method for measuring foot bone motions during *in-vivo* weight bearing gait (Kedgley *et al.,* 2009). This method uses x-ray images from two fluoroscopes taken simultaneously from different locations in order to track the alignment of the foot in real time by using three-dimensional (3D) bone models. By employing an accurate calibration technique the experimental set-up can be recreated in the virtual environment and the motion of the bones can be tracked in real time.

The aims of this study were to quantify the variation in pronation on a pes cavus and pes planus population when asked to walk: (1) barefoot, (2) wearing a pair of foam casted soft orthotics, (3) wearing a pair of foam casted hard orthotics. It is hypothesized that the pes cavus group will experience little variation while wearing any orthotic type by comparison to the pes planus group. It is also hypothesized that the pes planus group will experience a reduction in pronation when wearing the orthotic insoles, with the more rigid material resulting in a greater reduction.

4.2 METHODS

Ethics was obtained from the Research Ethics Board at The University of Western Ontario prior to the commencement of any data collection. A recruitment poster was

created for the Canadian certified pedorthist to explain the research study to potential volunteers.

4.2.1 DATA COLLECTION

Three (3) pes planus and three (3) pes cavus volunteers were recruited to participate in this study. These volunteers were not screened for minor pain, or deformities. Individuals with previous fractures in the lower extremities were avoided and pre-screened for. Each volunteer had their feet examined to ensure they fit the criteria for pes planus or pes cavus. Volunteers were asked to fill out a consent form after the study was explained as well as any risks involved. The volunteers were fitted with two pairs of custom-made orthotics with: (1) a 4mm plastazote (soft) and (2) 3mm RCH-500 (rigid) foam box casted orthotic as per usual clinical practice. The orthotics were casted by the same Canadian certified pedorthist at the Fowler Kennedy Sport Medicine Clinic, London, ON, Canada. When the orthotics were ready for wear the volunteers returned for the image collection.

The fluoroscopes were positioned so the two images of the foot gave optimal views of the calcaneus at the instant of midstance during walking gait. After positioning the fluoroscopes, they had to be calibrated using the RSA method. At least one image of the calibration frame was captured prior to the volunteer's arrival for the study. Each volunteer wore a wear wrap-around apron and kilt on their upper and lower body respectively, including a thyroid collar (figure 4.1). Sections 4.2.1.1 to 4.2.1.3 were completed in a randomized order. It is assumed that the order completed as presented in order to reduce repetition in the steps.

Figure 4.1: Platform and wrap-around leaded clothing. Image taken during a dynamic trial.

4.2.2.1   BAREFOOT

Each volunteer was instructed to stand barefoot on the platform placing their left foot in the field of view of both fluoroscopes. An x-ray technician ensured the two views of the calcaneus were optimal. The foot was adjusted accordingly to include the midfoot and entire tarsus. The x-ray technician then outlined the location of the volunteer's left foot to be used as a target location during the dynamic walking trials. Each volunteer was asked to walk at their preferred pace as the fluoroscope recorded the left foots motion at thirty (30) frames per second from heel strike to toe off. The captured images were checked to ensure that the calcaneus and tarsus were sufficiently visible for the subsequent RSA procedure prior to moving onto the next trial. If the calcaneus was not satisfactorily visible the trial was repeated. The barefoot condition was repeated two (2) times.

4.2.2.2   FOAM SOFT CASTED ORTHOTIC

Each volunteer was asked to wear the neutral cushioning running shoe (New Balance, model 882) with the custom-made foam soft casted orthotic insole inserted in place of the provided manufacturer's insole. Each volunteer was asked to walk at their preferred pace as the fluoroscopes recorded images of the left foot movement at 30 frames per second from heel strike to toe off. The images were recorded on the control PC in the adjacent control room. As with the barefoot trials, if the calcaneus was not satisfactorily visible the trial was repeated. The foam soft trial was repeated two times.

4.2.2.3   FOAM HARD CASTED ORTHOTIC

Each volunteer was instructed to wear the neutral cushioning running shoe (New Balance, model 882) with the custom-made foam hard casted orthotic. Each volunteer was asked to walk at their preferred pace as the fluoroscopes recorded the left foots motion at 30 frames per second from heel strike to toe off. The images were recorded on the control PC in the adjacent control room. As with the barefoot trials, if the calcaneus was not satisfactorily imaged the trial was repeated. The foam hard condition was repeated two times.

4.2.2 CALIBRATION

Two imaging devices, specifically, C-arm fluoroscopes with 9 inch image intensifiers (II) were used for the purpose of this study. A calibration frame is used to establish a laboratory coordinate system for the capture volume through which the test subject will walk and determines the locations of the two imaging devices relative to one another. A calibration frame designed by Kedgley was used as the calibration phantom

for this thesis (Kedgley, 2009). This custom designed calibration object is a cube with two fiducial planes and two control planes (figure 4.2). This custom designed calibration frame was constructed of 9.5mm thick acrylic sheet. Each fiducial plane was embedded with 45 beads (1mm in diameter) at known 3D locations. Each control plane was embedded with 45 beads (2mm in diameter) at known 3D locations. The frame was used to define the laboratory coordinate system. The steps required to successfully complete a calibration are based on a standard RSA algorithm in combination with the work of *Rougée et al.* (1993a and 1993b).

In order to calibrate the capture volume each imaging device must have a view of one fiducial plane and one control plane on the calibration box. The fiducial plane is used to calculate a transformation from the image coordinate system to the laboratory coordinate system. The control plane determines the location of the focal point from which the x-rays originate in the laboratory frame (Kedgley and Jenkyn, 2009). At least six fiducial and six control beads were visible to ensure a successful calibration. While this number of beads is the minimum needed for calibration, accuracy of the calibration procedure is increased when a greater number of beads can be utilized. Prior to proceeding with the calibration procedure it was ensured that no beads were overlapped in the image. If this were the case, manipulation of the calibration frame was necessary until a good image of the fiducial and control planes could be obtained for both fluoroscopes simultaneously. Images of the calibration frame were digitized, and corrected for pincushion distortion based on a standard RSA technique (Kedgley, 2009). The calibration device was designed and used to determine the relationship of the 3D

known bead locations with their 2D projections onto the image plane (Kedlgey and Jenkyn, 2009). The calibration algorithm was conducted to determine the parameters necessary to reconstruct the experimental set-up in a virtual environment. To continue the calibration an algorithm based on the work of *Rougée et al.* is modified to represent the experimental set-up.

Continuing the calibration requires a three-dimensional modeling program and the ability of representing the laboratory set-up as a perspective projection model. Using this concept the mathematical relationship between the 3D calibration points and the 2D image plane projections are defined. Using this model along with an optimization algorithm the parameters required to model the experimental set-up in the virtual environment are calculated. This perspective projection model will be explained for a single fluoroscope. The calibration setup used for this study is found in figure 4.2.
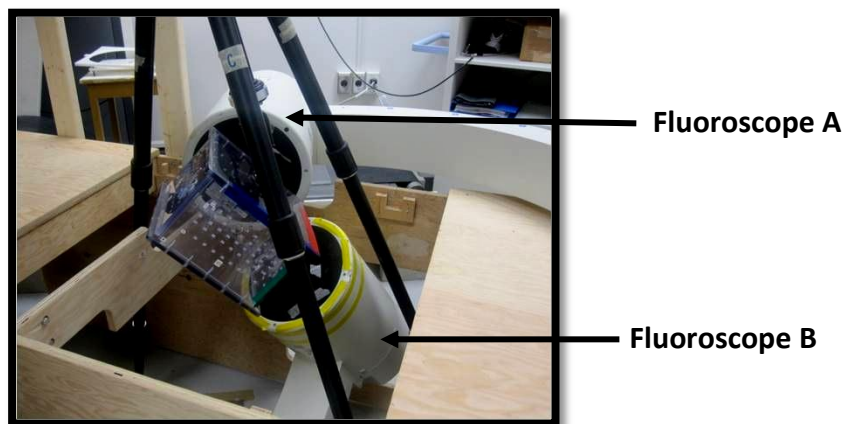
Figure 4.2: Calibration set-up for the study. The image intensifier (II) of each fluoroscope is labelled.

The optimization technique used the pixel size, and the mathematical relationship between the 3D calibration points and their 2D projection onto the image plane. A custom-written MATLAB script originally developed by Allen was modified for this study to match the calibration setup. By conducting a numerical optimization technique the location of the known 2D projections can be calculated. An initial estimate of the Euler angle rotation is calculated while minimizing the lower root mean squared error throughout the algorithm. A guide describing how to use the calibration parameters is outlined in Appendix E of Allen's 2009 thesis work. After completing the guide the experimental setup should be accurately modeled in the virtual environment. The process is repeated with a modified projection relationship for the second fluoroscope.

4.2.3 BONE MODEL CREATION

To accurately model the bone, three-dimensional models were segmented from a computed tomography (CT) scan of the volunteer's foot using the program OsiriX-DICOM Viewer (Advanced Open-Source PACS Workstation DICOM Viewer, Antoine Rosset, USA). Detailed steps describing the method on how to segment the bone(s) of interest from the foot using a Digital Imaging and Communications in Medicine (DICOM) image file and converting it to a useable file type, such as stereolithography (.stl) are provided in Appendix B. Figure 4.3 shows the 3D rendered bone model of the calcaneus, cuboid, navicular, and tibia/fibula. The landmarks of interest were located as described in chapter 1 (section 1.5.1) of this thesis and marked on each of the bone models as indicated.

(A) Calcaneus

(B) Cuboid

(C) Navicular

(D) Fibula (left), Tibia (right)
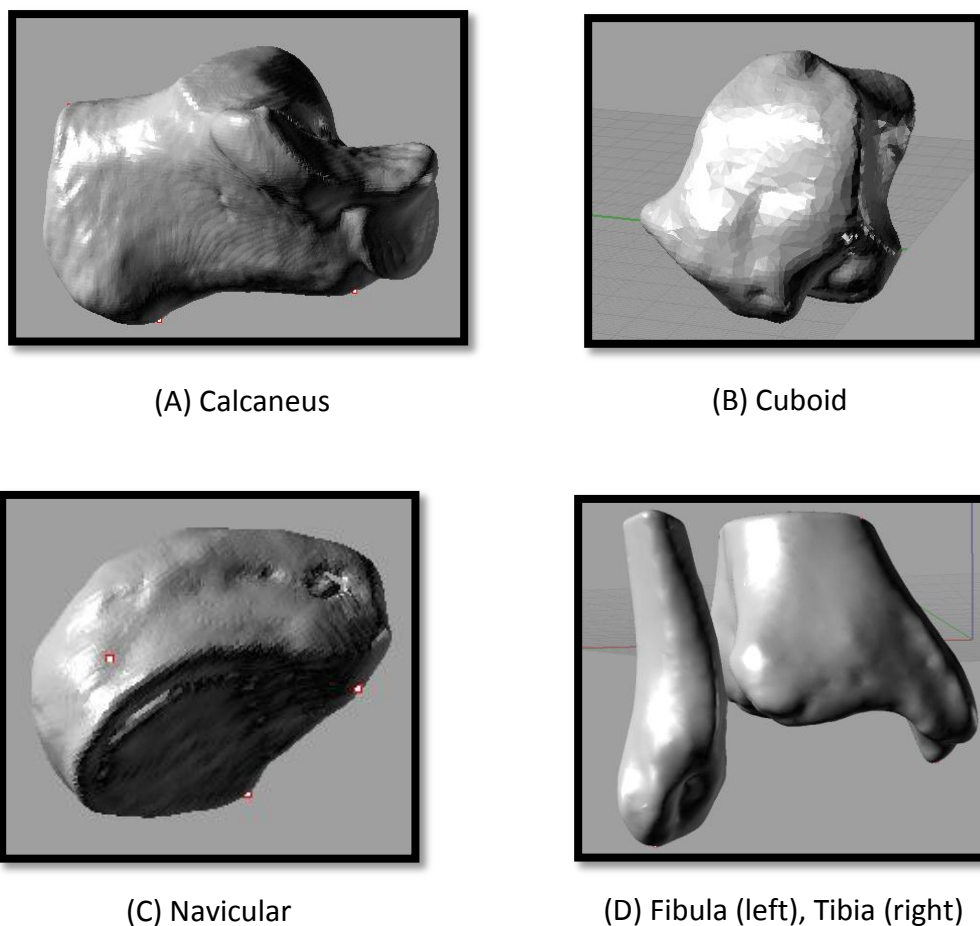
Figure 4.3: Rendered 3D model of: (A) calcaneus, (B) cuboid, (C) navicular, (D) tibia/fibula as viewed in Rhinoceros.

4.2.4 IMAGE PLANE MATCHING

Matching is done to recreate the pose of the bone as captured by the fluoroscopes. The computer bone models (section 4.3) are imported into the virtual environmental of the calibration. The bone (e.g. the calcaneus) is rotated and translated until the bone closely matches the pose captured by the fluoroscopes. This is most easily done by using easily identifiable landmarks and matching those closely (e.g. the medial process of the calcaneal tuberosity, labelled in figure 4.4) by increasing the lens length of

the projection camera model. The bone model is now moved by increments as small as 0.01mm and 0.01° until the silhouette's of the models bony landmarks completely matches the outline of the bony landmark on the image. The model is then viewed entirely to ensure that the overall match is still obtained. Once the match is complete the bony landmarks (figure 4.4) coordinates are exported into an excel spreadsheet.
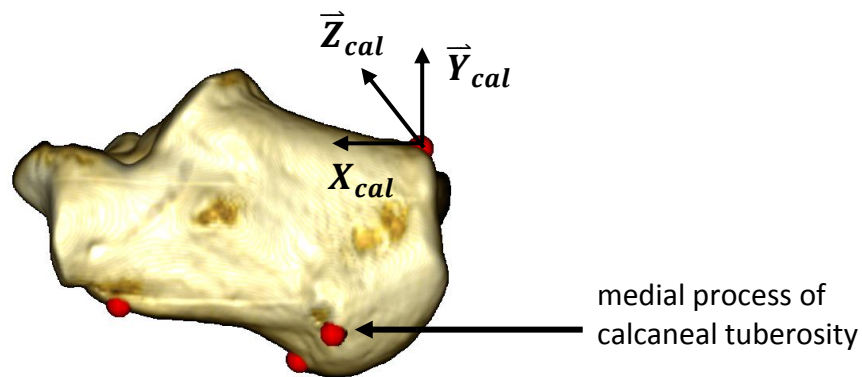
Figure 4.4: Calcaneus bone model with visual of its bone coordinate system and location of the medial process of the calcaneal tuberosity labelled. Model was used for the matching process to obtain the 3D pose of the bone during the various shoe conditions.

Images were collected at a rate of 30 frames per second; therefore, multiple frames were repeated in the matching process. A minimum of five frames were analyzed during midstance, this number was dependent on the speed the volunteer walked. The calcaneus, cuboid, navicular, and tibia/fibula were matched for each image frame. Custom MATLAB script developed for this thesis calculates the degree of pronation in the foot during the condition being analyzed. Pronation is defined as the combination of external rotation, dorsiflexion, and eversion. The custom script (Appendix C-Calcaneuspronation_kinematics.m) outputs the angle relative to the bones of interest

and divides the motion of pronation into three planes. The calcaneus with respect to the tibia/fibula is considered to have landmarks defined by the International Society of Biomechanics (ISB) therefore these bones were used to create the bone coordinate system. The motion of the navicular, and cuboid bones were also considered with respect to both the calcaneus and tibia/fibula coordinate systems.

This process is repeated for each condition studied (barefoot, foam hard orthotic, and foam soft orthotic). Fluoroscope images that were taken during the scenario of interest are imported into the virtual environment on the respective image plane and the model is matched. This is repeated for each bone (calcaneus, cuboid, navicular, tibia/fibula). The calcaneus, cuboid, navicular, and tibia/fibula are matched in figure 4.5, figure 4.6, figure 4.7, and figure 4.8 respectively.
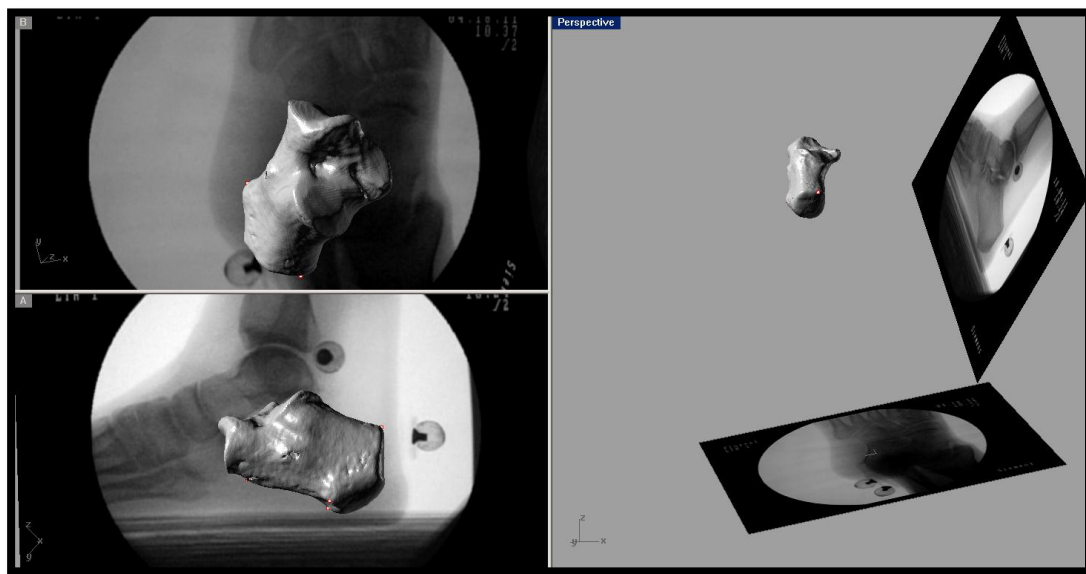
Figure 4.5: The calcaneus matched to the fluoroscopic images. Top left: Fluoroscope B, Bottom left: Fluoroscope A, Right: 3D model of the calcaneus.
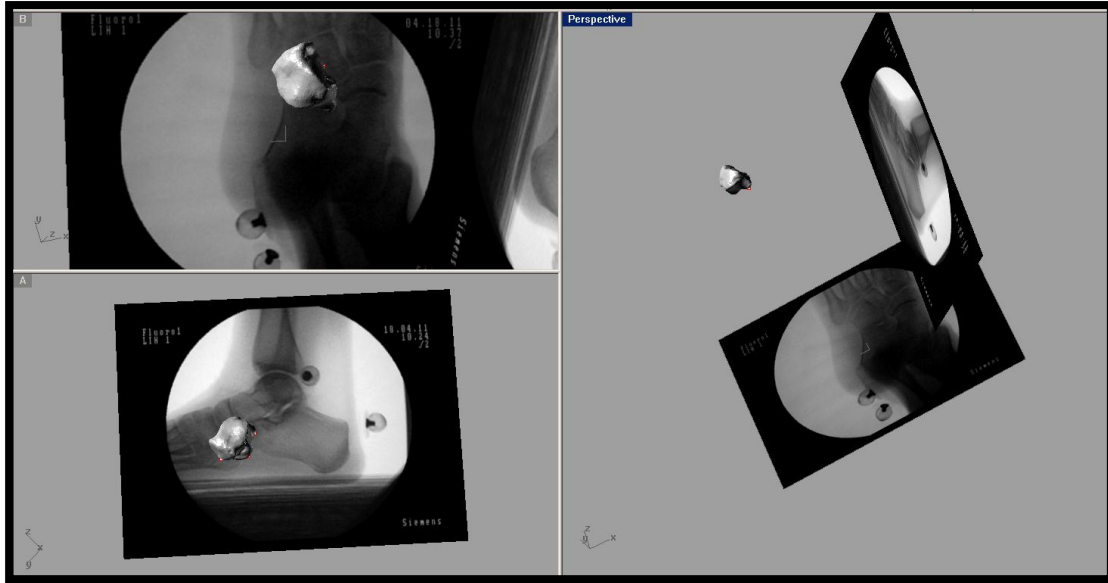
Figure 4.6: The cuboid matched to the fluoroscopic images. Top left: Fluoroscope B, Bottom left: Fluoroscope A, Right: 3D model of the cuboid.
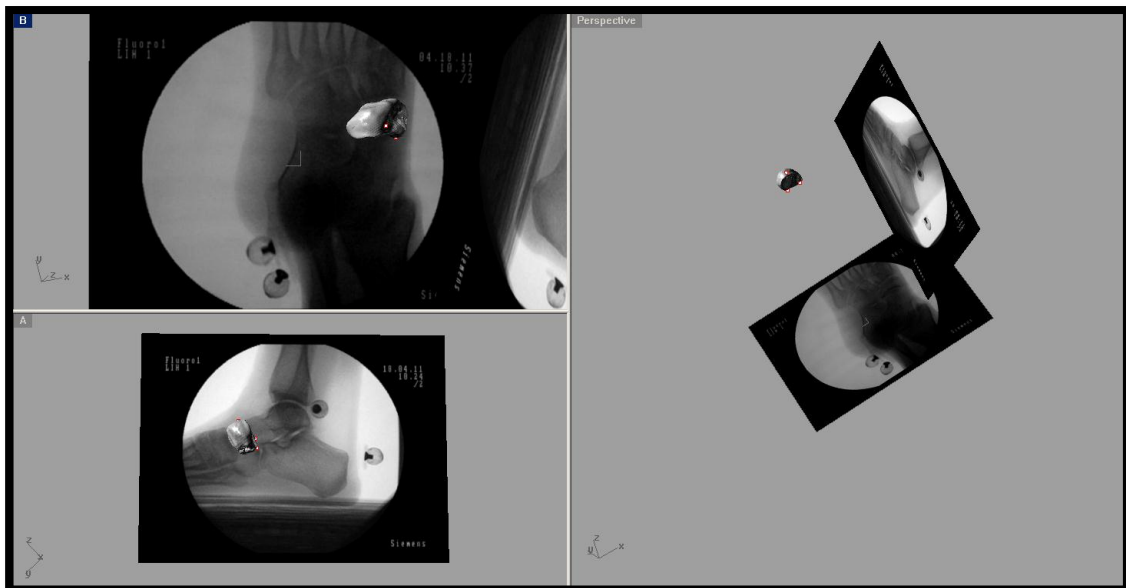
Figure 4.7: The navicular matched to the fluoroscopic images. Top left: Fluoroscope B, Bottom left: Fluoroscope A, Right: 3D model of the navicular.
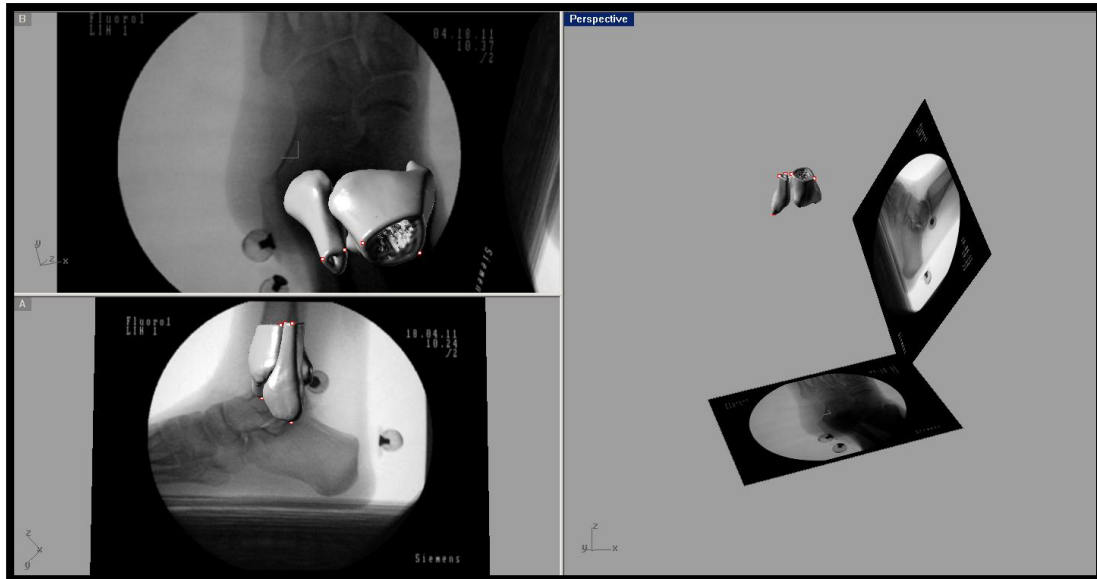
Figure 4.8: The tibia and fibula matched to the fluoroscopic images. Top left: Fluoroscope B, Bottom left: Fluoroscope A, Right: 3D model of the tibia and fibula.

A repeated measures analysis of variance (ANOVA) using SPSS was produced to test for differences between measurement conditions (SPSS; IBM Corporation, Armonk, NY, USA). A probability level of $p < 0.05$ was used to indicate significance. All levels of significance will be reported however, only where significance is found will the results of the statistical test be included in appendix F.

4.3 RESULTS

Using the output values from the transformation matrices calculation the impact of the different orthotic conditions (foam hard and foam soft) can be determined for the pes cavus and the pes planus groups studied in this chapter. The barefoot condition was used as the baseline measurement on an individual basis for the pes cavus and pes planus groups as shown in table 4.1 and table 4.2 respectively. The average effect on the

pes cavus and pes planus populations while wearing the foam soft and foam hard orthotics were analyzed. Figure 4.9, figure 4.10, and figure 4.11 contain the average effect as measured for the three planes of motion: internal rotation, plantarflexion, and inversion respectively.

Table 4.1: Barefoot baseline angle measurement for the three pes cavus subjects used in this study. All entries are in degrees.

Measurement	Subject#	cal wrt tibfib	nav wrt cal	cub wrt cal	nav wrt tibfib	cub wrt tibfib
External Rotation	9	26.67	-0.83	58.60	51.91	-46.46
	15	8.60	-38.65	37.98	70.45	32.69
	22	23.62	14.18	77.11	11.95	-48.38
	Average	19.63	-8.43	57.89	44.77	-20.72
	Standard Deviation	9.68	27.23	19.58	29.90	46.26
Dorsiflexion	9	175.46	-40.34	2.39	-153.01	-150.01
	15	178.17	-68.95	-7.77	-109.81	-156.93
	22	168.17	-44.25	26.97	-146.20	-170.66
	Average	173.93	-51.18	7.20	-136.34	-159.20
	Standard Deviation	5.17	15.51	17.86	23.23	10.51
Eversion	9	176.14	-51.27	-5.70	-123.01	-155.01
	15	175.18	-62.90	-12.02	-117.04	-158.31
	22	170.02	-47.43	53.37	-130.60	-156.66
	Average	173.78	-53.87	11.89	-123.55	-156.66
	Standard Deviation	3.29	8.06	36.07	6.80	1.65

Note: The output from the program was manipulated beyond this table to represent the results where positive represents the change in motion towards the direction that promotes an increase in supination.

Table 4.2: Barefoot baseline angle measurement for the three pes planus subjects used in this study. All entries are in degrees.

Measurement	Subject#	cal wrt tibfib	nav wrt cal	cub wrt cal	nav wrt tibfib	cub wrt tibfib
External Rotation	5	26.37	17.04	89.25	10.21	-59.23
	16	23.17	28.51	88.23	15.22	-60.40
	19	41.21	56.62	79.73	-13.01	-29.72
	Average	30.25	34.06	85.74	4.14	-49.79
	Standard Deviation	9.63	20.37	5.23	15.06	17.38
Dorsiflexion	5	35.67	29.47	89.97	21.80	-57.76
	16	25.84	34.56	89.77	28.15	-61.99
	19	42.70	41.90	58.05	13.19	-10.22
	Average	34.74	35.31	79.27	21.05	-43.32
	Standard Deviation	8.47	6.25	18.38	7.51	28.75
Eversion	5	29.66	26.93	84.58	9.07	-51.34
	16	24.50	29.96	87.52	10.59	-56.79
	19	39.64	50.76	75.72	4.15	-25.77
	Average	31.27	35.89	82.61	7.93	-44.63
	Standard Deviation	7.70	12.97	6.14	3.36	16.56

Note: The output from the program was manipulated beyond this table to represent the results where positive represents the change in motion towards the direction that promotes an increase in supination.
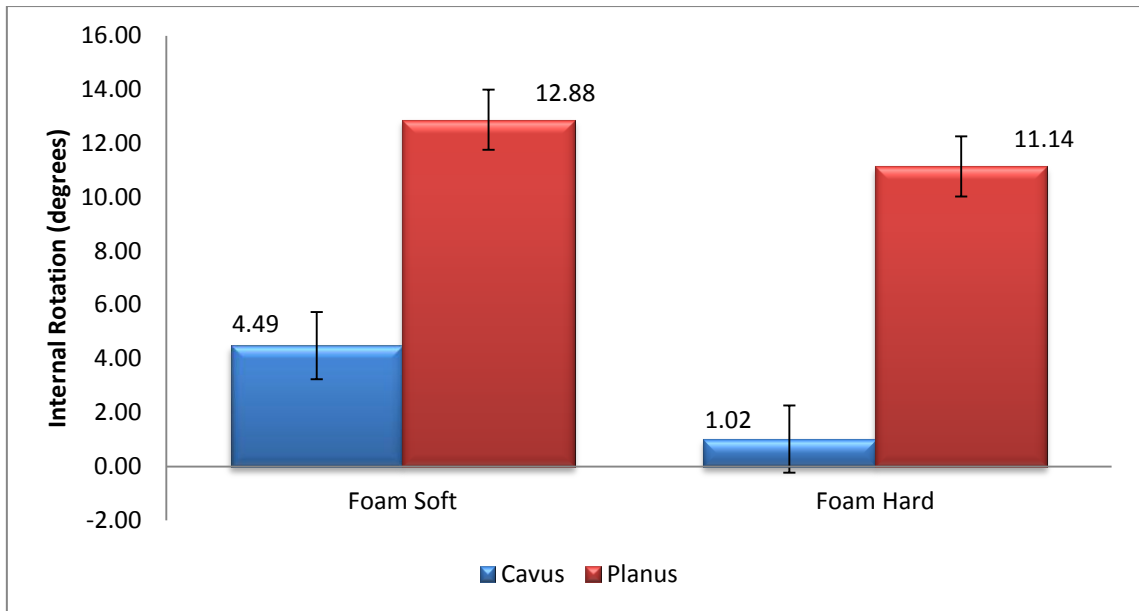
Figure 4.9: The average effect of wearing a foam soft and foam hard orthotics on both the pes cavus and pes planus populations studied for the plane of motion providing the change in internal rotation. The standard deviation is represented by the bars.
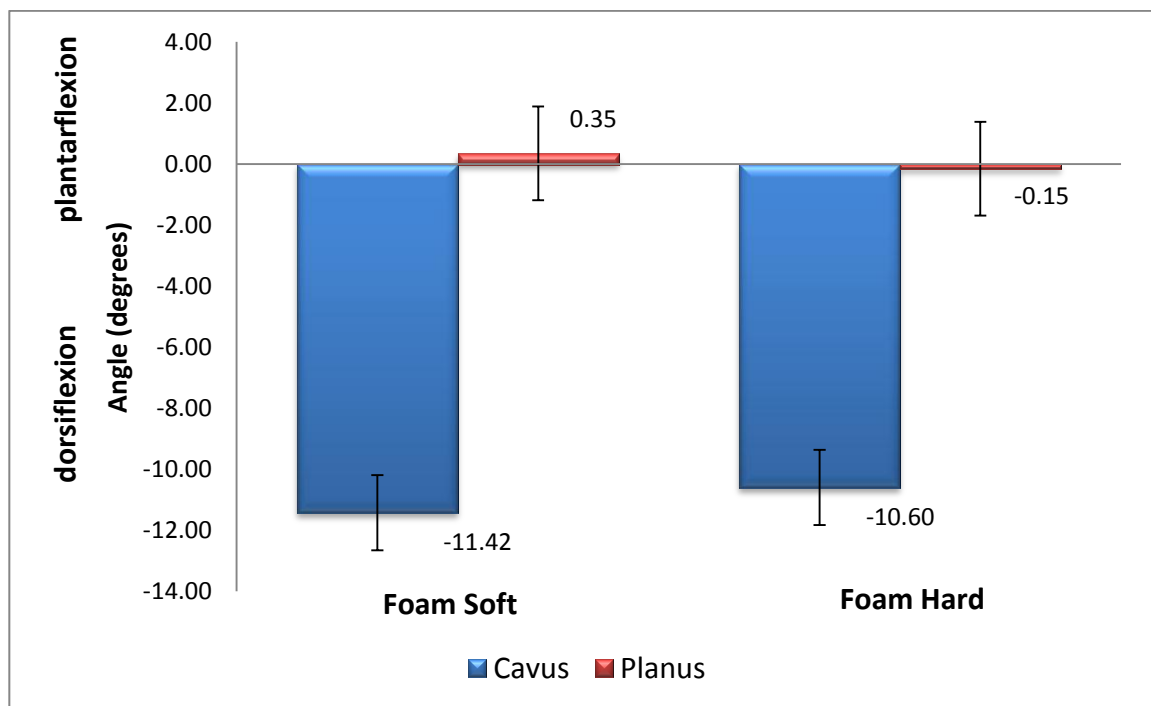
Figure 4.10: The average effect on the pes planus and pes cavus populations while wearing a foam soft and foam hard orthotic in the plantarflexion plane.
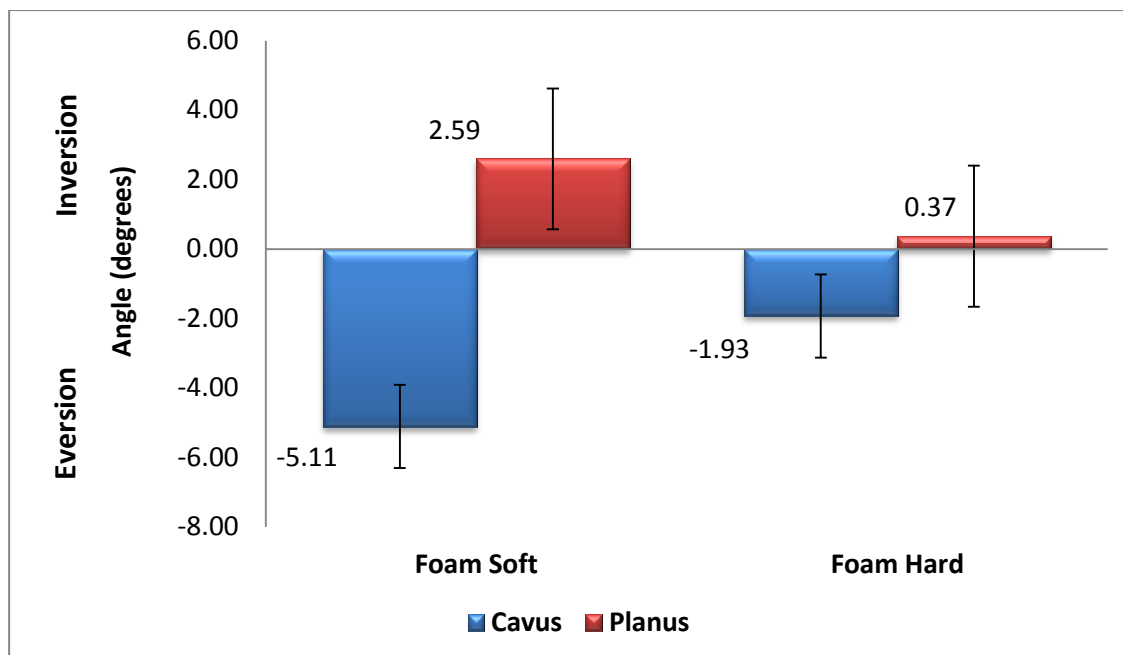
Figure 4.11: The average effect on the pes planus and pes cavus populations while wearing a foam soft and foam hard orthotic in the inversion/eversion plane of motion.

The calcaneus, navicular, cuboid, and tibia/fibula motion summarized for internal rotation, plantarflexion and inversion in table 4.3, table 4.4, and table 4.5 respectively for the pes cavus population wearing the foam soft orthotic. The calcaneus, navicular, cuboid, and tibia/fibula motion is summarized for internal rotation, plantarflexion and inversion in table 4.6, table 4.7, and table 4.8 respectively for the pes cavus population wearing the foam hard orthotic. The calcaneus, navicular, cuboid, and tibia/fibula motion is summarized in table 4.9, table 4.10, and table 4.11 for internal rotation, plantarflexion and inversion respectively for the pes planus population wearing the foam soft orthotic. The calcaneus, navicular, cuboid, and tibia/fibula motion summarized in table 4.12, table 4.13, and table 4.14 for internal rotation, plantarflexion and inversion respectively for the planus population wearing the foam hard orthotic.

Table 4.3: Results representing the change in the internal rotation angle for the pes cavus foot group while wearing the foam soft orthotic. All entries in degrees.

Foam Soft Orthotic: Internal Rotation

Subject#	cal wrt tibfib	nav wrt cal	cub wrt cal	nav wrt tibfib	cub wrt tibfib
9	9.31$^+$	12.43$^+$	0.72$^+$	11.59$^+$	1.47*
15	2.67$^+$	6.05$^+$	1.55$^+$	12.94$^+$	-1.59
22	1.48$^+$	-14.72	-21.69	26.20$^+$	19.51$^+$
AVERAGE	**4.49$^+$**	**1.25**	**-6.47**	**16.91$^+$**	**6.46$^+$**

<u>Note</u>: A negative value represents the opposite motion (i.e. external rotation). Those with a (*) represent a value which is significant to one standard deviation. Those with a (+) are significant to two standard deviations.

Table 4.4: Results representing the change in plantarflexion angle for the pes cavus foot group while wearing the foam soft orthotic. All entries in degrees.

Foam Soft Orthotic: Plantarflexion

Subject#	cal wrt tibfib	nav wrt cal	cub wrt cal	nav wrt tibfib	cub wrt tibfib
9	-4.92	12.51$^+$	18.03$^+$	-18.96	10.88$^+$
15	-30.49	-75.21	-40.70	-18.13	26.13$^+$
22	1.14	-10.21	13.26$^+$	16.75$^+$	-7.58
AVERAGE	**-11.42**	**-24.30**	**-3.14**	**-6.78**	**9.81$^+$**

<u>Note</u>: A negative value represents the opposite motion (i.e. dorsiflexion). Those with a (*) represent a value which is significant to one standard deviation. Those with a (+) are significant to two standard deviations.

Table 4.5: Results representing the change in the inversion angle for the pes cavus foot group while wearing the foam soft orthotic. All entries in degrees.

Foam Soft Orthotic: Inversion

Subject#	cal wrt tibfib	nav wrt cal	cub wrt cal	nav wrt tibfib	cub wrt tibfib
9	-16.90	23.79$^+$	-7.63	-39.44	15.24$^+$
15	3.41$^+$	14.05$^+$	-7.21	-8.06	6.17*
22	-1.85	-11.77	15.59$^+$	8.02$^+$	-1.66
AVERAGE	**-5.11**	**8.69$^+$**	**0.25**	**-13.16**	**6.59$^+$**

<u>Note</u>: A negative value represents the opposite motion (i.e. eversion). Those with a (*) represent a value which is significant to one standard deviation. Those with a (+) are significant to two standard deviations.

Table 4.6: Results representing the change in the internal rotation angle for the pes cavus foot group while wearing the foam soft orthotic. All entries in degrees.

Foam Hard Orthotic: Internal Rotation

Subject#	cal wrt tibfib	nav wrt cal	cub wrt cal	nav wrt tibfib	cub wrt tibfib
9	3.29$^+$	9.90$^+$	-4.68	-1.14	7.89$^+$
15	1.33	1.45	-0.71	-4.63	3.61$^+$
22	-1.57	-5.86	-4.01	17.16$^+$	3.95*
AVERAGE	**1.02**	**1.83**	**-3.13**	**3.79**	**5.15$^+$**

Note: A negative value represents the opposite motion (i.e. external rotation). Those with a (*) represent a value which is significant to one standard deviation. Those with a (+) are significant to two standard deviations.

Table 4.7: Results representing the change in plantarflexion angle for the pes cavus foot group while wearing the foam soft orthotic. All entries in degrees.

Foam Hard Orthotic: Plantarflexion

Subject#	cal wrt tibfib	nav wrt cal	cub wrt cal	nav wrt tibfib	cub wrt tibfib
9	-2.05	-2.09	-30.60	0.64	5.57$^+$
15	-27.18	-87.12	10.73$^+$	-3.03	23.88$^+$
22	-2.56	-8.55	6.88	8.38$^+$	-8.65
AVERAGE	**-10.60**	**-32.59**	**-4.33**	**1.99**	**6.93$^+$**

Note: A negative value represents the opposite motion (i.e. dorsiflexion). Those with a (*) represent a value which is significant to one standard deviation. Those with a (+) are significant to two standard deviations.

Table 4.8: Results representing the change in the inversion angle for the pes cavus foot group while wearing the foam soft orthotic. All entries in degrees.

Foam Hard Orthotic: Inversion

Subject#	cal wrt tibfib	nav wrt cal	cub wrt cal	nav wrt tibfib	cub wrt tibfib
9	-9.67	16.83$^+$	17.14$^+$	-26.02	11.97$^+$
15	-2.18	1.39$^+$	1.98$^+$	-1.59	2.92$^+$
22	6.07$^+$	-8.78	-0.66	10.61$^+$	8.96$^+$
AVERAGE	**-1.93**	**3.15$^+$**	**6.15$^+$**	**-5.66**	**7.95$^+$**

Note: A negative value represents the opposite motion (i.e. eversion). Those with a (*) represent a value which is significant to one standard deviation. Those with a (+) are significant to two standard deviations.

Table 4.9: Results representing inversion angle changes in the planus foot while wearing the foam soft orthotic. All entries in degrees.

Foam Soft Orthotic: Internal rotation

Subject#	cal wrt tibfib	nav wrt cal	cub wrt cal	nav wrt tibfib	cub wrt tibfib
5	2.46*	9.15$^+$	-5.48	-25.27	17.11$^+$
16	14.02$^+$	30.87$^+$	12.59$^+$	-33.05	-2.16
19	22.16$^+$	10.35$^+$	5.68$^+$	5.09$^+$	8.10$^+$
AVERAGE	**12.88**$^+$	**16.79**$^+$	**4.27**$^+$	**-17.74**	**7.68**$^+$

Note: A negative value represents the opposite motion (i.e. external rotation). Those with a (*) represent a value which is significant to one standard deviation. Those with a (+) are significant to two standard deviations.

Table 4.10: Results representing plantarflexion angle changes in the planus foot while wearing the foam soft orthotic. All entries in degrees.

Foam Soft Orthotic: Plantarflexion

Subject#	cal wrt tibfib	nav wrt cal	cub wrt cal	nav wrt tibfib	cub wrt tibfib
5	3.61$^+$	0.29	0.54	17.41$^+$	-11.02
16	0.45	18.98$^+$	-2.52	-12.75	-5.02
19	-3.01	-9.85	15.08$^+$	19.96$^+$	6.19$^+$
AVERAGE	**0.35**	**3.14***	**4.37***	**8.21**$^+$	**-3.28**

Note: A negative value represents the opposite motion (i.e. dorsiflexion). Those with a (*) represent a value which is significant to one standard deviation. Those with a (+) are significant to two standard deviations.

Table 4.11: Results representing inversion angle changes in the planus foot while wearing the foam soft orthotic. All entries in degrees.

Foam Soft Orthotic: Inversion

Subject#	cal wrt tibfib	nav wrt cal	cub wrt cal	nav wrt tibfib	cub wrt tibfib
5	9.94$^+$	1.35	-1.81	10.81$^+$	12.39$^+$
16	9.29$^+$	-11.56	7.18$^+$	22.49$^+$	4.17*
19	-11.45	-1.12	-4.26	-5.58	4.92$^+$
AVERAGE	**2.59**$^+$	**-3.78**	**0.37**	**9.24**$^+$	**7.16**$^+$

Note: A negative value represents the opposite motion (i.e. eversion). Those with a (*) represent a value which is significant to one standard deviation. Those with a (+) are significant to two standard deviations.

Table 4.12: Results representing inversion angle changes in the planus foot while wearing the foam hard orthotic. All entries in degrees.

Foam Hard Orthotic: Internal Rotation

Subject#	cal wrt tibfib	nav wrt cal	cub wrt cal	nav wrt tibfib	cub wrt tibfib
5	4.21^{+}	21.08^{+}	1.42	-58.58	8.99^{+}
16	7.62^{+}	26.54^{+}	10.11^{+}	-31.24	3.68^{+}
19	21.60^{+}	24.41^{+}	10.18^{+}	-24.71	4.18^{+}
AVERAGE	$\mathbf{11.14^{+}}$	$\mathbf{24.01^{+}}$	$\mathbf{7.23^{+}}$	**-38.18**	$\mathbf{5.62^{+}}$

Note: A negative value represents the opposite motion (i.e. external rotation). Those with a (*) represent a value which is significant to one standard deviation. Those with a (+) are significant to two standard deviations.

Table 4.13: Results representing plantarflexion angle changes in the planus foot while wearing the foam hard orthotic. All entries in degrees.

Foam Hard Orthotic: Plantarflexion

Subject#	cal wrt tibfib	nav wrt cal	cub wrt cal	nav wrt tibfib	cub wrt tibfib
5	0.68	-10.93	-8.09	30.00^{+}	-5.00
16	-2.99	6.04^{+}	-4.25	-7.23	-1.38
19	1.85^{+}	-3.19	26.40^{+}	15.60^{+}	14.00^{+}
AVERAGE	**-0.15**	**-2.69**	**4.69***	$\mathbf{12.79^{+}}$	**2.54***

Note: A negative value represents the opposite motion (i.e. dorsiflexion). Those with a (*) represent a value which is significant to one standard deviation. Those with a (+) are significant to two standard deviations.

Table 4.14: Results representing inversion angle changes in the planus foot while wearing the foam hard orthotic. All entries in degrees.

Foam Hard Orthotic: Inversion

Subject#	cal wrt tibfib	nav wrt cal	cub wrt cal	nav wrt tibfib	cub wrt tibfib
5	9.60^{+}	-3.94	3.84	18.17^{+}	7.42^{*}
16	3.80^{+}	-12.62	1.66	19.05^{+}	-0.57
19	-12.29	0.56*	-16.23	-1.28	-0.70
AVERAGE	**0.37**	**-5.33**	**-3.58**	$\mathbf{11.98^{+}}$	**2.05***

Note: A negative value represents the opposite motion (i.e. eversion). Those with a (*) represent a value which is significant to one standard deviation. Those with a (+) are significant to two standard deviations.

4.4 DISCUSSION

Many symptomatic individuals are diagnosed with a foot in the pes planus or pes cavus category. Malalignment in the foot is assumed to be the cause of pain treatable by a foot orthotic insole. The ability of a custom-made orthotic to realign bones in the foot has never been measured beyond a qualitative analysis, or when quantitatively measured with unrealistic assumptions such as treating foot as a rigid segment. The International Society of Biomechanics (ISB) has defined bone coordinate systems to allow researchers to measure clinically significant joint motions. The consistency of coordinate systems allows for results to be comparable across laboratories around the world (Wu *et al.,* 2002). These definitions have already been defined and accepted as clinically relevant motions by ISB. For the foot the relevant motion occurs with the calcaneus and the tibia/fibula complex (Wu *et al.,* 2002). The method used to obtain the joint coordinate systems in this study, are explained in detail in chapter 1, and were calculated in such a way to result in a coordinate system that matched the one accepted by ISB as close as possible. Figure 4.9, figure 4.10, and figure 4.11 were created to compare two orthotic types (foam soft and foam hard) as they affect the pes cavus and pes planus populations for the internal rotation, plantarflexion, and inversion planes of motion respectively. The overall average change in the internal rotation angle suggests that the pes planus population has a greater degree of expected change (figure 4.9). The overall average change in the plantarflexion angle suggests that the pes planus population has a greater degree of reducing dorsiflexion, however, the pes cavus group

showed a larger degree of change (figure 4.10). The average change for the inversion angle change has the least difference between foot types (figure 4.11).

The average effect caused by the foam casted orthotics for all foot types were tested for statistical significance using a repeated measures ANOVA. While wearing the foam soft orthotic no significant findings were found in the pes planus group in the internal rotation (p=0.153), plantarflexion (p=872) and inversion (p=0.747) plane of motion. While wearing the foam hard orthotic no significant findings were found in the pes planus group in the internal rotation (p=0.171), plantarflexion (p=926), and inversion (p=0.960) plane of motion. The lack of a significant finding for the pes planus group could be caused by the sample size being underpowered for the trend to be seen. It was expected that an overall decrease in pronation would be found during orthotic wear in the pes planus group with a larger sample size. The pes cavus group did not experience a significant change while wearing the foam soft orthotic for the internal rotation (p=0.250), plantarflexion (p=0.360), and inversion (p=0.490) plane of motion. The pes cavus group did not experience a significant change in motion while wearing the foam hard orthotic in the internal rotation (p=0.960), plantarflexion (p=0.330), and inversion (p=0.713) plane of motion. The remainder of the discussion will provide an overview of the impact orthotics had on the navicular and cuboids motion.

To determine if a condition had an effect on an individual level the concept of the normal distribution was used. Natural variance of several variables has the tendency to follow the normal distribution curve. Meaning that 68% of all cases will fit within one (1) standard deviation (SD), and 99.5% of all cases will fit within two (2) SD (Norman and

Streiner, 2003; Portney and Watkins, 2000). Therefore when deciding significance in the results those found to have one standard deviation of significance were represented with an asterisk (*) and those with two standard deviations of significance were represented with a plus (+) sign.

The navicular and cuboids motion was summarized in table 4.3, table 4.4, and table 4.5 for internal rotation, plantarflexion and inversion respectively for the pes cavus population wearing the foam soft orthotic. The navicular and cuboids motion was summarized in table 4.6, table 4.7, and table 4.8 for internal rotation, plantarflexion and inversion respectively for the pes cavus population wearing the foam hard orthotic. The change associated for the pes cavus population while wearing the foam soft orthotic experienced by the navicular with respect to the calcaneus included an increase in the inversion (>2SD) angle (table 4.5). The pes cavus population experienced an increase in the inversion angle (>2SD) while wearing the foam hard orthotic (table 4.8). The navicular with respect to the tibia/fibula demonstrated an increase in internal rotation (>2SD) while wearing the foam soft orthotic (table 4.3) for the pes cavus population. An increase in the internal rotation (>1SD) was experienced by the pes cavus population while wearing the foam hard orthotic (table 4.6) for the navicular with respect to the tibia/fibula.

The cuboid with respect to the calcaneus experienced no significant changes in alignment while wearing the foam soft orthotic in the pes cavus population. The pes cavus population experienced an increase in inversion (>2SD) while wearing the foam hard orthotic (table 4.8) for the cuboid with respect to the calcaneus. The pes cavus

population experienced an increase in internal rotation (>2SD), plantarflexion (>2SD), and inversion (>2SD) while wearing the foam soft orthotic for the cuboid with respect to the tibia/fibula (table 4.3, table 4.4 and table 4.5 respectively). The pes cavus population experienced an increase in internal rotation (>2SD), plantarflexion (>2SD), and inversion (>2SD) while wearing the foam hard orthotic (table 4.6, table 4.7 and table 4.8 respectively).

The navicular and cuboids motion was summarized in table 4.9, table 4.10, and table 4.11 for internal rotation, plantarflexion and inversion respectively for the pes planus population wearing the foam soft orthotic. The navicular and cuboids motion was summarized in table 4.12, table 4.13, and table 4.14 for the pes planus population wearing the foam soft orthotic in the three planes of motion: internal rotation, plantarflexion and inversion respectively. The calcaneus motion with respect to the tibia/fibula is also present so it's possible to see how the motions differ. The navicular with respect to the calcaneus experienced an increase in the internal rotation (>2SD) and plantarflexion (>1SD) plane for the pes planus population wearing the foam soft orthotic (table 4.9 and table 4.10 respectively). The pes planus population experienced an increase in the internal rotation angle (>2SD) for the navicular with respect to the calcaneus while wearing the foam hard orthotic (table 4.12). The navicular with respect to the tibia/fibula demonstrated an increase in plantarflexion (>2SD), and inversion (>2SD) while wearing the foam soft orthotic (table 4.10 and table 4.11 respectively). The navicular with respect to the tibia/fibula experienced an increase in plantarflexion

(>2SD), and inversion (>2SD) for the pes planus population while wearing the foam hard orthotic (table 4.13 and table 4.14 respectively).

The cuboid motion with respect to the calcaneus experienced an increase in internal rotation (>2SD), and plantarflexion (>1SD) while wearing the foam soft orthotic for the pes planus population. The cuboid motion with respect to the calcaneus experienced an increase in internal rotation (>2SD), and plantarflexion (>1SD) while wearing the foam hard orthotic for the pes planus population. The cuboid motion with respect to the tibia/fibula experienced an increase in internal rotation (>2SD), and inversion (>2SD) while wearing the foam soft orthotic for the pes planus population. The cuboid with respect to the tibia/fibula experienced an increase in internal rotation (>2SD), plantarflexion (>1SD), and inversion (>1SD) while wearing the foam hard orthotic for the pes planus population.

Although each participant in this study reacted with different outcomes it is evident that foam casted orthotics do change the alignment in the foot compared to the individuals barefoot condition. It was found that the planus group did have a higher degree of change overall, although this value was not found to be significant in all three planes of motion. The lack of significant findings is partly due to the small sample size and of course that human subjects all contain slightly different foot anatomy.

4.5 REFERENCES

Allen, A.-M. V. (2009). Development and Validation of a Markerless Radiostereometric Analysis (RSA) System. University of Western Ontario.

Kedgley, A. (2009). *Development of a fluoroscopic radiostereometric analysis system with an application to glenohumeral joint kinematics*. University of Western Ontario.

Kedgley, A. E., & Jenkyn, T. R. (2009). RSA calibration accuracy of a fluoroscopy-based system using nonorthogonal images for measuring functional kinematics. *Medical Physics*, *36*(7), 3176.

Kedgley, A. E., Birmingham, T. B., & Jenkyn, T. R. (2009). Comparative accuracy of radiostereometric and optical tracking systems. *Journal of Biomechanics*, *42*(9), 1350-1354.

Nordin, M., & Frankel, V. H. (2001). *Basic Biomechanics of the Musculoskeletal System*. (D. Leger, Ed.) (3rd ed., pp. 178-190). Baltimore: Lippincott Williams & Wilkins.

Norman, G. R., & Streiner, D. L. (2003). *Pretty Darned Quick Statistics* (3rd ed., pp. 5-52). Hamilton: BC Decker Inc.

Portney, L. G., & Watkins, M. P. (2000). *Foundations of Clinical Research: Applications to Practice* (2nd ed.). Upper Saddle River, New Jersey, USA: Prentice-Hall Inc.

Rougée, A., Picard, C. L., Trousset, Y. L., & Ponchut, C. (1993a). Geometrical calibration for 3D x-ray imaging. *Proceedings of SPIE*, *1897*, 161-169.

Rougée, A., Picard, C., Ponchut, C., & Trousset, Y. (1993b). Geometrical calibration of X-ray imaging chains for three-dimensional reconstruction. *Computerized medical imaging and graphics the official journal of the Computerized Medical Imaging Society*, *17*(4-5), 295-300.

Wu, G., Siegler, S., Allard, P., Kirtley, C., Leardini, A., Rosenbaum, D., Whittle, M., *et al.* (2002). ISB recommendation on definitions of joint coordinate system of various joints for the reporting of human joint motion--part I: ankle, hip, and spine. International Society of Biomechanics. *Journal of Biomechanics*, *35*(4), 543-548.

Yagerman, S. E., Cross, M. B., Positano, R., & Doyle, S. M. (2011). Evaluation and treatment of symptomatic pes planus. *Current opinion in pediatrics*, *23*(1), 60-7.

CHAPTER 5- THE EFFECT ON PRONATION WHILE WEARING FOAM CASTED ORTHOTIC IN THE NORMAL, PES PLANUS, AND PES CAVUS FOOT USING THREE DIFFERENT MEASUREMENT TECHNIQUES.

OVERVIEW: This chapter describes the effect of foam casted orthotics on the normal, pes planus, and pes cavus foot measured using a static method compared to the corresponding dynamic condition measurements conducted in the previous studies. A comparison of the two-dimensional measurement to the three-dimensional corresponding measurement is conducted to determine if the result obtained provides a similar change in bone alignment. Using bi-planar x-ray fluoroscopy an individual's static image is compared to the corresponding midstance image. The purpose of this study is to determine if a static image obtains similar results to a dynamic sequence of images collected during midstance. The second reason for this study was to determine if a two-dimensional measurement would obtain similar results when compared to the three-dimensional technique.

5.1 INTRODUCTION

Clinically, bone alignment in the foot can be estimated using optical motion capture, video analysis, magnetic resonance imaging (MRI), x-ray, computed

tomography (CT) or visually (Mattingly *et al.,* 2006). Pronation and supination of the foot arises from the motion of the bones within the foot. During gait the foot rolls inwards and comes into complete contact with the ground. The rolling of the foot distributes the impact and is critical to shock absorption. This inward roll is often called pronation. Clinically measuring the degree of pronation an individual experiences is important for footwear choice and orthotic use. However, using optical motion tracking the motion of the foot is not accurately measured. This is because the foot is treated as a single rigid segment and tracked with only three reflective markers when common marker sets such as Cleveland Clinic and Helen Hayes are used. Many of the bony landmarks of interest in the foot cannot be tracked independently with a reflective bead. It is also a challenge to mark bony landmarks with skin-mounted markers when wearing a shoe. Therefore it is difficult to quantify changes in foot bone alignment accurately with different footwear or orthotics using optical motion capture.

Hindfoot motion has been measured previously using goniometers (Inman, 1991; Kitaoka *et al.,* 1995), magnetic resonance imaging (MRI) (Mattingly *et al.,* 2006), and optical motion capture (Kedgley, 2009; Tulchin *et al.,* 2010). Goniometers and MRI devices can only be used during static scenarios. Static measurements have never been validated at the bone level to mimic the motion of the foot during dynamic conditions.

Fluoroscopy has been proven to be a feasible method to measure kinematics in the shoulder, knee and foot (Kedgley, 2009; Li *et al.,* 2008). Fluoroscopy has the advantage over optical motion capture in that x-ray imaging techniques can see bone kinematics through footwear. Fluoroscopy removes the need to modify footwear with

holes to attach skin mounted markers. Two dimensional (2D) imaging techniques capture kinematics using only one plane of motion. Previous studies have measured the sagittal plane motion of the human arch (Wearing *et al.,* 1998), and anterior-posterior x-rays have been used to determine arch height (Murley *et al.,* 2009). When measuring foot kinematics using a 2D radiographic approach standardization in the devices positioning becomes crucial if individuals are to be compared as well as conditions within the same individual. The location of the x-ray source in a 2D analysis can affect the angles measured due to out of plane movement such as rotational motion if using the lateral view (Brage *et al.,* 1994). 2D analysis is computationally much faster and easier to automate by comparison to three-dimensional (3D) techniques. The analysis has never been compared to the results of a corresponding 3D model analysis at the bone level in order to quantify its degree of accuracy.

Standard RSA is based on tracking markers embedded in the bone which can then be related to anatomical landmarks using bone models created from imaging techniques such as MRI or CT. Markerless RSA is performed by matching 3D computer bone models to the corresponding outline on the radiographs (Fox *et al.,* 2011). Markerless RSA has the advantage over standard RSA in that tantalum beads do not need to be implanted in the bones. The use of a CT scan to obtain bone models in addition to bi-planar x-ray fluoroscopy was used to quantify bone motion in this study.

Foot orthotics are commonly used to manage a range of lower limb overuse conditions (Landorf and Keenan, 2000). The aim of a foot orthotic insole is to realign the skeletal structures, alter movement patterns of the lower extremity and reduce painful

symptoms in the patient (Murley *et al.,* 2010; Collins *et al.,* 2007). The pes cavus population is defined as having a high arch in the foot and the pes planus population is defined as having a low arch in the foot. Orthotic devices can either be custom-made or purchased 'off-the-shelf'. Currently, there are three techniques for moulding an orthotic, plaster wrap, foam box, and the application of laser technology. The plaster casting technique has the patient lie prone in a figure four position during the process. A negative impression is taken while the patient's foot is locked in the subtalar neutral position. Laser scanning is a reverse engineering technique which models the foot either weight-bearing or nonweight-bearing to cast an orthotic. This study focuses on the foam box technique which has the practitioner guide the patient's foot into a foam tray that takes a partial weight-bearing negative impression of the foot while in the subtalar neutral position (Laughton *et al.,* 2002). The foam box technique eliminates the drying process required during the plaster casting method.

The purpose of this study is: (1) to determine if there is a difference between measuring hindfoot alignment during static versus dynamic weight-bearing conditions, and (2) to determine if a two-dimensional measure results in the same overall functional conclusions compared to the true 3D method of fluoroscopic bi-planar radiostereometric analysis. It was hypothesized that the dynamic weight-bearing condition would give a different hindfoot angulation compared to the corresponding static condition. It was also hypothesized that the two-dimensional measurement would not lead to the same functional conclusion about hindfoot behaviour compared to the 3D measurement.

5.2 METHODS

Ethics approval was obtained from the Health Sciences Research Ethics Board at The University of Western Ontario prior to the commencement of any data collection (Appendix A). The platform described previously (section 2.2.1) was used for the purpose of this study and allowed the test subjects to walk through the capture volume of the two fluoroscopes.

5.3 DATA COLLECTION

Four (4) normal arched, three (3) pes planus, and three (3) pes cavus volunteers were recruited to participate in this study. Normal arched volunteers were screened for pain and deformities. Those found with either were excluded from the study. The pes planus and pes cavus groups were not screened for minor pain or foot deformities provided these conditions did not affect their walking gait. An exclusion criterion for all three groups was a history of previous fractures anywhere in the lower extremity. All volunteers were fitted with two pairs of custom-made orthotics: (1) a 4mm plastazote (soft) and (2) a 3mm RCH-500 (rigid) foam box casted orthotic as per usual clinical practice. Orthotics were fitted by the same Canadian certified pedorthist at the Fowler Kennedy Sport Medicine Clinic, London, ON, Canada. When the orthotics were completed and ready for wear the volunteers returned for the fluoroscopic RSA testing session.

During the fluoroscopic testing session, the volunteer wore a wrap-around leaded apron and kilt including a thyroid collar to protect their upper and lower body

(figure 5.1). This ensured that the primary x-ray beam only exposed the foot and ankle and that no secondary scatter was absorbed by the body.

Figure 5.1: Platform and wrap-around leaded clothing.

5.3.1   DYNAMIC IMAGE COLLECTION

The images used for the dynamic portion of this study were collected during study 2 and study 4 of this thesis. Specifically, please refer to steps for the normal population outlined in section 2.2.2.1, section 2.2.2.3, and section 2.2.2.4 for the barefoot, foam soft orthotic and foam hard orthotic conditions respectively. Please refer to the steps outlined for the pes cavus and pes planus groups in section 4.2.2.1, section 4.2.2.2, and section 4.2.2.3 for the barefoot, foam soft, and foam hard orthotic conditions respectively.

5.3.2   STATIC IMAGE COLLECTION

5.3.2.1 BAREFOOT

Each volunteer was asked to stand on the platform barefoot. The volunteer was asked to place their left foot in the views of the two fluoroscopes. An x-ray technician

ensured the two views were optimal of the bony structures of interest (i.e. the entire hindfoot including the tarsal bones) was on the fluoroscopes screen display. The images were then captured and stored on the PC in the adjacent control room. The x-ray technician outlined the location of the volunteer's foot as a target footprint for future trials.

5.3.2.2   FOAM SOFT ORTHOTIC

Each volunteer was asked to wear the neutral cushion running shoe (New Balance, model 882) provided with the foam soft orthotic insole inserted. The volunteer was asked to place their left foot in the views of the two fluoroscopes as outlined on the platform by the technician. The x-ray technician ensured a complete view the structures of interest (i.e. the entire hindfoot and the tarsus) was on the fluoroscopes displays. The images were captured and stored on the PC in adjacent control room.

5.3.2.3   FOAM HARD ORTHOTIC

Each volunteer was asked to wear the neutral cushion running shoe (New Balance, model 882) provided with the foam hard orthotic insole inserted. The volunteer was asked to place their left foot in the view of the fluoroscope as outlined on the platform. The x-ray technician ensured a complete view of structures of interest (i.e. the entire hindfoot including the tarsus) was on the fluoroscopes displays. The image was captured and stored on the PC in adjacent control room.

5.3.3 DATA ANALYSIS

5.3.3.1 THREE-DIMENSIONAL ANALYSIS

The calibration process for the three-dimensional (3D) analysis can be found in section 2.2.3 of this thesis. The end result after following the calibration process outlined in chapter 2 will accurately produce the experimental setup in the virtual environment.

Following the calibration process 3D bone models are created using OsiriX-DICOM Viewer (Advanced Open-Source PACS Workstation DICOM Viewer, Antoine Rosset, USA). Detailed steps describing how to segment the bones of interest to create 3D bone models are provided in Appendix B. The models are then converted into a triangular mesh of file format stereolithography (.stl) for the image processing software program Rhinoceros to be able to recognize and use the files (Rhinoceros; Robert McNeel & Associates, Seattle, WA, USA). The landmarks of interest as described in chapter 1, section 1.6.1, were marked on each of the bones.

Once the 3D bone models are created and the calibration process is done, the matching process can be completed for the various conditions imaged during data collection. Details regarding the matching process are found in section 2.5. Once the matching process is complete the location of the bony landmarks are exported using the Rhinoscript program titled "ExportPoints" (Allen, 2009). The custom-written kinematics program titled Calcaneuspronation_kinematics.m (Appendix C) is used to calculate the change in pronation as represented by the three planes of motion: internal rotation, plantarflexion, and inversion. The results outputted from this custom-written kinematics

program will be used to compare the change in alignment while wearing the foam soft and form hard orthotics measured during static and dynamic trial conditions.

An overall 3D angle was calculated for comparative purposes with the 2D analysis to be conducted as described below. This was as completed by using equation 5.1 at the individual level.

$$\textbf{Overall 3D angle} = \sqrt{(\textbf{internal rotation}(\gamma))^2 + (\textbf{plantarflexion}(\alpha))^2 + (\textbf{inversion}(\beta))^2} \qquad \textbf{(Eq. 5.1)}$$

5.3.3.2 TWO-DIMENSIONAL ANALYSIS

Only one of the two fluoroscope images was used during the 2D portion of the analysis. Specifically, the left foot is analyzed from an oblique, dorsal-medial to plantar-lateral view in this study (figure 5.2). Each image was processed using custom-written software (MATLAB; Mathworks Inc., Natick, MA). The first program, Find_Points.m (Appendix C) determined the location of the landmarks. When using the Find_Points.m program the lateral and medial aspects of Chopart's line were identified (figure 5.2). A third point was used to create a vector that was tangent to the lateral portion of the calcaneus as drawn in figure 5.2. A second custom-written program, Angle_Calc.m (Appendix C), calculated the angle (θ) seen in figure 5.2 using the landmark locations as outputted from the Find_Points.m program. The angle between these lines was defined as the amount of calcaneal pronation calculated in 2D. The output value is then compared to the barefoot (baseline) condition to determine the effect of the different shoe conditions when measured using a 2D approach. An increase in the angle (θ)

represents an increase in pronation and, a decrease represents an increase in supination.
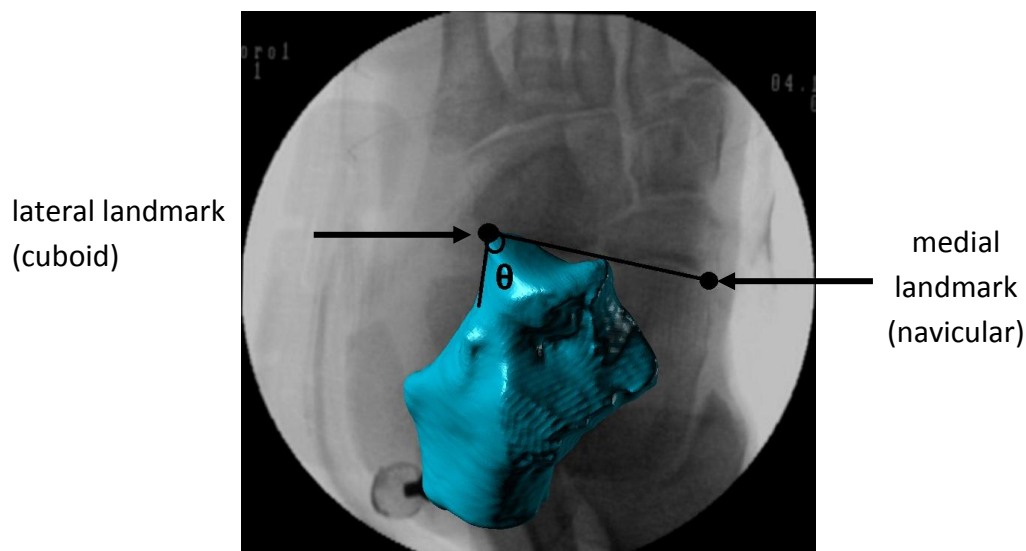
Figure 5.2: Calcaneus pronation angle (θ), lateral and medial landmark.

Using the results outputted from the 2D custom-written pronation angle program, Angle_Calc.m, a comparison of the 3D calculation can be completed (Appendix C). The 2D results are compared to the change in the overall 3D angle while the individual wears the custom-made orthotic during gait specifically at midstance. The 2D results are compared to the change associated with each plane of motion (internal rotation, plantarflexion, and inversion) experiences while the individual wears the custom-made orthotic during gait, specifically at midstance. A repeated measures analysis of variance (ANOVA) using SPSS was produced to test for differences between measurement conditions (SPSS; IBM Corporation, Armonk, NY, USA). A probability level of $p < 0.05$ was used to indicate significance. All degrees of significance are reported, however only significant outputs are found in Appendix F. Bland-Altman plots were created to compare the overall 3D angle measurement to the 2D pronation angle to

determine if the measurement technique agrees sufficiently to warrant using 2D in place of the 3D technique.

5.4 RESULTS

The internal rotation angle while barefoot was measured during a static trial and compared to a dynamic trial for each subject individually (figure 5.3). The plantarflexion angle while barefoot was measured during a static trial and compared to the corresponding dynamic trial at midstance for each subject individually (figure 5.4). The inversion angle while barefoot was measured during a static trial and compared to the corresponding dynamic trial for each subject individually (figure 5.5). A Bland-Altman plot was created to assess agreement between the barefoot static condition and the corresponding dynamic condition as measured for internal rotation, plantarflexion, and inversion in figure 5.6, figure 5.7, and figure 5.8 respectively.

	C	C	C	N	N	N	N	P	P	P
Static	33.71	26.39	42.97	13.25	48.06	23.66	24.31	25.89	22.20	26.22
Dynamic	26.37	23.17	41.21	15.47	46.47	47.68	31.20	26.67	8.60	23.62
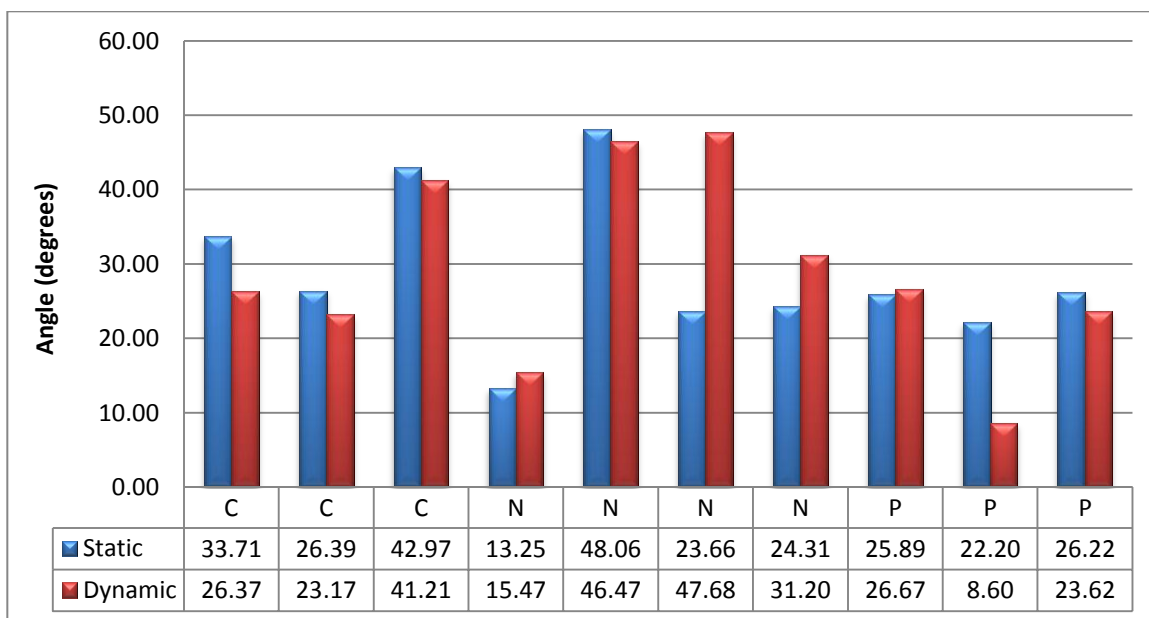
Figure 5.3: Individual internal rotation angle for the barefoot condition when measured standing statically or dynamically at midstance.

	C	C	C	N	N	N	N	P	P	P
Static	165.30	140.13	150.42	190.43	151.17	168.27	169.61	172.27	174.33	175.77
Dynamic	158.06	170.32	157.86	183.09	148.79	155.63	164.20	175.46	178.17	168.17
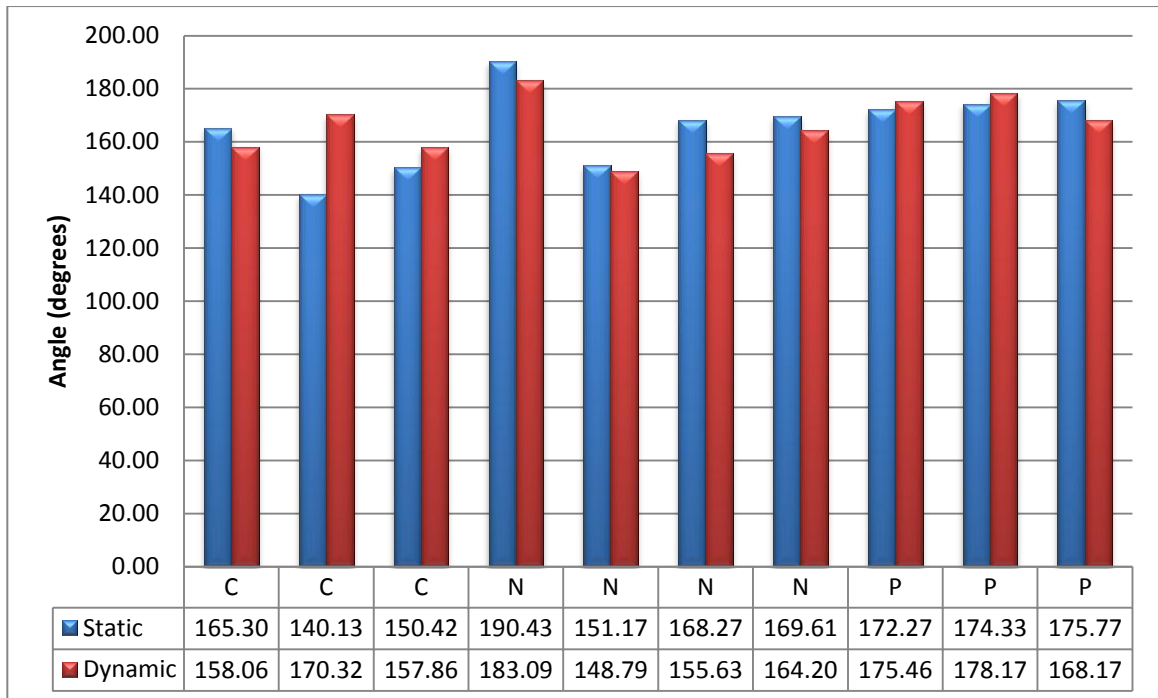
Figure 5.4: Individual plantarflexion angle for the barefoot condition when measured standing statically compared to the dynamic image at midstance.

	C	C	C	N	N	N	N	P	P	P
Static	164.28	164.99	166.44	169.49	145.38	167.42	160.57	150.49	155.96	152.34
Dynamic	168.79	169.28	157.79	166.70	150.75	157.79	152.06	142.70	155.85	154.53
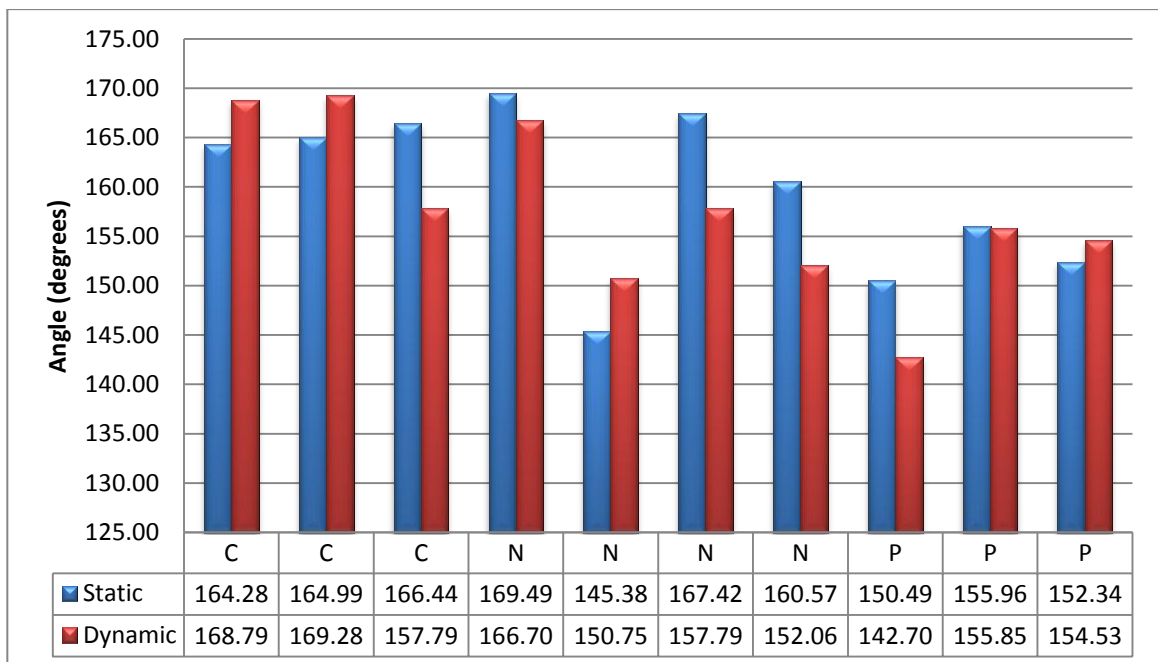
Figure 5.5: Individual inversion angle for the barefoot condition when measured standing compared to the dynamic image at midstance.
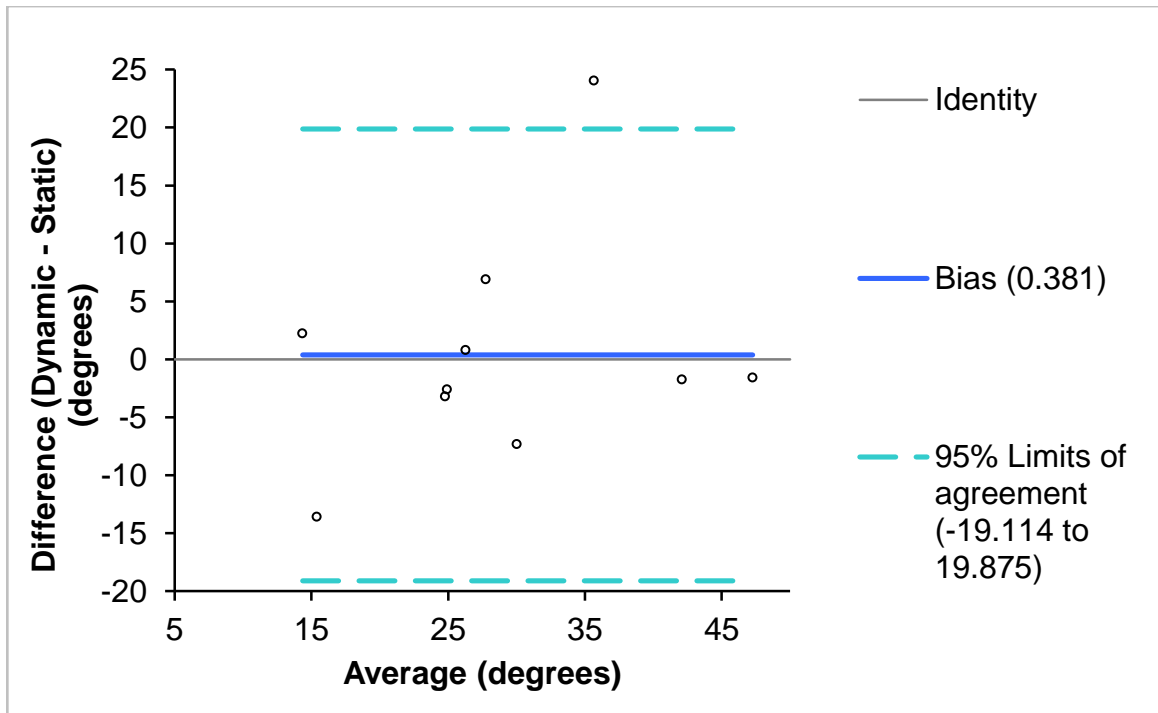
Figure 5.6: Bland-Altman plot for the static angle measurement compared to the dynamic angle for the barefoot condition for internal rotation.
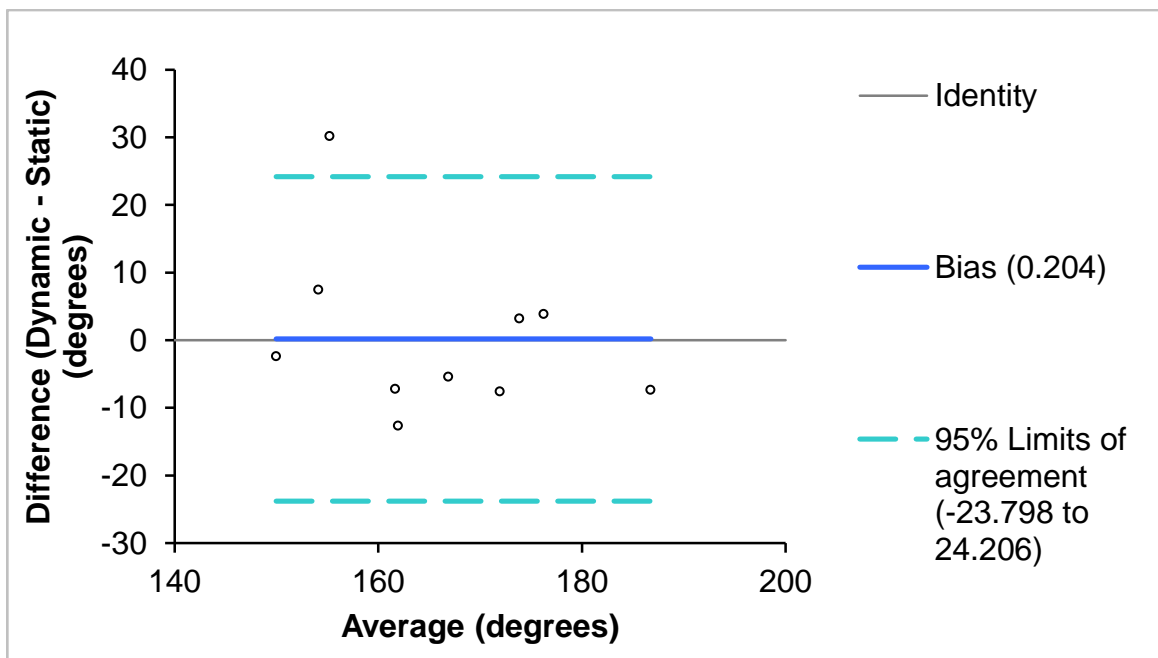
Figure 5.7: Bland-Altman plot for the static angle measurement compared to the dynamic angle for the barefoot condition for plantarflexion.
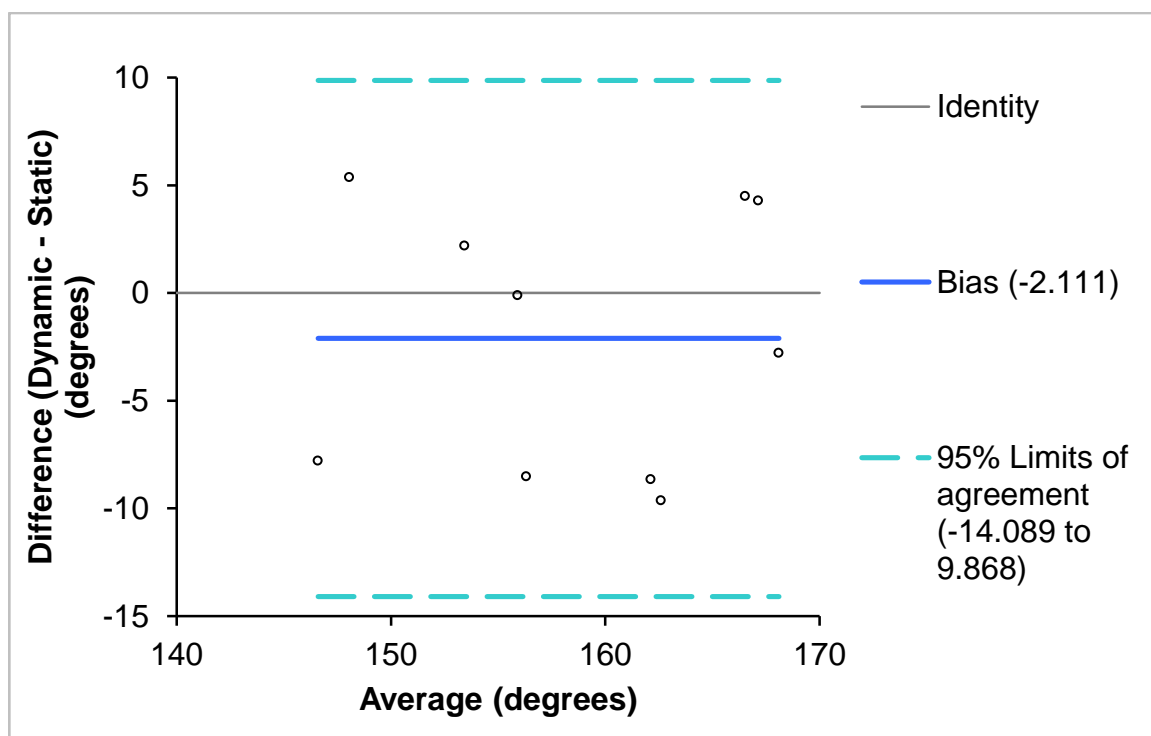
Figure 5.8: Bland-Altman plot for the static angle measurement compared to the dynamic angle for the barefoot condition for inversion.

The change in pronation while wearing the foam soft orthotic as measured in two-dimensions is shown graphically as compared with the overall 3D angle in figure 5.9. A Bland-Altman plot was created to assess agreement between the 2D pronation angle and the overall 3D angle as measured for the foam soft orthotic condition in figure 5.10. The change in pronation while wearing the foam soft orthotic as measured in two-dimensions (figure 5.2) is shown graphically as compared with the with the change associated with each plane of motion: internal rotation, plantarflexion, and inversion in figure 5.11, figure 5.12 and figure 5.13 respectively.
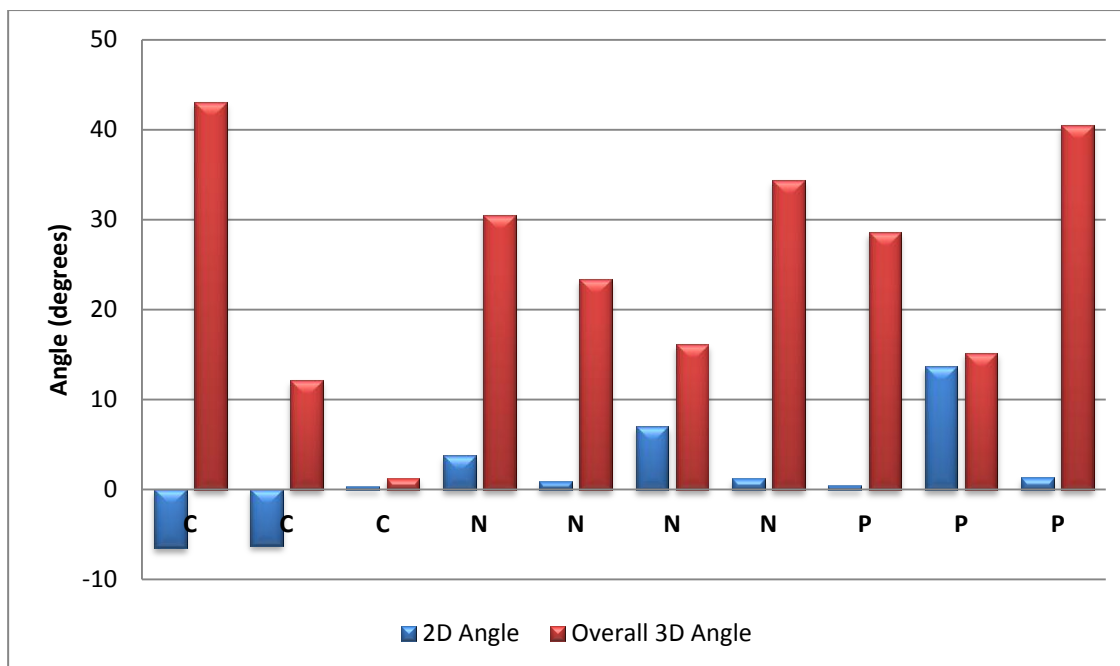
Figure 5.9: The change in pronation calculated with wearing the foam soft orthotic compared to the barefoot condition. The measurement was done using the 2D method (figure 5.2) and the change associated with the overall 3D angle.
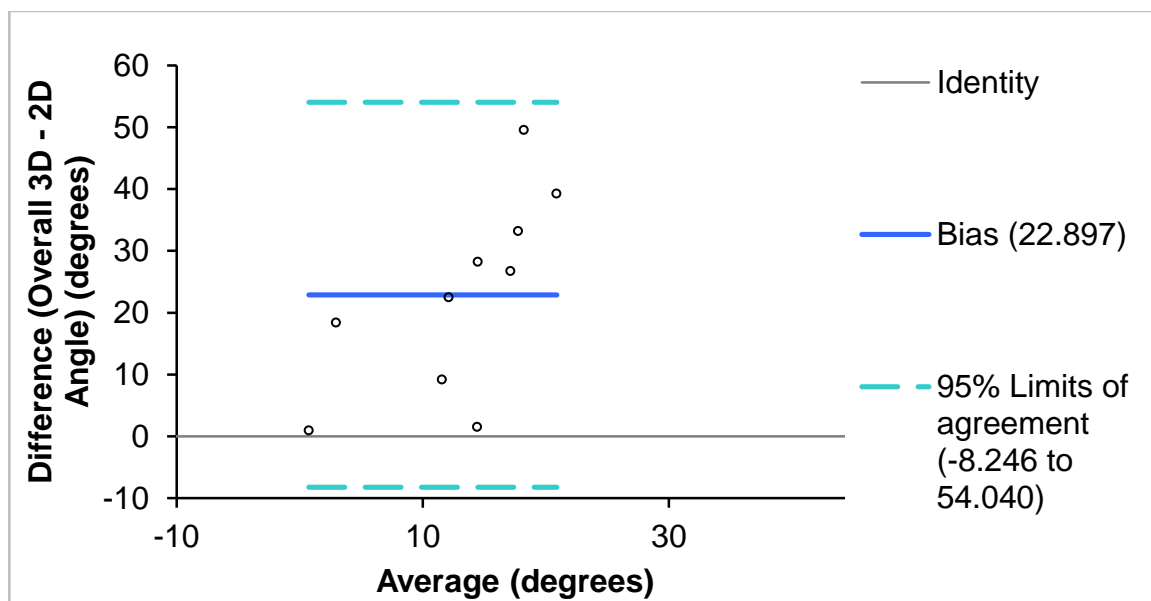
Figure 5.10: Bland-Altman plot for the overall 3D angle measurement with the 2D pronation angle for the foam soft condition from the dorsal-medial to plantar-lateral view.
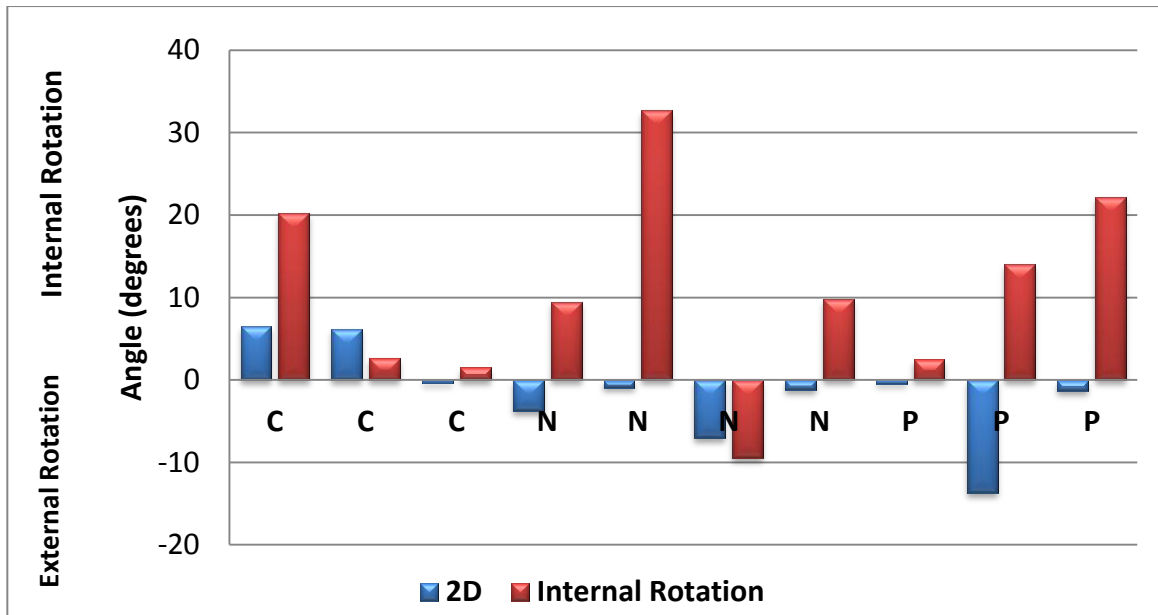
Figure 5.11: The change in pronation calculated with wearing the foam soft orthotic compared to the barefoot condition. The measurement was done using the 2D method (figure 5.2) and the change associated with the internal rotation plane of motion.
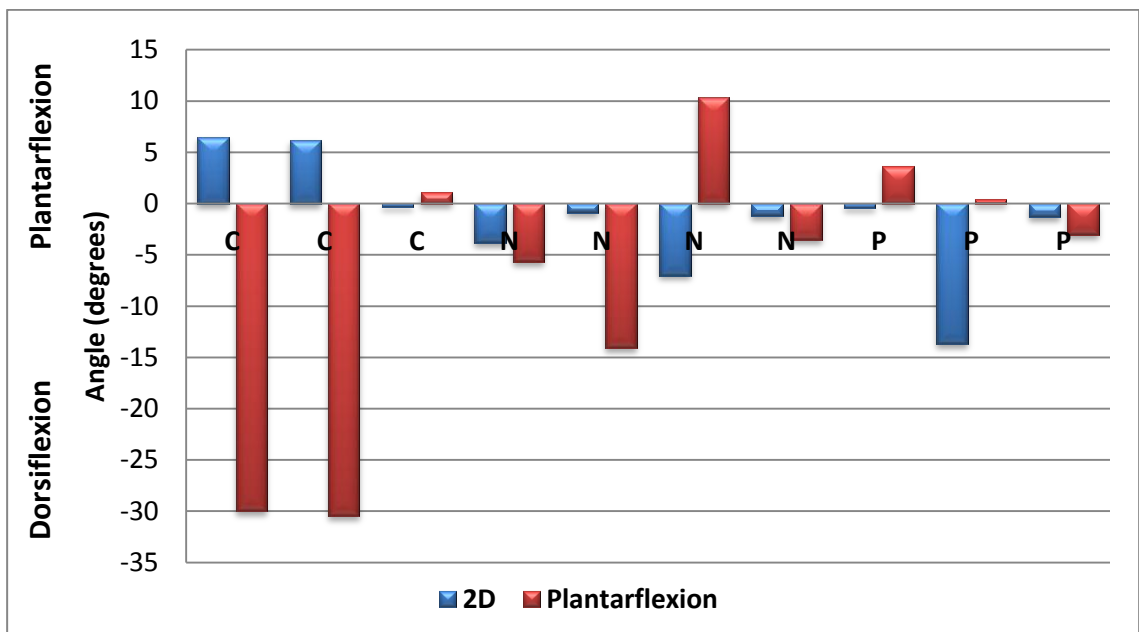
Figure 5.12: The change in pronation calculated with wearing the foam soft orthotic compared to the barefoot condition. The measurement was done using the 2D method (figure 5.2) and the change associated with the plantarflexion plane of motion.
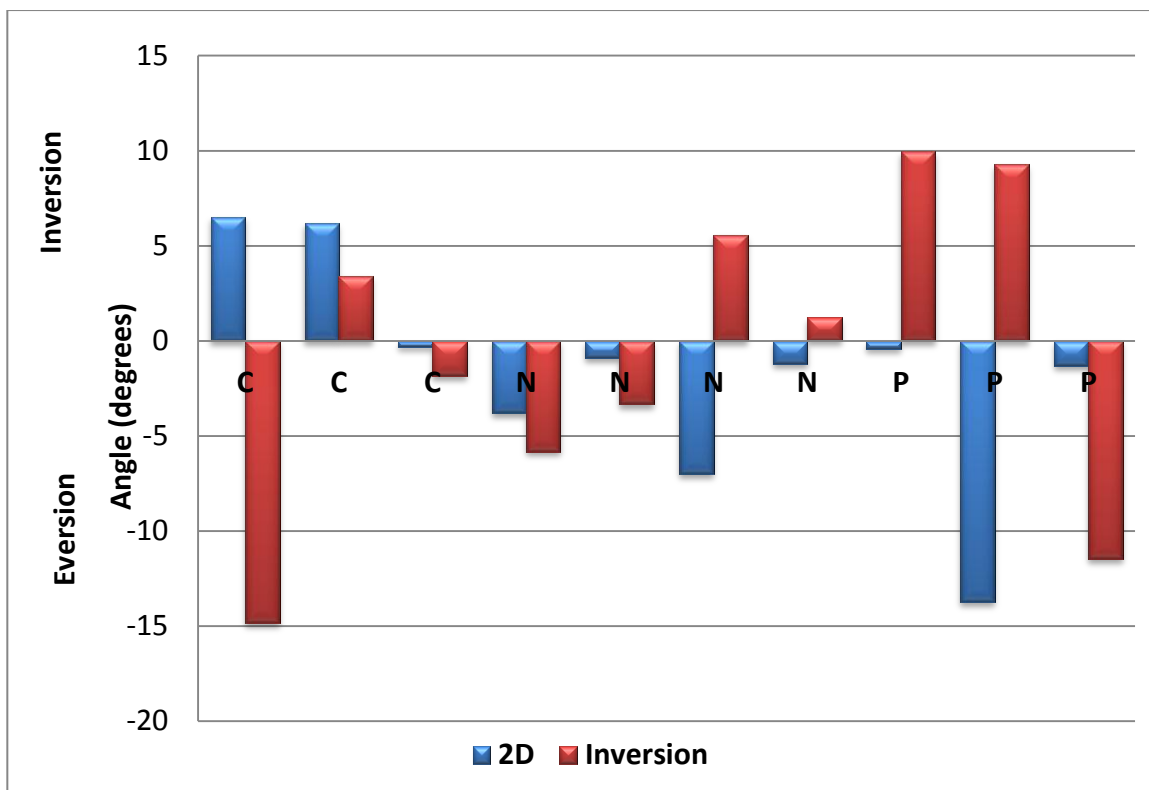
Figure 5.13: The change in pronation calculated with wearing the foam soft orthotic compared to the barefoot condition. The measurement was done using the 2D method (figure 5.2) and the change associated with the inversion plane of motion.

The change in pronation while wearing the foam hard orthotic as measured in two-dimensions is shown graphically as compared with the overall 3D angle in figure 5.14. A Bland-Altman plot was created to assess agreement between the 2D pronation angle and the overall 3D angle as measured for the foam hard orthotic condition in figure 5.15. The change in pronation while wearing the foam hard orthotic as measured in two-dimensions is shown graphically as compared with the with the change associated with each plane of motion: internal rotation, plantarflexion, and inversion in figure 5.16, figure 5.17 and figure 5.18 respectively.
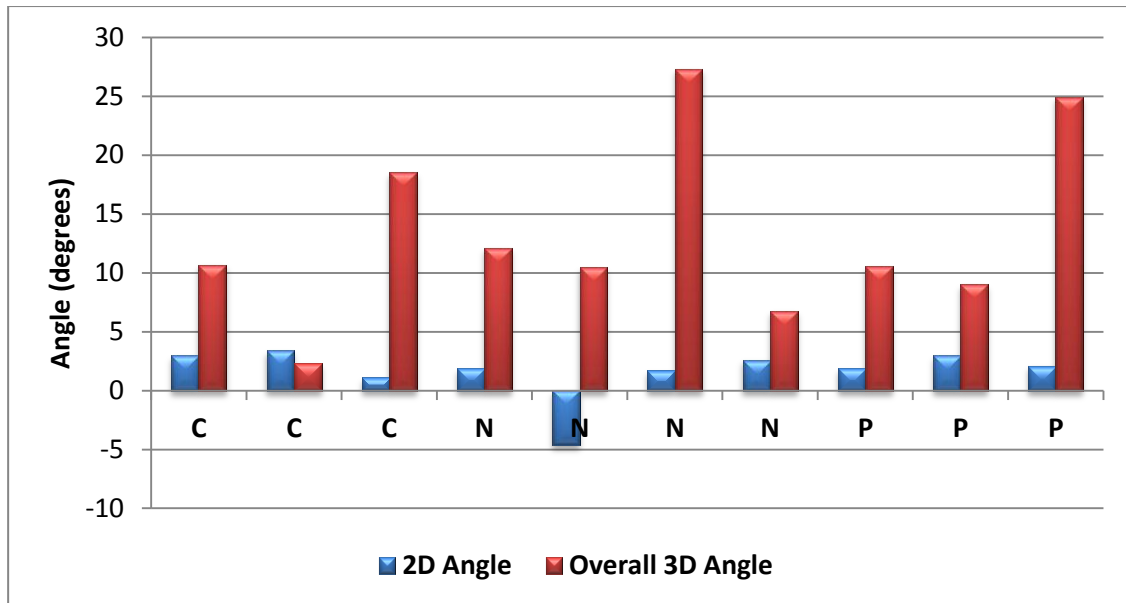
Figure 5.14: The change in pronation calculated with wearing the foam hard orthotic compared to the barefoot condition. The measurement was done using the 2D method (figure 5.2) and the change associated with the overall 3D angle.
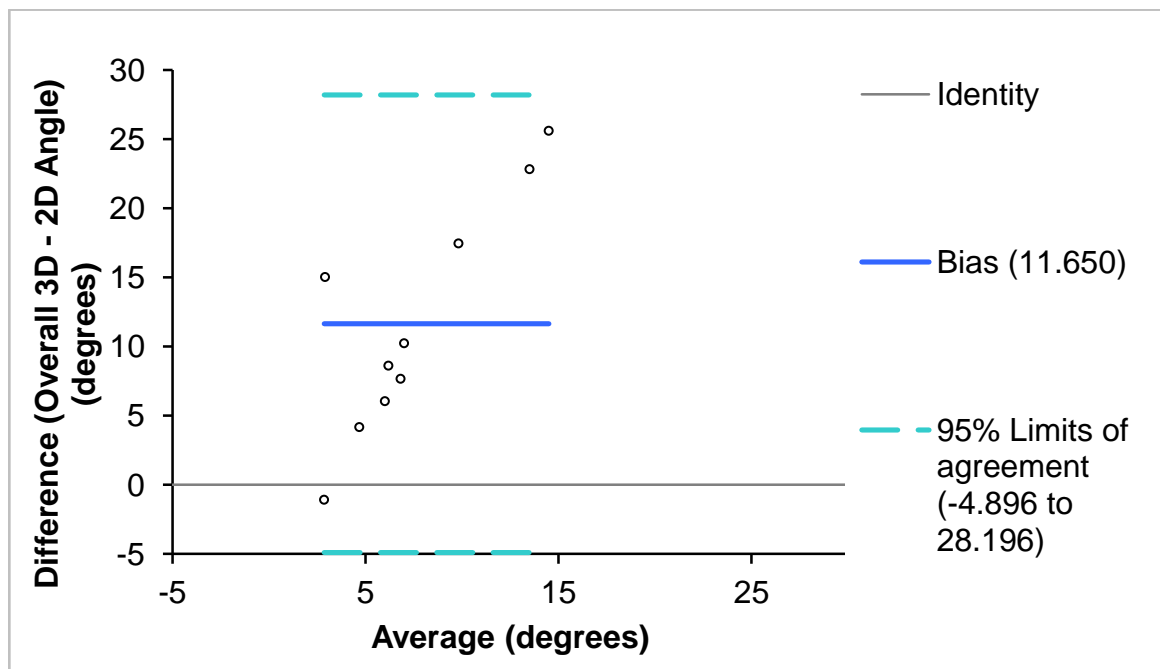
Figure 5.15: Bland-Altman plot for the overall 3D angle measurement with the 2D pronation angle during the foam hard condition from the dorsal-medial to plantar-lateral view.
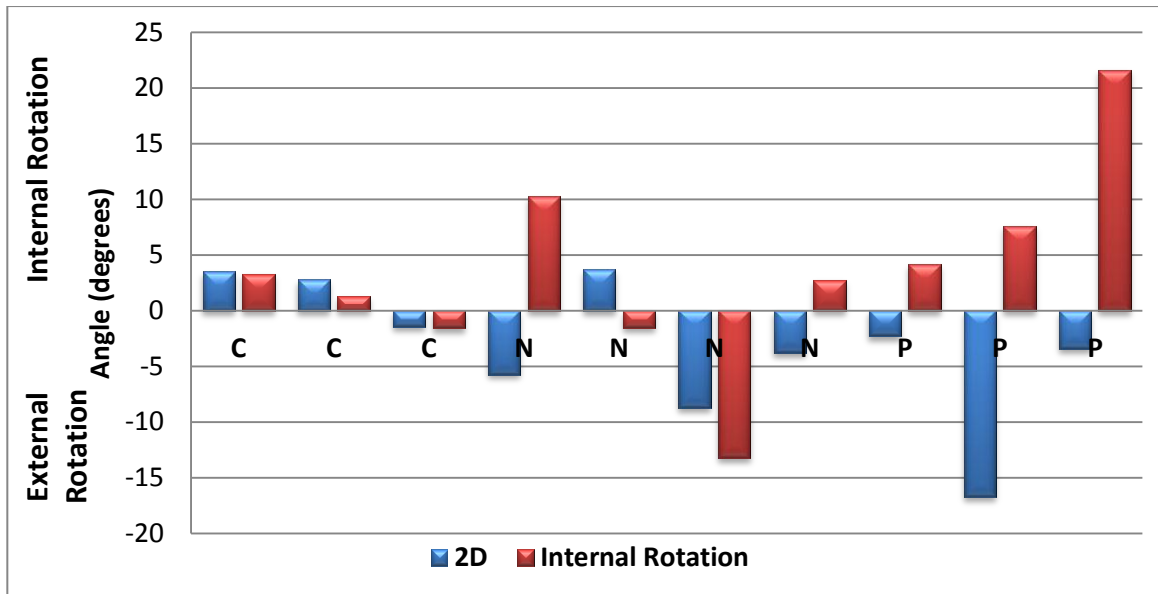
Figure 5.16: The change in pronation calculated with wearing the foam hard orthotic compared to the barefoot condition. The measurement was done using the 2D method (figure 5.2) and the change associated with the internal rotation plane of motion.
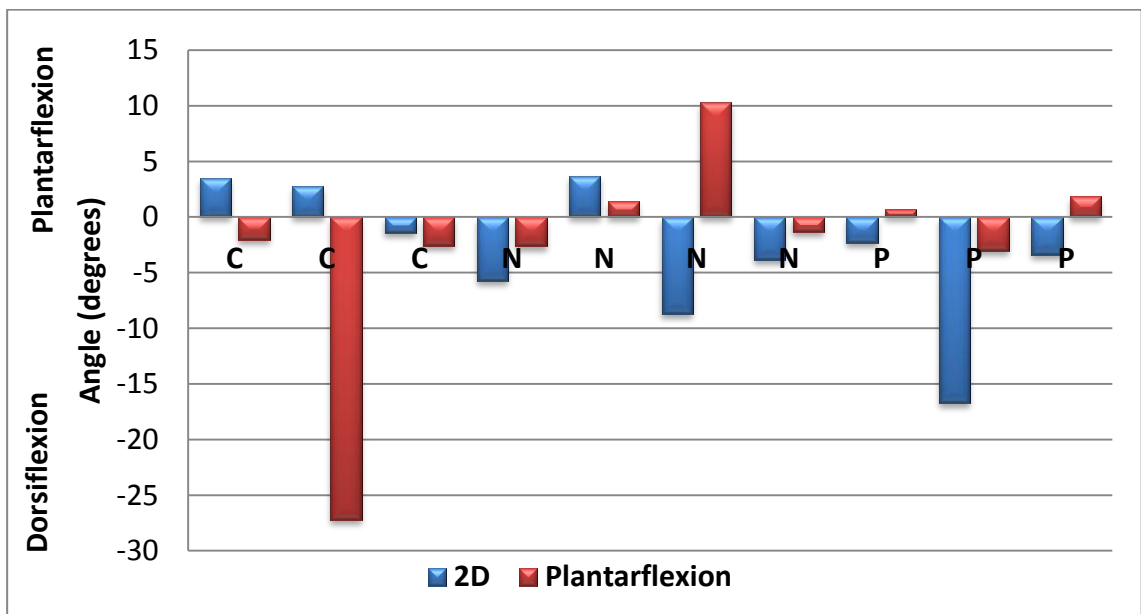
Figure 5.17: The change in pronation calculated with wearing the foam hard orthotic compared to the barefoot condition. The measurement was done using the 2D method (figure 5.2) and the change associated with the plantarflexion plane of motion.
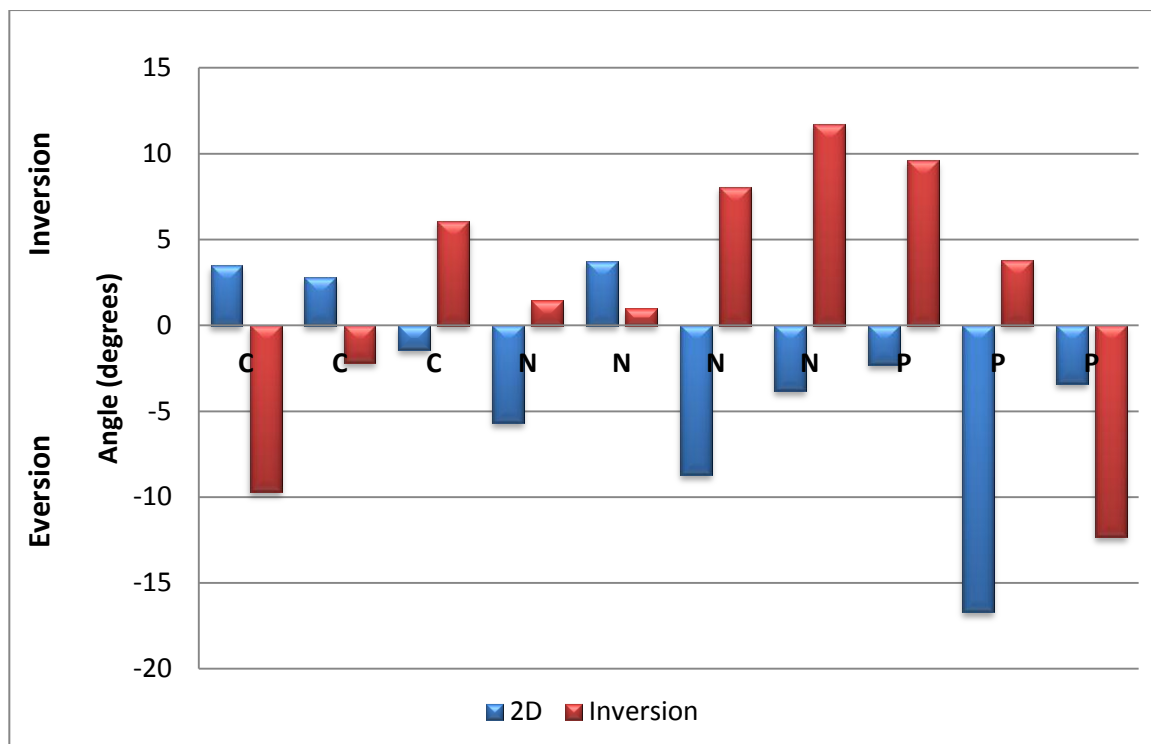
Figure 5.18: The change in pronation calculated with wearing the foam hard orthotic compared to the barefoot condition. The measurement was done using the 2D method (figure 5.2) and the change associated with the inversion plane of motion.

A Bland-Altman plot was created to assess agreement in measuring the degree of pronation between the 2D angle and the corresponding internal rotation, plantarflexion, and inversion plane of motion in figure 5.19, figure 5.20 and figure 5.21 respectively.
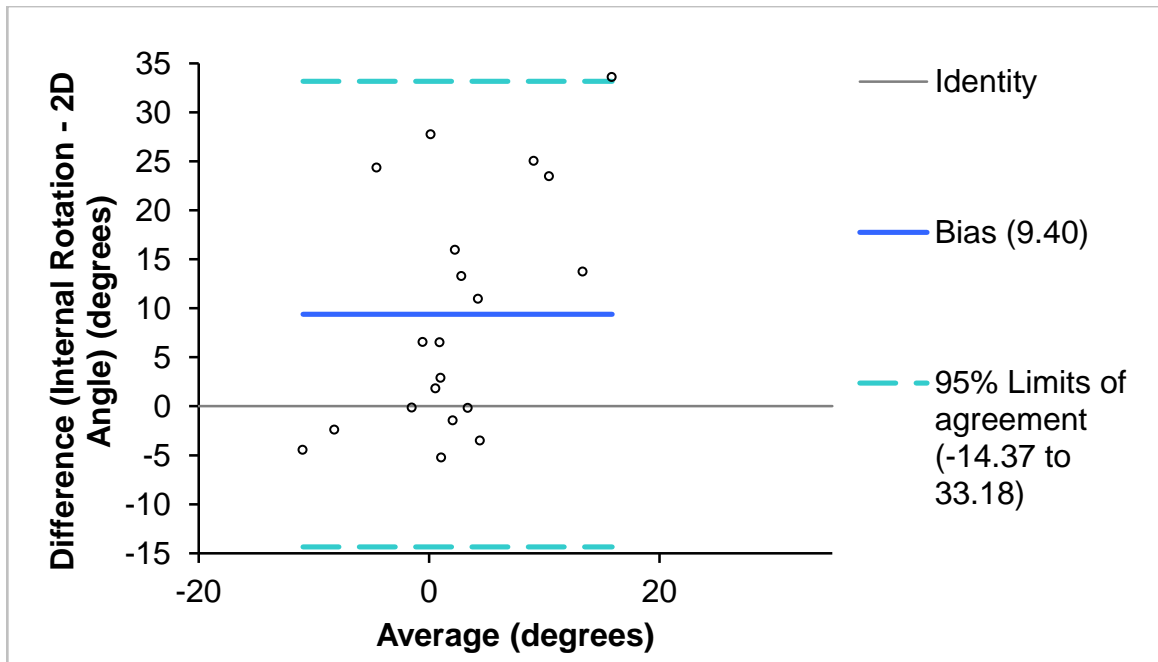
Figure 5.19: Bland-Altman plot for the 2D angle measurement and the internal rotation angle measurement during the foam soft and foam hard conditions.
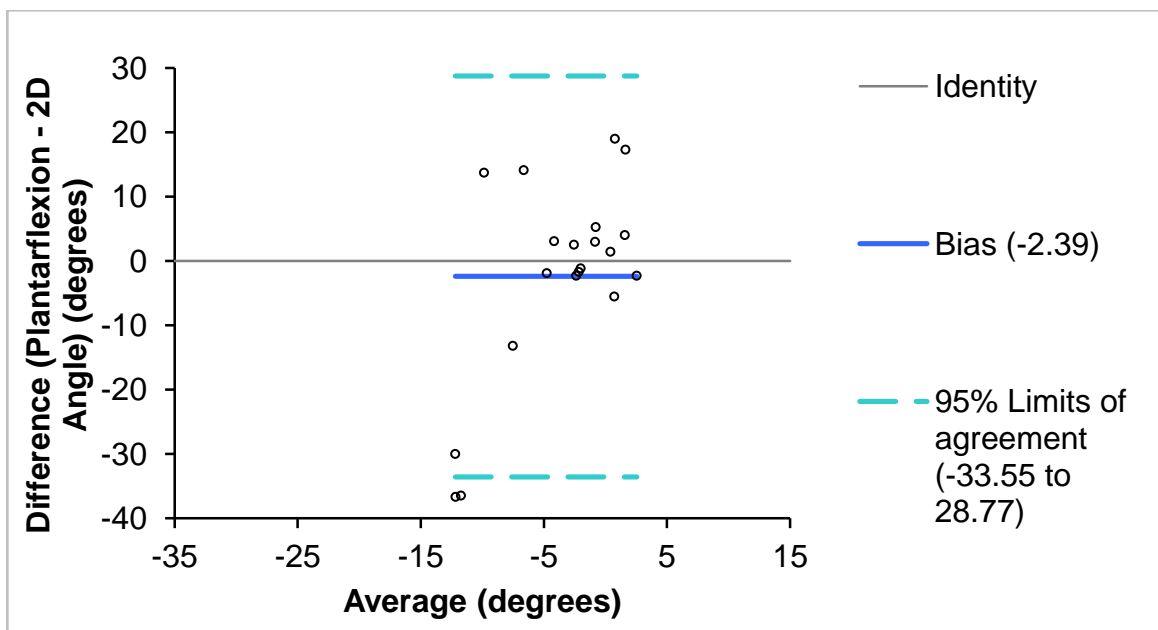
Figure 5.20: Bland-Altman plot for the 2D angle measurement and the plantarflexion angle during the foam soft and foam hard conditions at midstance.
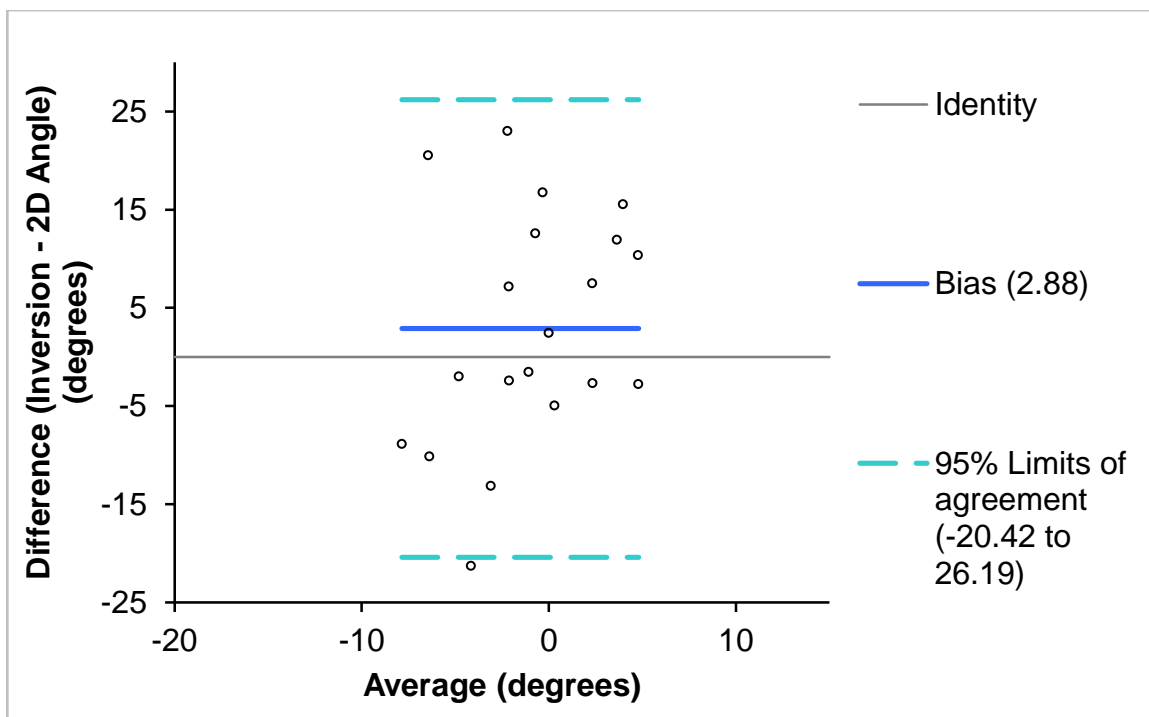
Figure 5.21: Bland-Altman plot for the 2D angle measurement and the inversion angle during the foam soft and foam hard conditions at midstance.

5.5 DISCUSSION

Common practice to date has been to determine the alignment of the foot bones using techniques such as goniometers, optical motion capture systems, MRI, and visually through on-site gait analysis. Goniometers and MRI devices have the disadvantage of only being able to measure accurately during static scenarios. The accuracy of a static measurements ability to mimic the real-world dynamic walking conditions has never been proven on the bone level prior to this study to the authors' knowledge. Figure 5.3, figure 5.4, and figure 5.5 compare the same individuals' hindfoot barefoot alignment measurements in quiet standing and during walking gait at midstance with the same three-dimensional analysis approach. Since the hindfoot experiences movement in three planes a comparison to the internal rotation, plantarflexion and inversion planes were

completed. To compare the degree of pronation measured when standing quietly the same volunteer was used during midstance. Using the three-dimensional bone model technique the static trial angle associated with each plane of motion was compared to the corresponding dynamic scenario. Figure 5.3 represents the internal rotation angle while barefoot during a static and dynamic condition. Figure 5.4 represents the plantarflexion angle while barefoot during a static and dynamic condition. Figure 5.5 represents the inversion angle while barefoot during a static and dynamic condition. It appears that most subjects had static results relatively close to the corresponding dynamic barefoot condition for all three planes of motion. Visually appearing to represent the dynamic scenario does not necessarily mean that the results are going to correlate.

In clinical measurements comparison of a new measurement technique needs to be assessed for agreement with the established method of measurement. Bland-Altman plots are used to determine if the new approach agrees sufficiently to replace the old techniques (Bland and Altman, 1986). When the limit of agreement is small the new technique is considered to show good agreement with the established method of measurement. The Bland-Altman plots used to determine agreement between the static weight-bearing measurements in place of dynamic measurements during midstance are plotted in figure 5.6, figure 5.7, and figure 5.8 for internal rotation, plantarflexion, and inversion respectively. Based on the results from the Bland-Altman plots the limit of agreement has a large range for internal rotation (-19.114° to 19.875°), plantarflexion (-23.798° to 24.206°), and inversion (-14.089° to 9.868°). This indicates that a static

weight-bearing measurement does not accurately mimic dynamic walking gait at midstance.

Another common approach used to simplify image analysis is evaluating data using a two-dimensional technique. Using a 2D technique can fail to describe complex multi-axial motion of the hindfoot (Mattingly *et al.,* 2006). Several studies have proven radiographic measurements to be more reliable than goniometers (Lamm *et al.,* 2005; Saltzman and El-Khoury, 1995). However, it is understood that the out-of-plane motion is still a challenge when using a 2D approach. It is quite difficult to ensure an individual walks in view of the fluoroscope perfectly to obtain a clinically relevant plane of motion. A comparison between the results of the 2D image analysis and the overall 3D angle for the foam soft and foam hard conditions were completed. A comparison between the results of the 2D image analysis to the 3D as represented by the three planes of motion for the foam soft and foam hard orthotic conditions were completed.

The effect on the hindfoot while wearing the foam soft orthotic was represented graphically in figure 5.9. Visually, it is quite apparent that the overall 3D angle does not measure the same degree of pronation change. However, this does not mean that there is a lack of agreement between the two techniques. A Bland-Altman plot was used to determine agreement between dynamic weight-bearing walking gait as measured in 3D compared to 2D during midstance (figure 5.10). The limit of agreement between the overall 3D calculation and the 2D angle is quite large (-8.25°-54.04°). This indicates that simplifying analysis into 2D does not accurately mimic the 3D motion the hindfoot experiences during walking gait while wearing a foam soft orthotic. Since the 2D

measurement can only truely represent a single plane of motion the 2D angle was also compared to each individual plane of motion to determine if the measurement was statistically different.

By visual inspection it appears as though there is a significant difference between the 2D measurement and the internal rotation plane of measurement (figure 5.11) when determining the amount of pronation the hindfoot is experiencing. The same conclusion would be drawn for the plantarflexion (figure 5.12) and inversion (figure 5.13) plane of motion. In some of the measurements the foam soft orthotic moved the foot by a large amount in individuals when measured across three planes of motion, however, in the 2D measurement technique much of this movement is not seen.

Similarly, by visual inspection it appears as though there is a significant difference in the 2D change in pronation and the individual planes of motion as represented in three-dimensions while wearing the foam hard orthotic by comparison to the barefoot baseline measurement value. It is noted that the change found in the calcaneal pronation angle measurement (figure 5.2) compared to the change in pronation detected through internal rotation (figure 5.9) planes measurement is relatively close in most individuals by a visual inspection. The plantarflexion (figure 5.10) and inversion (figure 5.11) planes of motion showed more drastic differences by comparison to the 2D calcaneal pronation angle.

Since a visual inspection is not a good method of comparison a repeated measures ANOVA was completed with a confidence interval of 95% to determine if the 2D found a significant change in motion while wearing the foam soft and foam hard

orthotic. No significant change in alignment was found while wearing the foam soft (p=0.414) orthotic, and foam hard (p=.140) orthotic as measured using the 2D approach. To determine if the 2D approach resulted in a similar change in alignment the 2D change was compared to the change associated with the individual planes of motion (i.e. 2D compared to internal rotation).

Bland-Altman plots were created to determine the limit of agreement in the change in pronation between the 2D angle measurement and the individual planes of motion as measured using the 3D technique. The range of the limit of agreement indicates that the 2D measurement does not reflect the results from the more accurate 3D motion for the internal rotation (-14.37° to33.18°), plantarflexion (-33.55° to 28.77°), and inversion (-20.42° to 26.19°) planes of motion.

The final test was to determine if the results show a significant change in conditions strictly for the 2D analysis technique. The change in calcaneal pronation as measured using the 2D technique did not find a statistical difference between the barefoot and foam soft orthotic condition. The change in calcaneal pronation as measured using the 2D technique did not find a statistical difference between the barefoot and foam hard orthotic condition.

5.6 REFERENCES

Allen, A.-M. V. (2009). *Development and Validation of a Markerless Radiostereometric Analysis (RSA) System*. University of Western Ontario.

Collins, N., Bisset, L., McPoil, T., & Vicenzino, B. (2007). Foot orthoses in lower limb overuse conditions: a systematic review and meta-analysis. *Foot & Ankle International*, *28*, 396-412.

Inman, V. T. (1991). *Joints of the Ankle*. Baltimore: Williams & Wilkins.

Kedgley, A. (2009). *Development of a fluoroscopic radiosterometric analysis system with an application to glenohumeral joint kinematics*. University of Western Ontario.

Kedgley, A. E., & Jenkyn, T. R. (2009). RSA calibration accuracy of a fluoroscopy-based system using nonorthogonal images for measuring functional kinematics. *Medical Physics*, *36*(7), 3176.

Kitaoka, H. B., Lundberg, A., & Luo, Z. P. (1995). Kinematics of the normal arch of the foot and ankle during physiologic loading. *Foot and Ankle*, *16*(8), 492-499.

Lamm, B., Mendicino, R., Catanzariti, A., & Hillstrom, H. (2005). Static *Hindfoot* Alignment A comparison of Clinical and Radiographic Measures. *Journal of the American Podiatric Medical Association*, *95*(1), 26-33.

Landorf, K.B., & Keenan, A. M. (2000). Efficacy of foot orthoses. What does the literature tell us? *Journal of the American Podiatric Medical Association*, *91*, 174-183.

Li, G., Van de Velde, S. K., & Bingham, J. T. (2008). Validation of a non-invasive fluoroscopic imaging technique for the measurement of dynamic knee joint motion. *Journal of Biomechanics*, *41*, 1616-1622.

Mattingly, B., Talwalkar, V., Tylkowski, C., Stevens, D. B., Hardy, P. a, & Pienkowski, D. (2006). Three-dimensional in vivo motion of adult hind foot bones. *Journal of biomechanics*, *39*(4), 726-33.

Murley, G. S., Landorf, K. B., & Menz, H. B. (2010). Do foot orthoses change lower limb muscle activity in flat-arched feet towards a pattern observed in normal-arched feet? *Clinical biomechanics (Bristol, Avon)*, *25*(7), 728-36. Elsevier Ltd.

Saltzman, C., & El-Khoury, G. (1995). The hindfoot alignment view. *Foot & Ankle International*, *16*(9), 572-576.

Tulchin, K., Orendurff, M., & Karol, L. (2010). A comparison of multi-segment foot kinematics during level overground treadmill walking. *Gait & Posture*, *31*, 104-108.

Wu, G., Siegler, S., Allard, P., Kirtley, C., Leardini, A., Rosenbaum, D., Whittle, M., *et al.* (2002). ISB recommendation on definitions of joint coordinate system of various joints for the reporting of human joint motion--part I: ankle, hip, and spine. International Society of Biomechanics. *Journal of Biomechanics*, *35*(4), 543-548.

CHAPTER 6- GENERAL DISCUSSION AND CONCLUSION

Overview: This chapter summarizes the findings of this research, outlines its strengths and limitations, and lists several recommendations. The potential for future research is addressed and the significance of this work is highlighted.

6.1 SUMMARY

Markerless radiostereometric analysis (RSA), while not a new technology, has recently been incorporated with fluoroscopy to provide a means for measuring dynamic kinematics with high precision and accuracy without requiring the insertion of tantalum beads. Using the markerless RSA system previously validated by both Allen and Kedgley for dynamic kinematic studies the objective of this study was to develop a measurement system for the hindfoot. The system used consists of two 9 inch portable C-arm fluoroscopy units and a desktop computer used to store the information. Images are digitized using custom-written software that was created in MATLAB. Calibration of the system was completed using a custom-made calibration frame (Kedgley, 2009). The bone models were created using OsiriX DICOM viewer and the experimental setup was recreated in the virtual environment using a solid modelling program, Rhinoceros. The bony landmarks of interest were followed in the virtual environmental and the calculation of their locations in three-dimensions was conducted using another custom-

written MATLAB program. Finally, another custom-written MATLAB program was used to determine the angle associated with each plane of motion for the bones with respect to each other (i.e. the navicular with respect to the calcaneus). The method of quantifying the kinematic measurements was outlined in Chapter 1. The effect of the foam casted orthotics, made from both soft and rigid materials were described in Chapter 2. The purpose was to quantify and compare the effect of foam casted orthotics on the hindfoot region of the foot when made from soft and rigid materials. It was hypothesized that both material types would reduce pronation in the foot. It was further hypothesized that the rigid material would result in a greater degree of reduced pronation. Five normal arched volunteers were tested to determine the measurable change in alignment caused by the different shoe conditions. Every individual was found to react different depending on the footwear condition being tested. Although the hypothesis was not proved to be statistically different it is believed that with more subjects the results may prove to have a statistically significant outcome.

The effect of plaster casted orthotics, made from both soft and rigid materials were described in Chapter 3. Once the foam casted orthotics were tested the orthotics molded using the plaster casting technique were measured for their effectiveness at altering pronation in the hindfoot. It was hypothesized that the plaster casting technique would reduce pronation and the rigid material type would have a greater effect at this reduction. The same five normal arched volunteers used in Chapter 2 were tested to determine the measurable change in alignment caused by the different shoe conditions. Every individual was found to react different depending on the footwear condition being

tested. Although the hypothesis was not proved to be statistically different it is believed that with more subjects the results may prove to have a statistically significant outcome.

The significance of Chapter 2 and Chapter 3 are in part to compare the results of the foam casted orthotic with the effectiveness of the plaster casted orthotic technique when designing an orthotic for a patient. Since one casting technique did not prove to be better at reducing pronation than the other the foam casted technique was used in subsequent chapters. The effect foam casted orthotics had on the pes cavus and pes planus populations were described in Chapter 4. The significance of this study was to quantify the variation in pronation on a pes cavus and pes planus population. It was hypothesized that the pes cavus group would experience little variation in their bone alignment while wearing any orthotic type by comparison to the pes planus group. It was further hypothesized that the pes planus group will experience a noticeable difference between the rigid and soft orthotics. Every individual was found to react different depending on the shoe condition being tested. It was found that the pes planus group experienced a greater degree of change while wearing an orthotic overall, although this change was not found to be significant in all planes of motion. It was found that the pes planus group experienced a significant change in bone alignment while wearing both the foam soft and foam hard orthotic in the plantarflexion plane of motion. The pes cavus group reacted as expected having little change in their bone alignment with orthotic use.

The effect on pronation while wearing a foam casted orthotic in the normal, pes planus and pes cavus foot types were compared using three different measurement

techniques. The significance of this study is to try and reduce the amount of time required in image analysis. Alternative measurement techniques are computationally less intensive then the three-dimensional dynamic technique used in the previous chapters. This study compared a foam orthotics effect on bone alignment while static weight-bearing to the corresponding dynamic condition while measured during walking gait at midstance. The second part of this study compared a two-dimensional measurement of the bone alignment to the overall 3D motion as measured by the three planes of motion in the previous studies. It was hypothesized that the dynamic study would provide a different angular change between conditions when compared to the corresponding static measurement. It was also hypothesized that the two-dimensional analysis would not provide similar results to any of the planes of motion or the overall 3D angle when measuring pronation.

When measuring agreement of the static measurements to the corresponding dynamic measurements at midstance the internal rotation plane, plantarflexion and the inversion plane of motion did not result in an accurate agreement to represent the dynamic motion. Based on the results from the Bland-Altman plot it is not recommended to use a static image analysis approach where dynamic motions more accurately mimic the use of the product tested (i.e. walking in a shoe versus standing in a shoe). When comparing the two-dimensional (2D) images from an oblique, dorsal-medial to plantar-lateral view to the internal rotation, plantarflexion and inversion planes of motion using a Bland-Altman agreement between the 2D and 3D measurement was not found. Upon completion of this study it is not recommended to

use a 2D analysis in place of a 3D one due to the fact that the motion in the other planes is not seen.

6.2 STRENGTHS AND LIMITATIONS

The strengths and limitations of each study will have some overlap due to the nature of this type of analysis. The primary goal of this analysis was to develop a tool for measuring hindfoot kinematics accurately using the previously validated markerless RSA system developed by Allen (Allen, 2009). The biggest limitation of this technique is the exposure of the test subject to ionizing radiation. Radiation comes in the form of a CT scan in addition to fluoroscopy images for kinematic data acquisition. The second limitation is that all images are manually digitized in its current implementation. This places a restriction on how fast the results can be processed. Third, only bony structures are well enough defined in the fluoroscopy images to be digitized. This means that soft tissue structures such as tendons or ligaments cannot be examined *in-vivo*.

Additional potential limitations of the studies include that the capture volume is quite small on the fluoroscopes, limiting the visible region. The maximum capture rate of the fluoroscopy units limits the speed of motions that may be performed, as blurring can occur if motions are performed too quickly. Furthermore, a bi-planar RSA setup may limit the range of motion of subjects.

There are limitations in the accuracy of the 3D bone models created and the markerless RSA calibration process. The 3D bone models do not perfectly capture the bones geometry due to factors such as imperfect segmentation and smoothing techniques that occur when creating the triangular mesh. Calibration is limited due to

factors such as: the manufacturing accuracy of the calibration frame and the distortion grid, the digitization process and the distortion correction process. These errors have been quantified together previously as a standard error of measurement of 0.032mm for translations and 0.121° for rotations (Kedgley and Jenkyn, 2009). Performing markerless RSA is an operator intensive task. It requires an investigator who is comfortable deriving new calibration equations based on the experimental set-up, and running software in multiple programs (Maple, MATLAB, and Rhinoceros). These constraints limit the amount of investigators capable of performing markerless RSA. The task requires extensive training and this will limit immediate clinical application.

The matching procedure is also an operator intensive task. To determine the skeletal kinematics an operator manually matches the 3D bone models to the two fluoroscopic images. This process is constrained to the operator's ability to detect different pixel shades as the operator must detect the exact edge of a bone in each image analyzed (Allen, 2009). The matching process is also affected by the patience of the operator; it can take several hours to match one bone to both fluoroscopic images. While this process has been proven accurate it varies based on the operator's perfection of a 'matched' 3D model. This was demonstrated previously in Allen's thesis work to have an intra-operator reliability of 0.58mm and 0.74° and an inter-operator reliability of 0.49mm and 0.75° (Allen, 2009).

The final limitation of this study is the sample size. Five normal arched volunteers were used in chapter 2 and chapter 3. Three pes cavus and three pes planus volunteers were used in chapter 4 of this study. The subjects used in Chapter 2 to Chapter 4 were

used in chapter 5 of this study. An increase in the number of subjects used would improve the accuracy of any conclusions drawn throughout this thesis.

The major strength to this research is due to the combination of fluoroscopy with a markerless RSA system. Dynamic conditions can be studied when a conventional stereographic system would not have this capability. The implantation of tantalum beads is removed when conducting markerless RSA. This means that the normal subject population can be studied as ethically the risk of infection, and need for unnecessary surgery is removed. The full range of motion in the foot can be examined which is not possible using an MRI examination. Finally, and perhaps the greatest advantage is the elimination of skin motion artifact that is inevitable when using optical or electromagnetic surface marker systems.

6.3 RECOMMENDATIONS AND FUTURE DIRECTIONS

Several recommendations can be made to improve the WOQIL fluoroscopic RSA system. These include:

1) Equipment

   a. The acquisition of fluoroscopes with larger image intensifiers would increase the field of view of each fluoroscope and therefore also greatly increase the capture volume of the RSA system. This would increase the range of motion in which kinematics can be analyzed in additional to increase the number of joints that can be examined simultaneously.

   b. Flat-panel detectors would improve accuracy of analysis technique as this type of system does not suffer from pin-cushion distortion as the image intensifiers in

WOQIL do (Yaffe and Rowlands, 1997; Seibert, 2006; Davies *et al.,* 2007; Kedgley, 2009). Davies *et al.* stated that image quality does not improve with the use of a flat-panel detector (Davies *et al.,* 2007). However Seibert stated that the image quality may be a function of operator experience and training on the new system type (Seibert, 2006).

2) Markerless RSA program

   a. The RSA program should be made more user-friendly for those users that are not familiar and comfortable with MATLAB. This process has been started and the graphical user interface (GUI) has been created, however, there are still bugs in this and they need to be worked out.

   b. An automated bead detection scheme (Cho and Johnson, 1998) should be implemented in order to reduce the amount of manual digitization required. This implementation is quite feasible and would reduce a large amount processing time. This system would require validation once completed to ensure its working accurately.

   c. Edge detection should be incorporated to outline the bones on the images prior to matching. These outlines would reduce the subjectivity of the matching process created by the estimation of the edge required by the operator.

   d. It is recommended that further attempts be made to reduce the radiation exposure to subjects during the markerless RSA process. Using a general 3D computer bone model instead of the 3D computer models created from the

individuals CT scan would drastically reduce radiation exposure to subjects. It is suggested that a generic bone model be compared to the actual results in this thesis to determine if the differences found in the results warrant the extra radiation to the subjects.
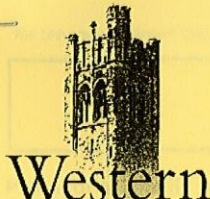
This facility allows for what seems like an endless list of future work. Kinematics can not only be measured prior to surgery but also on a normal population to determine the differences between subject groups. This system can be used to study the effect of a wide range of interventions beyond what was studied in this thesis including joint arthroplasty and reconstructive surgeries. The markerless RSA system used in this thesis has the ability to answer a broad range of biomechanical questions and therefore significantly contribute to the field of biomechanics in the future.

6.4 REFERENCES

Allen, A.-M. V. (2009). *Development and Validation of a Markerless Radiostereometric Analysis (RSA) System*. University of Western Ontario.

Cho, P. S., & Johnson, R. H. (1998). Automated detection of BB pixel clusters in digital fluoroscopic images. *Physics in medicine and Biology*, *43*(9), 2677-2683.

Davies, A. G., Cowen, A. R., Kengyelics, S. ., Moore, J., & Sivananthan, M. U. (n.d.). Do flat detector cardiac x-ray systems convery advantages over image-intensifier-based systems? Study comparing x-ray does and image quality.

Kedgley, A. (2009). *Development of a fluoroscopic radiosterometric analysis system with an application to glenohumeral joint kinematics*. University of Western Ontario.

Kedgley, A. E., & Jenkyn, T. R. (2009). RSA calibration accuracy of a fluoroscopy-based system using nonorthogonal images for measuring functional kinematics. *Medical Physics*, *36*(7), 3176.

Seibert, J. A. (2006). Flat-panel detectors: how much better are they? *Pediatric Radiology*, *36*(Suppl 2), 173-181.

Yaffe, M. J., & Rowlands, J. A. (1997). X-ray detectors for digital radiography. *Physics in medicine and Biology*, *42*(1), 1-39.

APPENDICES

APPENDIX A- ETHICS APPROVAL AND DOSAGE CALCULATION

Office of Research Ethics

The University of Western Ontario
Room 5150 Support Services Building, London, ON, Canada N6A 3K7
Telephone: (519) 661-3036 Fax: (519) 850-2466 Email: ethics@uwo.ca
Website: www.uwo.ca/research/ethics

Use of Human Subjects - Ethics Approval Notice

Principal Investigator: Dr. T.R. Jenkyn   **Review Level:** Full Board
Review Number: 17353   **Revision Number:**
Review Date: August 10, 2010   **Approved Local # of Participants:** 30
Protocol Title: Investigation of in-vivo foot and orthotic interactions with using optical motion capture and bi-planar x-ray fluoroscopy
Department and Institution: Mechanical & Materials Engineering, University of Western Ontario
Sponsor: NSERC-NATURAL SCIENCES ENGINEERING RSRCH COU
Ethics Approval Date: January 11, 2011   **Expiry Date:** April 30, 2011
Documents Reviewed and Approved: UWO Protocol , Letter of Information and Consent Form dated 8 Nov 2010 and Poster
Documents Received for Information:

This is to notify you that The University of Western Ontario Research Ethics Board for Health Sciences Research Involving Human Subjects (HSREB) which is organized and operates according to the Tri-Council Policy Statement: Ethical Conduct of Research Involving Humans and the Health Canada/ICH Good Clinical Practice Practices: Consolidated Guidelines; and the applicable laws and regulations of Ontario has reviewed and granted approval to the above referenced revision(s) or amendment(s) on the approval date noted above. The membership of this REB also complies with the membership requirements for REB's as defined in Division 5 of the Food and Drug Regulations.

The ethics approval for this study shall remain valid until the expiry date noted above assuming timely and acceptable responses to the HSREB's periodic requests for surveillance and monitoring information. If you require an updated approval notice prior to that time you must request it using the UWO Updated Approval Request Form.

During the course of the research, no deviations from, or changes to, the protocol or consent form may be initiated without prior written approval from the HSREB except when necessary to eliminate immediate hazards to the subject or when the change(s) involve only logistical or administrative aspects of the study (e.g. change of monitor, telephone number). Expedited review of minor change(s) in ongoing studies will be considered. Subjects must receive a copy of the signed information/consent documentation.

Investigators must promptly also report to the HSREB:
a) changes increasing the risk to the participant(s) and/or affecting significantly the conduct of the study;
b) all adverse and unexpected experiences or events that are both serious and unexpected;
c) new information that may adversely affect the safety of the subjects or the conduct of the study.

If these changes/adverse events require a change to the information/consent documentation, and/or recruitment advertisement, the newly revised information/consent documentation, and/or advertisement, must be submitted to this office for approval.

Members of the HSREB who are named as investigators in research studies, or declare a conflict of interest, do not participate in discussion related to, nor vote on, such studies when they are presented to the HSREB.

Chair of HSREB: Dr. Joseph Gilbert
FDA Ref. #: IRB 00000940

Ethics Officer to Contact for Further Information

☐ Janice Sutherland (jsutherl@uwo.ca)   ☑ Elizabeth Wambolt (ewambolt@uwo.ca)   ☐ Grace Kelly (grace.kelly@uwo.ca)

This is an official document. Please retain the original in your files.

cc: ORE File
LHRI

UWO HSREB Ethics Approval - Revision
V.2008-07-01 (rptApprovalNoticeHSREB_REV)   17353   Page 1 of 1

Figure A.1: Scanned copy of ethics approval obtained for this thesis.

LAWSON HEALTH RESEARCH INSTITUTE

FINAL APPROVAL NOTICE

RESEARCH OFFICE REVIEW NO.: R-10-576

PROJECT TITLE: Investigation of in-vivo foot and orthotic interactions with using optical motion capture and bi-planar x-ray fluorscopy.

PRINCIPAL INVESTIGATOR: Dr. Thomas Jenkyn

DATE OF REVIEW BY CRIC: March 16, 2011

Health Sciences REB#: 17353

Please be advised that the above project was reviewed by the Clinical Research Impact Committee and the project:

Was Approved

PLEASE INFORM THE APPROPRIATE NURSING UNITS, LABORATORIES, ETC. BEFORE STARTING THIS PROTOCOL. THE RESEARCH OFFICE NUMBER MUST BE USED WHEN COMMUNICATING WITH THESE AREAS.

Dr. David Hill
V.P. Research
Lawson Health Research Institute

All future correspondence concerning this study should include the Research Office Review Number and should be directed to Sherry Paiva, CRIC Liaison, LHSC, Rm. C210, Nurses Residence, South Street Hospital.

cc: Administration

Figure A.2: Scanned copy of the Critical Research Impact Committee (CRIC) approval.

Table A.1: The resulting dosage from the x-ray fluoroscopy machines during testing as well as the amount of time the fluoroscopes were on.

Subject	Fluoroscope A			Fluoroscope B		
	Exposure (mA)	kVp	Time (min)	Exposure (mA)	kVp	Time (min)
1	0.7	51	1.4	1.4	61	1.2
2	0.3	48	1.8	1.6	61	2
3	0.3	48	1.8	0.3	51	1.8
4	0.3	48	1.6	0.3	50	1.7
5	0.3	49	0.8	0.3	51	0.8
6	0.3	49	1.1	0.3	51	1.1
7	1.1	51	0.9	1.4	57	0.9
8	0.3	51	0.9	0.3	49	1.1
9	0.3	49	0.8	0.3	51	0.8
10	0.3	48	0.9	0.3	51	0.9
11	0.3	48	1	0.3	50	1
13	0.3	48	0.9	0.3	50	0.9
15	0.7	55	1.2	0.3	51	1.2
16/18	0.3	49	0.9	0.3	51	0.9
17	0.5	53	1.4	0.3	49	1.3
19	0.3	49	0.9	0.3	51	1
20	0.3	49	1.4	0.5	53	1.4
21	0.3	49	2.1	0.5	53	2.1
22	0.3	48	1	0.5	53	1
23	0.6	53	1.3	2.4	60	1.2
24	0.3	49	1.1	0.3	51	1
AVERAGE	0.39	49.6	1.2	0.56	52.2	1.21
SD	0.20	2.01	0.38	0.57	3.33	0.40

*Note: Subject 16/18 are the same subject but their testing was spread out over two testing dates because of a manufacturing error in the orthotics. The exposure and kVp values were identical on the two testing dates so the time recorded is cumulative over both testing dates.

APPENDIX B- OSIRIX DIGITIZATION INFORMATION

This appendix describes how to open the files generated by a CT scan in OsiriX, create models of the bones and digitize the locations of any bony landmarks.

B.1 IMPORTING THE SCAN AND SEGMENTING THE BONE

Note: Do not hit save throughout the process until this guide advises the user to do so

*** Hitting save will result in an error message during the process, and you may lose data ***

1) Open OsiriX. Choose the CT file group of interest.

2) An "important notice" will pop-up (figure B.1). Click "I agree".

Figure B.1: Pop-up window in OsiriX occurs when program is opened.

3) Select 3D Viewer from the menu bar-> 3D Volume Rendering.

4) Change the level of detail to fine, then click the 3D presets menu (figure B.2). In the 3D presets menu set the group to basic (should be default menu), chose low contrast. This should eliminate some of the noise in the image.

Figure B.2: 3D viewer setting changes.

5) Remove any bone you are not interested in leaving only one bone for segmentation purposes. Some of the useful tools (figure B.3):

a. Scissors: will remove or keep what is selected. To remove what you have selected hit the delete key. To keep what is selected hit the return key.

b. Poison: this will remove all bone that is touching the bone you are looking to remove. Useful for bones which have an obvious gap, but not a great feature for small bones. Use this feature first you can always undo anything if it deletes too much bone.

c. Magnifying glass: this will allow you to zoom in and out. This will be good for tight spaces.

d. ISO box: this wills all you to change your view.

e. Target button: allows you to identify landmarks of interest as a mesh form for further analysis.
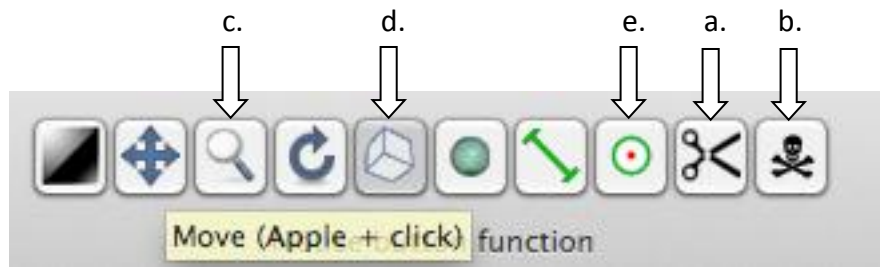
Figure B.3: The menu options for the 3D volume rendering section of bone segmentation.

Note: The letters in the figure refer to the above descriptions.

6) Once everything but the bone of interest has been removed enter the 3D presets menu (as done in step 4). Change the group type to Bone CT. From there pick the soft bone style. This will have the greatest success later for the segmentation task.

7) In the menu bar: select 3D Viewer ->3D surface rendering. The "surface setting" menu pops up automatically (figure B.4). It should be noted that the preset menu options are

not necessarily ideal for the bone of interest. It is not a bad idea to see how the default settings show the bone image. If the image is not desirable open the surface setting menu again (found on the main tool bar window). For the foot it was found that optimal bone settings were:

- Change resolution to the highest point rather than the midpoint default setting.

- Change the decimate to 0.1 from the 0.5 default setting

- Pixel value: this will be dependent on the bone. Go to a point where the holes created in this process have disappeared; however, be careful that the shape and contours of the bone have not been affected. You cannot just set a value for the pixels that will automatically work each time as this will affect the bones shape and size. This could affect results later on.

- You can change the colour of the bone if you wish, but Rhinoceros will just default it back to black mesh so not a crucial step.
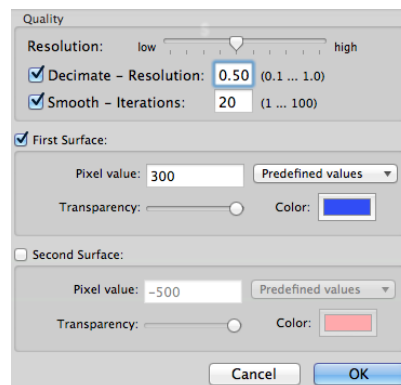
Figure B.4: Surface Rendering Settings menu.

8) The bone should be completely segmented and ready to be exported for further data analysis (figure B.5).
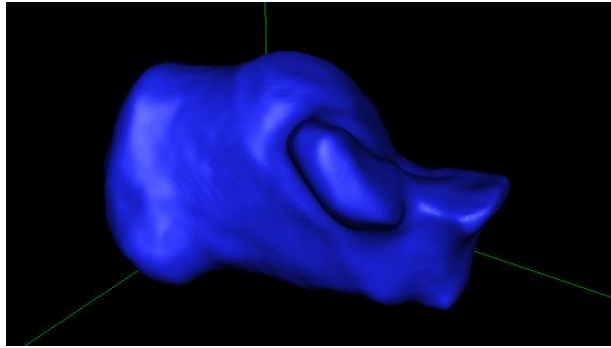
Figure B.5: Complete segmented bone. Calcaneus segmented from the left foot.

9) Export the bone as a stl or obj file type of file. The 3D-SR icon on the main menu (within surface rendering still) is where the stl and obj file type is available to export your image. Choose your folder to save to on the Macintosh computer. It proved to be important to save this file several times (with different names) and as both .stl and .obj file types. Loss of data can occur when transferring from a Macintosh to a PC, so several saves could avoid this situation. It will be necessary to type .stl or .obj (depending on the file type) on the end of the name once imported into the PC machine. Until this is done Rhinoceros will not recognize your file type.

10) The file can then be imported into Rhinoceros. Note you will have to change the import default in Rhinoceros to 'all files' in order for the segmented bone to be visible.

APPENDIX C- PRONATION KINEMATICS

This appendix contains the MATLAB script developed to calculate the alignment changes in the foot during gait and static fluoroscopy capture. This section also contains the code used for the two-dimensional study in chapter 5.

C.1- MATLAB KINEMATICS OF THE FOOT

```matlab
% Program:          Calcaneuspronation_kinematics.m
% Description:      Calculates the calcaneus pronation kinematics from the
%                   3D Ct scan and the anatomical landmarks
% Written by:        Kristen Bushey
% Date Written:     October 18, 2011
% Last Modified:    Jan 31, 2012
% NOTE: make sure calcaneus, cuboid and navicular landmarks are located in
% the correct rows in excel!!!
%Modified (June 24, 2012) to convert to positive directions reflecting
%the right-hand coordinate system rule for the body... There for lateral
%is associated with lateral of the right foot. Therefore if using a left
%foot lateral is actually point towards the center of the body.
%---------------------------------------------------------------------

%Initialize Variables
endline = [0 0 0 1];

%Obtain information about the data to be analyzed from the user
%data_folder = input('Enter the name of the folder with the digitized
points: ', 's');
data_dir = ['C:\Users\Kristen\Desktop\DATA (GOOD FOLDER)\Planus\Subject
19\Static\'];
%data_file1= input('Enter the name of the output file you wish to have:
', 's');
num_files = input('Enter the number of files to be analyzed: ');
start_file = input('Enter the value of the first file in the series: ');

for z = start_file:(start_file + num_files - 1)
    file_num = int2str(z);
    if z < 10
        data_file1 = strcat('Fluoro-000', file_num, '_analyzed.xls');
    elseif (z >= 10 && z < 100)
        data_file1 = strcat('Fluoro-00', file_num, '_analyzed.xls');
    elseif (z >= 100 && z < 1000)
        data_file1 = strcat('Fluoro-0', file_num, '_analyzed.xls');
    else
        data_file1 = strcat('Fluoro-', file_num, '_analyzed.xls');
    end
```

```matlab
%Obtain calcaneus information from the user (code will generate where
user is obtaining information)
%Up to folder location (if different change the data file to another
folder
%here)
anat_cal_landmarks_dir= data_dir;
%Landmark locations from Rhinoceros Output File (Generated using
%ExportPoints code)
%anat_cal_landmarks_file = input('Enter the name of the file with the
calcaneus anatomical landmarks from Rhino: ','s');
anat_cal_landmarks_filename=strcat('landmarks-fluoro-00',file_num,'cal',
'.xls');
anat_cal_landmarks = xlsread([anat_cal_landmarks_dir,
anat_cal_landmarks_filename], 1);
anat_cal_landmarks= anat_cal_landmarks(:,1:3);

%Calcaneus landmarks as located in excel.
calA= anat_cal_landmarks (1, 1:3);
calB= anat_cal_landmarks (2, 1:3);
calC= anat_cal_landmarks (3, 1:3);
calD= anat_cal_landmarks (4, 1:3);

%Calcaneus Bead Coordinate System (points exported from Rhino using
%exportpoints code)
%Calcaneus landmarks:
%ISB standard: upper ridge of calcaneus (def: calA) also origin for
tmatrix
%calB- medial process of the calcaneal tuberosity
%calC- origin site of the extensor digitorum brevis

%NOTE: Zcal_lab - Z direction vector for calcaneus in lab coordinate
system

calBA= calB-calA;
midAB= (calA+calB)/2;

%create lateral directing vector
Z1cal_lab= calBA;
Z1cal_lab_length= norm(Z1cal_lab);
Z1cal_lab= Z1cal_lab/Z1cal_lab_length;

%create anterior directed vector
X1cal_lab= calC-midAB;
X1cal_lab_length= norm(X1cal_lab);
X1cal_lab= X1cal_lab/X1cal_lab_length;

%Ensure everything is actually orthogonal (repeat cross products for
%final coordinate system information

Ycal_lab= cross(Z1cal_lab, X1cal_lab);
Ycal_lab_length= norm(Ycal_lab);
Ycal_lab= Ycal_lab/Ycal_lab_length;

Zcal_lab= cross(X1cal_lab, Ycal_lab);
```

```matlab
Zcal_lab_length= norm(Zcal_lab);
Zcal_lab= Zcal_lab/Zcal_lab_length;

Xcal_lab= cross(Ycal_lab, Zcal_lab);
Xcal_lab_length= norm(Xcal_lab);
Xcal_lab= Xcal_lab/Xcal_lab_length;

%Origin of T-matrix will be calD (calA in thesis document)
origin_cal=calD;

%T-matrix calcaneus wrt lab
Tlandmark_cal2lab= [Xcal_lab' Ycal_lab' Zcal_lab' origin_cal'];
Tlandmark_cal2lab= cat(1, Tlandmark_cal2lab, endline);
%create T-matrix lab wrt calcaneus
Tlab2cal= inv(Tlandmark_cal2lab);


%Cuboid Coordinate System
%Obtain Landmark Location From User. Input location of cuboid
%coordinate system
anat_cub_landmarks_dir= data_dir;
%landmarks as outputted from rhino
%anat_cub_landmarks_file = input('Enter the name of the file with the
cuboid anatomical landmarks from CT: ','s');
anat_cub_landmarks_filename=strcat('landmarks-fluoro-00',file_num,'cub',
'.xls');
%anat_cub_landmarks_filename=strcat(anat_cub_landmarks_file, '.xls');
anat_cub_landmarks = xlsread([anat_cub_landmarks_dir,
anat_cub_landmarks_filename], 1);
anat_cub_landmarks= anat_cub_landmarks(:,1:3);

%cubA lateral plantar tuberosity beside calcaneus facet
cubA= anat_cub_landmarks (1, 1:3);
%cubB medial plantar tuberosity beside calcaneus facet
cubB= anat_cub_landmarks (2, 1:3);
%cubC plantar tuberosity adjacent to 3rd cuniform
cubC= anat_cub_landmarks (3, 1:3);
%cubD triangular point located on the plantar side of the cuboid in
between
%the 4th and 5th metatarsal facets
cubD= anat_cub_landmarks (4, 1:3);

%create vectors originating from the origin location on the cuboid (A)

cubDA= cubD-cubA;

%create distal (anterior) directing vector (X) from A to D
X1cub_lab= cubDA;
X1cub_lab_length= norm(X1cub_lab);
X1cub_lab= X1cub_lab/X1cub_lab_length;

% create lateral directing vector (Z)
Z1cub_lab= cubB-cubA;
Z1cub_lab_length= norm(Z1cub_lab);
Z1cub_lab= Z1cub_lab/Z1cub_lab_length;
```

```matlab
 %create superior directed vector (Y)
Y1cub_lab= cross (Z1cub_lab, X1cub_lab);
Y1cub_lab_length= norm(Y1cub_lab);
Y1cub_lab= Y1cub_lab/ Y1cub_lab_length;

%Ensure all vectors are truly orthogonal redo cross products one more
%time using newly created vectors...

Zcub_lab= cross(X1cub_lab, Y1cub_lab);
Zcub_lab_length= norm(Zcub_lab);
Zcub_lab= Zcub_lab/Zcub_lab_length;

Ycub_lab= cross(Zcub_lab, X1cub_lab);
Ycub_lab_length= norm(Ycub_lab);
Ycub_lab= Ycub_lab/Ycub_lab_length;

Xcub_lab= cross(Ycub_lab, Zcub_lab);
Xcub_lab_length= norm(Xcub_lab);
Xcub_lab= Xcub_lab/Xcub_lab_length;


%Origin of T-matrix will be cubA
origin_cub= cubA;

%Tmatrix cuboid wrt lab coordinate system
Tlandmark_cub2lab= [Xcub_lab' Ycub_lab' Zcub_lab' origin_cub'];
Tlandmark_cub2lab= cat(1, Tlandmark_cub2lab, endline);
%Calculate inverse Tmatrix (lab wrt cuboid)
Tlab2cub= inv(Tlandmark_cub2lab);


%Navicular coordinate system
%Obtain navicular landmark from user. Change navicular data base if this
%is not in general bone landmark directory
anat_nav_landmarks_dir= data_dir;
%anat_nav_landmarks_file = input('Enter the name of the file with the
navicular anatomical landmarks from Rhino: ','s');
anat_nav_landmarks_filename=strcat('landmarks-fluoro-00',file_num,'nav',
'.xls');
anat_nav_landmarks = xlsread([anat_nav_landmarks_dir,
anat_nav_landmarks_filename], 1);
anat_nav_landmarks= anat_nav_landmarks(:,1:3);


%navA- navicular tuberosity (medial landmark)
navA= anat_nav_landmarks (1, 1:3);
%navB- most superior part of the navicular (generally located near the
%middle of the navicular but slightly to the lateral side)
navB= anat_nav_landmarks (2, 1:3);
%navC- triangular protrusion of navicular on the plantar side where the
%talus interacts with the bone.
navC= anat_nav_landmarks (3, 1:3);

navBC= navB-navC;
navCA= navC-navA;
midBC= (navB+navC)/2;
```

```matlab
%create superior directed vector (Y)

Y1nav_lab= navBC;
Y1nav_lab_length= norm(Y1nav_lab);
Y1nav_lab= Y1nav_lab/Y1nav_lab_length;

%create lateral directing vector (Z)

Z1nav_lab= navA-midBC;
Z1nav_lab_length= norm(Z1nav_lab);
Z1nav_lab= Z1nav_lab/Z1nav_lab_length;

%create proximal (or anterior) directed vector (X)

X1nav_lab= cross (Y1nav_lab, Z1nav_lab);
X1nav_lab_length= norm(X1nav_lab);
X1nav_lab= X1nav_lab/X1nav_lab_length;

%Enusre all vectors are truely orthogonal redo cross products one more
%time using newly created vectors...

Ynav_lab= cross(Z1nav_lab, X1nav_lab);
Ynav_lab_length= norm(Ynav_lab);
Ynav_lab= Ynav_lab/Ynav_lab_length;

Znav_lab= cross(X1nav_lab, Ynav_lab);
Znav_lab_length= norm(Znav_lab);
Znav_lab= Znav_lab/Znav_lab_length;

Xnav_lab= cross(Ynav_lab, Znav_lab);
Xnav_lab_length= norm(Xnav_lab);
Xnav_lab= Xnav_lab/Xnav_lab_length;

%origin of navicular (navA)
origin_nav= navA;

%T-matrix navicular wrt lab coordinate system
Tlandmark_nav2lab= [Xnav_lab' Ynav_lab' Znav_lab' origin_nav'];
Tlandmark_nav2lab= cat(1, Tlandmark_nav2lab, endline);


%Fibula/Tibia coordinate system
%Obtain tibia/fibular landmark information from the user. If this is not
%located in th3 directory
anat_tibfib_landmarks_dir= data_dir;
%anat_tibfib_landmarks_file = input('Enter the name of the file with the
tibia/fibula anatomical landmarks from Rhino: ','s');
anat_tibfib_landmarks_filename=strcat('landmarks-fluoro-
00',file_num,'tibfib', '.xls');
anat_tibfib_landmarks = xlsread([anat_tibfib_landmarks_dir,
anat_tibfib_landmarks_filename], 1);
anat_tibfib_landmarks= anat_tibfib_landmarks(:,:);
```

```matlab
%fibA- lateral malleolus on fibula
fibA= anat_tibfib_landmarks (1, 1:3);
%tibB- medial malleolus on tibia
tibB= anat_tibfib_landmarks (2, 1:3);
%tibC-  most medial portion of the top of the tibia
tibC= anat_tibfib_landmarks (3, 1:3);
%tibD- most lateral portion of the top of the tibia
tibD= anat_tibfib_landmarks (4, 1:3);
%%fibE- most medial portion of the top of the fibula
fibE= anat_tibfib_landmarks (5, 1:3);
%fibF- most lateral portion of the top of the fibula
fibF= anat_tibfib_landmarks (6, 1:3);
%midpoint between line drawn between fibA and tibB (not as accurate so
%removed)
%midAB1= anat_tibfib_landmarks (7, 1:3);

%midpoint of fibA and tibB
midAB= (fibA+tibB)/2;
%midpoint betweeen fibC and fibf
midCF= (tibC+fibF)/2;

%create lateral directing vector (Z)
Z1tibfib_lab= midAB-fibA;
Z1tibfib_lab_length= norm(Z1tibfib_lab);
Z1tibfib_lab= Z1tibfib_lab/Z1tibfib_lab_length;

%create superior directing vector (Y)
Y1tibfib_lab= midCF- midAB;
Y1tibfib_lab_length= norm(Y1tibfib_lab);
Y1tibfib_lab= Y1tibfib_lab/Y1tibfib_lab_length;

%create anterior directing vector (X)
X1tibfib_lab= cross(Y1tibfib_lab, Z1tibfib_lab);
X1tibfib_lab_length= norm(X1tibfib_lab);
X1tibfib_lab= X1tibfib_lab/X1tibfib_lab_length;

%Ensure vectors are all normal to each other (complete cross products
again
%with previously created vectors above)

%superior directing
Ytibfib_lab= cross(X1tibfib_lab, Z1tibfib_lab);
Ytibfib_lab_length= norm(Ytibfib_lab);
Ytibfib_lab= Ytibfib_lab/Ytibfib_lab_length;

%lateral directing
Ztibfib_lab= cross(X1tibfib_lab, Ytibfib_lab);
Ztibfib_lab_length= norm(Ztibfib_lab);
Ztibfib_lab= Ztibfib_lab/Ztibfib_lab_length;

%anterior directing
Xtibfib_lab= cross(Ytibfib_lab, Ztibfib_lab);
Xtibfib_lab_length= norm(Xtibfib_lab);
Xtibfib_lab= Xtibfib_lab/Xtibfib_lab_length;
```

```
 %orgin tib fib, midpoint of AB
origin_tibfib= midAB;


%T-matrix navicular wrt lab coordinate system
Tlandmark_tibfib2lab= [Xtibfib_lab' Ytibfib_lab' Ztibfib_lab'
origin_tibfib'];
Tlandmark_tibfib2lab= cat(1, Tlandmark_tibfib2lab, endline);


%Inverse of T-matrix... lab wrt. tibfib
Tlab2tibfib= inv(Tlandmark_tibfib2lab);


%manipulate T-matrices to form correct angles:


%Tmatrix cuboid wrt calcaneus
Tcub2cal= Tlab2cal * Tlandmark_cub2lab;
%Tmatrix navicular wrt calcaneus
Tnav2cal= Tlab2cal * Tlandmark_nav2lab;


%Tmatrix calcaneus wrt tibfib
Tcal2tibfib= Tlab2tibfib*Tlandmark_cal2lab;


%Tmatrix cuboid wrt tibfib
Tcub2tibfib= Tlab2tibfib*Tlandmark_cub2lab;


%Tmatrix navicular wrt tibfib
Tnav2tibfib= Tlab2tibfib*Tlandmark_nav2lab;


%EULER ANGLE ANALYSIS (cuboid wrt calcaneus)
alpha1= atan2((-Tcub2cal(1,2)), Tcub2cal(2,2));
gamma1= atan2 (-Tcub2cal(1,3), Tcub2cal(3,3));
beta1= atan2(Tcub2cal(2,3), Tcub2cal(3,3)*cos(gamma1));


alpha1= alpha1*180/pi;
beta1= beta1*180/pi;
gamma1= gamma1*180/pi;


%EULER ANGLE ANALYSIS ZXY analysis (navicular wrt calcaneus)

alpha2= atan2((-Tnav2cal(1,2)), Tnav2cal(2,2));
gamma2= atan2 (-Tnav2cal(1,3), Tnav2cal(3,3));
beta2= atan2(Tnav2cal(2,3), Tnav2cal(3,3)*cos(gamma2));


alpha2= alpha2*180/pi;
beta2= beta2*180/pi;
gamma2= gamma2*180/pi;


%EULER ANGLE ANALYSIS ZXY analysis (calcaneus wrt tibfib)

alpha3= atan2((-Tcal2tibfib(1,2)), Tcal2tibfib(2,2));
gamma3= atan2 (-Tcal2tibfib(1,3), Tcal2tibfib(3,3));
beta3= atan2(Tcal2tibfib(2,3), Tcal2tibfib(3,3)*cos(gamma3));


alpha3= alpha3*180/pi;
beta3= beta3*180/pi;
```

```matlab
gamma3= gamma3*180/pi;


%Euler Angle analysis ZXY (navicular wrt tibfib)
alpha4= atan2((-Tnav2tibfib(1,2)), Tnav2tibfib(2,2));
gamma4= atan2 (-Tnav2tibfib(1,3), Tnav2tibfib(3,3));
beta4= atan2(Tnav2tibfib(2,3), Tnav2tibfib(3,3)*cos(gamma4));


alpha4= alpha4*180/pi;
beta4= beta4*180/pi;
gamma4= gamma4*180/pi;


%Euler Angle analysis ZXY (cuboid wrt tibfib)
alpha5= atan2((-Tcub2tibfib(1,2)), Tcub2tibfib(2,2));
gamma5= atan2 (-Tcub2tibfib(1,3), Tcub2tibfib(3,3));
beta5= atan2(Tcub2tibfib(2,3), Tcub2tibfib(3,3)*cos(gamma5));


alpha5= alpha5*180/pi;
beta5= beta5*180/pi;
gamma5= gamma5*180/pi;


%OUTPUT ROWS Information (labelling the rows)
%Inversion/eversion
label_info1a={'Inversion/Eversion'};
output_write= fullfile(data_dir, data_file1);
xlswrite(output_write, label_info1a, 1, 'A9');
label_info1={'cal wrt tibfib', 'nav wrt cal', 'cub wrt cal', 'nav
wrt.tib','cub wrt tibfib'};
output_write= fullfile(data_dir, data_file1);
xlswrite(output_write, label_info1, 1, 'A10');



%OUTPUT ROWS Information (labelling the rows)
%Plantar Dorsi
label_info2a={'Dorsi/Plantar Flextion'};
output_write= fullfile(data_dir, data_file1);
xlswrite(output_write, label_info2a, 1, 'A5');
label_info2={'cal wrt tibfib', 'nav wrt cal', 'cub wrt cal', 'nav
wrt.tib','cub wrt tibfib'};
output_write= fullfile(data_dir, data_file1);
xlswrite(output_write, label_info2, 1, 'A6');


%OUTPUT ROWS Information (labelling the rows)
%Internal/External
label_info3a={'Internal/External Rotation'};
output_write= fullfile(data_dir, data_file1);
xlswrite(output_write, label_info3a, 1, 'A1');
label_info3={'cal wrt tibfib', 'nav wrt cal', 'cub wrt cal', 'nav
wrt.tib','cub wrt tibfib'};
output_write= fullfile(data_dir, data_file1);
xlswrite(output_write, label_info3, 1, 'A2');


%OUTPUT INFORMATION CUBOID WRT CALCANEUS
%beta1- inversion/eversion cub wrt cal
Beta1_angle_info = {beta1};
output_write= fullfile(data_dir, data_file1);
```

```matlab
xlswrite(output_write, Beta1_angle_info, 1, 'C3')

%alpha1- plantar/dorsi cub wrt cal
Alpha1_angle_info= { alpha1};
output_write=fullfile(data_dir, data_file1);
xlswrite(output_write, Alpha1_angle_info, 1, 'C7')

%gamma1- internal external rotation cub wrt cal
Gamma1_angle_info= {gamma1};
output_write=fullfile(data_dir, data_file1);
xlswrite(output_write, Gamma1_angle_info, 1, 'C11')


%OUTPUT INFORMATION NAVICULAR WRT CALCANEUS
%beta2- inversion/eversion nav wrt cal
Beta2_angle_info = {beta2};
output_write= fullfile(data_dir, data_file1);
xlswrite(output_write, Beta2_angle_info, 1, 'B3')

%alpha2- plantar/dorsi nav wrt cal
Alpha2_angle_info= {alpha2};
output_write=fullfile(data_dir, data_file1);
xlswrite(output_write, Alpha2_angle_info, 1, 'B7')

%gamma2- internal external rotation nav wrt cal
Gamma2_angle_info= {gamma2};
output_write=fullfile(data_dir, data_file1);
xlswrite(output_write, Gamma2_angle_info, 1, 'B11')

%OUTPUT INFORMATION CALCANEUS WRT TIBIA/FIBULA
%beta3- inversion/eversion cal wrt tibfib
Beta3_angle_info = {beta3};
output_write= fullfile(data_dir, data_file1);
xlswrite(output_write, Beta3_angle_info, 1, 'A3')

%alpha3- plantar/dorsi cal wrt tibfib
Alpha3_angle_info= {alpha3};
output_write=fullfile(data_dir, data_file1);
xlswrite(output_write, Alpha3_angle_info, 1, 'A7')

%gamma3- internal external rotation cal wrt tibfib
Gamma3_angle_info= {gamma3};
output_write=fullfile(data_dir, data_file1);
xlswrite(output_write, Gamma3_angle_info, 1, 'A11')


%OUTPUT INFORMATION NAVICULAR WRT TIBIA/FIBULA
%beta4- inversion/eversion nav wrt tibfib
Beta4_angle_info = {beta4};
output_write= fullfile(data_dir, data_file1);
xlswrite(output_write, Beta4_angle_info, 1, 'D3')

%alpha4- plantar/dorsi nav wrt tibfib
Alpha4_angle_info= {alpha4};
```

```matlab
output_write=fullfile(data_dir, data_file1);
xlswrite(output_write, Alpha4_angle_info, 1, 'D7')

%gamma4- internal external rotation nav wrt tibfib
Gamma4_angle_info= {gamma4};
output_write=fullfile(data_dir, data_file1);
xlswrite(output_write, Gamma4_angle_info, 1, 'D11')


%OUTPUT INFORMATION CUBOID WRT TIBIA/FIBULA
%beta5- inversion/eversion cub wrt tibfib
Beta5_angle_info = {beta5};
output_write= fullfile(data_dir, data_file1);
xlswrite(output_write, Beta5_angle_info, 1, 'E3')

%alpha5- plantar/dorsi cub wrt tibfib
Alpha5_angle_info= {alpha5};
output_write=fullfile(data_dir, data_file1);
xlswrite(output_write, Alpha5_angle_info, 1, 'E7')

%gamma5- internal external rotation cub wrt tibfib
Gamma5_angle_info= {gamma5};
output_write=fullfile(data_dir, data_file1);
xlswrite(output_write, Gamma5_angle_info, 1, 'E11')
end
```

C.2-TWO-DIMENSIONAL ANALYSIS: ANGLE CALCULATION CODE

```
%*********************************************************************
*****
% Program: Angle_Calc.m
% Measure angles from output of 'Find_points.m'
% Created by: Kristen Bushey
% Date Modified: June 15, 2011
%---------------------------------------------------------------------
-----


%Obtain excel file name from user with output points from Find_Points.m
data_folder = input('Enter the name of the folder that contains the
points files: ','s');
data_dir = ['M:\IntraOp\' data_folder '\'];

% Obtain information about a range of files if required
num_files = input('Enter the number of files to be analyzed: ');
start_file = input('Enter the value of the first file in the series: ');
data_file1 = input('Enter the start of the name of the file which
contains the object data: ','s');

i = 0;

for z = start_file:(start_file + num_files - 1)
    i = i + 1;

    if z < 10
        file_num = int2str(z);
        points_filename = strcat(data_file1, '-000', file_num,
'_points.xls');
    elseif (z >= 10 && z < 100)
        file_num = int2str(z);
        points_filename = strcat(data_file1, '-00', file_num,
'_points.xls');
    elseif (z >= 100 && z < 1000)
        file_num = int2str(z);
        points_filename = strcat(data_file1, '-000', file_num,
'_points.xls');
    elseif (z >= 1000 && z < 10000)
        file_num = int2str(z);
        points_filename = strcat(data_file1, '-000', file_num,
'_points.xls');
    else
        file_num = int2str(z);
        points_filename = strcat(data_file1, '-00', file_num,
'_points.xls');
    end

    % Pixel coordinates of chosen points (x,y)
    points2use = xlsread([data_dir,points_filename],1,'B1:C4');

    % Calculating angle between two lines created from four selected
points
    line_1_x = points2use(1,1)-points2use(2,1);
```

```
        line_1_y = points2use(1,2)-points2use(2,2);
        line_2_x = points2use(3,1)-points2use(4,1);
        line_2_y = points2use(3,2)-points2use(4,2);
        line_1 = [line_1_x line_1_y];
        line_2 = [line_2_x line_2_y];
        line_1_2_product = dot(line_1, line_2);
        line_1_length = norm(line_1);
        line_2_length = norm(line_2);
        line_1_2_L = line_1_2_product/(line_1_length*line_2_length);
        line_1_u = line_1/line_1_length;
        line_2_u = line_2/line_2_length;

        if ((line_2_u(2)-line_1_u(2))<0)
            angle = -acosd(line_1_2_L);
        else
            angle = acosd(line_1_2_L);
        end

        %output_filename = strrep(points_filename, 'points', 'analyzed');
        %output_write = fullfile(data_dir, output_filename);
        output_write = fullfile(data_dir, [data_file1, '_analyzed.xls']);
        points_analyzed = [line_1 line_2 angle];
        %xlswrite(output_write, points_analyzed, 1');
        range = ['A', int2str(i)];
        xlswrite(output_write, points_analyzed, 1, range);

end
```

APPENDIX D- ADDITIONAL DATA FOR CHAPTER 2

The standard deviations calculated for the normal population during barefoot, running shoe, foam soft orthotic and foam hard orthotic are summarized in this section.

Table D.1: The average standard deviation for each subject is shown below for internal rotation. The average standard deviation was calculated across all normal subjects.

Internal Rotation						
Condition	Subject	cal wrt tibfib	nav wrt cal	cub wrt cal	nav wrt tibfib	cub wrt tibfib
Barefoot	1	0.47	0.26	0.67	0.45	1.15
	2	0.58	0.59	0.15	1.65	0.64
	10	0.98	2.46	0.89	3.14	1.54
	11	1.96	1.33	9.27	1.24	4.75
	23	0.86	1.31	1.00	11.87	0.78
	Avg. SD	**0.97**	**1.19**	**2.40**	**3.67**	**1.77**
Neutral Cushion Running Shoe	1	1.53	0.94	1.37	1.51	0.54
	2	3.69	2.03	3.02	2.85	1.01
	10	0.92	1.41	1.59	1.77	0.52
	11	1.14	0.92	1.23	0.66	0.40
	23	2.63	2.39	2.39	3.66	1.62
	Avg. SD	**1.98**	**1.54**	**1.92**	**2.09**	**0.82**
Foam Soft	1	4.15	3.47	2.67	2.30	1.55
	2	0.74	2.69	1.06	0.98	0.93
	10	0.72	2.32	1.19	0.26	0.93
	11	2.38	0.12	0.00	3.25	0.67
	23	2.76	1.43	1.62	2.43	1.90
	Avg. SD	**2.15**	**2.01**	**1.31**	**1.84**	**1.20**
Foam Hard	1	1.94	2.41	3.33	0.29	1.59
	2	2.48	2.02	0.36	3.66	1.81
	10	4.71	0.33	10.04	7.42	10.12
	11	5.02	2.94	4.43	1.86	1.10
	23	4.19	2.30	0.21	3.56	2.01
	Avg. SD	**3.67**	**2.00**	**3.67**	**3.36**	**3.33**

Table D.2: The average standard deviation for each subject is shown below for plantarflexion. The average standard deviation was calculated across all normal subjects.

Plantarflexion						
Condition	Subject	cal wrt tibfib	nav wrt cal	cub wrt cal	nav wrt tibfib	cub wrt tibfib
Barefoot	**1**	0.19	0.52	4.56	0.64	3.64
	2	0.84	1.38	0.93	1.45	0.86
	10	0.59	2.64	8.47	3.67	2.31
	11	1.11	0.65	6.26	1.30	4.74
	23	1.99	5.28	6.70	9.04	1.70
	Avg. SD	**0.94**	**2.09**	**5.39**	**3.22**	**2.65**
Neutral Cushion Running Shoe	**1**	0.96	4.83	2.55	6.39	1.52
	2	1.52	1.05	6.18	1.39	3.60
	10	1.84	2.61	5.69	2.20	1.59
	11	1.19	1.31	5.03	0.83	2.44
	23	0.35	0.23	0.82	2.12	3.12
	Avg. SD	**1.17**	**2.01**	**4.05**	**2.59**	**2.45**
Foam Soft	**1**	1.55	1.43	12.41	2.58	2.18
	2	1.35	1.91	2.55	0.78	0.44
	10	1.25	0.97	0.95	0.65	1.53
	11	1.26	0.22	0.00	0.95	0.87
	23	2.04	1.54	7.11	2.46	3.00
	Avg. SD	**1.49**	**1.21**	**4.60**	**1.48**	**1.60**
Foam Hard	**1**	1.22	0.94	6.17	1.23	1.42
	2	1.55	0.32	5.00	4.05	2.41
	10	1.99	0.29	11.69	2.25	5.99
	11	1.84	1.71	3.46	1.04	1.26
	23	3.53	1.35	10.11	0.30	1.49
	Avg. SD	**2.02**	**0.92**	**7.29**	**1.77**	**2.51**

Table D.3: The average standard deviation for each subject is shown below for inversion. The average standard deviation was calculated across all normal subjects.

Inversion						
Condition	**Subject**	**cal wrt tibfib**	**nav wrt cal**	**cub wrt cal**	**nav wrt tibfib**	**cub wrt tibfib**
Barefoot	**1**	0.34	0.13	6.18	0.16	5.14
	2	0.44	0.23	0.59	0.59	2.08
	10	0.82	1.53	14.90	1.67	4.61
	11	2.59	0.98	12.63	2.88	5.75
	23	3.37	5.60	4.79	7.09	4.96
	Avg. SD	**1.51**	**1.69**	**7.82**	**2.48**	**4.51**
Neutral Cushion Running Shoe	**1**	0.96	0.41	6.63	1.53	3.18
	2	6.22	1.03	5.32	3.62	1.95
	10	1.34	0.96	6.64	2.11	1.52
	11	0.84	0.26	3.82	0.81	1.67
	23	2.51	0.70	4.47	2.80	3.35
	Avg. SD	**2.37**	**0.67**	**5.38**	**2.17**	**2.33**
Foam Soft	**1**	4.45	4.25	12.18	1.07	3.14
	2	1.45	1.55	1.87	0.21	1.69
	10	0.77	0.29	1.98	0.43	0.82
	11	2.83	0.00	0.00	2.71	2.11
	23	1.99	1.56	2.18	0.72	1.59
	Avg. SD	**2.30**	**1.53**	**3.64**	**1.03**	**1.87**
Foam Hard	**1**	1.12	0.39	9.50	0.83	3.98
	2	3.45	0.83	3.10	2.94	1.51
	10	5.33	0.27	14.96	6.28	1.38
	11	3.32	1.31	4.48	1.62	2.11
	23	1.12	0.63	6.91	1.77	0.99
	Avg. SD	**2.87**	**0.68**	**7.79**	**2.69**	**2.00**

APPENDIX E- ADDITIONAL DATA FOR CHAPTER 3

Table E.1: The standard deviation associated with the angle measurements in all three planes of motion for the soft plaster casted orthotic. All entries in degrees.

Soft Plaster Casted Orthotic						
Measurement	**Subject#**	**cal wrt tibfib**	**nav wrt cal**	**cub wrt cal**	**nav wrt tibfib**	**cub wrt tibfib**
Internal Rotation	1	0.72	1.28	1.86	1.13	2.40
	2	4.30	1.24	5.54	2.01	1.53
	10	1.52	1.50	0.71	0.80	0.77
	11	0.57	0.93	0.64	0.33	0.20
	23	0.43	1.25	0.96	0.92	1.04
	Average	**1.51**	**1.24**	**1.94**	**1.04**	**1.19**
Plantarflexion	1	3.98	2.07	3.07	3.50	1.65
	2	4.98	5.67	1.23	1.75	2.57
	10	4.55	2.65	0.96	1.89	0.40
	11	10.71	2.03	1.86	3.97	3.60
	23	9.02	1.17	2.01	1.66	1.17
	Average	**6.65**	**2.72**	**1.83**	**2.55**	**1.88**
Inversion	1	4.08	2.14	2.54	0.97	3.22
	2	2.99	5.13	1.03	1.20	2.56
	10	3.46	0.77	1.63	0.47	0.31
	11	5.09	2.33	2.73	1.68	3.00
	23	4.74	1.81	0.96	1.36	1.06
	Average	**4.07**	**2.43**	**1.78**	**1.14**	**2.03**

Table E.2: The standard deviation associated with the angle measurements in all three planes of motion for the rigid plaster casted orthotic. All entries in degrees.

Rigid Plaster Casted Orthotic						
Measurement	**Subject#**	**cal wrt tibfib**	**nav wrt cal**	**cub wrt cal**	**nav wrt tibfib**	**cub wrt tibfib**
Internal	1	0.91	0.38	0.96	4.17	1.50
	2	1.32	0.80	1.70	1.77	2.58
	10	0.45	0.84	0.78	0.61	1.21
	11	0.70	1.02	0.53	2.15	0.64
	23	4.00	1.33	0.68	7.84	4.77
	Average	**1.48**	**0.87**	**0.93**	**3.31**	**2.14**
Plantarflexion	1	2.48	1.80	1.06	4.47	1.41
	2	3.51	3.47	1.48	1.65	3.08
	10	3.46	1.10	1.50	2.05	1.76
	11	11.41	1.16	2.03	3.02	3.46
	23	37.12	2.31	2.05	2.22	1.62
	Average	**11.60**	**1.97**	**1.62**	**2.68**	**2.26**
Inversion	1	3.79	1.00	1.21	1.15	3.82
	2	0.71	2.92	0.74	0.96	2.94
	10	0.92	0.99	1.51	0.45	1.55
	11	1.96	2.13	2.76	3.21	3.49
	23	22.90	2.06	1.26	2.59	1.44
	Average	**6.06**	**1.82**	**1.50**	**1.67**	**2.65**

APPENDIX F- STATISTICAL ANALYSIS

This appendix contains the statistical results for all subjects.

Only statistical analyses are included for those that resulted

in a significant finding.

F.1   STATISTICAL RESULTS

No results in this study were found to be significant using the ANOVA repeated measures approach.

CURRICULUM VITAE

KRISTEN M. BUSHEY

POST-SECONDARY EDUCATION:

Master of Engineering Science- Mechanical and Materials Engineering

University of Western Ontario (2009-2012)

Bachelor of Engineering- Biological Engineering

University of Guelph (2003-2008)

TEACHING EXPERIENCE:

Teaching Assistant

MME 2213

Engineering Dynamics

University of Western Ontario (2010)

Teaching Assistant

MME 3379

Materials Selection

University of Western Ontario (2010)

Teaching Assistant

MME 3334

Thermodynamics II

University of Western Ontario (2011)

AWARDS AND HONOURS:

DEAN'S HONOUR LIST (2003-2004, 2008)

POSTERS:

Bushey, K, Balsdon, M, Dombroski, C, Jenkyn, T.R (August 2011). A Comparison of The Affect of Soft and Rigid Custom-made Corrective Orthotics And Over-the-counter Proprioceptive Feedback Orthotics on Hindfoot Pronation During Gait: A Two-dimensional Dynamic Fluoroscopic Study**.** American Society of Biomechanics Conference, Long Beach, CA, USA.

Balsdon M, **Bushey K**, Dombroski C, Jenkyn T. Investigating In-Vivo Motion of the Medial Longitudinal Arch with Different Orthotic Types Using Lateral Fluoroscopy Images During Dynamic Gait (August 2011). American Society of Biomechanics Conference, Long Beach, CA, USA.